


Doctorate in Astronomy, Astrophysics, and Space Science

Cycle XXXIV

Revealing the Chemical Evolution History of the Milky Way Halo with RR Lyrae Stars

Juliana Crestani

Supervisors: Giuseppe Bono (Tor Vergata), Alan Alves-Brito (UFRGS)
Coordinators: Nicola Vittorio (Tor Vergata), Kepler de Souza Oliveira (UFRGS)
Deputy Coordinator: Francesco Piacentini (Sapienza)

Rome, December 3rd, 2021

Abstract

The Galactic Halo is the component of the Milky Way that can preserve the clearest signatures of the accretion of satellites required for the built-up of the Galaxy according to the Λ cold dark matter paradigm. The nature of these primordial satellites, their relationship to the current dwarf galaxies distributed around the Milky Way, and the fraction of the current Halo stellar population that originated from them are all open questions. The abundance of different chemical elements carries information about the enrichment timescale and physical parameters (e.g. mass distribution function, star formation rate) of the stellar system where a given star was formed. Thus, studying a variety of elements is fundamental in order to properly identify the progenitor systems of different stars, to constrain models of galactic formation, and to understand stellar nucleosynthesis itself. In particular, measurements of heavier species and robust ages for stellar tracers are severely lacking.

The RR Lyrae stars (RRLs) are old ($\geq$ 10 Gyr) radial pulsators with well defined period-luminosity relations in near-infrared (NIR) bands. These relations allow for precise distance determinations and make the RRLs excellent probes of the chemical structure of the Halo. The RRLs are classified according to their pulsation mode, with the RRab pulsating in the fundamental mode, the RRc in the first overtone, and the RRd, very few in number, in a mixed mode. High resolution spectroscopic studies of these stars are scarce. Such studies are fundamental for the investigation of α elements, Fe-peak elements, and neutron(n)-capture elements. They are also necessary for the calibration of photometric indexes and low resolution (LR) spectroscopic estimates of metallicity that can be applied to large samples.

In this work, we used data collected with nine high-resolution (HR) spectrographs installed at eight different large telescopes and by two LR surveys (SEGUE-SDSS, LAMOST). We applied the methodology of HR spectroscopy to a sample of 162 RRLs (138 RRab, 23 RRc, 1 RRd) covering a wide range in metallicity ([Fe/H] from -3.2 to 0.2). Our spectroscopic investigaton is based on a list of atomic lines with updated transition parameters. We meticulously removed lines that showed evidence of blending or of dependence on effective temperature. Using this line list, we obtained measurements of the light odd-Z elements Na and Al; the α elements Mg, Si, S, Ca, and Ti; the Fe-peak elements Sc, V, Cr, Mn, Fe, Co, Ni, Cu, and Zn; and the n-capture elements Sr, Y, Zr, Ba, La, Ce, Pr, Nd, and Eu. In particular, our investigation includes the bona fide tracer of the s-process Ba, its r-process counterpart Eu, and the poorly studied rare earth Pr. Using stars in common with other HR literature investigations, we brought abundance measurements of another 85 RRLs (65 RRab, 20 RRc) into our chemical abundance scale.

We used these HR, high quality measurements to probe the chemical evolution history of the Halo, and also to compare it to the other Galactic components and nearby dwarf galaxies. In this regard, the RRLs present the unique advantage of being old tracers with precise distance measurements, while other commonly employed stellar populations

have very poorly constrained ages and distances. We found that a sample of metal-rich, α-poor RRLs is present at low Galactic heights. In the [α/Fe] versus [Fe/H] plane, this sample displays a smooth continuity with the rest of the RRLs in the Halo, pointing to a shared origin. Furthermore, this sample traces the metal-rich tail of the Halo that is poorly covered by other stellar tracers and displays a behavior with metallicity that is at odds with the other Galactic components (Bulge and Disk), but similar to the Sagittarius dwarf spheroidal. We performed the same comparison for the other chemical species and discussed the effects of NLTE corrections, different line lists, and systematics due to evolutionary effects. By applying the same HR analysis to a sample of six non-variable giants and seven field dwarfs, we showed that differences in abundance, especially for α elements, between field stars of varied ages and the RRLs are intrinsic.

The ΔS method provides metallicity estimates for RRLs with LR spectra. The number of available LR spectra for RRLs is about two orders of magnitude larger than HR spectra. Therefore, a finely tuned LR metallicity estimator is an extremely valuable counterpart to the more accurate but scarcer HR measurements. The ΔS method results are widely used in the calibration of photometric methods such as Fourier parameter decomposition. Until recently, this method was only applied to RRab stars outside the phase interval of the rising branch of the light curve and relied on the metallicity scale of Zinn & West (1984), which is not linear with modern HR measurements. Using the HR results for 143 RRLs (111 RRab, 32 RRc), we developed a brand new calibration of the ΔS method in the same metallicity scale as our HR results. It can be applied to the whole pulsation cycle of both RRab and RRc pulsators, with preliminary evidence that it is valid for the RRd as well. We applied this new calibration to a sample of 7768 RRLs (5196 RRab, 2572 RRc) for which no HR spectra are available and found excellent agreement with the results derived in HR.

The complete sample with 247 RRLs studied in HR is the largest and most homogeneous data set of old stellar tracers studied in the literature. It provides constrains on all major chemical families for the oldest stellar component in the Galaxy covering 3 dex in metallicity. Our sample covers a significant fraction of the Halo starting at a Galactocentric distance of approximately 4 kpc, with HR measurements reaching 26 kpc, and LR metallicity estimates extending as far as 150 kpc. These results are crucial not only for Galactic formation modeling but also in the investigation of nucleosynthetic processes due to its homogeneity in both abundance scale and age, its spatial distribution, and its wide metallicity coverage. Furthermore, the new calibration of the ΔS method is applicable, for the first time, to RRLs of all pulsation modes observed at any phase, without the requirement of detailed photometric studies or carefully timed observations. The work performed in this thesis has also been partially or fully employed by our group in various investigations, including probing the fine structure of the Bailey diagram and its relation to the Oosterhoff dichotomy, the development of new barycentric velocity estimators and velocity curve templates, and a new calibration of the Fourier parameter decomposition method using our new metallicity scale.

Abstract

O Halo Galáctico é o componente da Via Láctea que preserva os traços mais claros da acreção de satélites responsável pela formação da Galáxia de acordo com o paradigma Λ-CDM. A natureza desses satélites primordiais, sua relação com as galáxias anãs atualmente distribuídas ao redor da Via Láctea, e a fração da população estelar do Halo que se originou neles são todas questões em aberto. A abundância de diferentes elementos químicos traz informações sobre o tempo de enriquecimento e parâmetros físicos (por exemplo, função de distribuição de massa, taxa de formação de estrelas) do sistema estelar onde uma determinada estrela se formou. Assim, o estudo de uma variedade de elementos é fundamental para identificar adequadamente os sistemas progenitores de diferentes estrelas, para restringir modelos de formação galáctica e para compreender a própria nucleossíntese estelar. Em particular, faltam dandos observacionais para as abundâncias das espécies mais pesadas assim como idades bem determinadas para as estrelas utilizadas.

As estrelas do tipo RRL têm idades $\geq$ 10 Gyr e apresentam pulsações radiais com relações período-luminosidade bem definidas no infravermelho. Essas relações permitem uma determinação precisa da distância da estrela. Assim, elas são excelentes traçadoras da estrutura química do Halo. As RRLs são classificadas de acordo com seu modo de pulsação, com RRab apresentando o modo fundamental, RRc o primeiro harmônico, e RRd um modo misto. Estudos espetroscópicos em alta resolução (HR) dessas estrelas são limitados. Tais estudos são essenciais para a investigação de diversas espécies químicas como os elementos α, aquelas do pico do Fe, e aquelas produzidos por captura de nêutrons. Eles também são necessários para a calibração de índices fotométricos e estimativas de metalicidade baseadas em espectroscopia de baixa resolução, que podem ser aplicados a grandes amostras.

Neste trabalho, utilizamos dados coletados com nove espectrógrafos HR instalados em oito grandes telescópios diferentes e por duas pesquisas em baixa resolução (LR, SEGUE-SDSS, LAMOST). Aplicamos a metodologia da espectroscopia HR a uma amostra de 162 RRLs (138 RRab, 23 RRc, 1 RRd) cobrindo uma ampla gama em metalicidade ([Fe/H] de -3,2 a 0,2). Nossa investigação espectroscópica é baseada em uma lista de linhas atômicas com parâmetros de transição atualizados. Removemos meticulosamente as linhas que mostravam evidência de blending ou dependência da temperatura efetiva. Usando esta lista de linhas, obtivemos medições dos elementos leves Na e Al; os elementos α Mg, Si, S, Ca, e Ti; os elementos do pico do Fe Sc, V, Cr, Mn, Fe, Co, Ni, Cu, e Zn; e os elementos formados pela captura de nêutrons Sr, Y, Zr, Ba, La, Ce, Pr, Nd, e Eu. Em particular, nossa investigação inclui Ba, formado principalemente pelo processo s, Eu, seu homólogo do processo r, e Pr que é pouco estudado. Usando estrelas em comum com outras investigações da literatura HR, transformamos medidas de abundância de outras 85 RRLs (65 RRab, 20 RRc) para nossa escala de abundância química.

Utilizamos estas medidas HR de alta qualidade para sondar a história da evolução química do Halo, e também para compará-la com outros componentes Galácticos e

galáxias anãs próximas. A este respeito, os RRLs apresentam a vantagem única de serem velhas e terem distância bem determinadas, enquanto outras populações estelares geralmente empregadas têm idades e distâncias ambíguas. Descobrimos que uma amostra de RRLs ricas em metal e pobres em elementos α existe em alturas galácticas baixas. No plano [α/Fe] versus [Fe/H], esta amostra exibe uma continuidade com o resto dos RRLs no Halo, sugerindo uma origem comum. Além disso, esta amostra traça a população rica em metal do Halo que é mal representada por outras populações estelares e exibe um comportamento com metalicidade em desacordo com os outros componentes galácticos (Bojo e Disco), mas semelhante a anã esferoidal em Sagitário. Realizamos a mesma comparação para as outras espécies químicas e discutimos os efeitos das correções NLTE, diferentes listas de linhas e efeitos sistemáticos que surgem da evolução estelar. Ao aplicar a mesma análise HR a uma amostra de seis gigantes não-variáveis e sete anãs de campo, mostramos que as diferenças de abundância, especialmente para elementos α, entre as estrelas de campo de idades variadas e as RRLs são intrínsecas.

O método ΔS fornece estimativas de metalicidade para RRLs com espectros LR. O número de espectros LR disponíveis para RRLs é cerca de duas ordens de magnitude maior do que espectros HR. Portanto, um estimador de metalicidade LR cuidadosamente calibrado é uma alternativa extremamente valiosa já que medidas HR, embora mais mais precisas, são também mais escassas. Os resultados do método ΔS são amplamente utilizados na calibração de métodos fotométricos como a decomposição de parâmetros de Fourier. Até recentemente, este método era válido somente para a estrelas RRab fora do intervalo de fase do ramo ascendente da curva de luz e se baseava na escala de metalicidade de Zinn & West (1984), que não é linear com as medidas modernas em HR. Usando os resultados HR para 143 RRLs (111 RRab, 32 RRc), desenvolvemos uma nova calibração do método ΔS na mesma escala de metalicidade que nossos resultados HR. Ela pode ser aplicado a todo o ciclo de pulsação tanto das variáveis RRab quanto das RRc, com resultados preliminares mostrando que ela é válido também para as variáveis RRd. Aplicamos esta nova calibração a uma amostra de 7768 RRLs (5196 RRab, 2572 RRc) que não possuem espectros HR disponíveis e encontramos excelente concordância com os resultados derivados em HR.

A amostra completa com 247 RRLs estudados em HR é o maior e mais homogêneo conjunto de dados de estrelas velhas estudadas na literatura. Ela fornece dados a todas as principais famílias químicas para o componente estelar mais antigo da Galáxia, cobrindo 3 dex em metalicidade. Nossa amostra cobre uma fração significativa do Halo começando em uma distância Galactocêntrica de aproximadamente 4 kpc, com medidas HR alcançando 26 kpc, e estimativas de metalicidade em LR chegando a 150 kpc. Estes resultados são cruciais não apenas para a modelagem da formação galáctica, mas também para a investigação dos processos nucleossintéticos devido a sua homogeneidade tanto na escala de abundância como na idade, sua distribuição espacial, e sua ampla cobertura em metalicidade. Além disso, a nova calibração do método ΔS é aplicável, pela primeira vez, às RRLs de todos os modos de pulsação observadas em qualquer

fase, sem a exigência de estudos fotométricos detalhados ou observações cuidadosamente cronometradas. O trabalho realizado nesta tese também foi parcial ou totalmente empregado por nosso grupo em várias investigações, incluindo a sondagem da estrutura fina do diagrama Bailey e sua relação com a dicotomia de Oosterhoff, o desenvolvimento de novos estimadores de velocidade baricêntrica e modelos de curvas de velocidade, e uma nova calibração do método de decomposição de parâmetros de Fourier usando nossa nova escala de metalicidade.

Puoi tu annodare
i legami delle Pleiadi
o sciogliere i vincoli di Orione?
Fai tu spuntare a suo tempo
la stella del mattino
o puoi guidare l'Orsa
insieme con i suoi figli?
Conosci tu le leggi del cielo
o ne applichi le norme sulla terra?

Giobbe, 38:31-33

Contents

List of Figures

List of Tables

Chapter 1

Introduction

The hierarchical built up of galaxies is an established theory for decades now. Starting with the seminal work of Searle & Zinn (1978), the scenario of large galaxies[1] forming through the accretion of smaller protogalaxies has firmly superseded that of a single gas cloud that suffers a monolithical collapse (Eggen et al., 1962). The former relies on the existence of protogalactic fragments undergoing their own independent chemical evolution and coalescing into a larger structure. This process results in a galaxy with several different stellar systems somewhat mixed together throughout billions of years of dynamical relaxation and chemical evolution. While clumped together as a single system, these substructures preserve signatures, of varying clarity, of their origin both in the orbits and in the chemistry of the stars that compose them. Indeed, most elements in stellar atmospheres remain largely unchanged during stellar evolution, with the notorious exception of the LiCNO group and a few n-capture elements. Thus, their atmospheric abundances reveal much of the molecular clouds that formed these stars.

Increasingly precise observations of large numbers of stars made it possible to look for substructures directly on chemical and kinematic planes (e.g. Majewski et al., 2003). These substructures contain groups of stars with similar chemistry and kinematics, therefore possibly sharing a same origin such a disrupted galaxy that was long accreted by the Milky Way. This strategy, commonly known as "chemical tagging" (e.g. Freeman & Bland-Hawthorn, 2002; Blanco-Cuaresma et al., 2015), gained much traction with the release of Gaia (Gaia Collaboration et al., 2016) and the Apache Point Observatory Galactic Evolution Experiment (APOGEE, Majewski et al., 2017) data. These long-waited surveys carry a wealth of information on stellar streams, providing powerful constraints for models in the Λ-CDM paradigm that can recover the nature of these Galactic building blocks. Their total mass, their similitude or lack thereof to the current satellite dwarf galaxies, and how much of their stellar population is responsible for the

[1] A scenario where the monolithic collapse of a single gas cloud gives origin to a galaxy can describe the formation of small galaxies such as dwarf spheroidals, but it cannot account for the complexity of larger ones such as the Milky Way.

current observable stellar population of the Milky Way are all open questions.

With its low density and long quenched stellar formation, the Halo is the component of the Galaxy that can best preserve the signatures of satellite accretion. According to some theoretical simulations and observations, it may present a dual nature with an inner and outer Halo with different density distributions, metallicity peaks, and kinematics. On the observational front, there is a lack of consensus regarding the current structure and formation timescale of the Halo, with different studies reaching very discordant conclusions. We will discuss this in depth in the next chapter.

The conflicting results found in the literature are not altogether surprising. Indeed, the Halo is an ancient structure formed by an array of different stellar populations. Many stellar generations separate us from the epoch of Galactic formation and accretion events, making tracers younger than the expected epoch of the accretion event simply inadequate for investigations of Halo formation. Different studies employ different tracers, often with very poor age constraints. The most commonly used tracers are main sequence stars and red giants. The former cover a broad range in stellar masses and ages, while the latter offer only a lower limit in age, being older than ≈0.5-1.0 Gyr. A precise knowledge of metallicity gradients, density profiles, and kinematic properties are all fundamental in disentangling different scenarios of Halo formation. Thus, an accurate description of the a Galactic substructure and its history requires four major ingredients: i) ages, ii) distances, iii) chemical abundances, and iv) a significant sample size. Unsurprisingly, obtaining all of them at once is one of the chimeras of astrophysics.

The determination of stellar ages is a notoriously difficult endeavor in most cases, however, and we must rely on the usage of only certain types of stars that are old (Beaton et al., 2018). Such is the case of the RRL type variables. For the most part, only low mass stars that have lived long enough to exhaust hydrogen in their cores are able to undergo the short period pulsations and create the very characteristic light curves that define these stars. Indeed, it is possible that a younger star, though binary evolution, can present variations that mimic an RRL light curve (Pietrzyński et al., 2012). However, such systems are expected to represent only a small fraction of stars currently identified as RRLs (Prudil et al., 2019), with only one RRL being convincingly shown to belong to a binary system (Kervella et al., 2019). Therefore, a sample of RRLs can firmly be assumed to be over ≈ 10 billion years old.

Other than age, distance is another fundamental parameter that is all but impossible to determine for individual stars except those so close to the Sun that parallaxes can be measured with any certainty. In this, RRLs are also uniquely useful because they obey period-luminosity (PL) and period-luminosity-metallicity (PLZ) relations that can be used to determine their tridimensional position in the Galaxy. Their incredible usefulness has long been counteracted by observational difficulties due to their short period pulsations ($\lesssim$ 1 day) and very high effective temperatures (≈ 6000 to 8000 K), but the current 4 and 8-m class telescopes have remedied these issues. Furthermore, the results of For et al. (2011), Sneden et al. (2017), and Magurno et al. (2019) show that consistent

chemical abundance values can be recovered during most of the pulsation cycle, dispelling fears that the radial motions of the stellar atmosphere would introduce artificial variations in detected abundances. This opened the door for a dramatic increase in the scarse numbers of high resolution spectroscopic studies of RRLs in the literature.

High resolution spectroscopy is the cornerstone of chemical abundance analysis, but the acquisiton and study of HR spectra is still a very time-demanding endeavor. Multiple automated tools exist to extract the necessary parameters for the study of stellar atmospheres (e.g. Smolinski et al., 2011), but unsurprisingly there is a trade-off between sample size and precision of measurements. More importantly, RRL stars are rarely included in large investigations due to the difficulty in observing high quality spectra and deriving well constrained parameters in a variable atmosphere in an automatic fashion. Thus, most studies of RRL stars do not rely on automatic estimates and, consequently, employ only a small sample size. This means that a dedicated effort is needed to properly study a significant sample of RRLs with the methods of HR spectroscopy. It is also essential to develop and calibrate metallicity indicators that can make up for their smaller accuracy with the sheer number of observed stars. This is the case of both the ΔS method and the Fourier parameter decomposition method. The ΔS method makes use of low resolution (R $\approx$ 2000) spectra of RRL to provide [Fe/H] estimates based on a calibration that associates metallicity the equivalent widths of the CaII K line and Balmer lines[2]. It requires high resolution spectra for its calibration, with the most widely used one dating to the early 90s (Layden, 1994, hereafter Layden94). The Fourier parameter decomposition method is based solely on photometric light curves, providing an astonishing number of metallicity estimates including for RRLs that have never been observed spectroscopically. It relies on decomposing a light curve as a Fourier series, and associating some coefficients of this series with a spectroscopic metallicity.

In this work, we adopted the approach of random phase observations of RRL stars to determine chemical abundances using the largest database of high resolution RRL spectra in the literature. We determined high resolution metallicities and chemical abundances for 162 stars, several of which have no previous HR investigations. Furthermore, we used stars in common with previous works in order to bring other HR estimates into our chemical abundance scale, ending up with 247 RRLs (138 RRab, 23 RRc, 1 RRd) with HR measurements of a variety of chemical species. We used stars with our own high resolution metallicity measurements to create a brand new calibration of the ΔS method, developing a new equation and metallicity scale that eliminates the nonlinearity of previous calibrations and that, the first time, includes all phases of the pulsation cycle and first overtone pulsators. We applied the new ΔS calibration to a sample of 7768 stars with only low resolution spectra.

[2]In its original formulation by Preston (1959), the ΔS method relied on computing the difference between the spectral type of the RRL as given by the CaII K line and the spectral type given by the H_γ Balmer line.

This rich database of homogeneous, coeval metallicity results were further explored by our group in a series of investigations, two of which will be briefly mentioned in this thesis: the development of a new calibration of the Fourier parameter decomposition method which for the first time includes RRc stars (Mullen et al., 2021, Mullen et al., in preparation); and the unraveling of the long-standing mystery of the Oosterhoff dichotomy (Fabrizio et al., 2021a). The same data set was also used for the development of brand new velocity template curves for the precise determination of barycentric velocities of RRLs (Braga et al., 2021a) and, with those, develop a new approach to the Bailey diagram using pulsation tracers different atmospheric layers (Bono et al., 2020). These investigations add a wealth of information to our knowledge of RRLs and the Galactic halo, and provide other researchers with a framework to investigate Galactic formation that operates on several levels: chemical and kinematic, observational and theoretical, photometric and spectroscopic.

Throughout this work, we will refer to the quantity [X/Fe] = log(X/H) - $\log(X/H)_{\odot}$ - log(Fe/H) as the abundance of element X. When it becomes necessary to refer to the quantity [X/H] instead, we will do so explicitly. We will use the terms "metallicity" and "iron abundance" interchangeably, to signify the solar-scaled iron abundance [Fe/H]. Furthermore, we will employ the letter η to denote the median of the quantity being discussed (e.g. metallicity distribution, difference between abundance estimates for the same group of stars). The uncertainty associated with it is the error of the median. Unless otherwise noted, the letter σ denotes the absolute median deviation, the median-based counterpart to the mean-based standard deviation.

This thesis is structured as follows. We present the details of Galactic formation and structure in Chapter 2 that are most relevant to the present thesis. In Chapter 3 we will introduce the stellar tracers central to this investigation, the RRLs, including the history of their study, their evolutionary status, pulsational mechanisms and observational difficulties. Their importance for the study of Galactic formation in particular will be discussed in Chapters 3.8. In Chapter 4, we will discuss how stellar atmospheres and chemical abundances are determined, and the importance of different families (i.e. α, Fe-peak, and n-capture elements) regarding stellar evolution models and chemical enrichment history. In Chapter 5, we describe our spectroscopic sample and in Chapter 6 the methodology adopted throughout this work.

The computation of atmospheric parameters, chemical abundances, and their uncertainties is described in Chapter 7. These results were used to derive a new calibration of the ΔS method in Chapter 8, and to investigate metallicities and the [X/Fe] versus [Fe/H] plane for elements of all families of chemical species in Chapter 9. Other investigations that used the results of this thesis are briefly described in Chapter 10. An overview of the work done in this thesis and final remarks are given in Chapter 11.

Chapter 2

The Galactic components and their formation

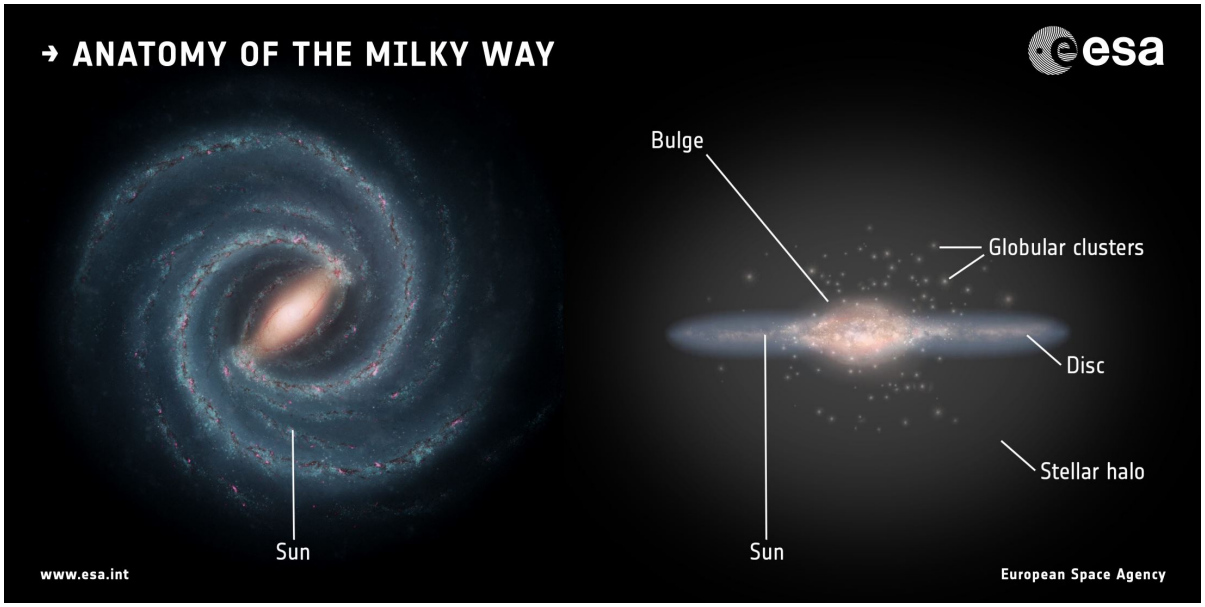

Figure 2.1: Artistic impression of the Milky Way galaxy from a face-on (left) and an edge-on (right) orientation. In the latter, the major Galactic components are indicated, as well as the globular cluster (GC) population. Image by the European Space Agency (ESA).

Galactic formation is a vast and largely unsettled topic, with both theoretical simulations and empirical observations offering a range of scenarios for both the Milky Way and galaxies in general. The seminal work of Eggen et al. (1962), using observations for over 200 field dwarfs, theorized that the monolithical collapse of a primordial gas cloud gave origin to the Galaxy in its entirety, with the process beginning 10 billion years ago.

The contraction of this massive gas cloud produced areas of higher density that would become GCs and other ancient star-forming regions, resulting in clusters and stars with highly eccentric orbits. In time, the angular momentum of this gas cloud stopped the collapse in the radial direction but allowed it to continue perpendicularly to it, generating a gas disk where a younger generation of chemically-enriched stars could form. While a pressure-supported contraction at more recent times would result in a radial abundance gradient, a free-fall regime at such early epochs would result in stars where kinematics and chemistry were uncorrelated, and no radial abundance gradient, as observed by the authors.

A bit over a decade later, Searle & Zinn (1978) performed a significant update to the then-available chemical abundances and distances of GCs. They explored 19 clusters at Galactocentric distances greater than 8 kpc and found no metallicity gradient in the Halo. This empirical evidence was still compatible with a free-fall collapse scenario, but the authors offered that the data was equally well described by a scenario where multiple stellar systems or gas clouds were hierarchically accreted. In both cases, the stellar systems, whether accreted or formed in-situ, would have had time to reach dynamical equilibrium with the Galaxy and display no coupling of chemistry and kinematics. However, the authors offered a key constrain coming up not from metallicity, but from the difference in horizontal branch (HB) morphology among GCs. They observed that the metal-poor GCs at smaller radii had different HB morphologies from their large radii counterparts. Assuming the GCs are coeval, this would mean that a radial gradient in either He or CNO abundance exists only for metal-poor GCs. The authors then made the tentative simpler preposition that the Galactic GCs are actually not coeval, but that the inner Halo GCs were formed within a time scale of 0.1 billion years, while those in the outer Halo continued to form over a period exceeding 1 billion years. This prolongued and possibly episodic cluster formation requires the infall of gas external to the Galaxy in a dissipative accretion. This infalling gas would compose transient condensations that are accreted across a period longer than the dynamical time scale of the Halo, resulting in GCs that formed before reaching dynamical equilibrium with the Galaxy, i.e. being accreted. Regardless of details, this complex scenario already challenged the idea of galactic formation as a close, dissipationless system. The authors then made the final jump by proposing that these transient condensations could be thought of as protogalactic fragments themselves, perhaps even similar to observed gas-rich irregular galaxies, opening the door to a major paradigm shift in theories of Galactic formation.

As the number and quality of GC observations increased, details of the above scenario were refined (e.g. Ashman & Zepf, 1992) or even challenged, such the assumption of an age spread among Galactic GCs (e.g. Zinn, 1985). Regardless, the occurence of merging events became a significant concern in the description of Galactic formation and is required by the cold dark matter paradigm (e.g. Bullock & Boylan-Kolchin, 2017). Modern large data sets and all-sky surveys brought a breakthrough with the observation of stellar streams and accreted populations, such as the Sagittarius dwarf (Ibata et al.,

1994) and its streams (Figure 2.2), Gaia Enceladus (Belokurov et al., 2018; Helmi et al., 2018), and the Sequoia (Myeong et al., 2019). These discoveries cemented the scenario of a galaxy that is built up by the disruption and accretion of pre-existing stellar populations of various sizes.

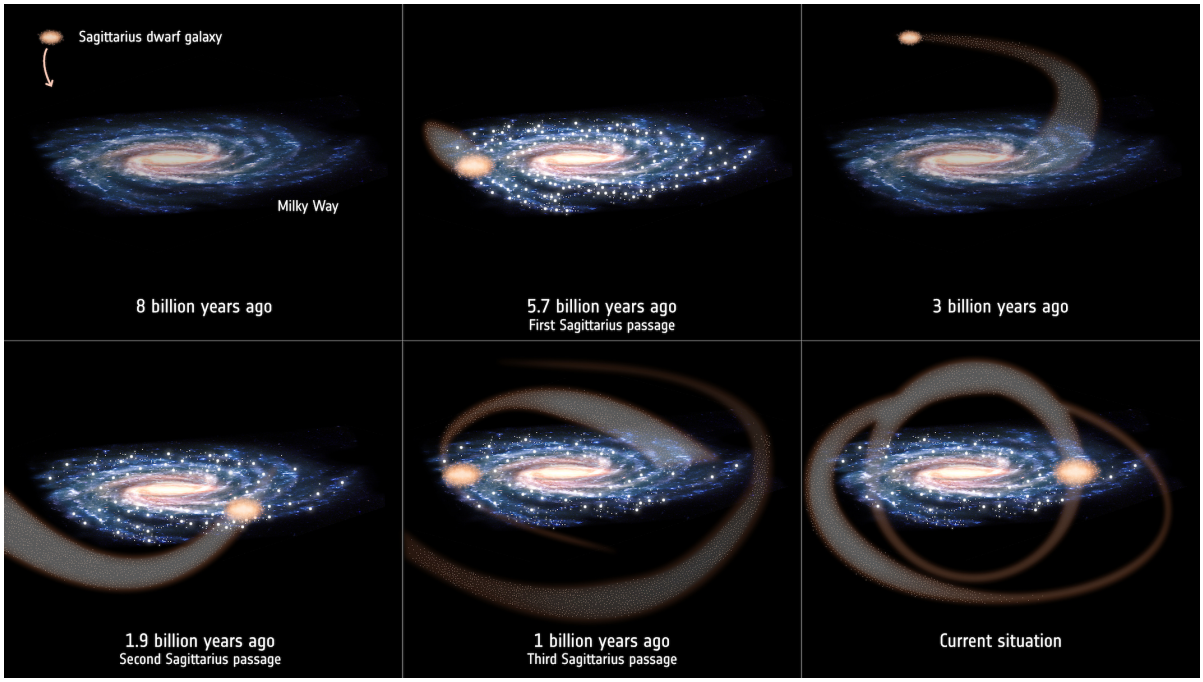

Figure 2.2: Artistic impression of the accretion of the Sagittarius dwarf spheroidal by the Milky Way, with stellar streams (tail behind the dwarf spheroidal core) and regions of triggered star formation (bright spots in the disk of Milky Way). Predicted epochs are indicated in the bottom of each panel. Image by ESA.

Several questions remain open regarding the merging mechanisms and time scales, the fraction of in situ and ex situ (i.e. accreted) Galactic stellar populations, and the nature (e.g. mass, chemical evolution history) of the accreted protogalactic systems. Furthermore, it is still unclear how the different substructures within the Galaxy, illustrated in Figure 2.1, came to be. Indeed, the formation of the Halo, Disk, and Bulge, their connection to one another, whether these substructures are themselves composite, whether their spatial limits can be sharply determined at all, and how many stars from one component migrate into another are all still matters of intense debate. For the purposes of this thesis, a few comments on the Bulge and Disk are useful before we move on to the Halo.

2.1 The Bulge and Disk

Starting at the innermost region of the Galaxy, one finds the Bulge at the bottom of the gravitational potential well. It is possible that the Bulge is a primordial Galactic component formed through an early dissipational collapse, or early merging events. It is unquestionable that the Bulge contains a significant old stellar population as it holds RRLs and also GCs which are, within uncertainties, coeval with Halo GCs. However, it is also possible that the Bulge, or at least part of it, was formed due to a buckling instability between the bar and the ancient Disk. This would mean that the Galaxy has a pseudobulge formed via secular evolution, and not a classical bulge which would be similar to a spheroidal dwarf galaxy. Detailed observations, including chemical and kinematic studies, of this highly reddened region are essential in order to determine whether the Galaxy has a classical bulge or pseudobulge, or even a combination of the two. Indeed, the current shape, its relationship to the bar, density profile, and age distribution of the Bulge are still matters to be resolved (see McWilliam, 2016; Bensby et al., 2017; Barbuy et al., 2018, and references therein).

The Milky Way, like most massive galaxies, has a disk component that is believed to be formed by the settling of both "native" and accreted gas into a plane set by the galaxy's angular momentum. It is possible for a disk component to emerge in the earliest epochs of galactic formation, making it coeval with the spheroidal component. In the case of the Milky Way, the present-day disk has a large quantity of gas and young stellar populations, but no evidence of unambiguously old stars. Indeed, no GC or RRL has ever been detected in the so-called "thin" Disk. However, a plane structure with a scale height larger than the thin Disk does contain both and also signatures of a chemical enrichment history that is different from that of the thin Disk. It is unclear whether this "thick" Disk is a merely a transition between the Disk and the Halo, or whether it is the remnant of the primordial "thin" Disk. The formation of the bar and a buckling instability of the primordial Disk could have resulted in the drifting of primordial Disk stars into the Bulge, and merging events could have kinematically heated the primordial Disk, launching some of its stellar population into the Halo while also causing its increase in scale height. As more gas fell into the plane of the Disk, a new "thin" Disk would then form at ages 1-2 Gyrs younger than the Halo, possibly following an inside-out pattern (Sellwood, 2014; Bono et al., 2015; Bland-Hawthorn & Gerhard, 2016; Grisoni et al., 2017; Monachesi et al., 2019, and references therein).

In short, a few major scenarios are possible, each one with an array of debated details. They can be grouped as "serial" or "parallel" approaches. In the serial approach, each Galactic component formed in sequence, while in the parallel approach they are coeval but evolve both as isolated and as interacting systems. In both cases, both minor and major merging events can be invoked to describe specific empirical results. Furthermore, it is unclear how much of each component was formed through an initial monolithic collapse, how much purely through accretion, and what was the time scale of each of

these processes. In this regard, a few words of caution about simulations are useful. Hybrid models of stellar haloes rely on running small scale cosmological simulations including only dark matter (i.e. dissipationless models), and then assigning a stellar mass to the dark matter haloes based on the observed luminosity function of nearby satellite galaxies. These models depart from the assumption that the stellar halo is built exclusively through merging events, without a significant in situ star formation realized through dissipative mechanisms. Meanwhile, cosmological hydrodynamical simulations require the fine tuning of dissipation mechanisms such as SNe feedback and, while they predict in situ halo populations, the fraction of native stars could be biased in a number of ways (Font et al., 2011; McCarthy et al., 2012, and references therein).

Clearly, a few key observational constraints would greatly benefit the theoretical modeling of galactic formation with its many poorly constrained variables and flexible assumptions. The position of the Sun right between two spiral arms and near the plane of the Disk results in a great difficulty in studying the Disk itself, and the large quantities of gas and dust all but completely obscure the Bulge in wavelengths shorter than the NIR. Thus, the Galactic component that is the most accessible to detailed investigations is the Halo. This is the component that we will focus on in this thesis.

2.2 The Halo

The Halo is believed to hold just about 1% of the Galaxy's stellar mass. In general, its stellar population displays high orbital eccentricities in a spheroidal or near spherical configuration. Despite its old age, quenched star formation, and low density, the Halo is not unlike the Bulge and Disk in complexity. Like for those two components, there are multiple theories regarding the built-up of the Halo, with conflicting scenarios both in simulations and in observations. A few key questions of interest are: is there any fraction of the Halo that was formed via the collapse of a single gas cloud, and if so, how large is this fraction?; how massive were the ancient galaxies that were accreted by the Milky Way?; when did the merging events occur?; are traces of such merging events still detectable (i.e. clumps in the abundance and/or phase space, spatial stellar streams)? are the current dwarf satellite galaxies any similar to the accreted galaxies?; do GCs and field Halo stars share a common origin?; is there a division between inner and outer Halo and, if so, what drove the formation of each subcomponent, where is their spatial division, and in which way are they different?

2.2.1 Metallicity gradient

Both in situ and ex situ Halo populations can display a flat metallicity gradient with Galactocentric radius, depending on the timescale of star formation. Using a sample of 302 RRLs in low resolution, Layden94 found a very flat iron gradient ([Fe/H] $\approx$ -1.6,

with σ=0.3) over 10-40 kpc, with a more metal-rich component inside the solar circle. This result is supported by Fernández-Alvar et al. (2017) who found no evidence of a gradient from 10 to 80 kpc, with a sample of 400 field stars observed in APOGEE and with atmospheric parameters derived by the APOGEE Stellar Parameters and Chemical Abundances Pipeline (ASPCAP, Holtzman et al., 2015; García Pérez et al., 2016), and also by Conroy et al. (2019) with a sample of 4232 giants. A flat metallicity gradient is not altogether incompatible with the shallow slope detected by Xue et al. (2015) who found a decrease of 0.1-0.2 dex from ≈10 to 100 kpc using over 1750,000 giants from the SEGUE-SDSS dataset, which is composed of spectroscopy acquired by the Sloan Extension for Galactic Understanding and Exploration and photometry acquired by the Sloan Digital Sky Survey (Yanny et al., 2009).

Interestingly, classical Cepheids in the Disk do display a negative metallicity gradient that is followed by the [X/H] abundances of α elements in all quadrants of the Disk, pointing out to a quite homogeneous chemical enrichment across this Galactic component (Genovali et al., 2015). The Cepheid variables cover an age range from approximately 10 to 300 Myr, thus being young stellar tracers. The [Ca/Fe] versus period plane for these stars show a negative trend with increasing period. As period is a strong proxy for their age, this means that the youngest Cepheids have lower Ca abundances than their older counterparts. This result is mentioned here to underline the importance of firm age constraints for the stellar populations under scrutiny. Furthermore, if there is an abundance gradient, it may be too shallow to be detected in low resolution measurements, or with small sample sizes, even without the added spread caused by mixed age samples.

2.2.2 The dual Halo hypothesis

Both Carollo et al. (2007) and Kinman et al. (2012), using data from SEGUE-SDSS, proposed a dual Halo scenario with a division at a Galactocentric radius near 15 kpc. Their results show a inner Halo with higher orbital eccentricities, a small net prograde motion (between 0 and 50 kms^{-1}), a metallicity distribution that peaks at [Fe/H] = -1.6 dex with extended tails on both sides, and a flattened spatial-density distribution. In contrast, they detected a wide range of orbital eccentricities for the outer Halo, alongside a strong retrogade motion (between -40 and -170 kms^{-1}), a metallicity distribution that peaks at [Fe/H] = -2.2 and is skewed towards lower metallicities, and a near spherical spatial-density distribution. This notorious result was sharply challenged in detail by Schönrich et al. (2011) and Schönrich et al. (2014), with several other works either giving support to or disagreeing with specific statements.

After the high profile publication of Carollo et al. (2007), multiple studies found that the radial density distribution of the Halo is better described by a broken power law, with the outer Halo displaying a steeper slope, although the idea had already been proposed in the 60s. The radius at which the break happens, however, varies greatly from study to study, with values ranging from approximately 15 kpc to 35 kpc and paired with varied

slopes (see Table 6 of Bland-Hawthorn & Gerhard, 2016). Furthermore, this break in the density distribution is challenged by other investigations, and is likely dependent on the adopted spheroidal flattening. For example, Sesar et al. (2011) found a broken power law and a constant flattening within 35 kpc, and Sesar et al. (2013) found that, within 30 kpc, a single or broken power law describes an oblate ellipsoid equally well. Meanwhile Iorio et al. (2018), covering the same radial range, found a flattening that smoothly decreased with radius, and a single power law density distribution. Adjusting the same model, Iorio et al. (2018) found that, within $d_G \approx 20$ kpc, the Halo is more spherical at small z distances from the disk ($|z| \leq 10$ kpc), and more elongated at larger |z| until $d_G \approx 30$ kpc, and then once again more spherical for larger d_G (see their Figure 2). Xue et al. (2015) found that the density distribution is fitted equally well by a broken power law in an ellipsoid with constant flattening, or a single power law in an ellipsoid with a break with flattening instead. The more recent investigation of Mackereth & Bovy (2020) found a single power law and a flattened ellipsoid once more.

It is important to bear in mind that density and structure investigations are strongly affected by the size and completeness of the sample, and by the adopted distance relations, while studies involving orbits rely on adopted Galactic potential models and on precise proper motions and radial velocities. We refer the reader to Schönrich et al. (2014) for detailed descriptions on the impact of each of these quantities, and of sources of statistical biases such as assuming Gaussian symmetry when treating skewed distributions.

Moving on to chemistry, Mackereth & Bovy (2020) investigated a division of the Halo based on 835 red giants with Mg abundances computed automatically by ASPCAP. They found that the population with higher Mg abundance has a more eccentric orbits and steeper density profile than the population with lower Mg abundance. Morever, they noted that the density distributions were well fit with a single power law, but with the caveat that a cut was introduced at about 20 kpc due to small sample size beyond this radius. However, the eccentricities e they computed using a simple Milky Way potential have a continuous distribution that increases monotonically up to $e \approx 1$, after which a peak is reached. Thus, a division into high and low eccentricity at e=0.7 is largely arbitrary.

The notion of a double sequence in the abundance of α elements (which includes Mg) in the local Halo goes back to Nissen & Schuster (2010). However, the separation between "thick" Disk and Halo is hampered by uncertainties in distances, proper motions, and the adopted velocity distribution, as explained in Section 4 of Nissen & Schuster (2010). Furthermore, the "low Mg" sequence in their data abruptily stops at [Fe/H] higher than approximately -0.7 dex. Indeed, the proposed separation is made clear precisely by this absence of metal-rich, Mg-poor stars, as the gap between the two sequences is not easy to discern unless the different populations are color-coded (see their Figures 1 and 5). The situation is the same for the claimed double sequence in Fe-peak and n-capture elements in Nissen & Schuster (2011), with the added complication that these elements

are usually very sensitive to NLTE effects in dwarfs.

The separation in chemistry was investigated once more by Bensby et al. (2014) with a larger sample of 714 local Disk dwarfs that reaches super-solar metallicities. They detected a double sequence in the [Ti/Fe] versus [Fe/H] plane (see their Figure 15), but the two groups could not be clearly separated into thick and thin Disk (see their Figure 19). The same difficulty in kinematic separation was found for O for 825 local cold stars by Ramírez et al. (2013) (see their Figures 10 and 11). A double sequence may actually be absent in their data in the first place (see their Figure 9). Any semblance of a double sequence is heavily dependent on the fact that there is an apparently absence of O-poor stars for [Fe/H] lower than approximately -0.5 dex. Indeed, the range where the separation is most clear in Bensby et al. (2014) is between -0.8 and -0.2 dex, while in Ramírez et al. (2013) it is only present at -0.5 and lower if at all. Bensby et al. (2014) suggests that age may be a more reliable separator than kinematics, and they compute generally larger ages for the high α population (see their Figure 22).

Thus, as with the structural quantities of flattening and density distribution, it is unclear whether a bimodality in α element abundances is present in the solar neighborhood. If there is such bimodality in chemistry, it is possible that the division is not among Halo stars as claimed by Nissen & Schuster (2010), but rather involve either Halo and thick Disk versus thin Disk stars, or simply a young versus old population. The absence of a metallicity gradient in the Halo also casts doubt over the existence of stellar populations that underwent a different enrichment mechanism and remain radially segregated.

2.2.3 The field population

Both the number of accreted sattelites and their mass influence whether the Halo is smooth or clumpy in spatial, kinematic, and chemical planes, with the added complication that, depending on how early merging events happened, the relaxation time of the Halo may be enough to dillute traces of accreted populations. Iorio et al. (2018), with a sample of 21,600 RRLs, found a spatially smooth Halo within approximately 30 kpc, with a few identifiable substructures as the Virgo overdensity, in agreement with the results of Deason et al. (2011) which were based on approximately 20,000 blue HB stars and blue stragglers.

The field Halo stars in the literature cover a very wide metallicity range, all the way from slighly sub-solar to a very extended metal-poor tail that reaches [Fe/H] as low as -4 dex, with a few scattered stars that are even more metal-poor. The Bulge and the Disk reach super-solar values as high as 0.2 dex, but go no lower than [Fe/H] $\approx$ -1.4 dex. This is very relevant in the discussion regarding the merging events that built up the Halo. It is noteworthy that the nearby dwarf galaxies orbiting the Milky Way do not display a metal-poor tail at all, challenging the notion that these objects are relics of the early universe, and similar to the building blocks of the Halo (Helmi et al., 2006).

A few investigations support a scenario where a fraction of the field Halo population

was stripped from GCs, with cited figures going from a few percent to 50% (Koch et al., 2019a, and references therein). The higher ratios are difficult to reconcile with the metallicity distribution of the Halo, because Galactic GCs display a strongly bimodal metallicity distribution and do not reach [Fe/H] lower than approximately -2.5 dex. Another line of inquiry regarding the plausibility of this scenario is the comparison of the number ratio of RRc to RRab in GCs and the same number ratio in the Halo. This approach was revisited using part of the results of this thesis and published in (Fabrizio et al., 2021a). A similar approach was used by Fiorentino et al. (2015), which compared the pulsational properties of the RRL populations of Galactic GCs, nearby dwarf galaxies, and the Halo, offering strong constraints on their relationship.

In general, the Halo is said to display a high α element abundance than other Galactic components, but this is a natural consequence of its metallicity regime. We refer the reader to Chapter 4.3.2 for a detailed discussion on the α elements and their trend with metallicity as it will be useful for the discussion below. In brief, the [X/Fe] versus [Fe/H] plane for α elements displays a very characteristic trend. In particular, [α/Fe] is flat in the metal-poor regime, and then at a certain [Fe/H] it begins a steady decrease as metallicity increases, the so-called "knee". The exact [Fe/H] where this decrease begins is strongly dependant on the chemical enrichment history of the population in question. Interestingly, the [α/Fe] versus [Fe/H] trends for Halo field stars and for dwarf galaxies are not the same, with Halo stars being significantly more α-enhanced for metallicities above [Fe/H] $\approx$ -1.5 dex (Shetrone et al., 2001; Tolstoy et al., 2003), i.e. the "knee" in the dwarf galaxies occurs at lower metallicities than in the Halo. Here, it is important to note that the small number of metal-rich Halo stars in the literature hinders comparisons with other stellar populations because the "knee" is not well constrained.

The large data sets coming from Gaia and APOGEE allowed for the kinematic identification of multiple stellar streams and isolated populations. However, caution must be taken in their interpretation. Similar substructures in density and kinematics planes can be created by accreted satellites of very different masses (and consequently enrichment histories), and there is a considerable overlap between accreted and in situ stellar populations in the velocity planes (Jean-Baptiste et al., 2017). The chemical approach to disentangling hypotheses of Halo formation is fundamental. The determination of chemical abundances for a variety of chemical species species offers fundamental constraints into the nature of the stellar systems accreted by the Milky Way.

The simulations of Robertson et al. (2005) and Font et al. (2006) suggest a scenario of few massive early mergers being responsible for most of the accretion events that formed the Milky Way. The large datasets from Gaia, Gaia-SDSS, and APOGEE carry evidence of such major merger events. Both Belokurov et al. (2018) and Di Matteo et al. (2019) found a kinematic imprint pointing to a single progenitor satellite that was accreted at about 10 Gyr ago, significantly heating up the old Galactic Disk. This interaction may be responsible for most if not all of the inner Halo stellar population, and the authors of both works present the hypothesis of no significant in situ population

in this Galactic component. More recently, Naidu et al. (2020), using a sample of over 5680 giants within 50 kpc from the Galactic centre, concluded that the Halo is entirely composed of substructures in the chemical and kinematic planes, with no significant in situ population except close to the plane of the Disk, i.e. the "thick" Disk. Their results point to a scenario where, at distances beyond 15 kpc, the Halo field population is the result of two major merger events: the Sagittarius dwarf and Gaia Enceladus.

Another important constraint to the nature of the accreted galaxies is brought forward by the RRLs. A population of RRLs with high amplitude ($A_V \gtrsim 0.75$ mag) and short periods ($P \lesssim 0.48$ d) is present in the Milky Way at intemerdiate to high metallicities, but not in low mass dwarf galaxies with a slower chemical enrichment history (Fiorentino et al., 2017). This evidence is a very promising line of inquiry after the discovery of Gaia Enceladus and, very recently, of a massive structure embedded in within 4 kpc of the Galactic centre (Horta et al., 2021). However, it is still unknown whether all high amplitude and short period RRLs can be associated to one or two progenitors.

Chapter 3

The RR Lyrae stars

One of the most significant changes in stellar structure for low mass stars occurs when the H in their cores is depleted and He core burning begins. This causes them to reach a relatively stable thermodynamical equilibrium that places them in the HB – a region of the color-magnitude diagram (CMD) that is very wide in color and very narrow in magnitude. Similarly, in the theoretical counterpart of the CMD, the Hertzprung-Russel diagram, they are located in a region with a wide range in effective temperature ($T_{\rm eff}$) and a narrow range in luminosity (log(L)). The HB represents a late evolutionary stage of low mass stars, requiring over 10 Gyr of evolution.

The He core mass of HB stars is very similar along the whole width of the HB, with values ranging from ≈ 0.48 to 0.50 $M_\odot$. The broad range in color, or in $T_{\rm eff}$, is largely a consequence of differences in envelope mass after the mass loss that occurred during the red giant branch (RGB) phase. If the mass loss caused the total mass of the star to be of the order of ≈ 0.5 to 0.8 $M_\odot$, the star will reach the precise conditions to become radially pulsating. Indeed, it will be an RRL variable and be positioned in a CMD or in a Hertzprung-Russel diagram right where the HB intercepts the instability strip ($M_V \approx$ 0.6 mag, $\log(L/L_\odot) \approx 1.6$ dex, Figure 3.1). This interception is often called the "RR Lyrae gap" in the CMDs of GCs, but the term is misleading. The gap only exists because these variable stars are simply not represented in most single epoch studies. Their mean magnitude, which requires multiple observations, would place them at about the same luminosity level as the rest of the HB but authors in general avoid representing single observations of variables.

Thus, the RRL are hot ($T_{\rm eff} \approx 6000$ to 8000 K, spectral types A–F), bright ($M_V \approx$ 0.6 mag), and, most importantly, old (over ≥ 10 Gyr) low mass (≈ 0.5 to 0.8 $M_\odot$) stars. There is evidence that binary evolution could lead to younger stellar structures capable of mimicking the light curves of RRLs, but only one case of such structure is known in the literature (Pietrzyński et al., 2012). Indeed, the total number of RRLs that *may* belong to a binary system remains at a few percent (Prudil et al., 2019) and only one RRL has been convincingly shown to have a binary companion (Kervella et al., 2019).

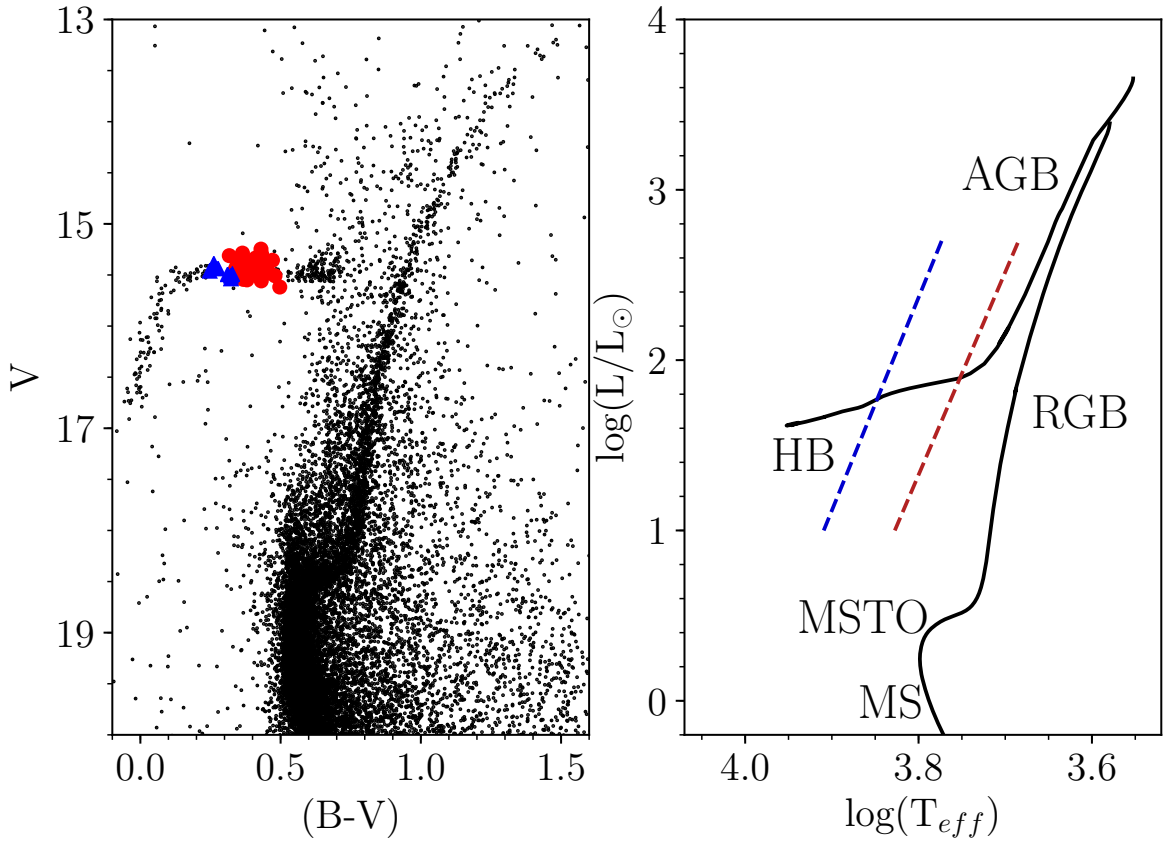

Figure 3.1: *Left:* Color-magnitude diagram for NGC 6723 (Lee et al., 2014), with the fundamental mode and first overtone RRLs represented by red crosses and blue circles, respectively. *Right:* Herzprung-Russel diagram with a typical GC isochrone from the Bag of Stellar Tracks and Isochrones (BaSTI) database (Pietrinferni et al., 2006). The labels indicate the positions of the main sequence (MS), main sequence turn-off (MSTO), RGB, and HB. The dashed lines indicate the blue and red edges of the instability strip near the region of interest (Marconi et al., 2015).

The RRL were formerly believed to represent metal-poor populations, but now are known to be formed at a wide range of metallicites ([Fe/H] $\approx$ -2.5 to solar), making them ideal old population tracers for a wide range of chemical enrichment histories. These stars are intrinsic radial pulsators with short periods ranging from 0.2 to 1.0 day. The time variation of their luminosity creates distinctive light curves that can be visually categorized into two types, RRab and RRc. The first presents a sawtooth shape with larger amplitude and longer periods, while the second displays more sinusoidal variations with smaller amplitudes and shorter periods (Figure 3.2). In a period-amplitude, also

called a Bailey diagram[1], the two types occupy very distinct regions for visual and NIR bands (Figure 3.3). Furthermore, RRab are colder and concentrate on the redder side of the instability strip, while RRc are hotter and remain in the bluer side.

A small number of RRLs have been found to be pulsating in both fundamental mode and first overtone (Goranskij, 1981; Nemec, 1985), making up the double mode type RRd. There is disputed evidence for the existence of second-overtone pulsators as well as simultaneous first- and second-overtone pulsators (e.g. Stothers, 1987; Alcock et al., 2000). A long period amplitude modulation, the Blazhko effect (Blažko, 1907; Jurcsik et al., 2018), has been observed in RRab and RRc stars, being far more likely to occur in the former. Indeed, over a third of RRab stars are likely to display Blazhko modulation.

Most importantly, the RRLs obey period-luminosity (PL) and period-luminosity-metallicity (PLZ) relations in NIR bands such as the JHK bands, with mid-infrared bands also showing promising preliminary results (e.g. Madore et al., 2013; Muraveva et al., 2018). They are standard candles that trace old populations in a wide range of metallicities, a counterpart to the young classical Cepheids and far more abundant and theoretically understood than type II Cepheids. In the following sections, we will present a bit of the history behind the study of RRLs and their observational difficulties. Afterwards, we will explore in greater detail their their usage as stellar tracers (Chapter 3.3), evolutionary status (Chapter 3.4), pulsation mechanisms (Chapter 3.5), and PL relations (Chapter 3.6). We will review some of the methods of metallicity derivation that, once calibrated with HR spectroscopy, can be applied for a variaty of purposes and environments such as obscured regions invisible in optical wavelengths or large datasets where statistical studies are possible (Chapter 3.7). With this in mind, we will discuss their usage in the study of the Galactic Halo in Chapter 3.8).

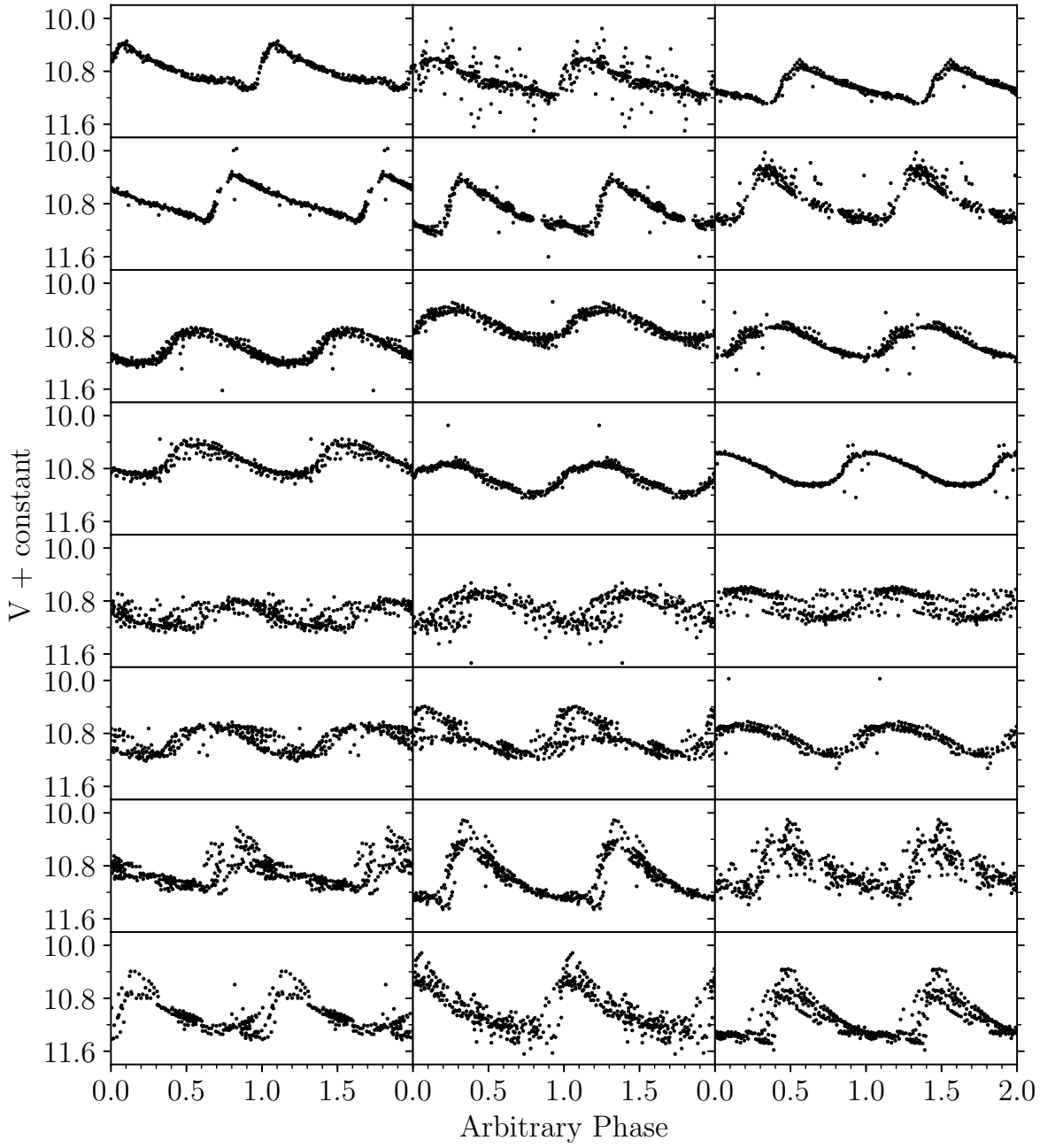

Figure 3.2: Folded light curves for RRab (first and second rows), RRc (third and fourth rows), RRd (fifth and sixth rows), and RRLs with Blazkho modulation (seventh and eighth rows). All data is from Drake et al. (2017). The V magnitudes have been shifted for clarity. Each figure covers an interval of 2 mag.

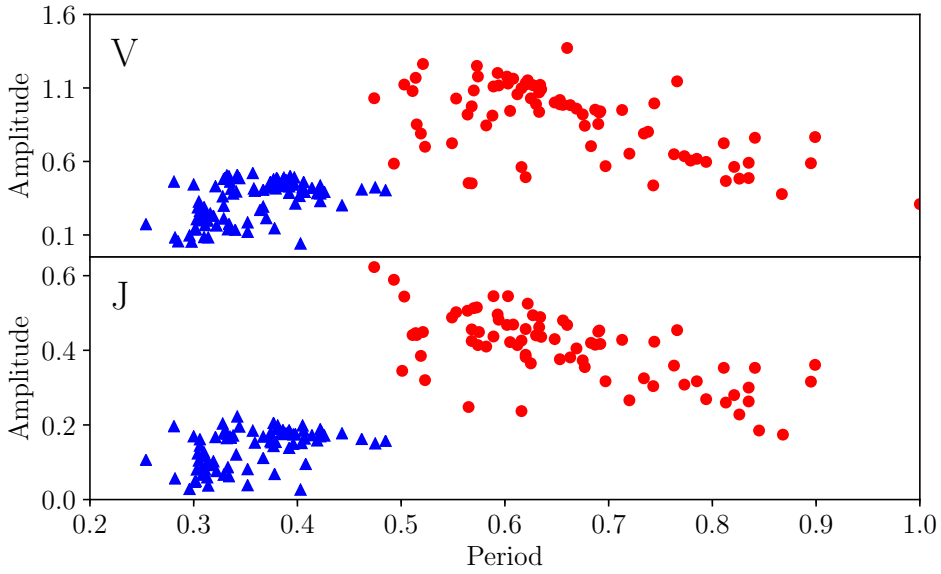

Figure 3.3: Period-amplitude diagrams in V (top) and J (bottom) bands for RRLs in ω Centauri (Braga et al., 2016, 2018). RRab stars are represented by red circles, and RRc stars by blue triangles.

3.1 A bit of history

The late 19th century was a time of rapid scientific progress. Astrophysics, newly born just a few decades before with stellar spectroscopy, was advancing by leaps and bounds as new observational data was parsed through. An ambitious program of stellar classification was started by Edward Pickering (July 19, 1846 – February 3, 1919) at the Harvard College Observatory, which included the development of new observational techniques and instruments (Bailey, 1919), producing a wealth of information. The program included Williamina Fleming (15 May 1857 – 21 May 1911) and the notorious team of "woman computers" who carefully classified thousands of spectra, grouping stars by spectral type, and identified a number of variable stars (Figure 3.4). Among sixty-four new variable stars, Pickering et al. (1901) listed one in the constellation of Lyra that would become an observational favorite due to its brightness and large amplitude in magnitude that allowed the most precise studies of these peculiar objects. While not the first of its kind to be discovered, RR Lyrae became the bona fide representative of its family.

Through the work of Edward Pickering, Williamina Fleming, and Solon Bailey (December 29, 1854 – June 5, 1931), it became evident that most stellar clusters hosted a

[1]The period-amplitude diagram was widely used by Solon Bailey in his pioneering investigations of RRLs in Galactic GCs in the early 20th century.

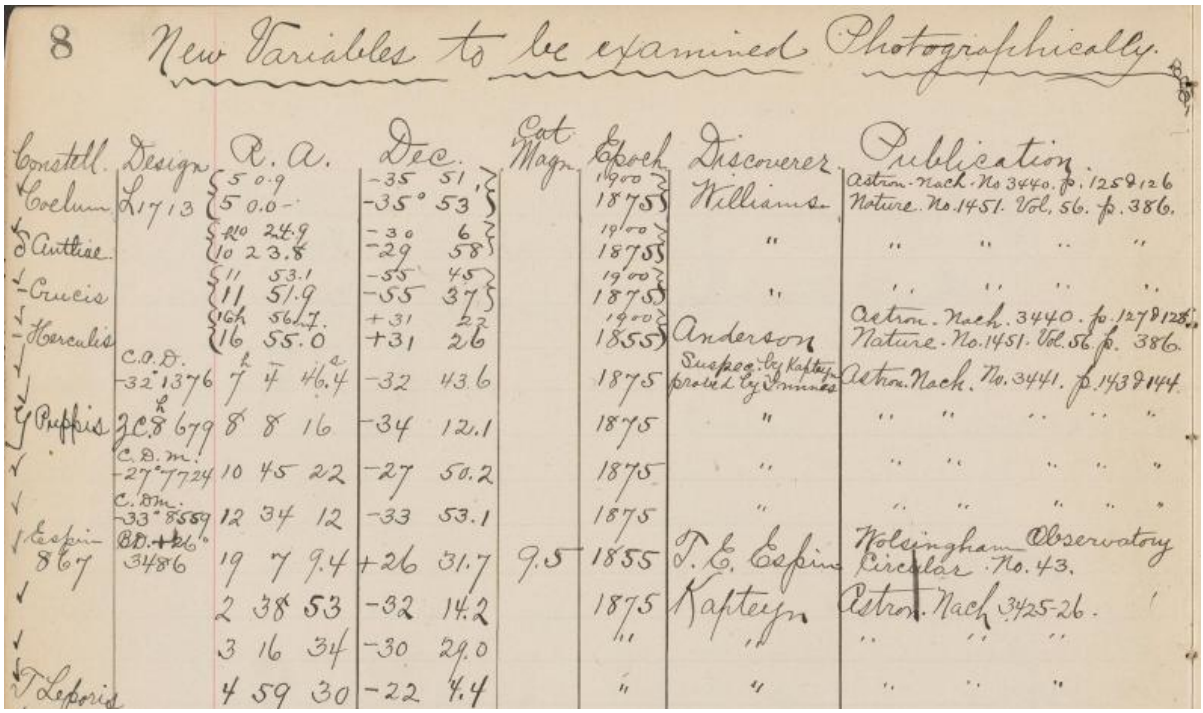

Figure 3.4: Observational notes from Fleming (1893).

large number of variable stars (Pickering, 1895). Going through photographic plates of 23 GCs, Solon Bailey and his team discovered over 500 variables (Bailey & Pickering, 1913) and observed that they had very similar light curves and roughly the same brightness. In their conclusions, they stated binarity was a probable source of the observed variation, but admitted the necessity of waiting for better instruments that would provide higher quality spectroscopic data. Soon, Harlow Shapley (November 2, 1885 – October 20, 1972) presented a challenge to the binarity hypothesis, underlining that mutually orbiting stars could not reproduce the peculiar light curves with such quick variations, and that the spectral features of these "cluster-type Cepheid stars" or "short-period Cepheids" changed smoothly between spectral types, supporting the existence of a single object with radial pulsations (Shapley, 1914, 1916, and references therein).

Thermodynamical explanations for the pulsation mechanism were already surfacing in those early years (Martin & Plummer, 1915; Eddington, 1918). Shortly afterwards, the first work recognizing that the Sun was composed primarily of H and He was published (Payne, 1925), although this groundbreaking conclusion was at first rejected by the scientific community and the author was led to call her own results spurious. The key piece of the puzzle, namely nuclear astrophysics and how it related to stellar evolution, was still some three decades away (e.g. Schönberg & Chandrasekhar, 1942; Hoyle & Schwarzschild, 1955). In the meantime, observations piled up as theoretical models

lagged behind, and every few years seemed to bring a new case of "the plot thickens" involving variable stars.

By 1902, Solon Bailey had already noted that the so-called short-period cluster-type variables presented noticeable differences of shape and amplitude in their light curves, which prompted him to divide these objects into three subclasses – a, b, and c (Bailey, 1902). Schwarzschild (1940) later noticed that types a and b were physically indistinguishable, belonging to a single class RRab, composed of fundamental mode pulsators, while the RRc class represented the first overtone pulsators. Blažko (1907) noted a variation in period in the light curve of RW Draconis. Shapley (1916) observed a similar phenomenon in RR Lyrae itself, and noticed a change in maximum magnitude. This periodic modulation came to be known as the Blazhko Effect and remains a mystery over a century later. Another piece of the puzzle and matter of ongoing debate is the so-called Oosterhoof Dichotomy, an apparent segregation between Galactic GCs based on their metallicity and the mean period of their RRL population (Catelan, 2009b; Catelan & Smith, 2015, and references therein). It was pointed out by Oosterhoff (1939) and based on results from Grosse & Schorr (1932).

Perhaps most interesting, however, was the discovery that established variable stars as astronomical distance determinators. Leavitt & Pickering (1912) found a linear relation between brightness and period in a group of fifty nine Cepheid variables in the Small Magellanic Cloud, that is, at about the same distance from the Earth. Therefore, roughly speaking, the period of one such star would give its intrinsic brightness, which, compared against their observed brightness, would allow the determination of its distance [2]. This PL relation was involved in some of the greatest paradigm shifts in the history of astronomy: 1) the Sun is not at the center of the Galaxy (Shapley, 1918); 2) there are other galaxies (Hubble, 1925); and 3) the Universe is expanding (Hubble, 1929). We refer the reader to Gingerich (1999) for a brief overview of the early cosmological debate with its fascinating twists and turns.

Soon it became evident that type II Cepheids, classical Cepheids, and RRLs traced distinct populations. Indeed, both classes of Cepheids are formed only in metal-rich environments, and classical Cepheids are very young ($\approx$ 200 Myr). Thus, both type II Cepheids and RRL trace old populations, with the latter covering a broad range in metallicity and vastly outnumbering the rarer and poorly understood type II Cepheids. However, there was no clear PL relation for RRLs, as they occupy a narrow interval in visual magnitudes as the CMDs of GCs clearly demonstrate. Yet that interval varies from GC to GC, underlining a dependence on metallicity. This difficulty meant that the usefulness of cluster RRLs as standard candles depended on good metallicity estimates of their host GCs, and establishing a calibration in the first place relied on having such

[2]Barring issues with zero-point calibration, interstellar extinction, and the fact that, when this PL relation was discovered, there was no awareness of the distinction between Classical Cepheids and Type II Cepheids (Baade, 1956).

estimates for a large number of GCs on the same metallicity scale - indeed, it is much easier to determine the metallicity of a GC and then associated it to its RRL, than to directly determine the metallicity of an RRL (see Chapter 3.2). Clearly, this means that field RRL remained mostly ignored, a problem that is compounded by the fact that it is not immediately obvious whether field and cluster RRL have comparable chemical enrichment histories. Moreover, observed magnitudes are photometric quantities subjected to interstellar extinction, one of astronomy's greatest Achilles heels.

With the work of Schwarzschild (1940), there was already an understanding that "cluster-type variables" were most likely a peculiar type of low mass HB stars that, in a CMD, were confined to a color range where no non-pulsating star could be found. The full explanation of the mechanism behind their pulsation remained mysterious for a while longer until, in 1948, S. Zhevakin brought forward the theory of a critical He ionization zone that would drive stable oscillations of the observed amplitudes (Zhevakin, 1963; Jørgensen & Petersen, 1967). While RRLs were originally thought to trace metal-poor populations only, it soon became clear that they cover a wide range of metallicities up to Solar values (Preston, 1961), proving themselves powerful tracers for old populations with a variety of chemical enrichment histories. Unlike their Cepheid counterparts, however, there was still no clear way to employ their pulsational characteristics for distance determination.

The advent of NIR photometric detectors changed the scenario dramatically. They allowed the discovery that RRLs do obey a PL relation in the K band (Longmore et al., 1986), radically increasing the precision of distance estimates using them. In those longer wavelength bands, extinction is dramatically lower, and the complex interplay of age, evolutionary effects, metallicity, and temperature far less significant (Chapter 3.6). This empirical discovery was later supported by nonlinear convective modeling, which describes in detail the topology of the instability strip as well as secondary features of the light curve (Bono & Stellingwerf, 1994; Bono et al., 2000). These models allow a theoretical calibration of the PL relations and their dependence on chemical composition (Bono et al., 2001).

3.2 Observational difficulties

Refining both evolutionary models and the PLZ relations relies on having a number of RRLs with high precision metallicity estimates. Yet there are less than a hundred HR spectroscopic studies of field RRLs in the literature, and even fewer that investigate the abundances of chemical species other than iron. Two major observational difficulties are behind this scarcity of information – these stars are hot, and they pulsate. Regarding the first difficulty, spectroscopic derivation of atmospheric parameters relies on the presence of a significant number of FeI and FeII lines, but very high effective temperatures make absorption lines scarce. This problem can be alleviated by using spectrographs with a

wide wavelength coverage and making sure observations obtain a high SNR so that even weak lines can be measured. While uncertainties increase with temperature due to the decreasing number of lines, only at a fraction of the relatively short hot phase can the uncertainties becomes insurmountable.

As for the second difficulty, obtaining high dispersion and high SNR data in large amounts is expensive and time-consuming in general, but there are added complications due to the radial pulsation of the stellar envelope. Simply put, the exposure time necessary for high SNR in smaller telescopes is likely to be long enough to cover dramatic changes in the atmosphere of a star that completes a pulsation cycle in a matter of hours. The changes in velocity of an envelope that is expanding in an accelerated manner, and then contracting similarly so, introduces absorption line smearing due to Doppler effect. This causes widening in spectral features and makes any study that relies on the shape of absorption lines impossible.

Fortunately, this problem can be mitigated in a few ways. An exposure time as short as a few minutes in an 8m class telescope is sufficient to avoid line smearing in most of the pulsation cycle while achieving high SNR. The outcome is the same for 4m class telescopes for bright enough stars. In particular, very HR spectrographs allow for spectral degradation, which decreases the resolution and increases the SNR. In smaller telescopes, stacking short observations of the same pulsation phase for stars that are too faint for short exposures is a very useful technique. It requires carefully synchronizing observation time with pulsation period so that all spectra to be stacked are obtained at roughly the same phase. This approach guarantees that absorption lines have essentially the same shape. The trade-off is, then, between telescope size and complexity of observation schedule. The reliability of metallicity estimates across the pulsation cycle even for a 2.4m class telescope has been investigated in the past (e.g. For et al., 2011; Liu et al., 2013) and confirmed in this work.

The groundwork for making sense of these complex objects has been laid throughout decades, and with the next generation of extremely large telescopes coming by quickly, large telescopes are ever more accessible. The reasons for studying RRLs despite observational difficulties are manifold: their pulsational characteristics are independent of reddening; they are representatives of an evolutionary stage, namely He core burning, that most stars in the universe go through; they trace old populations in a wide range of metallicities and chemical enrichment histories; they are ubiquotous in GCs, which are both the laboratories for testing stellar evolutionary tracks and the stage of a decades-long debate regarding the presence of multiple stellar populations in a given cluster; they obey PL relations that allow for direct distance determination even for field stars; they are ubiquotous in the Halo, allowing for a precise study of its formation history and present structure; they are standard candles that provide an independent confirmation of the widely used Cepheid distance scale and can offer constraints from Galactic structure to the expansion rate of the Universe; and they are quite fascinating stars by themselves, with complex theoretical modeling that can still be greatly improved by

refined observational constraints.

3.3 Stellar tracers

The RRLs are representative of old populations in a wide metallicity range (Marconi et al., 2015). It is no surprise that they are so common in GCs, as most of these objects are believed to be older than approximately 10 Gyr (Kruijssen et al., 2019). Very metal-rich and very metal-poor GCs may fail to produce RRLs if their horizontal branches are restricted to either side of the instability strip. The effect of age and metallicity on a simple stellar population is illustrated in Figure 3.5. The HB morphology in GCs and which parameters beyond age and metallicity are necessary to describe it has been a matter of intense debate for decades, however (e.g. Lee et al., 1994; Dorman, 1995; Torelli et al., 2019). The "second parameter problem" points to at least a third physical quantity that makes coeval GCs of similar metallicities have dramatically different HB morphologies.

This phenomenon may be related to the presence of multiple stellar populations in these clusters. GCs were formerly thought to be bona fide simple stellar populations, characterized by a single age and chemical composition, but mounting evidence throughout decades led to the conclusion that most of them have had more than one formation event (e.g. Osborn, 1971). A second generation of stars would display a different chemical enrichment pattern, as it would be formed with gas polluted by the more massive stars of the first generation.

Light element variations are observed in all GCs, while Fe and heavier species are found to vary in a handful of the most massive ones. The precise source of these very peculiar variations, namely Na-O and Al-Mg anticorrelations, is a hotly debated topic and touches the very fundamentals of stellar evolution models (Gratton et al., 2012; Bastian & Lardo, 2018). Combinations of photometric filters can successfully separate populations in the main sequence, subgiant branch, and red giant branch (e.g. Bedin et al., 2004; Piotto et al., 2007). HB stars have a large intrinsic spread in color and temperature, both of which are sensitive to metallicity. Overall metallicity is more influenced by lighter elements, some of which are the ones touched by the multiple population phenomenon. This has brought forth the idea that there may be a segregation in the HB with the blue side hosting only the first population, and the red side having both populations mixed together (Marino et al., 2014; Jang et al., 2014).

Even more importantly, the enrichment of a second stellar generation results in He abundance variations (D'Antona et al., 2002; Bragaglia et al., 2010; Milone et al., 2018). RRLs that have higher He abundance at fixed metallicity are systematically brighter (Chapter 3.4), have smaller pulsation amplitudes, and longer pulsation periods (Marconi et al., 2018). This allows precise measurements of RRL to provide independent He estimates, which would be a powerful constraint in the multiple stellar population scenario

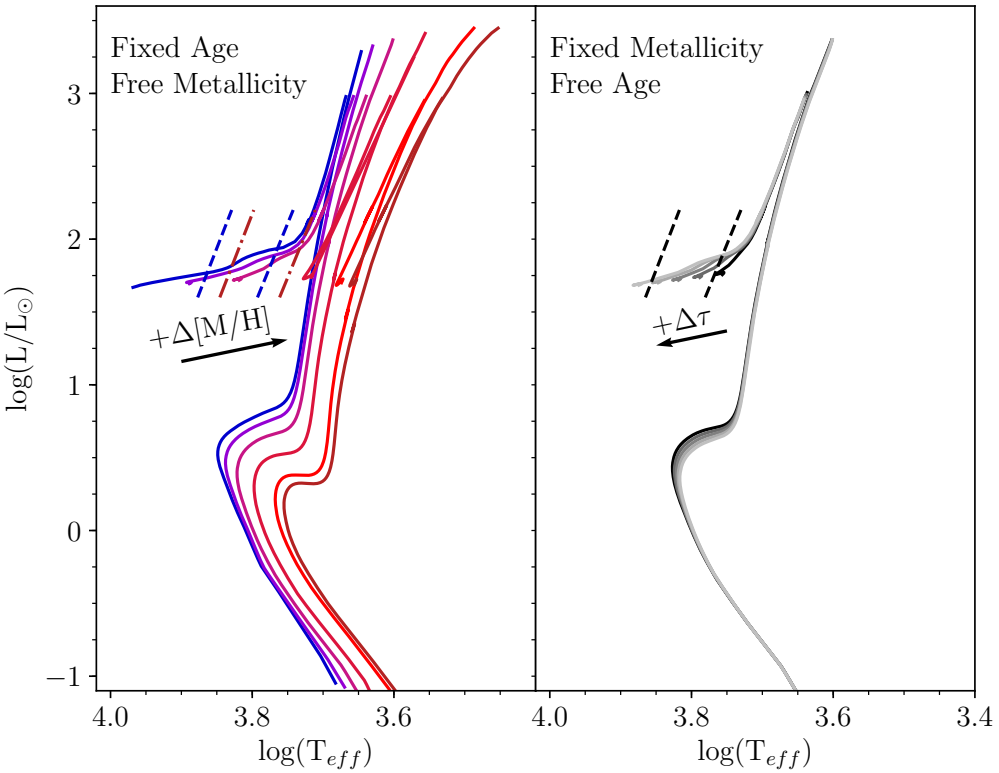

Figure 3.5: *Left:* Isochrones for a fixed age of 10 Gyr and a metallicity range of [M/H] = -2.3 – 0.4 dex. The dashed and dot-dashed lines indicate the edges of the instability strip for the lowest and highest metallicity, respectively. The arrow indicates the direction of metallicity increase in the HB. *Right:* isochrones for fixed metallicity [M/H] = -1.3 dex and an age range τ = 9 – 11 Gyr. The dashed lines indicate the edges of the instability strip for the considered metallicity. The arrow indicates the direction of age increase in the HB. All models were taken from the α-enhanced BaSTI database.

regarding pollution mechanisms and the HB morphology debate (Lee et al., 1994; Rich et al., 1997; Recio-Blanco et al., 2006; Catelan, 2009b).

The second most abundant chemical species in the universe is notoriously tricky to measure directly from stellar spectra due to the absence of transition lines in effective temperatures lower than about 10,000 K. The surface of stars in the Extreme HB can reach those temperatures, but these stars are not present in all GCs, and both gravitational settling and radiative levitation can change their atmospheric chemistry from their original composition (Moehler et al., 2014). This is not the case for RRLs due to their extended convective envelope. Marconi et al. (2018) found that an increase in He from the canonical value Y = 0.245 to Y = 0.30 – 0.40 increases both luminosity and pulsation period, yet the PLZ (PLZ) relations remain nearly unchanged. The mean

B and V band magnitudes, however, and the PLZ relation in the R band, display a significant dependence on He content.

On the a larger scale side of things, both satellite dwarf galaxies and some Local Group galaxies are close enough to have detectable HBs and RRLs. The latter have been observed as far as ≈2 Mpc in the Sculptor group (Da Costa et al., 2010). This is extremely advantageous in the study of Galactic formation, as it allows the investigation of satellite accretion and the hierarchical build-up of the Milky Way. Being old, RRL are unique among stellar tracers and standard candles because they preserve a snapshot of the chemical conditions of early epochs. The PL relation is very fortunate in this regard as well, as it allows to place field stars tridimensionally, which is in most cases impossible with other kinds of stars, and detect substructural remnants of accretion events (Drake et al., 2013).

The similitude or lack thereof between Galactic RRLs and their dwarf galaxy counterparts constrains the nature of the building blocks of the Halo. High amplitude short period RRLs are not found in dwarf galaxies with a mean [Fe/H] $\lessapprox$ -2 dex. Indeed, they seem to exist only in populations with metallicities higher than [Fe/H] from -1.4 to -1.5 dex, approximately. Interestingly, above this metallicity range, their presence is strongly correlated with the luminosity of the host. They seem absent in the faint satellites, but are plentiful in the Halo and in bright satellites of both the Milky Way and Andromeda, pointing out to the necessity for these Halo building blocks to be large indeed (Fiorentino et al., 2017; Monelli et al., 2017). This will be discussed further in Chapter 3.8.

It bears mentioning that on an even larger scale, namely a cosmological one, RRLs remain invaluable. They are the old aged counterpart to classical Cepheids, and far more common and theoretically understood than type II Cepheids. With their short periods and consequent less time consuming observations, they are unique in the cosmic distance ladder as primary distance indicators for old populations in a wide range of metallicities (Beaton et al., 2018). This allows for an independent measurement of the Hubble constant H_0 in an era where measurement precision increases and error bars shrink, but the values of H_0 derived by different cosmological experiments are still at dramatic disagreement (see Figure 1 of Beaton et al., 2016).

Indeed, H_0 determinations using cosmic microwave background modeling and the Cepheid distance ladder differ by more than 3 σ on their means, and the tension has been increasing with every new dataset. Calibrations using RRLs observed by Gaia and the Large Synoptic Survey Telescope (Ivezić et al., 2019) will allow for an accuracy better than 3 % on H_0, and so the time is ripe to develop the necessary toolset for distance determinations in a variety of environments (Braga et al., 2019).

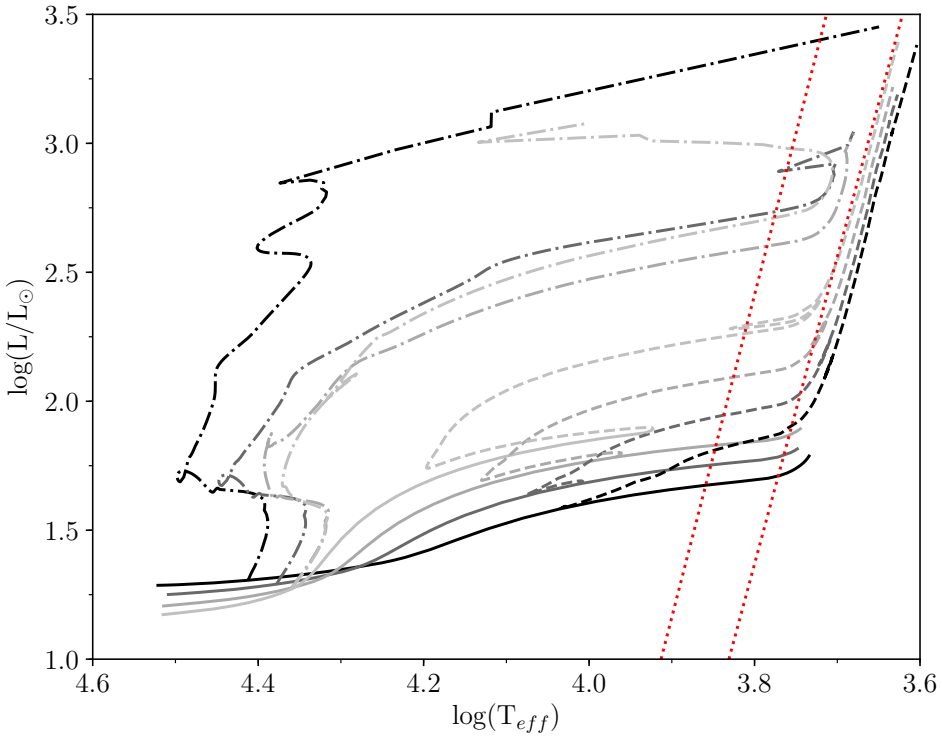

Figure 3.6: Luminosity and temperature effects of He variations for [M/H] = -1.27 dex. From darkest to lightest, Y=0.246, 0.300, 0.350, and 0.400. The full lines indicate the zero-age HB for each Y. Evolutionary paths off the zero-age HB for M=0.5 and M=0.6 $M_{\odot}$ are indicated by dot-dashed and dashed lines, respectively. The red dotted lines indicate the edges of the instability strip. All models were taken from the α-enhanced BaSTI database.

3.4 Evolutionary properties

Extremely metal-poor stars are rarely observed. This leads to the assumption that the first few stellar generations after the Big Bang were composed mostly of intermediate and high mass stars that evolved into their deaths long ago. The exact mechanism connecting metallicity and the fragmentation of molecular clouds is poorly understood in these primordial population and the initial mass function governing them is a matter of debate (Kroupa, 2001; Karlsson et al., 2013, and references therein). Once metallicity values reach about -4 dex, however, the initial mass function of most stellar systems seems to have become quite similar all across the Galaxy and nearby universe.

Observed mass functions display peaks that shift from about 0.4 $M_{\odot}$ in old systems to about 0.2 $M_{\odot}$ in young stellar forming regions (Chabrier, 2003; Bastian et al., 2010). This means that low mass stars, with their long lifetimes, make up the bulk of observable populations. Such stars spend most of their lifetime in the main sequence, fusing H into

He in their cores for time periods of the order of ten billion years. Once they are left with an inert He core, the only source of energy is the H shell burning in layers surrounding the growing and contracting core at increasingly larger radii and, consequently, lower temperature regions. The core heats up as it grows, counteracting gravitational contraction with electron degeneracy pressure. The envelope is slowly pushed outwards by the energy output of the H burning shell, increasing the radius and consequently luminosity of the star while at the same time decreasing its surface temperature. This evolutionary phase is known as the RGB due to its morphology in a CMD (Figure 3.1). The envelope expansion causes a stochastic mass loss that is notably difficult to model. While the evolution along the RGB itself is very insensitive to this mass loss, the later structure of the star is radically affected by it.

The inert He grows in mass to $\approx 0.48 - 0.50$ $M_\odot$ while remaining tightly fixed at a radius of just $0.03 - 0.04$ $R_\odot$ (Iben, 1971). At this point, the central temperatures reach 10^8 K and ignite a series of unstable He burning events, the first and strongest of which is called the He-flash. It takes place across a timescale of millions of years. These "flashes" occur off-centre in the core and then move inwards, where the temperature is actually lower due to energy loss by neutrinos. The energy released in these events first increases the kinetic energy of the electrons up to $k_B T$ without changing pressure. This lifts the electron gas degeneracy, causing the core to expand and be left with a density is of the order of 10^4 g/cm^3. Without the degenerate gas pressure at its bottom, the envelope contracts to reach gravitational equilibrium once more.

The star is now in the zero-age HB. It burns He into C in a convective core via the triple-α process, with an efficiency $\epsilon_{3-\alpha} \propto \rho^2 T^{40}$. The H shell burning via the CNO cycle persists with an efficiency $\epsilon_{\mathrm{CNO}} \propto \rho T^{17}$, leaving the star with two energy sources (Figure 3.7, left panel). The luminosity of the star at this point depends on its composition. The more metal-rich, the fainter it will be (Figure 3.8). Changes in He abundance also affect the star. An increase in the He abundance Y decreases the overall efficiency of the core burning, consequently extending the HB lifetime of the star, but it also increases the efficiency of the H burning shell in such a way that the total luminosity is higher (Figure 3.6).

Evolutionary effects will cause the star to leave the zero-age HB by both increase in luminosity and changes in effective temperature, creating the intrinsic width of the HB. The onset of core He burning happens at a very tight mass range, and yet differences of envelope mass create a wide extension in effective temperature. Here, the mass loss that happened during the RGB phase dramatically influences the structure of the star. A thinner envelope means a surface at smaller radius, and therefore at higher temperature. Moreover, if the mass loss was such that the total mass of the star falls to ≈ 0.65 $M_\odot$, the star will be located in the instability strip and develop radial pulsations.

Not only stars that land straight in the instability strip in the zero-age HB do so. Stars that arrived at hotter temperatures may venture into the instability strip later on as they evolve into the AGB, as evident in the bottom panel of Figure 3.8. Some

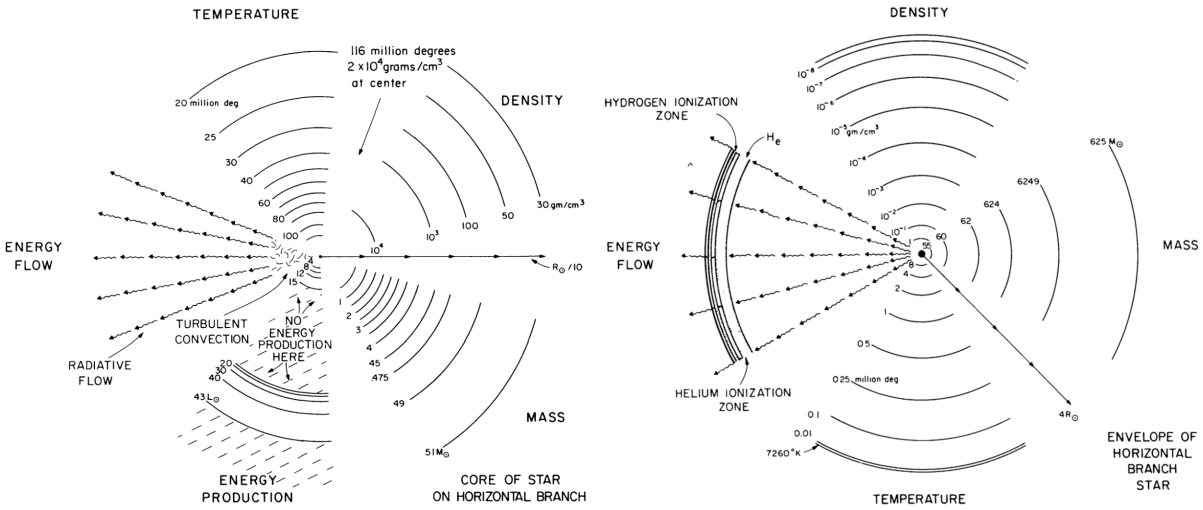

Figure 3.7: Schematic representation of the structural variables in the core (left) and envelope (right) of a HB star. Image from Iben (1971).

stars beyond the red edge may develop blueward loops and visit the instability strip repeatedly. With a lifetime of the order of 100 Myr, a HB star will undergo multiple changes. As long as the star crosses the temperature range of the instability strip, it will develop radial pulsations. And as long as it does so while burning He in its core, it will be an RRL variable. This brings up the question of what exactly drives these pulsations. It is clear that the mechanism behind it must depend on the mass of the envelope, as stars leave the RGB without any other significant structural difference between them.

3.5 Pulsation mechanisms

Stars can be considered to be in gravitational equilibrium, but they are not static. Thermodynamical quantities, energy production and gravity are at a continuous interplay that maintains a delicate balance. The radiative opacity κ_{R} of a stellar layer depends on its density ρ and temperature T in a relation of the form $\kappa_{\mathrm{R}} \propto \rho \mathrm{T}^{-7/2}$, the so-called Kramers opacity law (Kramers, 1923; Eddington, 1926). This proportion remains the same if the opacity is dominated by bound-free or free-free absorption. As a stellar layer is gravitationally compressed, which leads to an increase in temperature, its opacity decreases. Lower opacities result in greater energy loss by radiation. The pressure and gravity in the layer reach stability once more, and any pulsations are dampened. This makes for slightly variable but overall very stable stars. How, then, would the pulsations be periodic and self-sustaining? And why would stable, large amplitude pulsations be restricted to a certain envelope mass range, and, consequently, to an effective temperature range?

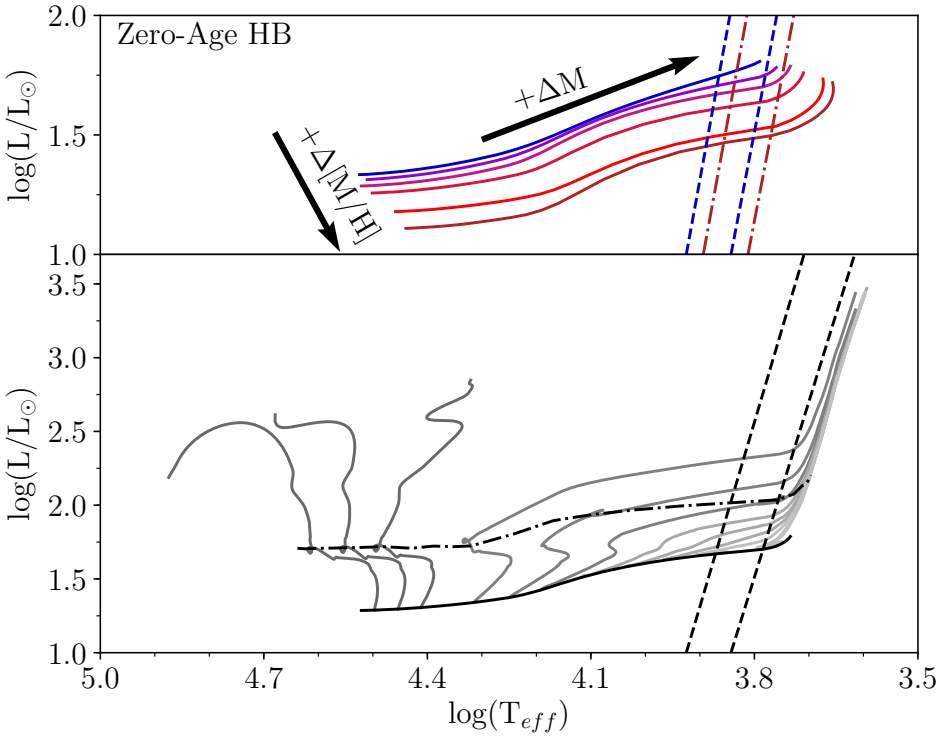

Figure 3.8: *Top:* Zero-age HB for metallicities [M/H] = -2.3, -1.8, -1.3, -0.7, 0.1, and 0.4 dex. The dashed lines indicate the instability strip edges for [M/H] = -2.3 dex, and the dot-dashed lines the same for [M/H] = 0.4 dex (Marconi et al., 2015). The arrows indicate the direction of increase of metallicity and mass. *Bottom:* Evolutionary path off the zero-age HB for [M/H]=-1.3 dex. The lowest three masses are 0.492, 0.495, 0.50 $M_{\odot}$. Between 0.50 $M_{\odot}$ and 0.70 $M_{\odot}$, increments are of 0.20 $M_{\odot}$. The dashed lines indicate the edges of the instability strip. The dot-dashed black line indicates the end of core He-burning. All models were taken from the α-enhanced BaSTI database.

The answer came in the doctoral thesis of Zhevakin (Zhevakin, 1963; Jørgensen & Petersen, 1967): partial ionization of H and He. If the temperature is high enough to ionize either of those most abundant species, opacity will necessarily increase even though temperature is increasing. Radiative energy loss becomes less efficient, and the layer retains energy, increasing its temperature even more. The pressure built-up forces the layer to expand instead of settle in equilibrium. But this only happens if the envelope is not so massive as to hinder this outward push. As the layer expands and cools down, the ionized atoms will return to their fundamental state, allowing energy loss via radiation to become efficient once more and allowing the cycle to continue. The increase in opacity with temperature is known as the κ mechanism, while the energy retention and entropy increase during the layer compression is known as the γ mechanism.

In a purely adiabatic approximation, pulsation periods can be determined with reasonable accuracy, but it is impossible to investigate which stellar structures will achieve stable pulsations and why (Christy, 1966). Indeed, the growth of pulsational amplitudes and the maintenance of periodicity rely on deviations from adiabatic behavior (Cox, 1967; Stellingwerf, 1974, 1975). The nonadiabatic terms, even though small, cause variations in thermodynamic quantities to not be exactly in phase and make the motion of the envelope deviate from a standing wave. This effect is pronounced in the H and He partial-ionization zones, where the adiabatic exponent Γ_3 drops to convection instability values (Figure 3.9).

Located near the surface of the star, the partial-ionization zones act as driving regions. Depending on their depth, the work they realize overcomes the damping of deeper layers. They move through several radii during a pulsation cycle, acting as the heat engines that cause the observable pulsation of the RRLs even as the innermost layers of the envelope remain stationary. This is visible in Figure 3.9, where the panels from top to bottom respectively show the work integral, the adiabatic coefficient Γ_3, and the opacity for a classical Cepheid. In all panels, the abscissa is the temperature, which serves as a proxy for pulsation phase as well. In Figure 3.10, the temperature (left panel) and radial velocity (right panel) versus phase are shown. The lines in each panel mark the different atmospheric layers. Thus, the figure illustrates how temperature and velocity behave, layer by layer, in the atmosphere of a first overtone pulsator across its pulsation cycle. While the absolute values of temperature and velocity may not perfectly describe an RRL, the pulsation mechanism and the behavior of the atmospheric layers is the same for both RRLs and classical Cepheids.

H and He are ionized at temperatures of about 12,000 and 40,000 K, respectively. These temperatures are easily reached in the envelope of HB stars (Figure 3.7, right panel), but only in the instability strip the ingredients for stable pulsations via the κ and γ mechanisms are found. The first is a thin enough envelope that can be pushed by the partially ionized layers, but not so thin that heat easily escapes through it or that it does not have enough mass to initiate contraction. The second is that the envelope cannot be too cold, or convection would quench the κ mechanism due to its shorter timescale. The first ingredient is related to the blue edge of the instability strip, while the second to the red edge (Bono et al., 1995a).

Secondary features in the light curve and the detailed topology of the instability strip, including the regions occupied by fundamental and first overtone pulsators, depend on the changing convection efficiency of the two partial-ionization zones (Bono & Stellingwerf, 1994). Therefore, a very careful modeling of convection is necessary. Indeed, the blue and red edges of the fundamental and first overtone regions are not parallel nor quite linear with temperature. This is shown in Figure 3.11, where the area of the instability strip in a Hertzprung-Russel diagram is shown, with the areas of the fundamental and first overtone pulsators shaded in blue and beige, respectively. The edges separating each region (solid lines) depend both on effective temperature and luminosity. Furthermore,

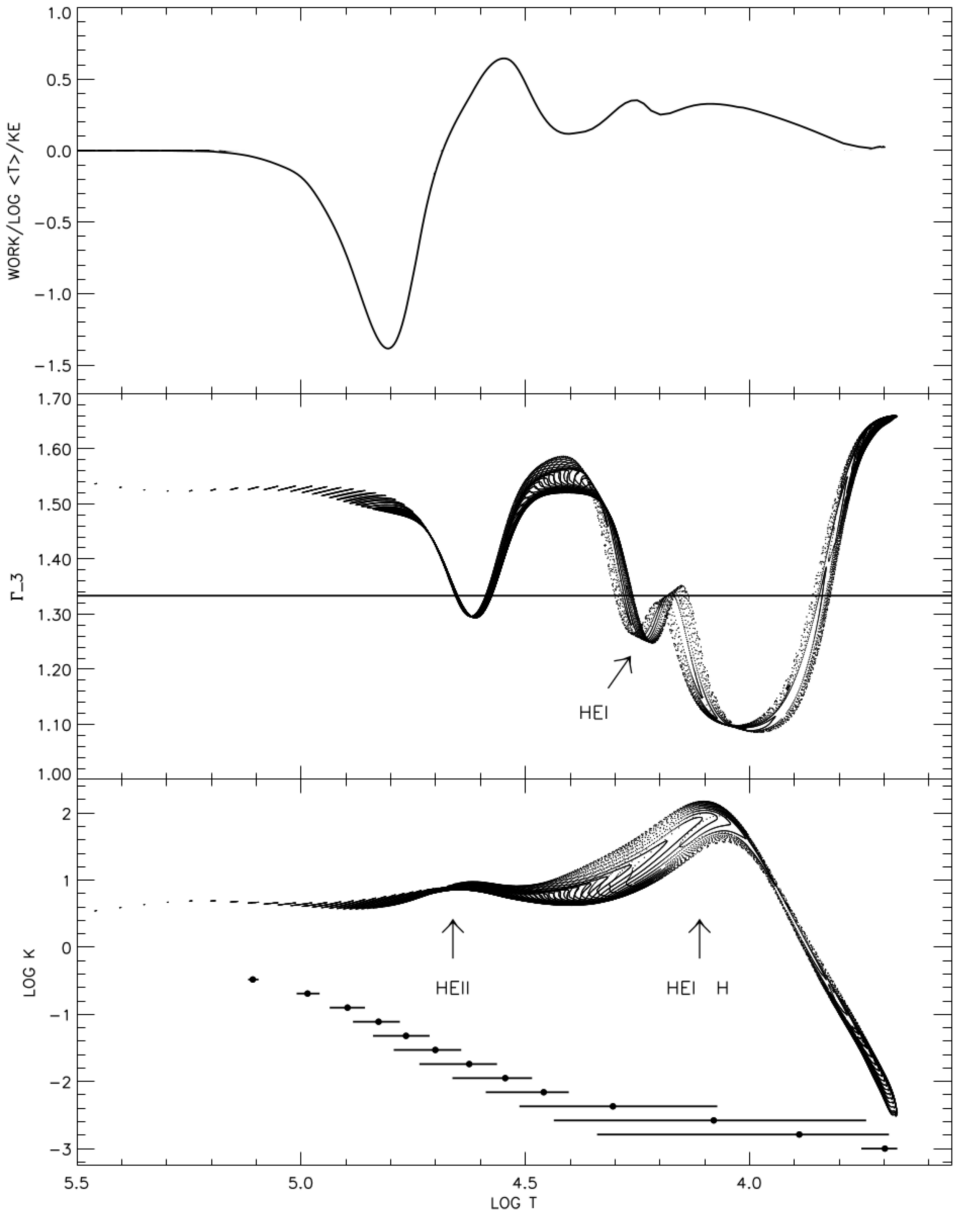

Figure 3.9: *Top:* Work integral as a function of temperature the full cycle of a classical Cepheid. The valley coincides with the damping region. The innermost peak is located at the He ionization zone, and the outmost the H ionization zone. *Middle:* Adiabatic coefficient Γ_3 versus temperature for the same star. The horizontal line marks the limit of instability to convection. *Bottom:* Opacity versus temperature for the same star. The horizontal bars indicate the temperature range swept by each layer, with the dot indicating the mean. Arrows indicate the partial-ionization regions. Figure adapted from Bono et al. (1999).

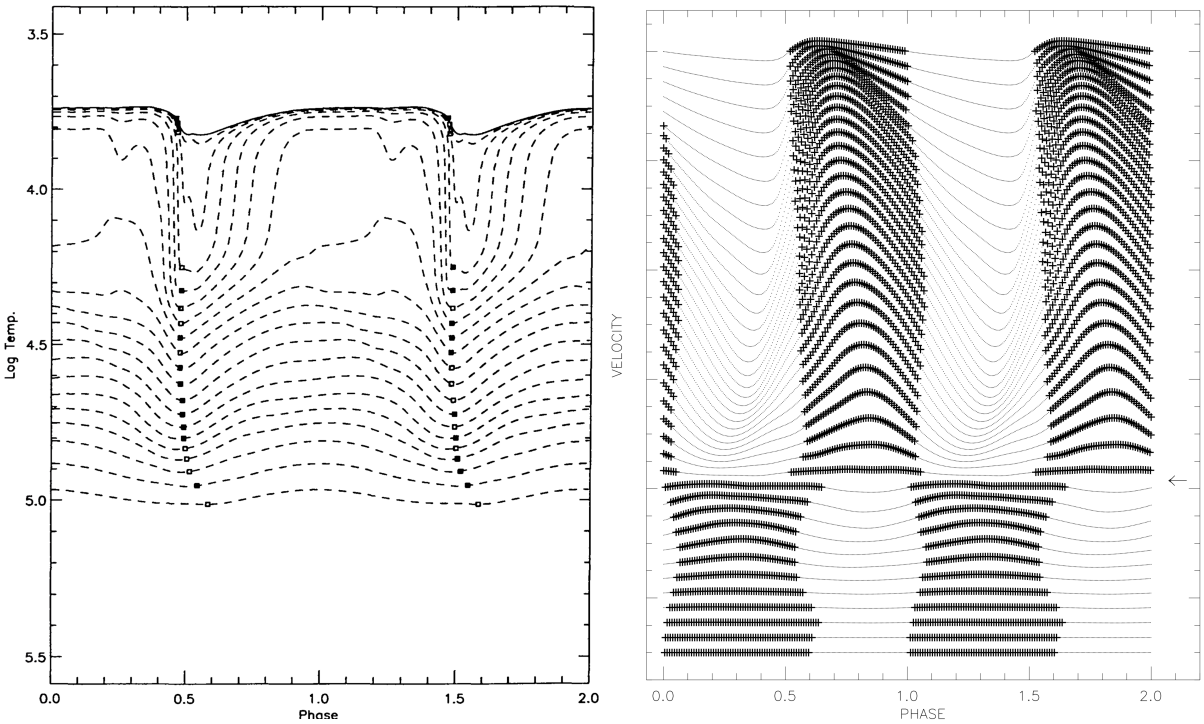

Figure 3.10: *Left:* Temperature versus phase for the outermost zones of a first overtone pulsator. The surface zone is represented by a full line. The squares mark the point of minimum radius for each curve. *Right:* First overtone velocity versus phase for the whole envelope. The velocity scale is arbitrary. Dots and plus signs mark the regions of contraction and expansion, respectively. The arrow indicates the nodal line. Figures from Bono & Stellingwerf (1994) and Bono et al. (1999).

the regions overlap, creating a temperature and luminosity range (pink region in the figure) where RRab and RRc can exist, as well as mixed-mode pulsators.

This mode overlap region is one of the culprits of the so-called Oosterhoff dichotomy Oosterhoff (1939). The dichotomy consists a metal-intermediate and metal-poor GCs having different average pulsation characteristics for their RRL populations, with the metallicity division happening at [Fe/H] $\approx$ -1.5 dex. The metal-intermediate GCs appear to host an RRab population with a mean period of $<P_{ab}> \approx$ 0.55 d, a relatively small number of RRc variables, and a red or evenly populated HB. Meanwhile, their metal-poor counterparts have $<P_{ab}> \approx$ 0.65 d, about the same number of RRab and RRc stars, and a blue HB. This divides the Galactic GCs into Oosterhoof type I, the former case, and Oosterhoff type II, the latter, leaving a gap between them in the mean period versus metallicity plane that is not observed in satellite dwarf galaxies (Figure 3.12).

The transition region between RRab and RRc types in the instability strip moves to lower temperatures for higher metallicities due to changes in convection efficiency of

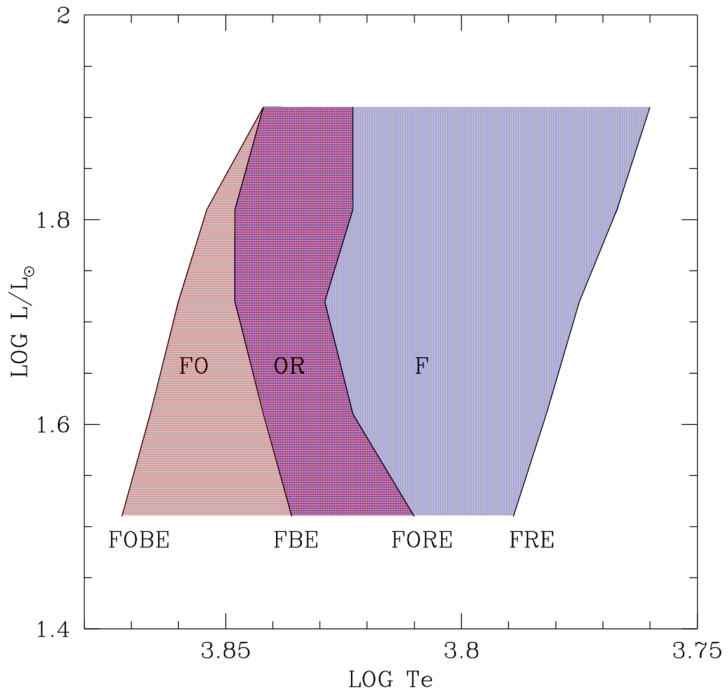

Figure 3.11: Predicted Herzprung-Russel diagram of the instability strip for Z = 0.0001, Y = 0.24, and M = 0.65 $M_{\odot}$. First overtone (FO) pulsators exist in the region between the first overtone blue edge (FOBE) and red edge (FORE). Fundamental mode (F) pulsators exist between the fundamental mode blue edge (FBE) and red edge (FRE). In the OR region, both RRab and RRc can exist, as well as mixed mode pulsators. Figure adapted from Marconi (2009).

the H and He partial-ionization zones (Bono et al., 1995b, 1999). Sollima et al. (2014) suggests that this hysteresis mechanism coupled with the peculiar age and metallicity distribution of Galactic GCs explains the Oosterhoff gap rather naturally, but see also the discussion by Fabrizio et al. (2019).

3.6 PLZ Relations

The RRLs occupy a narrow range in observed visual magnitudes and this by itself suggests their usefulness as standard candles. To determine the distance of a star via their distance modulus, both apparent and absolute magnitudes are necessary, and so there are two fundamental sources of uncertainty – one observational and another theoretical. On the observational front, reddening can range from negligible in Halo objects to insurmountable in some regions of the Disk such as towards the Galactic Centre.

As discussed in Chapter 3.4, the zero-age HB has a dependency on metallicity and

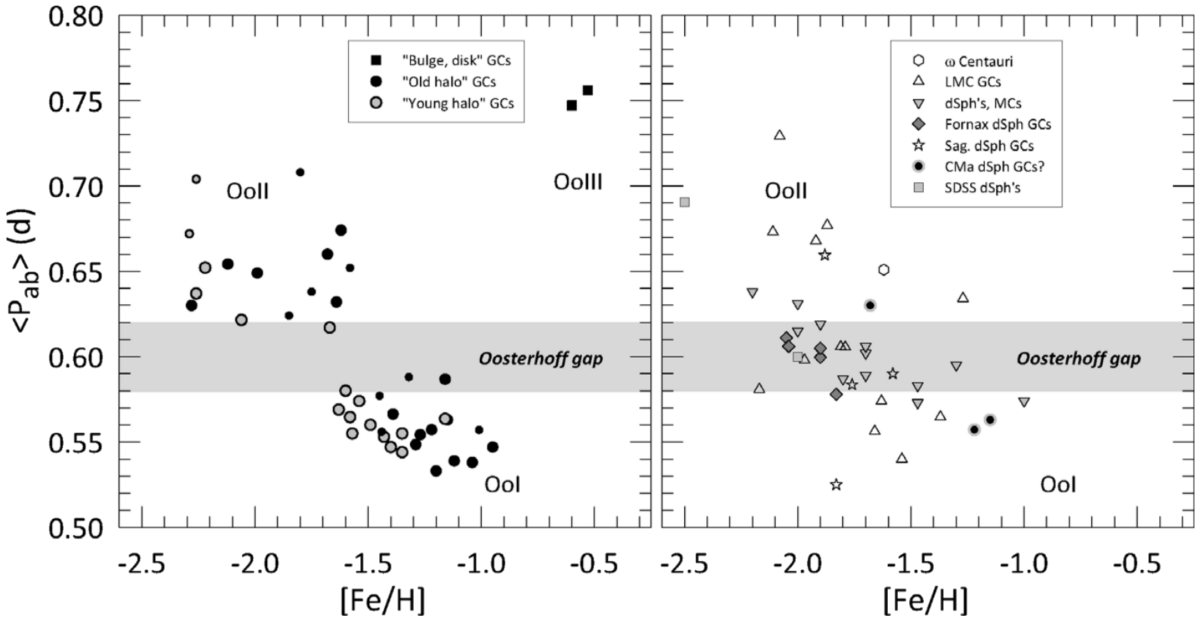

Figure 3.12: Mean period of fundamental mode RRLs versus metallicity for Galactic GCs (left), and for field and GC stars in dwarf galaxies (right) as indicated in the legend. Image from Catelan (2009a).

the evolution of core He-burning introduces changes in luminosity. This creates an intrinsic spread in the magnitudes of HB stars in any given population, including synthetic ones, from $\approx$ 0.1 to 0.5 mag (Sandage, 1990). A 0.1 mag uncertainty in distance modulus creates a 10 % uncertainty in distance. Furthermore, when we speak of apparent magnitudes of variable stars, mean values are the ones being considered. This requires either many observations to trace a complete light curve, or a few coupled with a well calibrated template.

Empirical calibrations rely on GCs as their stars can be assumed to have the same age and chemical composition. Their CMDs coupled with radial velocity determinations allow for easy identification of member stars. Yet there is disagreement in the literature about both the zero-point and slope of a linear average absolute magnitude dependence on metallicity. Evaluations of the zero-point span a 0.3 mag interval (Caputo et al., 2000; Di Criscienzo et al., 2004), while for the slope the figure is about 0.2 mag at [Fe/H] = -1.5 dex (Cacciari & Clementini, 2003).

A key improvement in the usage of RRLs as standard candles happens when we move from visual to NIR bands (Figure 3.13), where they do obey a PL relation with a nearly constant slope regardless of metallicity (Longmore et al., 1986, 1990; Bono et al., 2003; Catelan et al., 2004; Marconi et al., 2015). This is due to the different response of the bolometric correction in the NIR when compared to the optical regime (Bono et al., 2001). With a smaller dependence on luminosity, M_K is less sensitive to evolutionary effects,

while the greater dependency on temperature creates a significant slope (Figure 3.14). Furthermore, the standard deviation of the PLZ relations is $\sigma \approx 0.10$ in visual bands, while in NIR bands they fall to $\sigma \approx 0.04$ (Marconi et al., 2018).

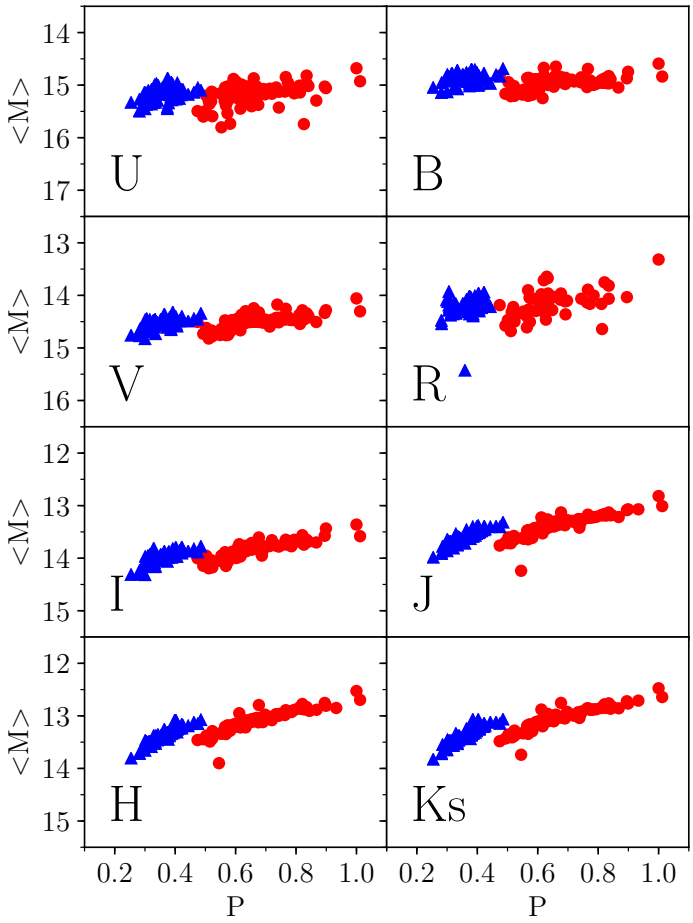

Figure 3.13: Visual and NIR period-magnitude relations for RRLs in ω Centauri (Braga et al., 2016, 2018). The vertical axes represent the mean observed magnitudes for the band indicated in each plot. RRab stars are represented by red circles, and RRc stars by blue triangles.

If good quality photometry is available, a color term increases the precision of distance estimates. A limitation in PL-color relations arises when differential reddening is a concern such as in directions towards the Bulge. This problem can be addressed by the usage of Wesenheit pseudo-magnitudes and Wesenheit indices, which combinations of observed magnitudes constructed in such a way as to be reddening-free as long as the reddening law is universal (Madore, 1982; Inno et al., 2013). Period-Wesenheit relations mimic period-luminosity-color relations and can be employed in directions where reddening is significant (Di Criscienzo et al., 2004). The limitation of this technique

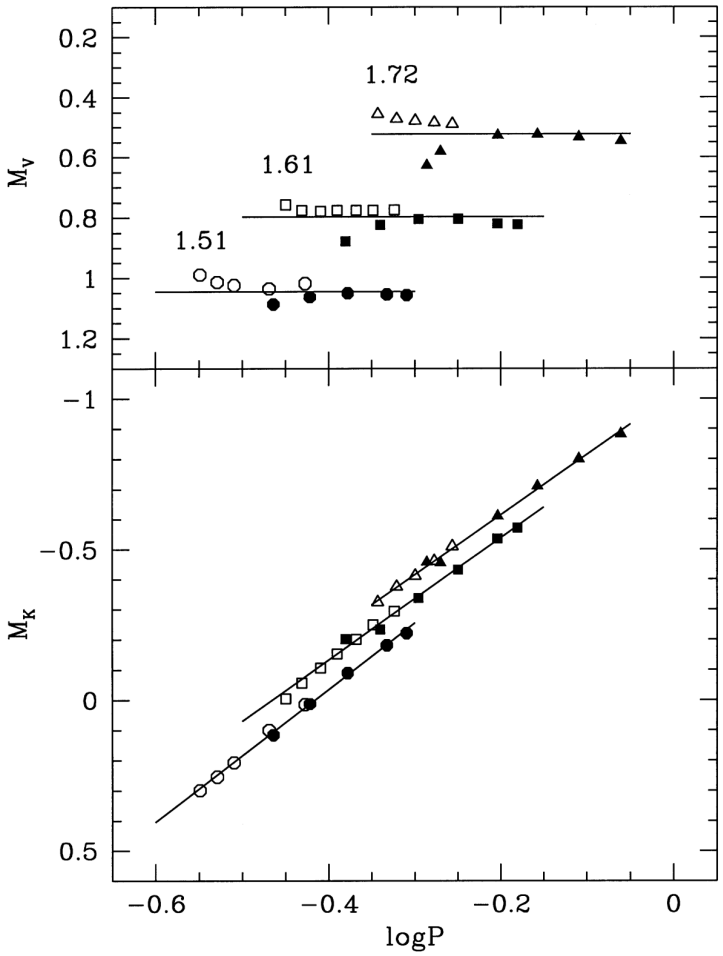

Figure 3.14: *Top:* Predicted M_V magnitudes for RRab (filled symbols) and RRc (open symbols) at fixed mass and metallicity, for the three different luminosities indicated by the labels. The periods of first overtone pulsators are fundamentalized. *Bottom:* The same but for the K band. The lines represent the PL_K relations for the same three luminosity values. Image from Bono et al. (2001).

is the need of multi-band photometric observations, with Wesenheit pseudo-magnitudes requiring at least two bands, and Wesenheit indexes requiring at least three. In the case of variable stars, this means that either well-sampled light curves or simultaneous multi-band observations are crucial.

Theoretical modeling is invaluable for the calibration of PL and PLZ relations. As we have seen, the HB as a whole, in its width in temperature, is an envelope mass sequence. In the instability strip this also means a pulsation period sequence. Thus, the dependence of absolute magnitude on temperature, via the bolometric correction, can be replaced by a dependence on period (Bono et al., 2003). The pulsation equation connects periods,

luminosity, mass, temperature, and chemical composition. Models also allow an independent investigation of He content (Marconi et al., 2018), a difficult undertaking that makes itself increasingly fundamental due to the multiple stellar populations problem in GCs (Chapter 3.3).

If good metallicity estimates are available, a PLZ relation sharply increases the precision of absolute magnitude estimates. Such estimates coupled with accurate (V-K) colors allow for an independent measurement of intrinsic luminosity (see Figure 1 of Bono et al., 2003). At fixed chemical composition, intrinsic luminosity is the parameter most affected by evolutionary effects. This is an advantage of colors using visual and NIR photometry because visual bands are very sensitive to luminosity, but also sensitive to interstellar extinction and very weakly dependent on period, while the opposite is the case for NIR bands. Indeed, in regions where the visual extinction is known with an accuracy of 0.03 mag, the (V-K) colors allow the evaluation of luminosities with a formal accuracy of about 0.03 dex.

Cleary, the usage of NIR pulsational observables gives us an array of advantages in determining both distances and stellar parameters:

- light curves are relatively easy to sample in short-period variables such as RRLs;
- due to the more symmetric shape of light curves in the NIR, mean magnitudes require fewer points to compute;
- pulsation periods are powerful observables as they are unaffected by distance;
- the K band is one order of magnitude less affected by reddening than visual bands;
- having a weaker response to evolutionary effects, uncertainties in the PLZ relations for NIR bands are smaller by a factor of three when compared to visual bands at fixed photometric error;
- NIR light curves are dominated by variations in stellar radius (Madore et al., 2013), and are therefore less sensitive to nonlinear phenomena;
- the luminosity dependence of NIR absolute magnitudes is small, with an uncertainty of 0.1 dex in luminosity introducing a change of ≈ 0.07 mag in M_K (Bono et al., 2003);
- the slope of PLZ relations is significant, and not affected by metallicity (Marconi et al., 2015);
- coupled with V magnitudes, K magnitudes allow for intricate study of intrinsic luminosity.

The NIR brings a few limitations as well. Perhaps the most relevant is the complexity in planning ground-based observations to account for the large influence of sky thermal background emission. The depth that can be reached even with the largest telescopes

reaches only some Local Group galaxies although this scenario will change with NIR space telescopes. The smaller pulsational amplitudes in the K band also bring about the necessity of very accurate measurements. This difficulty can be remedied by high quality NIR light curves that allow for derivation of periods and amplitudes with fewer observed data points (Braga et al., 2019).

Photometric data for RRLs and the theoretical framework to interpret them abound, but high precision metallicity estimates are still lagging behind. This is especially the case with field RRLs, of which less than ≈ 150 have been studied with HR spectroscopy and even fewer have measurements of elements other than iron. Increasing these figures will aid in the development of less resource-consuming but still homogeneous metallicity indexes that will, in turn, provide estimates for the large number of stars required to verify all varieties of PL relations. This will be discussed in the following chapter.

3.7 Methods of metallicity estimation

Most direct metallicity estimates for RRLs in the literature come from LR spectroscopy, variations of the ΔS method, photometric indexes such as the hk index, and Fourier decomposition analysis (Layden, 1994; Jurcsik & Kovacs, 1996; Rey et al., 2000; Drake et al., 2013; Chadid et al., 2017). Values for [Fe/H] computed with HR spectroscopy are available for ≈ 140 field RRLs (Magurno et al., 2018; Chadid et al., 2017). For GCs, the work of Magurno et al. (2019) introduced about ≈ 200 stars from ω Centauri, and the literature has mostly scattered spectra that do not increase the total figure by much. This limitation is compounded by the fact that most GCs do not have similarly large numbers of RRLs. HR estimates are difficult to obtain, but essential for the calibration of the less resource consuming techniques that allow for large homogeneous samples.

Each of these methods and its derivatives have an array of strengths and weaknesses, which lead to different applicabilities. Telescope time, knowledge of light curves, the presence of Blazhko stars, crowded fields, highly reddened regions, differential reddening, and so on, are all complications that require specific strategies to tackle, hence the multiplicity of metallicity estimate techniques. HR spectroscopy is clearly the least efficient of all of them. Yet it is the one that is indispensable for the calibration of all others.

3.7.1 The Phase-Average-Parameters method

For et al. (2011) analysed 11 field RRab stars across the entire pulsation cycle and showed that the atmospheric parameters vary in a very regular manner with pulsation phase. This was shown to be the case for RRc stars as well by Sneden et al. (2017) with a sample of 19 RRc stars. The idea was further developed by Magurno et al. (2019). They presented a detailed HR spectroscopic study of RRLs in ω Centauri. With 200 spectra

of 113 stars, the work nearly doubles the number of HR abundance estimates for RRLs available in the literature. They used this large sample to investigate the behavior of the atmospheric parameters of RRLs based on phase. Considering all stars together in order to sample the full pulsation cycle, they performed a polynomial fit of each of the atmospheric parameters versus phase, providing thus an empirical relation where, by providing the phase, it is possible to compute typical values of T_{eff}, log(g), and ξ_t.

This approach is called the Phase-Average-Parameters (PAP). The results for the RRab outside phases of maximum light are better than some estimates based on photometric indexes. For the RRc the uncertainties are still too large, suggesting that either a larger sample or a division of first overtone pulsators based on some quantity, such as metallicity, may be necessary. The method is an interesting route to investigate as it allows the computation of atmospheric parameters for stars in obscured regions such as towards the Bulge. Coupled with NIR spectra, these parameters allow estimates of chemical abundances as well in areas that are currently unexplored due to their high reddening.

3.7.2 Photometric estimates

The hk index (Rey et al., 2000) is a photometric metallicity estimate that requires a single epoch observation at any phase. It relies on determing a color based on the Caby photometric system, which is an expansion of the uvby system that includes a fifth filter centered on the CaII K and CaII H lines. This color, called the hk index, is associated with a metallicity through a calibration. It carries the intrinsic advantage of photometry in that large fields can be observed at once, and the intrinsic disadvantage that reddening must be well known.

Recently, Bono et al. (2019) introduced REDIME, an algorithm uses different PL and PLZ relations, solved iteratively, to provide reddening, distance, and metallicity estimates simultaneously. In order to achieve this, it requires mean magnitudes on six different bands, including both visual and NIR photometry. As mean values are needed, at least ten phase points per band per star are necessary. This high observational cost is justified by the capacity REDIME has of deriving all three parameters at once even for Blazhko stars and field stars, with a precision that allow He constant studies as well. The Large Synoptic Survey Telescope (LSST, Ivezić et al., 2019) time series survey will count with simultaneous observations on six different bands (u, g, r, i, z, and y), but PL relations will need to be calibrated for them.

Another purely photometric method is the Fourier Parameter Decomposition of light curves. It is based on describing V band light curves as a series of sine functions of the form

$$V = A_0 + \sum_i A_i \sin(i\omega(t - t_0) + \phi_i)$$

Kovacs & Zsoldos (1995) defined the quantities p_i and p_j as functions of pulsation period, A_i and ϕ_i. Coupled with a set of constants c_{ij}, this allowed them to make a fit of the form

$$[\mathrm{Fe/H}] = \sum_i \sum_j c_{ij}\ p_i\ p_j$$

Discrepancies were detected between predicted and spectroscopically derived metallicities even for stars with well defined light curves without any peculiarities. Jurcsik & Kovacs (1996) addressed the issue by increasing the number of calibrating stars, now including estimates done with ΔS method described below. The new formulation of their method depends only on the pulsational period, and the Fourier phase term ϕ_{31}. It introduces tests between the parameters that help detect peculiar stars. The light curves were fitted with a 15th order Fourier sum of sine functions. The final metallicity calibration has the form

$$[\mathrm{Fe/H}] = \text{-}5.038 - 5.394\ \mathrm{P} + 1.345\ \phi_{31}$$

Other calibrations exist in the literature, with the shared principle of an analytical fit of metallicity as a function of period and a phase component of the Fourier decomposition of sine or cosine functions. The Fourier decomposition method is extremely popular due ease of deriving the necessary parameters and adapting it to different photometric bands. Long running surveys provide a wealth of results on this front. The Optical Gravitational Lensing Experiment (OGLE) provides P and I-band based ϕ_{31} in its RRL catalogues (Smolec, 2005; Soszyński et al., 2011), while Gaia provides [Fe/H] values derived from the Fourier decomposition method adapted to its photometric bands. Hajdu et al. (2018) developed a related method using Principal Component Analysis of well-sampled K_s band light curves to estimate metallicities with a precision of 0.20 – 0.25 dex. While these uncertainties are larger than the residual scatter of the classic method employing V and I magnitudes ($\approx$ 0.15 dex), the calibration of a K_s relation makes use of a band used by the VISTA Variables in the Via Lactea (VVV) survey (Minniti et al., 2010).

This approach to deriving metallicities from light curves is very efficient. Relationships do exist between luminosity, metallicity, light curve rising times, and amplitudes, and a phase parameter of a Fourier decomposition can serve as an easily measurable proxy for those. The ϕ_{31} parameter covers a wide enough range of values that uncertainties still allow for the study of correlations of interest. But ϕ_{31} itself is simply a parameter of a mathematical decompositions of light curves and has no physical meaning. It is unclear how it responds to evolutionary effects or He abundance changes. A Fourier decomposition method is intrinsically unable to reproduce secondary features as they are discontinuities.

Absolute magnitudes derived from Fourier decomposition are unreliable for individual stars, and intrinsic colors are very discrepant (Cacciari et al., 2005). Hajdu et al. (2018)

found that the I band relations suffer from systematics with longer period and shorter amplitude RRLs displaying higher metallicities even on the well-known monometalic GC M3. The authors concluded that the issue extends to other bands as well. The variety of calibrations carries the need to transform metallicity scales in order to compare samples. The two calibrations employed by Deras et al. (2018) on NGC 6171, one for RRab and the other for RRc stars, disagree by 0.30 dex on their means, with the value for RRc stars agreeing with spectroscopic estimates. Furthermore, the method cannot be applied to Blazhko stars as their pulsational amplitude varies. At least a third of RRab stars are subject to Blazhko modulation. Long, multi-epoch monitoring is necessary to identify this effect in order to be able to remove the affected stars from a given sample.

3.7.3 The ΔS method

The ΔS method is based in LR spectroscopy, and as such provides a balance between observational efficiency and precision in metallicity estimates while retaining physical meaning. It was introduced by Preston (1959) and consists in computing the difference between the spectral type derived from the K line of CaII when compared to the one derived by the H_γ line. The H_γ Balmer line is a proxy for temperature, while the K line is sensitive to both temperature and metallicity, making ΔS a measurement of metallicity. Butler (1975) expanded the original work by deriving the "H spectral type" from the mean value of the equivalent widths of three H features (H_β, H_γ and H_δ), creating a new metallicity calibration (Figure 3.15). Both works concluded that the value for ΔS changes along the pulsation cycle of RRab stars and is only reliable during minimum light, while Kemper (1982) showed that the difference for RRc is only about 0.1 dex in [Fe/H].

Walker & Terndrup (1991) applied the Suntzeff et al. (1991) methodology to derive ΔS metallicities for 59 RRLs in Baade's Window, finding a narrow distribution peaked at [Fe/H] = -1 dex in the Zinn & West (1984) scale. Kunder & Chaboyer (2008), on the other hand, found a wide distribution peaked at [Fe/H] = -1.25 dex in the Bulge using the Fourier decomposition method on Massive Compact Halo Objects (MACHO) survey (Alcock et al., 2001) data, a result supported by the OGLE data analysis of Pietrukowicz et al. (2012) after appropriate metallicity scale conversions. They compared stars in common with Walker & Terndrup (1991) and found some large differences. They suggest that the interstellar CaII K-line strength in the region of the Bulge may be responsible for these deviations, as they would introduce significant uncertainties on the ΔS value. HR spectral studies of RRLs in the Bulge are, therefore, necessary for clarify this disagreement.

The largest and most widely used ΔS calibration and metallicity scale is, to this day, the one developed by Layden94 (Dambis et al., 2013; Fabrizio et al., 2019, see e.g.), although later ones exist (e.g. Gratton et al., 2004b). It was produced using 19 RRab stars at minimum light phases. Using stars in common with seven GCs, Layden94 applied

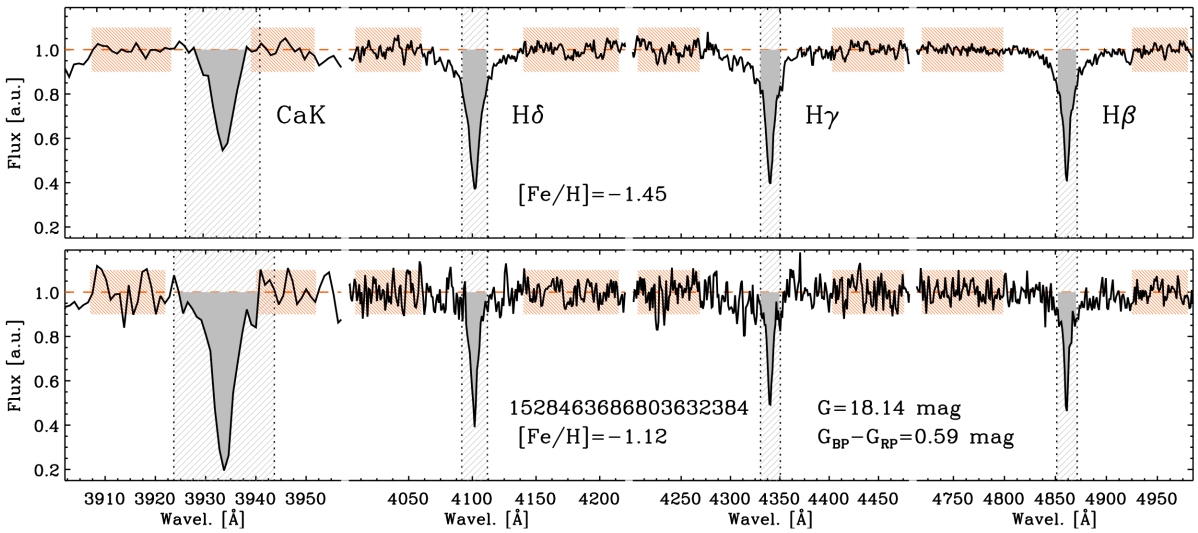

Figure 3.15: Normalized spectra for two RRLs with the CaII K line and Balmer lines used for the ΔS method. The orange regions are used for continuum placement. The hatched gray regions denote the wavelength range considered for the equivalent width measurement. Figure adapted from Fabrizio et al. (2019).

a metallicity scale transformation in order to provide values in the Zinn & West (1984) scale, which was at the time the preferred scale for GC investigations. The modest number of RRL observed with HR spectroscopy introduced a significant limitation in the sampling of the full metallicity range of these stars. The metal-poor and, even more so, the metal-rich tails were only weakly accounted for. Even more importantly, the calibration was developed for RRab stars only, and only for phases of minimum light. This means that spectroscopic observations had to be preceeded by photometric light curves that allowed for the precise determination of periods and reference epochs. Furthermore, these observations had to be timed in such a way as to ensure that spectra would be collected at the correct phase.

Chadid et al. (2017) compared results from the Layden94 ΔS calibration to 130 HR spectroscopic metallicity measurements of RRLs coming from seven literature sources. It is worth noticing that these sources were all published from 1995 to 2015, a time of large increase of spectroscopic observations of RRL. This fairly recent time window also means that the metallicity scales of different HR studies were converging due to modern spectrographs and increasingly similar, updated iron transition parameters. Indeed, Chadid et al. (2017) found that the metallicity scales of these studies differed from one another by constants, without any linear or higher order trend – this is a result that we confirm as well. After estimating the scale shift, they put all HR values into the same scale in order to compare them to values derived through the Layden94 ΔS calibration. They found that the relation of the two scales displayed a nonlinear trend and modest scatter

(see the bottom panel of their Figure 7). The latter is an acceptable result considering the ΔS method is a LR estimate. The former, however, means that metallicities are increasingly overestimated the more metal-poor the RRL is, and increasingly underestimated the more metal-rich it is. This results in an artificial narrowing of the metallicity distribution of a given sample: both the metal-poor and metal-rich tails are smeared into the metal-intermediate region, and details of the distribution are lost.

This trend between the Layden94 ΔS estimates and HR measurements is unsurprising. Indeed, the results of that ΔS calibration were put through a transformation into the Zinn & West (1984) scale through GC stars. The latter was developed using a mixture of photometric and spectroscopic indexes calibrated with the few HR spectra available at the time and is known to have a nonlinear correspondence with current HR metallicity scales (see Figure 9 of Carretta et al., 2009). The GC metallicity scale was updated with the extensive work included in Carretta et al. (2009) and related papers by the same authors, however an updated calibration of the ΔS method was still missing.

Recently, Fabrizio et al. (2019) investigated the possibility of applying the ΔS method to phases beyond minimum light. They showed that the equivalent width variation of the H lines and the CaII K line are mirrored across the pulsation phases, remaining constant except for the very short lived phase where nonlinear phenomena take hold in the stellar atmosphere. This important result reinforces that a large quantity of LR spectra for RRL can be acquired in an efficient manner. However, as the Layden94 ΔS calibration did not include phases beyond minimum light, the behavior of uncertainties was unclear and the question regarding whether the calibration was ideal remained unanswered. Furthermore, their results also dependend on a painstaking comparison of equivalent width systems between different spectrographs, because the Layden94 calibration was built using earlier spectrographs that could present very different responses and, in order to have reliable measurements and reliable uncertainty estimates, the exact same procedure had to be followed, including mimicking the responses of the spectrographs used in the calibration.

Thus, it became clear that the literature was sorely missing an update to the ΔS method that i) used a modern HR metallicity scale, ii) could account for all phases and provide accurate uncertainties, iii) did not depend on equivalent width system transformations, and iv) could be extended to first overtone, and perhaps double mode, pulsators. A new calibration of this LR spectroscopic method allows for the study of RRL samples in a manner that, unlike HR spectroscopy, is time-efficient and that, unlike photometric indexes, relies solely on physical assumptions. The LR metallicity estimates, vastly outnumbering the HR measurements and newly calibrated into a homogeneous scale, can reach greater distances into the Galactic halo and trace regions untouched by HR spectroscopy.

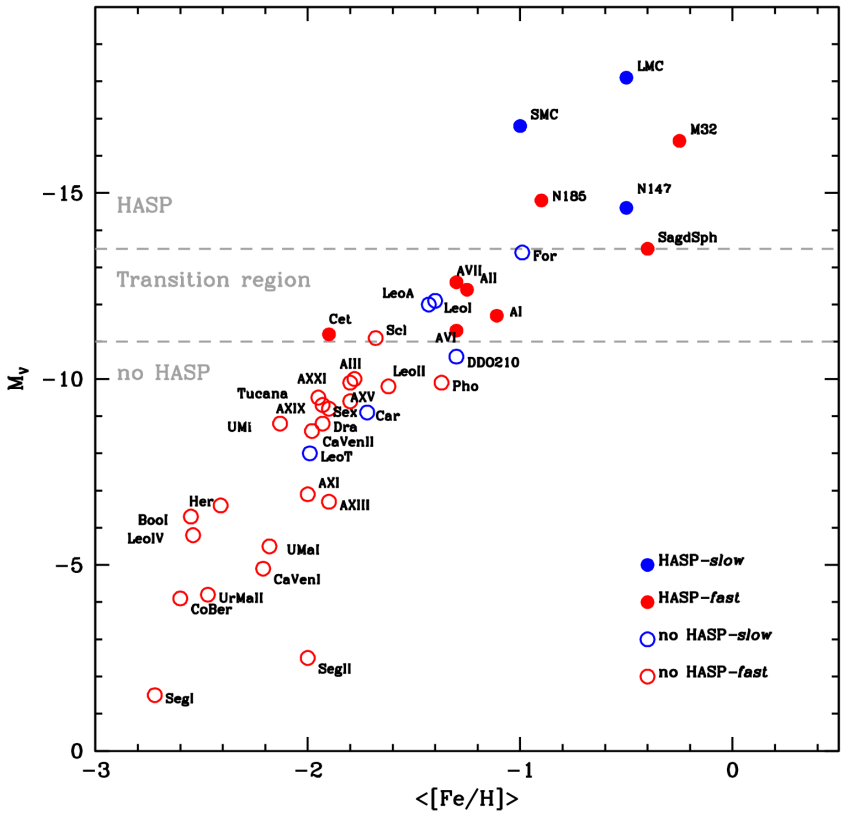

Figure 3.16: Luminosity versus metallicity distribution of all Local Group dwarf galaxies with available short-period studies. Filled circles indicate the presence of HASPs, and empty circles their absence. Blue symbols represent galaxies that had a fast stellar formation rate, with the majority of their stars having ages greater than 10 Gyr, while red symbols represent galaxies with a slow stellar formation rate, dominated by young and intermediate-age stars. Image from Fiorentino et al. (2017).

3.8 RR Lyrae stars and the building blocks of the Halo

As discussed in Chapter 2, the canonical scenario of Galactic formation relies on a hierarchical accretion of sattelites, with small galaxies forming earlier and merging into larger galaxies (e.g Bullock et al., 2001). This idea was suggested by Searle & Zinn (1978) and is supported by ΛCDM simulations, but several questions remain open: what was the nature of these earlier mergers?; are the current satellite dwarf galaxies representative of the building blocks of the Milky Way; how much of the Halo stellar population underwent in-situ formation and how much of it is accreted?

When it comes to all these questions, RRLs are especially useful with their wide

metallicity range, old age, and PLZ relations. Furthermore, the existence of the peculiar RRLs with high pulsational amplitudes and short periods is of particular interest. These HASPs are present in the Halo at metallicities higher than [Fe/H] = -1.5 dex and yet are completely absent in the satellite dwarf galaxies (Fiorentino et al., 2015, 2017). They are found, however, in the Large Magellanic Cloud and the Sagittarius dwarf spheroidal (Sgr dSph), and at similar rates as in the Halo (Figure 3.16).

The existence of these relatively metal-rich yet old stars in brighter, and consequently more massive, systems confirms that their chemical enrichment was fast. The smaller systems, on the other hand, did not reach a high enough metallicity at an early enough epoch to produce HASPs and therefore could not have provided the Halo with these objects via accretion events. Furthermore, in the intermediate luminosity range ($M_V \approx$ -11 to -13.5 mag), dwarf galaxies with and without HASPs coexist in a metallicity range of about 1 dex, indicating that parameters beyond host baryonic mass, and consequently chemical enrichment efficiency, play a role in the formation of these peculiar stars. Both the nature of the Halo building blocks and of HASPs themselves are exciting open questions to be tackled in the years, and datasets, to come.

Chapter 4

Stellar atmospheres and chemical abundances

The whole of spectroscopic chemical analysis relies on the formation of absorption lines by the presence of chemical species in the atmosphere of a star. As we know from quantum mechanics, bound-bound and bound-free electronic transitions depend on the absorption of photons of a precise energy that is determined by the transition in question. This translates to an absorption feature in a very specific wavelength. The final shape of a given line is not, however, simply a Dirac delta function. It rather depends strongly on a variety of physical quantities such as the number of atoms that undergo the transition, and the thermodynamical characteristics of the environment.

The environment is a layer of the stellar atmosphere, described theoretically by a temperature, pressure, opacity and, in one-dimensional models, a short scale non-thermal velocity term dubbed the microturbulent velocity. Therefore, it is necessary to first and foremost determine the atmospheric parameters. Those, paired with the observed absorption lines and their theoretical parameters, allow for an estimate of the chemical abundance of a given element. The reader is referred to Gray (2005) and Salaris & Cassisi (2005) for an in-depth treatment of the phenomena behind the formation of absorption lines, from the uncertainty principle to the optics of the detector, with the complex mathematical formulation they require.

Different chemical species are created in different astrophysical sites (e.g. during the explosion of massive stars, or the thermal pulses of old low mass stars) that can be associated to different timescales. To study the present-day chemistry of a star is to investigate both its evolution and formation history (see e.g. Matteucci, 2003; Johnson, 2019). The latter is always tied to the formation history of the larger structure it belongs to. In this chapter, we will describe the methods used in this project for the determination of the atmospheric parameters of the stars in our sample (Chapter 4.1) and of their chemical abundances (Chapter 4.2). Then, we will describe the major chemical families and how they trace different chemical enrichment mechanisms (Chapter 4.3).

The same techniques adopted in this work were first applied to non-pulsating stars in the inner Halo GC NGC 6723. They resulted in the published paper Crestani et al. (2019).

4.1 Determination of atmospheric parameters

One-dimensional atmospheric models assume a number of layers in LTE described by a set of thermodynamical quantities. Each given model is uniquely defined by four quantities: the surface or effective temperature $T_{\rm eff}$; the surface gravity log(g); the metallicity [M/H]; and the microturbulent velocity ξ_t. These models are usually provided as a grid that the end-user interpolates to create the specific atmosphere of interest. Here, we will describe the spectroscopic approach to the determination of these four quantities. On a fundamental level, the strength of an absorption line depends on

1. the quantity of absorbers, i.e. the quantity of atoms capable of undergoing the transition that creates the line, directly related to the abundance of the element of interest;
2. the opacity generated by all chemical species present in the atmosphere;
3. the temperature, pressure, and microturbulent velocity of the layer where the absorption happens;
4. the excitation potential EP, transition probability, and oscillator strength of the specific line in question.

The first, second and third items are fixed by the model atmosphere itself. The fourth is part of the line list, built mainly through laboratory measurements. For our purposes, all the extremely elaborate theoretical framework is reduced to two determinations: which model atmosphere best describes the star in the moment it was observed; which abundance value of a given species is capable of reproducing, in that atmosphere and for each line of interest, the equivalent line width or line profile. The equivalent width of a line is defined as the width of a rectangle that has the height of the continuum level and the same area as the line in question.

This area can be computed in multiple ways. Usually, and this is the approach used in the present work unless noted otherwise, a Gaussian function is fitted to the observed line or at least the core of the observed line, and the area is defined as the area under the fitted Gaussian. The width in wavelength to be considered for the computation of this area may be either the width between the intersections of the fitted Gaussian with the observed or fitted continuum, or a limited range such as only the core of the line. This latter case is relevant when measuring very strong lines that have wings that deviate from a Gaussian profile and could bias the fitted function. Indeed, these wings

are formed by transitions happening outside of the atmospheric layer where the core of the line is being formed and consequently describe different thermodynamical quantities. Depending on the type of investigation a given work is realizing, the profile of these wings may be relevant. For the situations describe below, however, neglecting these wings is a completely viable decision, especially because the vast majority of lines employed in this work are not strong enough to have significant wings.

The equivalent line width method is applied to FeI and FeII lines for the determination of the model atmosphere. It relies on the measured curves of growth of each line. The curve of growth is a representation of the reduced equivalent width $\log(W/\lambda)$ as a function of the abundance log(A), according to a relation with the form:

$$\log\left(\frac{w}{\lambda}\right) \propto \log(A) - 5040\ \frac{\chi}{T} - \log(\kappa_\nu)$$

where w is the equivalent width of the line measured directly from the spectrum. The line list provides the central wavelength λ of the line and its excitation potential χ. The atmosphere model provides the temperature T of the layer where the line is formed and its opacity κ_ν. The abundance log(A) is defined as the logarithm of the number of line absorbers of the chemical species of interested divided by the same for Hydrogen. What an automatic code such as the *abfind* driver of MOOG (Sneden, 1973a) does is compute an empirical curve of growth considering the input atmosphere and the parameters for each single line in the line list. The code then compares the measured reduced equivalent width with the one computed by the curve of growth, finding the corresponding abundance.

Note that the curves of growth present distinct regions, one of which is approximately linear. However, for higher abundances and larger equivalent widths, the curves reach a saturation zone beyond which large changes in abundance only weakly affect equivalent width. This can be seen in Figure 4.1, where the linear region is indicated by an orange dashed line between two orange dots. Clearly such non-linear regimes are to be avoided, as even small equivalent width uncertainties in this non-linear region propagate into large errors in abundance. Lines that are too small, on the other hand, suffer from large uncertainties because of the continuum placement. Therefore, we only used lines with equivalent widths between 15 and 180 Åfor most elements. Those display a Gaussian profile core, show smaller dependence on the pressure of the layer where they are formed, are safely within the linear region of the curve of growth, and are significantly deeper than the continuum noise. For elements with too few lines such as Eu and Pr, we allowed for smaller equivalent widths when the quality of the spectrum permitted a robust continuum placement. This was done because, for these elements, the choice was between having a potentially less precise measurement and having no measurement at all.

Temperature is the parameter that most strongly affects the shape of a curve of growth when line list values are fixed. The number of atoms that are excited from a given state i to a given state j satisfies Eq. 4.1, the Boltzmann equation, where N

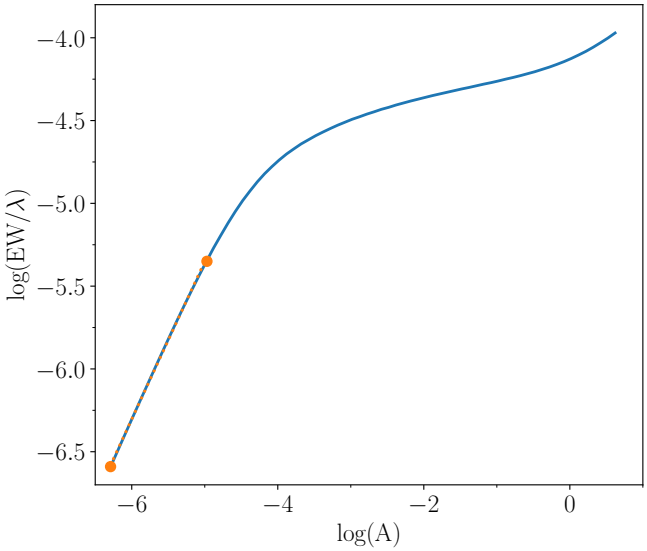

Figure 4.1: Curve of growth for an arbitrary line. The logarithm of the abundance (A) is on the x axis, while the logarithm of the reduced equivalent width (EW/λ) is on the y axis. The two orange dots connected by an orange dashed line denote the approximate limits of the region where the curve of growth displays a linear behavior.

is number of atoms per unit volume, g the statistical weight and χ the energy of the transition between the levels indicated by the subscript, k_B the Boltzmann constant, and T the temperature of the gas where the transition takes place.

$$N_j = N_i \frac{g_j}{g_i} e^{-\chi_{ij}/k_B T} \tag{4.1}$$

If the model $T_{\rm eff}$ is too low, the same measured equivalent width would require a larger number of absorbers, i.e. a higher abundance, to make up for the smaller fraction of excited atoms. But each transition line responds differently to $T_{\rm eff}$, especially due to their different excitation potentials. This is fortunate because the abundance of a given element is fixed, and so removing disagreements in the abundance given by different lines of the same species allows for a determination of $T_{\rm eff}$ (Figure 4.2). Iron lines are most often adopted for this purpose because they are the most plentiful, they cover a wide range in excitation potential, and they are the ones with the most reliable laboratory measurements. Removing the trend of FeI abundance with EP by changing $T_{\rm eff}$ is what is called reaching excitation equilibrium.

When the transition is between a bound and a free state, the statistical weight of the latter includes the number of possible states the free electron may occupy. This leads to Eq. 4.2, the Saha equation, where N_e the number of electrons, m_e the electron mass, h the Planck constant, and χ_{ion} the ionization potential. The quantities N_i and N_j are

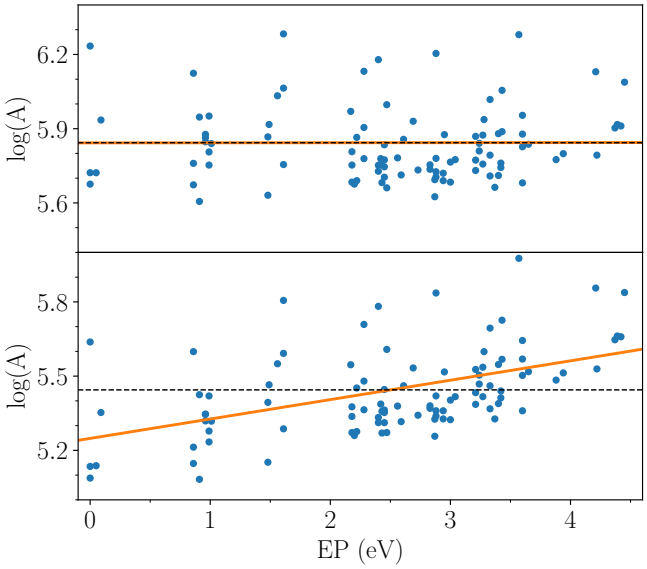

Figure 4.2: *Top:* Abundance of FeI lines as a function of excitation potential for an atmosphere in excitation equilibrium. The black dashed line indicates the linear fit of the points, while the orange full line indicates the mean abundance. *Bottom:* The same, but for an effective temperature 500 K lower.

once more the number of atoms per unit volume for the initial state i and for the final state j, respectively.

$$\frac{N_j N_e}{N_i} = \frac{(2\pi m_e k_B T)^{3/2}}{h^3} \frac{2g_j}{g_i} e^{-\chi_{ion}/k_B T} \tag{4.2}$$

The quantity N_e k_B T is nothing more than the partial pressure of the ideal electron gas. This pressure dependency arises because the possible states of the free electron carry the three-dimensional spatial coordinates via the linear momentum. The volume term cancelled out when only the nuclei were considered, but here it appears again as the electrons are added. The exchange of volume for pressure is of course very convenient. Just as the temperatures of all layers are defined by the effective temperature adopted in the model, the pressures of all layers are fixed by the surface gravity log(g). Ionized species are, therefore, more sensitive to pressure changes and respond very strongly to changes in surface gravity. Changing log(g) heavily influences the abundance derived by FeII lines, and when the latter agrees with the abundance derived by FeI lines, ionization equilibrium has been reached.

The microturbulent velocity ξ_t is a variable introduced in plane-parallel atmospheric models to account for line broadening due to small-scale turbulence cells in the gas, a type of mixing-length parameter. The small-scale refers to these cells having dimensions that are small compared to the mean free path of a photon at the stellar radius of interest.

This broadening cannot be described by thermal broadening alone. Qualitatively, a higher ξ_t translates into a more Gaussian profile for the absorption line even when many absorbers are present (i.e. abundance of a given species is higher), and prevents the saturation of the line into a Lorentzian profile. The influence of microturbulent velocity on weak lines is negligible, but it heavily affects lines with larger equivalent widths. With this in mind, ξ_t is constrained by the condition that both weak and strong lines give the same abundance value. In practice, this means eliminating any trends between FeI abundance and reduced equivalent width.

When these three atmospheric parameters (T_{eff}, log(g), ξ_t) are constrained, the mean iron abundance given by the curves of growth of all FeI and FeII lines is adopted as the metallicity value for the atmospheric model. This last characteristic is responsible for opacity values and is heavily simplified by the fact that the model atmospheres already account for typical chemical mixtures, either Solar-scaled or α-enhanced. The latter has the same effect on the global metallicity [M/H] as the former with an adjustment of iron abundance via the relation

$$[\mathrm{M/H}] = [\mathrm{Fe/H}] + \log(0.638[\alpha/\mathrm{Fe}] + 0.362)$$

where $[\alpha/\mathrm{Fe}]$ is the mean abundance of α-elements (Salaris et al., 1993). Thus, the models require the input of a [Fe/H] value instead of a detailed abundance pattern, with Solar-mixture or α-enhanced models using the appropriate transformation to [M/H].

In short, an atmospheric model is based on a combination of temperature, surface gravity, microturbulent velocity, and chemical abundance of each species. The best combination of parameters is found by:

1. changing the model T_{eff} in order to remove the trend between line-by-line FeI abundances and EP, which satisfies the condition of excitation equilibrium;
2. changing the model log(g) until abundances of FeI and FeII lines are in agreement, which satisfies the condition of ionization equilibrium;
3. changing the model ξ_t until there is no trend between FeI abundances and $\log(w/\lambda)$, which means both weak and strong lines are in agreement;
4. using the resulting FeI and FeII abundance as an input of the model [Fe/H];
5. repeating the process until the difference of the abundances of FeI and FeII, and all the described slopes, are smaller than internal uncertainties.

All atmospheric parameters have varying influences on the abundance of each line. Even when a dependence is not explicit, it can appear implicitly, e.g. k_ν carries a temperature and a chemical mixture dependency. Therefore, the last step described above is necessary in order to refine the final result.

4.2 Computation of chemical abundances

Once the atmospheric parameters are constrained, the line-by-line abundance for all species is computed either using the equivalent width method or the spectral synthesis method. The first has been described in the previous section. It can be applied to any isolated line without hyperfine structure with an equivalent width within the linear range of the curve of growth ($\approx$ 15 – 180 Å). This is because the definition of an equivalent width relies on the assumption of a Gaussian shape. This assumption is often not valid in the case of absorption lines created by transitions with hyperfine splitting, or in the case of a line that is so close to another, i.e. blended, that the Gaussian shape of its core cannot be constrained.

The spectral synthesis method consists in creating a synthetic spectrum in the region of the line of interest, for the atmosphere that has already been adopted and considering the resolution of the observed spectrum. The only parameter to be changed is the abundance of the chemical species in question until the profiles of both synthetic and observed spectra agree (Figure 4.3). This requires a precise line list that describes in detail the internal structure of the line and any nearby lines that are blended with it. This is of special concern for all lines with hyperfine splitting.

The hyperfine splitting results in transitions separated by about 1 – 10 mÅ and can desaturate absorption lines. The Manganese line in Figure 4.3, for example, is the result of fifteen transitions and is not Gaussian. Clearly, synthesizing it requires a very fine knowledge of each of the involved transitions. The energy splitting of a given line is usually determined empirically in high precision laboratory settings. The lines of heavier species that can be detected in stars are often affected by hyperfine splitting (HFS) to the point that Gaussian approximations result in very discrepant abundances (Prochaska & McWilliam, 2000). Spectral synthesis is also necessary even for simple transitions in the near-IR because of the myriad of molecular transition lines that result in both blended lines of interest and displacements of the continuum. This problem is significant in colder stars and lower resolutions.

4.3 The chemical families

The investigation of chemical species brings invaluable information on multiple levels of astrophysics. Empirical studies rely on good descriptions of the atomic transitions to be measured, and of other lines that may affect the profile of a given absorption feature in stellar atmospheres. These studies, on their turn, provide abundances that help constrain models of nucleosynthesis, supernovae explosions and yields, and galactic formation. Studying multiple elements is essential in order to constrain all these different levels of inquiry, from the reliability of atomic transition parameters to Galactic enrichment processes. In the following, we discuss four groups of chemical species that are often

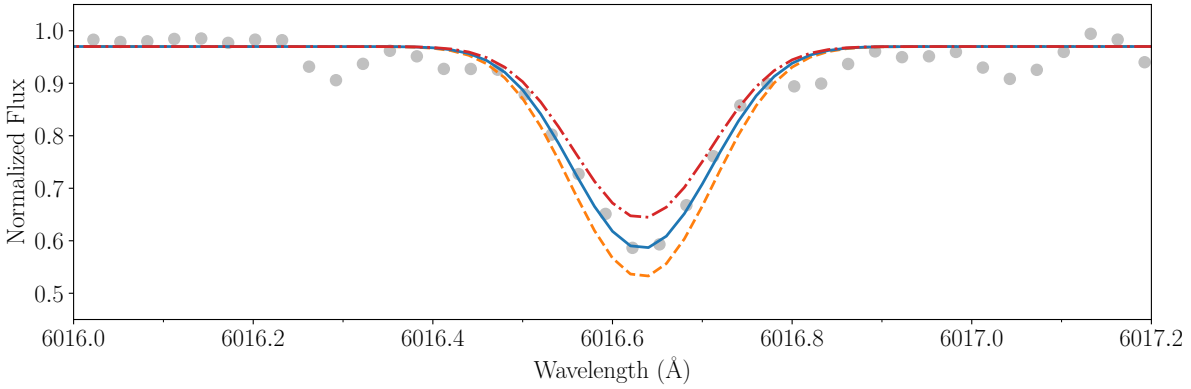

Figure 4.3: Example of the spectral synthesis method for a Manganese line with hyperfine structure. The blue full line is the best fit, with the dashed red line and dot-dashed blue orange representing variations of 0.15 dex in [Mn/Fe].

included in the study of stellar populations in the context of Galactic formation.

4.3.1 Light elements

There is a large interest in the light elements He, Li, C, N, O, Na and Al due to their variations within GCs. These compact, old clusters have long been assumed to be simple stellar populations, born of a single molecular cloud and therefore containing stars with the same chemical pattern. Unexpected differences in the abundance of certain light elements have been known for many decades, but only rather recently the idea of multiple episodes of stellar formation within the same globular cluster has become a matter of intense debate.

The basic assumption of the multiple stellar populations scenario is the existence of a first generation containing stars chemically similar to the field at the same [Fe/H] that evolve and provide chemical enrichment of a second generation. Thus, both the less massive first generation stars, which are still evolving, and the second generation population would be detectable, with significant variations in light elements but not in heavier species such as iron. None of the current hypotheses on the nature of the polluters and the mechanism behind the detected number ratio between the two stellar generations can fully explain observational constraints (Bastian & Lardo, 2018; Lardo et al., 2018).

Light element variations - namely, C and O deficiency, and enhancement in N, Na, and Al (Carretta et al., 2004) in a fraction of cluster stars, have been detected in several stellar evolutionary stages, and even in stars too cold to deplete their central O or to complete the NeNa and MgAl chains as to create the observed enrichment and depletion patterns. This supports the idea that abundance differences are intrinsic, i.e. it was

present in the molecular cloud that gave origin to the stars in question, and is not a consequence of evolutionary effects. An anticorrelation between Na and O appears to be ubiquitous, and perhaps a Mg-Al anticorrelation may be a feature of massive and metal-poor GCs (e.g. Gratton et al., 2004a, 2012). A He enhancement accompanies the Na and Al enhancement, but He is a notoriously difficult element to measure and fewer observations are available. Interestingly, Li is also detected in some Na-rich stars. This light element is quickly destroyed at relatively low temperatures, and thus a second stellar generation that has any detectable Li would have been enriched by pristine, unprocessed gas that has never been heated to temperatures higher than $\approx$ 2.5 MK (Prantzos & Charbonnel, 2006). Meanwhile, variations of heavier species seems restricted to the most massive GCs. These clusters may have a distinct formation process, such as being the surviving cores of disrupted dwarf galaxies as may be the case of ωCentauri (Bekki & Freeman, 2003). AGB winds carry a signature of high C, and thus this light element is used together with the n-capture elements in the detection of AGB enrichment.

When it comes to field stars, it is often mentioned that both Na and Al display α-like behavior in the Disk and Bulge due to a steady decrease from an enhanced plateau that mimics the "knee" of the α elements (McWilliam, 2016; Duong et al., 2019). However, it is important to bear in mind that the number of well-studied metal-poor stars in the Bulge and Disk is very limited. When stars from the Halo are included, the trend with metallicity for these two odd-Z elements appears to have very unique characteristics. In particular, the Al abundances undergo a sharp jump for metallicities between approximately -1.5 and -1.0.

The measurements for Halo field stars in Figure 4.4 come mostly from the compilation of Frebel (2010), and so it is unclear whether their literature sources applied NLTE corrections to their measured transitions. This is important because the most easily measurable Al and Na lines are subject to strong NLTE effects that depend on T_{eff}, log(g), and metallicity (see Figure 2 of Andrievsky et al., 2008), with corrections as high as 0.9 dex. Cayrel et al. (2004) investigated a sample of very metal-poor ([Fe/H] $\lesssim$ -2) field dwarfs and giants for a variety of chemical species. By applying the NLTE corrections suggested by Andrievsky et al. (2007) and Andrievsky et al. (2008), they obtained results for both Na and Al show constant abundance for [Fe/H] between -3.7 and -2.5, with [Na/Fe] $\approx$ -0.2 and [Al/Fe] $\approx$ -0.1. The mixture of results with and without NLTE corrections and different metallicy range coverages make a comparison with the literature very difficult for these two odd-Z elements.

4.3.2 α-elements

It was long believed that the so-called α-elements could be grouped together because they were produced by the successive capture of α particles, which consist of two protons and two neutrons. The α-element abundance [α/Fe] is oftentimes considered as a simple mean of the abundances of two or more elements among O, Si, Ca, and Ti. This is an

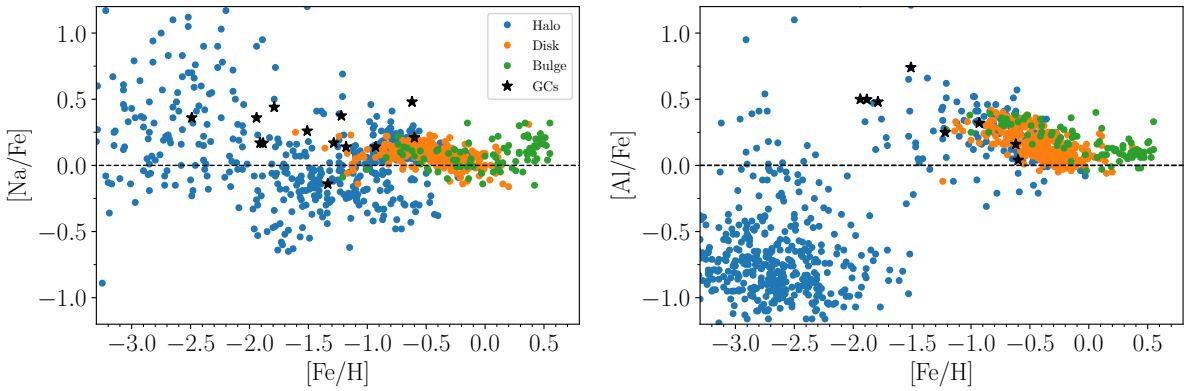

Figure 4.4: The [X/Fe] versus [Fe/H] plane for the light odd-Z elements in field stars of different Galactic components, and for GCs. Halo sources: Burris et al. (2000); Stephens & Boesgaard (2002); Frebel (2010); Nissen & Schuster (2010, 2011). Disk sources: Reddy et al. (2003, 2006); Ishigaki et al. (2013); Battistini & Bensby (2016). Bulge sources: Bensby et al. (2017). GC sources: Pritzl et al. (2005); Sakari et al. (2011); Çalışkan et al. (2012); Gratton et al. (2013); Hanke et al. (2017); Carretta et al. (2017); Johnson et al. (2017); Koch et al. (2019b); Koch & Côté (2019); Crestani et al. (2019).

assumption that can only be made if those abundances increase in lockstep. More recent nucleosynthetic models have shown that the formation channels of different isotopes and the astrophysical sites where they occur vary, although their release into the interstellar medium remains confined to core-collapse supernovae (SNe II) for the most part (see, for example, McWilliam, 2016, and references therein).

O and Mg are thought to be largely created in hydrostatic nuclear burning in massive stars and then released in SNe II events, with some production in the AGB phase, while Si and Ca are produced mostly by explosive nucleosynthesis in SNe II events with a smaller quantity also being produced in SNe Ia. For Ti, the SNe Ia events may be far more significant, as models of core-collapse SNe yields predict a much lower abundance than what is observed (Woosley & Weaver, 1994; Kobayashi et al., 2006; Nomoto et al., 2006). It is important to note that the dominant Ti isotope is actually $^{48}_{22}$Ti, which is not a multiple of an α particle. Yet the trend of Ti with metallicity follows those of other α-elements very closely, althought at somewhat higher values. This suggests that, regardless of the precise formation channels, these chemical species are likely formed at similar rates in similar astrophysical sites. If the interest of a given investigation is to trace enrichment mechanisms, e.g. supernovae types, instead of element formation processes, it is quite reasonable to group together elements that show similar trends with metallicity, although care must be taken regarding zero-point differences. The [α/Fe] values in the literature corresponds to a mean abundance of Si, Ca, and Ti.

The strong dependence on core-collapse SNe makes α-element abundances particu-

larly useful in galactic archaeology. Massive stars evolve quickly and, upon undergoing core-collapse, release large quantities of α-elements into the interstellar medium. Most of the iron produced during their evolution, however, remains locked away inside their core. Therefore, a high ratio of α-elements to iron is a clear signature of rapid chemical enrichment produced by massive single stars through SNe II events. Thus, the [α/Fe] versus [Fe/H] plane for a given population displays a characteristic trend that sheds light on its initial mass function (IMF) and star formation rate (SFR) (Figure 4.5). An IMF that favors massive stars is reflected in a higher overall [α/Fe]. These massive stars evolve quickly and enrich the interstellar medium with the ejecta from SNe II, creating a footprint of roughly constant [α/Fe] for a wide metallicity range.

At some point, the low mass stars reach the end of their longer lifetime as well, with single stars enriching the interstellar medium through pulsations in the AGB phase that release mostly C, N, F, and heavy elements (Karakas & Lattanzio, 2014). If they are part of a binary system, however, they give origin to SNe Ia events instead. These supernovae expell large quantities of iron, causing the the [α/Fe] ratio to begin a steady decrease as metallicity keeps increasing. This forms a so-called *knee* in the [α/Fe] versus [Fe/H] plane. If the SFR is high, the stellar population in question will reach higher metallicity values before the onset of SNe Ia, shifting the *knee* to a higher metallicity. This SFR dependency has been explored at length to characterize the chemical enrichment history of Galactic components (Figure 4.6) and dwarf galaxies (Figure 4.7), and investigate both possible shared origins and reasons for differences.

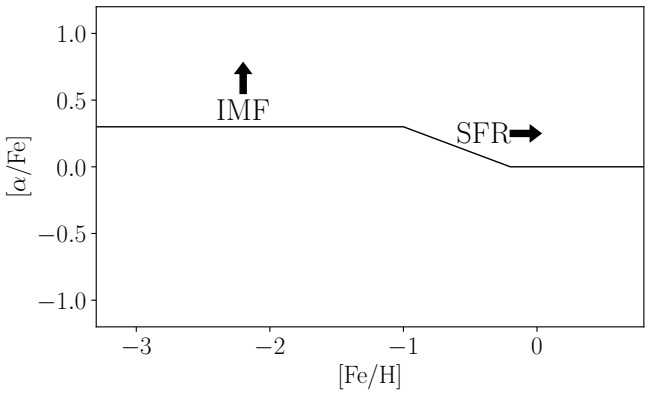

Figure 4.5: Schematic representation of the *knee* in the [α/Fe] versus [Fe/H] plane in a given stellar population. The initial mass function (IMF) defines the maximum [α/Fe] values. The star formation rate (SFR) defines the metallicity [Fe/H] where the [α/Fe] values start to decrease. Image adapted from McWilliam (1997).

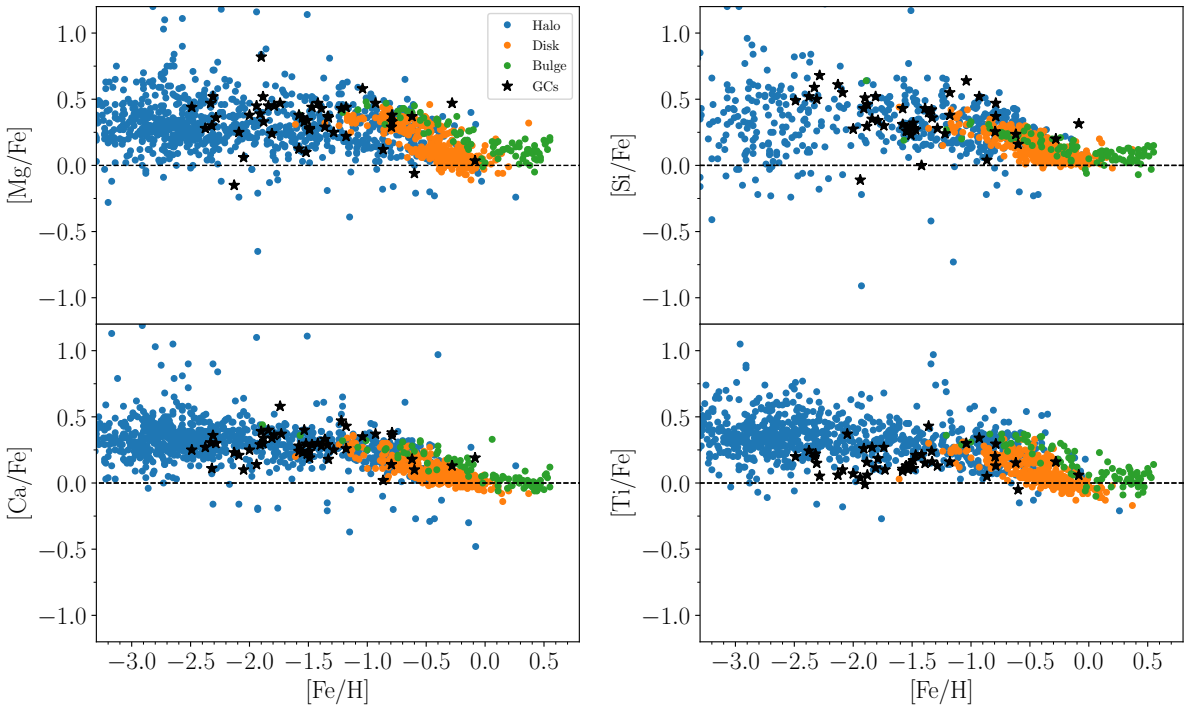

Figure 4.6: The [X/Fe] versus [Fe/H] plane for the α elements in field stars of different Galactic components, and for GCs. The data sources are the same as in Figure 4.4.

4.3.3 Fe-peak elements

Species from the so-called Fe-peak, running from Sc to Zn, have formation sites that are varied and the details of their production are uncertain, with different isotopes being formed at various rates in different reactions (Woosley et al., 2002). While they are often studied together, they display varied trends with metallicity (Figure 4.8). Transitions that result in the most easily observable lines for heavy odd-Z species are subjected to strong hyperfine splitting that must be taken into careful account in the computation of abundances, lest they end up sometimes severely overestimated or suggesting spurious trends (Prochaska & McWilliam, 2000). Furthermore, many lines of Fe-peak transitions are subjected to considerable NLTE effects that may also give rise to spurious results when populations with very different effective temperatures are compared (Thorsbro et al., 2018).

While Sc is still normally considered part of the group, Ti is most often considered an α element and, indeed, very often included in computations of average [α/Fe] abundances. Sc, V, and Co also display a trend with metallicity that is similar to trend set by α elements in field stars, pointing to a shared dependence on massive stars (Battistini & Bensby, 2015, and references therein). The trends in different Galactic components are

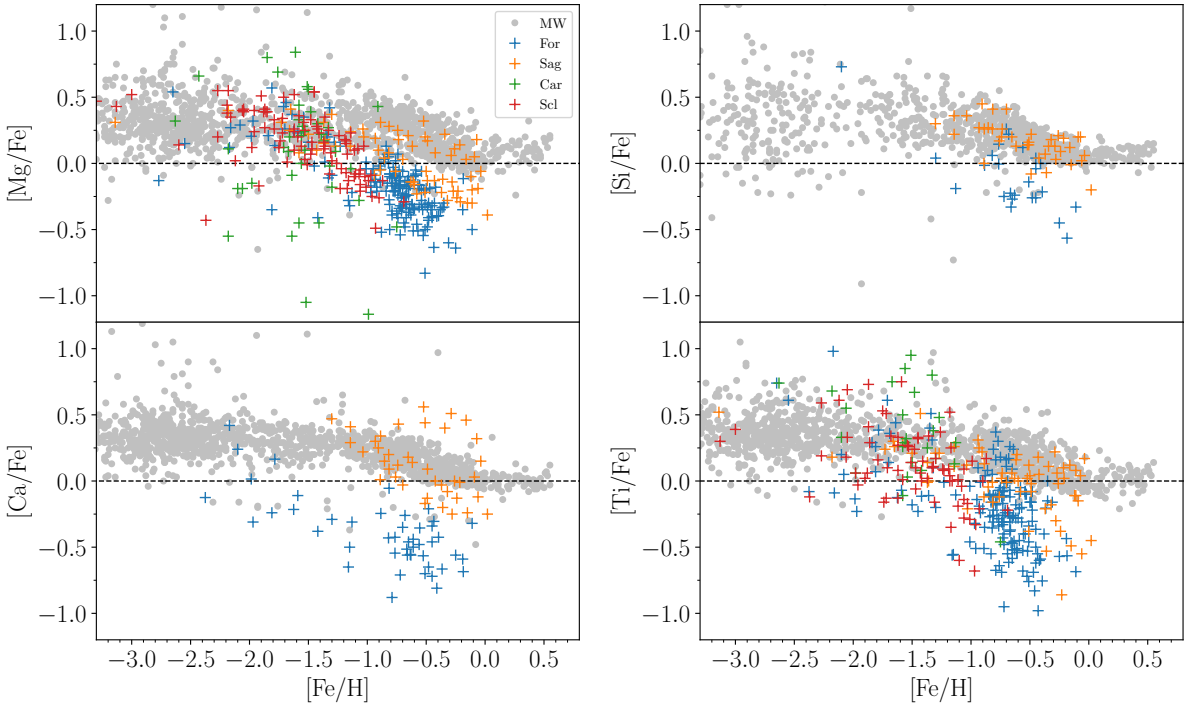

Figure 4.7: The [X/Fe] versus [Fe/H] plane for the α elements in the Galaxy and in the classical dwarf galaxies Fornax, Sagittarius, Carina, and Sculptor. The dwarf galaxy data sources are Sbordone et al. (2007); Carretta et al. (2010); Lemasle et al. (2014); Reichert et al. (2020).

not identical, however. The Bulge and Disk show slightly different V and Co trends (Lomaeva et al., 2019). Interesingly, considering Bulge GC stars instead of field stars, Gratton & Sneden (1991); Prochaska & McWilliam (2000); Ernandes et al. (2018) report a flat trend for both Sc and V for metallicities from [Fe/H] = -1.5 to solar. Differences in Sc may be due to the dependence of its production on the progenitor metallicity and mass (Woosley & Weaver, 1995; Nomoto et al., 2013), which in turn make this species particularly sensitive to details of the chemical enrichment history. Nucleosynthetic models do not detect a strong metallicity dependency for V (Kobayashi et al., 2011), but its formation channels are still not well known and may actually be more efficient in SNe Ia than in SNe II. The formation of the third α-like Fe-peak element, Co, is also debated (see e.g. Kobayashi & Nakasato, 2011; Kobayashi et al., 2011; McWilliam, 2016). At solar metallicity, ScII lines seem to be robust against NLTE effects, making them the preferred diagnostic for abundance determinations of this species (Zhang et al., 2008). It is important to note that lines of both CoI and CoII are subject to NLTE effects that are very pronounced in the metal-poor regime and, unfortunately, not well constrained (Bergemann et al., 2010).

The α-like trend set by Sc, Ti, V, and Co is not shared by their neighbor Mn. Indeed, Mn is notoriously under-abundant in both field and GC stars for subsolar metallicities (e.g. Ernandes et al., 2018). Its production is sensitive to several quantities that are hard to constrain, such as core collapse SNe model mass cut, explosion energy, and ratio of SNe Ia to SNe II, that also affect the production of other Fe-peak species such as Cr and Co. The difficulty of constraining abundance of Mn together with that of other elements is compounded by the fact that its most easily measurable lines need significant NLTE corrections that alter considerably its trend with Fe in the metal-poor regime. On the one hand, the NLTE corrections making the trend flat, in disagreement with the SNe yield models that predict a lockstep production of Mn and Fe (Bergemann & Gehren, 2008). On the other hand, the NLTE corrections also suffer from significant uncertainties. Thus, the nucleosynthesis of Mn is poorly known and is likely to remain such at least until better NLTE computations become available. Care must be taken when considering Mn in a description of Galactic enrichment, and also when comparing abundances of populations with very different stellar atmospheres.

The situation is better for Cr and Ni. These two elements have an impressively low scatter in the [X/Fe] versus [Fe/H] plane. Cr and Ni shows a flat trend for Bulge and Disks, with Ni possibly showing a modest enhancement in the metal-rich regime for thin disk stars (McWilliam, 2016). For CrI lines, NLTE corrections solve the inconsistencies between observations and models, and the discrepancy with results derived from CrII transitions, while a disagreement between atmospheric and meteoritic Solar values persists (Bergemann & Cescutti, 2010).

Details of the formation channels of Cu are still debated, but it is believed to be mostly formed through the s-process. This means that, because of the dependence of the s-process on metallicity, Cu production is metallicity-dependent in addition to progenitor mass dependent. Cu abundances show markedly different behavior in different Galactic components. For all components, Cu shows a notorious deficiency in the metal-poor regime which slowly decreases until [Fe/H] $\approx$ -0.8 dex, after which [Cu/Fe] reaches a plateau at solar value (see Figure 12 of McWilliam, 2016). The trend set by Bulge stars, however, does not plateau, but rather continues a steady increase and reaches super-solar Cu abundances as high as 0.5 dex at solar metallicity. McWilliam (2016) ascribes the flattening of the trend with metallicity for Halo and Disk stars to the time delay effect of SNe Ia. In this scenario, the SNe Ia in the Halo and Disk begin to become significant at [Fe/H] $\approx$ -0.8 dex and supply the interstellar medium with Fe but not Cu, effectively flattening the trend. This process would be different in the Bulge, as its Cu abundance continues in a steady increase, pointing to a higher star formation rate in the Bulge than in the rest of the Milky Way and, consequently, a greater influence of SNe II up to higher metallicities. This means that in the Bulge there is a delay of the onset of the plateau in [Cu/Fe].

Zn is believed to be formed through similar channels as Cu and released virtually only in SNe II, but with a much smaller production via the s-process. Results for Disk

stars show a mostly flat trend with metallicity, with abundances slightly super-solar up to [Fe/H] ≈ -0.2 dex. At metallicities higher than [Fe/H] ≈ -0.2 dex, a shallow decrease may be present in the Bulge (Barbuy et al., 2015) but, due to limited data, it is unclear whether different Galactic components display different trends in this element.

The limitations of nucleosynthetic models, NLTE correction grids, and the heterogeneous considerations of HFS in the literature all make the investigation of Fe-peak elements challenging. At the same time, it is in cases such as this that a homogeneous high resolution analysis of coeval stars becomes even more important. It bears mentioning that variable stars such as the RRLs and the Cepheids are an excellent laboratory for the study of NLTE corrections.

4.3.4 Neutron-capture elements

As with Fe-peak species, odd-Z n-capture elements often boast strong HFS effects in their line formation and display varied trends with metallicity (Figure 4.9). Defined as all species with atomic number greater than 30, they are produced as heavy nuclei capture neutrons that, if unstable, are transformed into protons via β decay. In neutron-poor environments, where the neutron capture timescale is longer than the β decay timescale, the s-process dominates, while the r-process occurs in neutron-rich environments. Both the s- and r-process encompass multiple channels likely to occur in different astrophysical sites, with a metallicity dependence on the production of n-capture elements as a whole (Travaglio et al., 2004). The main source of s-process elements is believed to be AGB stars although other sites are possible (see e.g. Hansen et al., 2013, and referecens therein), with a production that is heavily dependent on mass and metallicity (e.g. Sneden et al., 2008; Bisterzo et al., 2014; Karakas & Lattanzio, 2014; Karakas & Lugaro, 2016). Merging neutron stars and the neutrino winds of core-collapse SNe are the likely sites of the rapid(r)-process. Details of this process are not well understood (e.g. Woosley et al., 2002; Thielemann et al., 2011), but recent findings are promising (Drout et al., 2017).

Most n-capture elements can be produced by either process at different rates. Considering solar isotopic ratios, Sneden et al. (2008) quotes 85% of Ba as being produced via the s-process. The figures for Y, La, Ce, Pr, and Nd are, respectively, 72%, 75%, 81%, 49%, and 58%. These values are in good agreement with the estimates computed by Bisterzo et al. (2011) except for Y, for which they found a figure of 92%. Most works also agree that Eu and Dy are produced nearly exclusively via the r-process. Eu has a small number of good, unblended transitions in stellar atmospheres, but Dy is unmeasurable in most cases. Thus, Eu abundance is the best tool to determine the presence of r-process enrichment empirically. Its s-process counterpart, Ba, counts with only a few lines that are all very strong and quickly saturate in colder or more metal-rich stars such as Classical Cepheids. In such cases, Y and La are adopted as the s-process tracer due to their weaker lines.

The quality of available spectra, lines, and NLTE corrections all influence the scat-

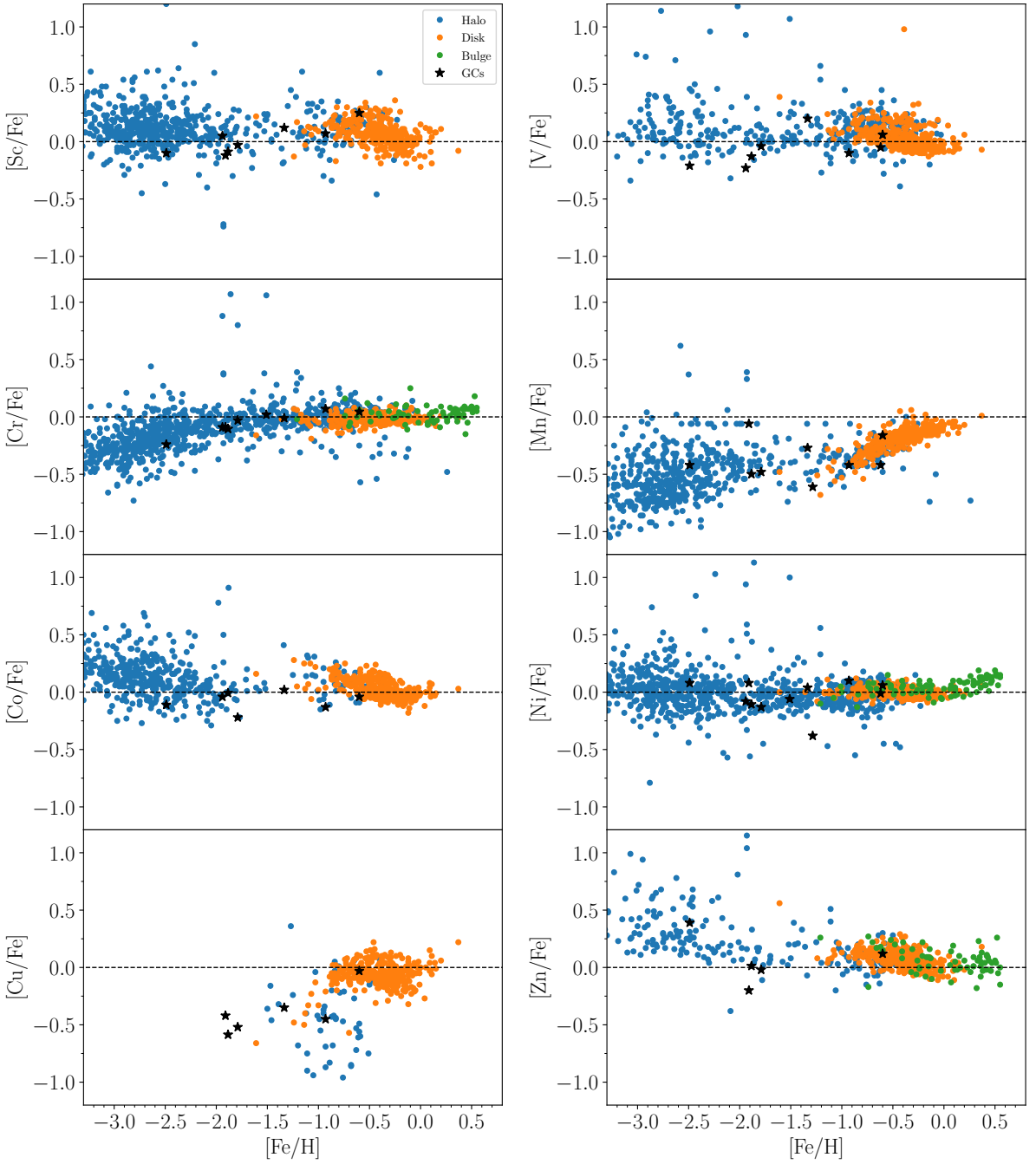

Figure 4.8: The [X/Fe] versus [Fe/H] plane for the Fe-peak elements in field stars of different Galactic components, and for GCs. The data sources are the same as in Figure 4.4.

ter in the [X/Fe] versus [Fe/H] plane. However, another source of scatter in measured

abundances in the same stellar population may be intrinsic and carry important information about nucleosynthesis and Galactic evolution. This is the case for Sr (For & Sneden, 2010). This light s-process element has strong, well known transitions that can be easily measured across a wide range of metallicities. Hansen et al. (2013) found that lines from its ionized species SrII are only minimally affected by NLTE effects that, even when accounted for, still display a significant scatter that nucleosynthetic models fail to reproduce. They underline that SrI lines require NLTE corrections based on effective temperature and metallicity and, while SrII abundances largely do not, they are very sensitive to surface gravity. This is a concern when the method of Fe ionization equilibrium is used to compute log(g) because, depending on the atmospheric parameters, the NLTE effects on the Fe lines may be significant, which in turn cause significant uncertainties in log(g) and, finally, in abundances of ionized species such as SrII. Thus, comparisons done with the literature must be taken with special care as the treatment of all these effects is not homogeneous across studies. It is important to note, however, that in the sample of dwarfs and giants employed by them, the Sr abundances in an LTE and those in a full NLTE analysis (including NLTE corrections of Fe lines and surface gravity), have differences of the order of 0.2 dex (see their Table 4).

The scatter in Y abundances is smaller but also significant (Frebel, 2010) and several open questions remain regarding this n-capture element. It is assumed to be produced mostly via the s-process channels but its trend does not follow the trend of Ba, with Y lacking enhanced stars in the metal-poor regime (Frebel, 2010), and being mostly flat in the metal-intermediate and -rich regimes (Reddy et al., 2003, 2006). A study of Disk Classical Cepheids da Silva et al. (2016) detected a flat slope of [Y/Fe] versus Galactocentric distance while there is an increase in [X/Fe] with Galactocentric distance for La, Ce, Nd, and, indeed, for the r-process Eu as well. In general, GCs display a depleted Y that steadily increases until it reaches a plateau at Solar value at about [Fe/H] $\approx$ -0.5 dex, at which point its scatter also decreases (Pritzl et al., 2005). One exception is Palomar 12, which displays a Y abundance remarkably lower than other GCs and Galactic field stars, but similar to that of satellite dwarf galaxies. Interestingly, Magurno et al. (2019) identified a group of RRLs in the metal-rich component of ωCen that is considerably enhanced in Y ([Y/Fe] $\gtrsim$ 0.5) when compared to both to RRL in the metal-poor component of ωCen and in the field. Another mystery involving Y and RRLs was found by Liu et al. (2013). They detected a severe Y depletion for metallicities higher than [Fe/H]$\approx$ -1 dex in sample of 23 field RRLs. The authors found radial velocities suggestive of a Disk, and not Halo, membership for these stars. With the same sample, Magurno et al. (2018) found that this Y depletion in the metal-intermediate and metal-rich regime is at odds with RRLs GCs, Halo, and Disks, and suggested these stars belong to the Bulge instead. The investigation of this n-capture element in RRLs is fundamental to clarify the behavior of Y in different environments, and its production channels.

Among the species in the first n-capture peak, Zr displays the lowest spread and

the clearest trend with metallicity. It is enhanced in metal-poor stars and undergoes a steady decrease as metallicity increases. This α-like trend points to an astrophysical formation site with a short timescale, in disagreement with the identification of Zr as dominant s-process element made by several studies. Indeed, Bisterzo et al. (2011) and Simmerer et al. (2004) list its s-process component at 97% and 81%, respectively, with other works in the literature presenting lower figures that still remain at near 70%. McWilliam (2016) presents the hypothesis that the s-process may dominate the production of Zr at solar metallicities, but that other mechanisms associated with massive stars and shorter enrichment timescales dominate at lower metallicities. This is particular important because the other elements believed to be dominated by the s-process have flat abundance trends with metallicity in the metal-intermediate to -rich regime, and a large spread, both of which are not found in measurements of Zr. In Figure 2 of Battistini & Bensby (2015), a clear that Zr reaches a plateau at [Fe/H] $\approx$ -0.2. This gives support to the hypothesis of a change in the rates of different production channels for this element.

Ba, first element of the second peak, has a large scatter at metallicities lower than [Fe/H] $\approx$ -2, with a significant number of Galactic field and classical dwarf galaxy stars being Ba-rich, although the majority of Galactic field and all ultrafaint dward galaxy stars are strongly depleted in Ba, with values as low as [Ba/Fe] $\approx$ -2 and lower (Frebel, 2010). At slightly higher metallicities, both Galactic field and GC stars show similar trends in the [Ba/Fe] versus [Fe/H] plane, with a nearly constant value ([Ba/Fe] $\approx$ -0.4) up to [Fe/H] $\approx$ -1 dex. This suggests that s-process contributions are not significant in the higher metallicity end of the metal-poor regime (Pritzl et al., 2005). For metallicities higher than [Fe/H] $\approx$ -1, Ba displays a sharp increase and reaches a plateau at solar abundance for [Fe/H] $\approx$ -0.5 and higher.

The second element of the second peak is La. As mentioned above, it is believed to be mostly an s-process element that should follow closely both Y and Ce. Burris et al. (2000) shows a flat trend in the [La/Fe] versus [Fe/H] plane at solar La abundances on average, with a higher scatter in the metal-poor regime. Battistini & Bensby (2016), observing metallicities greater than [Fe/H] $\approx$ -0.8, detect a negative slope that terminates at [La/Fe] $\approx$ -0.2 at super-solar metallicites.

The third and fifth elements of the second peak, Ce and Nd, are more sparsely measured than the other n-capture elements. It is unclear what the behavior of Ce is in the metal-poor regime, but Reddy et al. (2003, 2006); Battistini & Bensby (2016), using Disk stars, detect a flat trend for metallicities higher than [Fe/H] $\approx$ -1. The first of the cited studies found the same behavior in Nd, however the latter two detected a shallow negative slope from [Nd/Fe] $\approx$ 0.3 to -0.2 in the same metallicity range. A stronger decreasing trend was found in Disk Classical Cepheids for super-solar metallicities (da Silva et al., 2016).

The one r-process element with a significant number of measurements in the literature is Eu, a member of the second peak, with a handful of weak although unblended lines in the optical range. It displays an opposite trend to Ba, starting at very high values

in the metal-poor regime ([Eu/Fe] $\approx$ 0.5) that undergo a sharp decrease as metallicity increases, reaching abundances as low as [Eu/Fe] $\approx$ -0.2 for super-solar metallicities (Pritzl et al., 2005; Reddy et al., 2006). This sharp difference between the trends for Ba and Eu means that the slope of the abundance of a n-capture element with [Fe/H] for metal-intermediate and -rich regimes can be used a proxy for the contribution of the s- r-process channels in its production. A flat trend is achieved by elements expected to be dominated by the s-process, while a steep decrease with increasing metallicity is the signature of r-process elements. An ideal example of this is Nd, with a slope that is shallower than Eu, in accordance with being almost equal parts an s- and r-process element. It is also of note that Eu displays a trend with metallicity that is comparable to the α elements, as expected for a tracer of a fast enrichment process, but the scatter is significantly larger when compared to the Mg trend. The scatter decreases and becomes comparable with that of the α element at metallicites [Fe/H] $\approx$ -1.5 dex. This could be evidence that r-process production was rare in the early Galaxy and that poor mixing resulted in only isolated regions being enriched by them. This mixing would become more efficient later on (Sneden et al., 2008). It is important to note, however, that this scenario relies on the existence of an age-metallicity relation, i.e. that metal-poor stars tend to be older, and metal-rich stars younger.

The recent laboratory measurements of transition probabilities performed by the Wisconsin group (e.g. Den Hartog et al., 2002, 2003; Lawler et al., 2009) have greatly improved the quality of spectroscopic studies of n-capture elements. However, measurements in the literature still suffer from significant scatter. This is partially due to the presence of HFS in many lines of heavier species that are treated differently across studies, and the overall scarcity of unblended absorption lines. The latter is particularly significant in hot stars such as the RRLs and HB stars where all metallic lines are shallower.

4.4 A word of caution regarding the [X/Fe] versus [Fe/H] plane

Here, it is essential to underline that the trend of different elements in the [X/Fe] versus [Fe/H] plane provides robust results regarding enrichment processes, but that the absolute abundance values themselves and averages between multiple species must be taken with caution, especially across different studies but also within the same investigation. This is because absolute values are heavily dependent i) on the quality of the line transition parameters, ii) on which lines are used, iii) which NLTE corrections, when applicable, are applied, and iv) the formation channels of the element in question. These three points deserve to be discussed in a bit more detail, as they are relevant to all spectroscopic studies of chemical abundances.

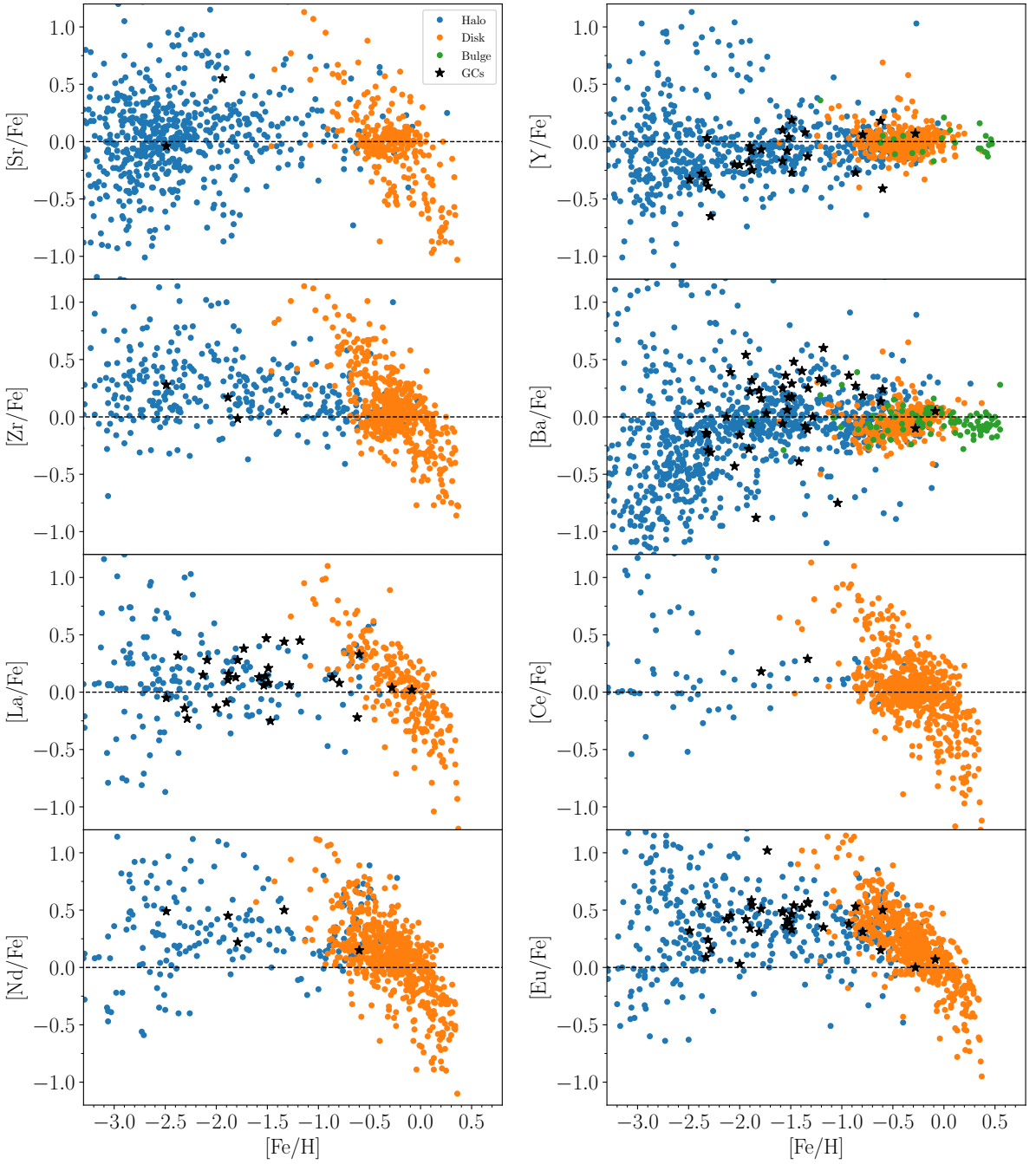

Figure 4.9: The [X/Fe] versus [Fe/H] plane for the n-capture elements in field stars of different Galactic components, and for GCs. The data sources are the same as in Figure 4.4.

- **i) the quality of line parameters:** It is clear that different line lists are a source of significant inhomogeity when considering results from different studies. Inves-

tigations of chemical abundances are converging to a certain level of homogeinity in the past two decades, but this is not the case for all chemical species. Perhaps surprisingly, Ca is one of the chemical species that is lagging behind in updated laboratory studies. A variety of transition parameters even for the same lines are currently in use in the literature, producing zero-point offsets as larger as 0.2 dex Pancino et al. (2010). This is a concern even for the internal homogeinity of individual studies, and care must be taken that all employed lines have parameters coming from the same source, or sources known to be on the same scale. Another very popular element, the easily measurable Mg, also suffers from a lack of updated transition parameters.

This is also relevant when considering absolute abundance values, e.g. abundance of the metal-poor plateau in the [X/Fe] versus [Fe/H] plane for α elements. Two elements display a plateau at the same [X/Fe] may not mean they are formed at the same rate. A careful investigation of all line parameters must be done before such claims can be made. This is of particular importance for the fine tuning of nucleosynthetic models.

- **ii) which lines are used:** This problem is tightly related to the first issue listed here, namely the quality of transition parameters. Abundances coming from two lines of the same element may have a zero-point shift that is only evident when both lines are present in the same star. This is very important when a single line does not cover the entire metallicity range. Consider, for example, a pair of lines for a given element, where one of them is very strong, and the other very weak. In the metal-poor regime, the strong line is measurable, but the weak line is too shallow and not detectable at all. In the metal-rich regime, the strong line becomes saturated and cannot be used reliably, and the weak line is finally strong enough to be measurable. Thus, in the [X/Fe] versus [Fe/H] plane, one line defines the trend from metal-poor to -intermediate, and another from metal-intermediate to -rich. In case the two lines have a zero-point shift in their abundances, this scenario could give rise to a spurious trend in the [X/Fe] versus [Fe/H] plane, or even obfuscate the existence of a real trend.

- **iii) the NLTE corrections:** Some lines of several elements are known to suffer NLTE effects that make the abundances derived through them show dependence in other parameters such as T_{eff} and metallicity. Different correction grids exist for a few elements, but the biggest concern when employing them is that the grids usually cover a very limited range of atmospheric parameters and rarely reach simultaneously the low surface gravities and high temperatures of HB stars. Furthermore, each individual line that is subjected to NLTE effects must be corrected individually, and corrections are only available for a limited number of lines. The problem of NLTE corrections is mitigated by the availability of multiple lines for

the same element. This allows for the usage of lines that do not suffer NLTE effects as “pivot points” against which the lines with NLTE effects can be compared.

Chapter 5

Spectroscopic data sets

We collected the largest sample of both proprietary and publicly available spectra of RRL in the literature from a variety of high, medium and low resolution spectrographs. Different subsets of this sample were employed at different stages of the investigations performed by our group. Thus, for clarity, only the spectra employed in chemical abundance analysis as shown in this thesis are described here. Numbers shown in published papers may vary due to differences in how samples were selected at the time and in how many spectra were available.

5.1 The high resolution spectra

A total of 407 HR, high SNR spectra for 162 field RRLs (138 RRab, 23 RRc, 1 RRd) were acquired with the nine spectrographs listed in Table 5.1. Using spectra from multiple spectrographs and even multiple research organizations is riddled with challenges. Bulk treatment of spectra is limited by the widely different instrumental set ups that result in different wavelength coverages, different SNRs, different fits file header keywords, and different presentation when it comes to spectral apertures and bands. This means that a very careful analysis was done with each individual spectrum to ensure all results were as reliable as possible.

A SNR of at least $\gtrapprox 50$ per pixel is needed in order to derive reliable equivalent width measurements. Thus, for spectra that had a small number of lines in regions with high enough SNR, we used the approach of spectrum stacking. For this purpose, as a first step, we selected spectra for the same star and instrument collected at similar phase. Then, as a second step, we superposed the Doppler-shift corrected spectra to be stacked in order to verify visually that absorption features were well aligned and of similar shape. This is a safeguard against accidentaly stacking spectra collected at different phases, because the similar absorption lines confirm that the spectra were collected at similar stellar atmospheric conditions. This careful aligning of lines also ensures that no line smearing

Table 5.1: Typical characteristics of each instrument used in this work.

Spectrograph	Telescope	Telescope size	Wavelength Range (Å)	Resolution	SNR
echelle	du Pont	2.5 m	3700 – 9100	27,000	70
UVES	VLT	Array of four 8 m	3000 – 6800	35,000 – 107,000	76
X-shooter	VLT	Array of four 8 m	3000 –10200	18,400	86
HARPS	3.6m	3.6 m	3700 – 6900	80,000 – 115,000	45
FEROS	2.2m MPG/ESO	2.2 m	3500 – 9200	48,000	53
HARPS-N	TNG	3.58 m	3900 – 6900	115,000	65
HRS	SALT	≈11.1 m x 9.8 m	3900 – 8800	40,000	61
HDS	Subaru	8.2 m	5060 – 7840	60,000	95
echelle	STELLA	Array of two 1.2 m	3860 – 8820	55,000	74

The wavelength ranges and resolutions are approximate. Different instrumental configurations result in different values, including wavelength coverage gaps. The archival data for UVES displayed a significant variety of configurations. Only the most representative values are shown.

occurs. This process resulted in 243 spectra that were analysed individually. Of these, 51 were acquired with the echelle spectrograph at du Pont (Las Campanas Observatory), 74 with UVES (Dekker et al., 2000) and 16 with X-shooter (Vernet et al., 2011) at the VLT (ESO, Cerro Paranal Observatory), 18 with HARPS (Mayor et al., 2003) at the 3.6m telescope and two with FEROS (Kaufer et al., 1999) at the 2.2m MPG telescope (ESO, La Silla Observatory), five with HARPS-N (Cosentino et al., 2012) at the Telescopio Nazionale Galileo (Roque de Los Muchachos Observatory), 47 with HRS (Crause et al., 2014) at SALT (South African Astronomical Observatory), 28 with the HDS (Noguchi et al., 2002) at Subaru (National Astronomical Observatory of Japan), and two with the echelle spectrograph (Weber et al., 2012) at STELLA (Izaña Observatory).

Representative spectra for each of these spectrographs are shown in Fig. 5.1. Of the 243 final spectra that we analysed, 178 were collected with high SNR and did not require stacking, 26 were the result of the stacking of two spectra, and 39 of three to seven spectra.

We acquired UVES spectra for 6 non-variable HB stars identified by Afşar et al. (2018). These spectra were collected with the Habitable Zone Planet Finder (HPF, Mahadevan et al., 2012) (HPF) spectrograph installed on the 10-meter Hobby-Eberly Telescope at the McDonald Observatory in Texas. They are described in detail in Sneden et al. (2021). We applied to this sample the full spectroscopic analysis used with the RRLs, including the same line list. Additionally, we obtained UVES and FEROS spectra from the ESO Archive for 10 non-variable HB stars in For & Sneden (2010) in order to measure the heavy elements that were not included in their analysis. Due to the high temperature of these stars, measurements could only be reliably made for five of them. Note that for these stars, we adopted the atmospheric parameters derived by For &

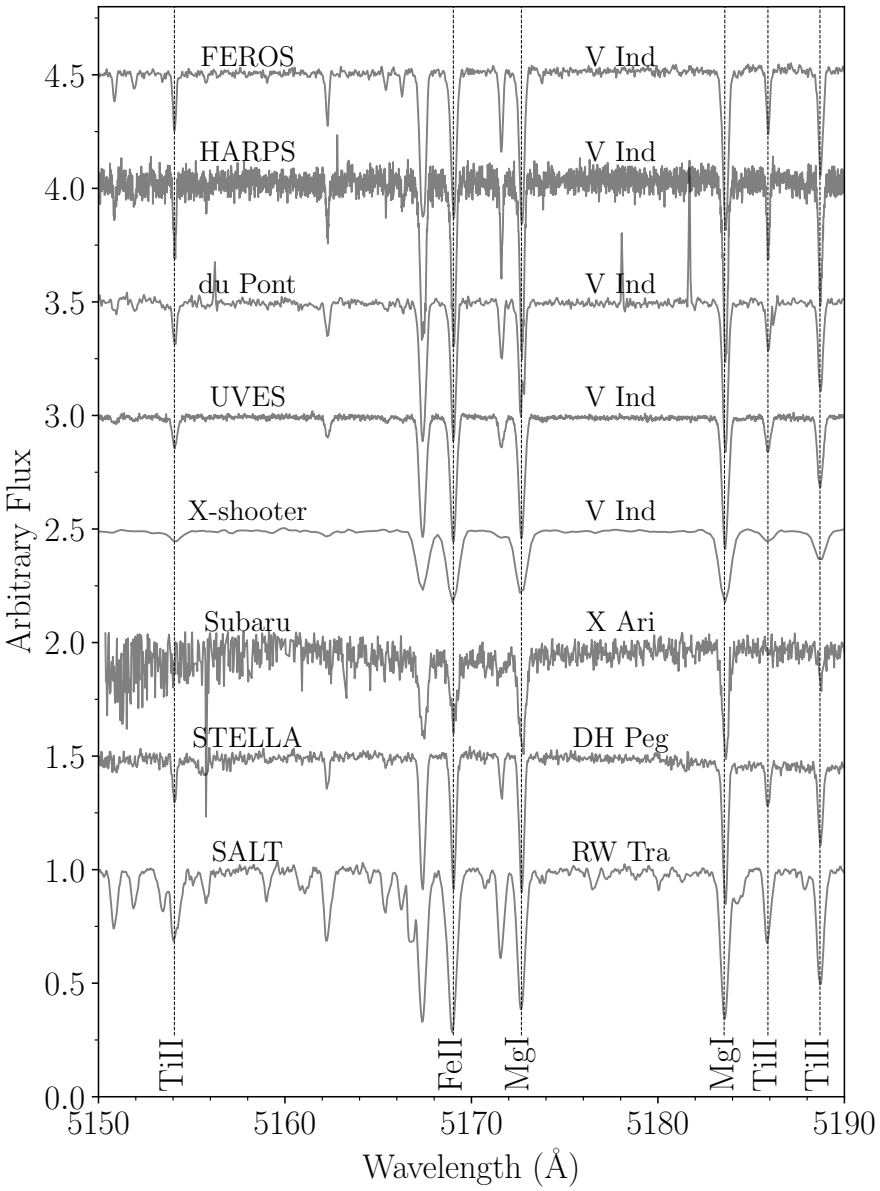

Figure 5.1: Representative high resolution spectra for all spectrographs used in this work. The top five spectra are of V Ind ([Fe/H] = -1.63± 0.03, RRab) at the same pulsation phase. They are followed by random phase spectra for X Ari ([Fe/H] = -2.59±0.05, RRab), DH Peg ([Fe/H] = -1.37±0.05, RRc), and RW Tra ([Fe/H] = 0.13±0.06, RRab). The dashed lines indicate the iron and α-element absorption lines in this wavelength region.

Sneden (2010), as will be explained further in Chapter 5.3. In order to have a small sample of dwarfs for comparison purposes, we also collected UVES spectra from the ESO Archive for seven field Halo dwarfs. These stars were studied in detail by Nissen & Schuster (2010). We applied the full spectroscopic analysis to them, and derived atmospheric parameters and chemical abundances of interest for them using the same line list employed in the study of the RRLs and HB stars.

5.2 The low resolution spectra

We gathered 6,291 LR spectra for 4,876 RRLs (3,378 RRab, 1,498 RRc) collected by the Sloan Extension for Galactic Exploration and Understanding Survey of the Sloan Digital Sky Survey (SEGUE-SDSS, Yanny et al., 2009) with the 2.5m Sloan Foundation Telescope at the Apache Point Observatory. These were joined to another 5,110 spectra collected for 3,672 (2,479 RRab, 1,193 RRc) with the Large sky Area Multi-Object fiber Spectroscopic Telescope (LAMOST), operated by the by the National Astronomical Observatories of the Chinese Academy of Sciences (NAOC), for the LAMOST Experiment for Galactic Understanding and Exploration survey (Zhao et al., 2012). Most individual stars with SEGUE-SDSS or LAMOST spectra only have one or two exposures. Thus, a defective spectrum could seriously damage the metallicity estimate for a given star. With this in mind, we visually verified each spectrum with SNR $\lesssim$ 15 near the CaII K line individually to ensure that its CaII K line and at least one Balmer line were of good enough quality.

We also collected over 6,600 HR spectra using the same spectrographs listed in Table 5.1. These spectra were not included in the HR sample described in Chapter 5.1 either because they were redundant (i.e. they had good SNR but we already had enough HR measurements for the RRL in question), or because they had low SNR and were not adequate for the full spectroscopic analysis in HR. They were downgraded to the SEGUE-SDSS spectral resolution of R $\approx$ 2,000 and are hereafter considered LR spectra. The largest fraction of the degraded HR spectra, 6,327 in total, was paired to HR measurements and used in the new calibraton of the ΔS method.

5.3 The samples

The 243 spectra for 162 field RRLs (138 RRab, 23 RRc, 1 RRd) described above are included in the TW-RRL sample, where TW stands for "this work". A subset of these have previous high resolution measurements in the literature, allowing us to compute the necessary shifts to bring results from these literature works to our chemical abundance scale. All the works considered, their acronyms, the number of stars in common with this work, and the number of stars adopted from them are shown in Table 5.2. The

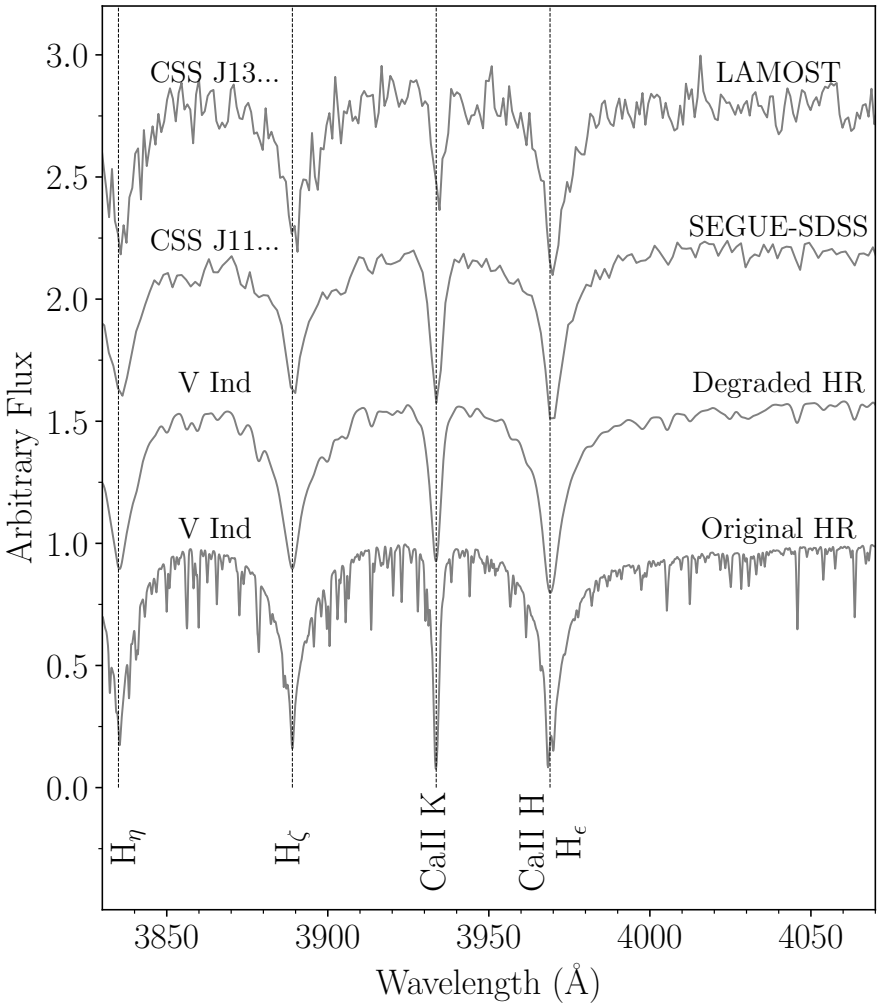

Figure 5.2: From top to bottom: representative low resolution spectra collected with LAMOST (first) and with SEGUE-SDSS (second). The third spectrum is a representative of the degraded HR spectra sample. It was collected with UVES and degraded to the typical SEGUE-SDSS resolution (R≈2000). The fourth spectrum is the same as the third one before being degraded, and is included for comparison purposes. The top two spectra are for the stars CSS J131259.8+370702 and CSS J111115.9+195657, while the bottom two are for V Ind. All three RRLs have similar metallicities, with [Fe/H] ≈ -1.6 dex. The CaII K and H lines, and the Balmer lines H_η, H_ζ, and H_ϵ are indicated by dashed lines.

Table 5.2: Literature studies of RRLs considered in this work, the number of their stars in common with the TW-RRL sample (N_{common}) and the number of their stars which are included in the Lit-RRL sample ($N_{adopted}$). The bottom three rows list, for completeness, the studies from which we adopted no values because we have HR spectra for the stars included in their samples and could, therefore, apply our own HR spectroscopic analysis to them.

Source	N_{common}	$N_{adopted}$
A18	13	17
C17	13	15
C95	8	2
F96	4	5
F10	1	1
F11	5	6
G14	2	6
L96	8	10
N13	7	35
P15	8	10
S17	5	14
H11	2	None
K10	1	None
L13	23	None

Sources – A18: Andrievsky et al. (2018); C17: Chadid et al. (2017); C95: Clementini et al. (1995); F96: Fernley & Barnes (1996); F10: For & Sneden (2010); F11: For et al. (2011); G14: Govea et al. (2014); H11: Hansen et al. (2011); K10: Kolenberg et al. (2010); L96: Lambert et al. (1996); L13: Liu et al. (2013); N13: Nemec et al. (2013); P15: Pancino et al. (2015); S17: Sneden et al. (2017).

RRL in those works for which we do not have our own measurements, once brought to our chemical abundance scale, make up the Lit-RRL sample (65 RRab, 20 RRc). See Chapter 7.2 for details on how multiple measurements were treated. Measurements for RRLs in these works that were in common with the present work were not considered except for the derivation of the chemical abundance scale shift. This means that a few important literature sources of HR measurements for RRLs are not included in our analysis because we could obtain our own values for all stars included in them. They are also listed in Table 5.2 for completeness.

Note that the measurements taken from F10, F11, S17 and C17 are natively in our scale and require no shifts. All four of these works were made in collaboration with one of our group (Christopher Sneden), and three of them with two of our group (Christopher Sneden, George Preston). They used the same methodology as we used in the present work, and very similar atomic transitions with largely the same sources of log(gf) values,

resulting in a temperature and metallicity scale that is, within the errors, identical to the one developed in this work. Indeed, comparing results for stars in common between the present work and F11, C17, and S17, we obtain the following differences of under 0.10 dex for [Fe/H] and of the order of 0.15 dex or smaller for [X/Fe] considering most species. These differences are quite similar to the difference given by multiple observations of the same star in the same investigation. Note that F10 was focused on non-variable horizontal branch stars, but it employed the same line list and instrument as F11 and thus we can safely assume that the differences found between the present work and F11 are the same as for F10. It bears mentioning that F10 and F11 caution the reader regarding their Ni measurements as their spectra had few good lines. The stars in common between both works and the present work show that the former give [Ni/Fe] abundances about 0.40 dex higher than the latter. Even so, we opted to keep values coming from F10, F11, S17, and C17 without modification as they offer an immediate verification of the trends found in the present work. The reason for this will become clear in Chapter 9.3, in particular regarding Si measurements.

Additionally, we included the results for 46 non-variable HB stars from F10 in the Lit-HB sample. Since F10 did not analyse some of the heavier elements included in the present work, we employed HR spectra collected with UVES and FEROS for five of their stars in order to obtain measurements for Ce, Nd, and Pr. For this purpose, we adopted the atmospheric parameters derived by F10. These values are considered part of the Lit-HB sample. For the six non-variable HB stars identified by Afşar et al. (2018) for which we also obtained UVES, FEROS, and HARPS spectra, we performed the full spectroscopic analysis, determining atmospheres and abundances homogeneously with the TW-RRL sample. These six stars make up the TW-HB sample. We also performed the same full spectroscopic analysis on seven field Halo dwarfs included in the analysis of Nissen & Schuster (2010) and with spectra collected with , and these stars make up the TW-Dwarfs sample.

For the new calibration of the ΔS method, we joined results from the TW-RRL sample, and from F11, S17 and C17 in order to create the CHR sample (111 RRab, 32 RRc). These are stars for which both homogeneous HR metallicities are available without any need for scale transformations, and for which we had degraded HR spectra that covered the CaII K line and at least one Balmer line.

Stars with only LR spectra, either native or downgraded from HR, for which we derived ΔS measurements with our new calibration will simply be referred to as the ΔS sample. These stars do not have any HR metallicity estimates. For this reason, some LR spectra listed in the previous Section were used for internal consistency checks, but not included in this sample.

Note that there are no stars in common between the TW-RRL, Lit-RRL, Lit-HB, and ΔS samples. In case a single star had multiple measurements, we gave preference to our own HR estimate, followed by a literature HR estimate, and then finally, absent both of those, a ΔS estimate. We did not consider literature measurements of stars for which

we performed our own measurments. Any literature stars in common with the TW-RRL sample were used exclusively to derive the chemical abundance shifts necessary to bring their source work into our scale. If a single star had measurements from multiple HR literature sources, we brought them all to our scale and then took the median value, as explained in more detail in Chapter 7.2.

To summarize, the samples in this thesis are as follows:

- **TW-RRL:** 162 RRLs (138 RRab, 23 RRc, 1 RRd) for which the atmospheric parameters and chemical abundances were derived in this work using HR spectroscopy.
- **CHR:** 143 RRL (111 RRab, 32 RRc) with high resolution metallicities derived either in this work (91 RRab, 20 RRc), F11 (5 RRab), S17 (12 RRc), or C17 (15 RRab). These were coupled with 6,327 LR measurements either from SEGUE-SDSS, LAMOST, or degraded HR spectra, in order to create the new ΔS calibration. There are stars in this sample that are in common with either the TW-RRL or the Lit-RRL.
- **TW-HB:** 6 non-variable HB stars with atmospheric parameters and chemical abundances derived with the same methodology and line list as the TW-RRL.
- **TW-Dwarfs:** 7 field Halo dwarfs with atmospheric parameters and chemical abundances derived with the same methodology and line list as the TW-RRL
- **Lit-RRL:** 85 RRLs (65 RRab, 20 RRc) for which the HR chemical abundance values were taken from the literature and brought to our scale.
- **Lit-HB:** 46 non-variable HB stars with HR chemical abundance values taken from F10. We added measurements for Ce, Pr, and Nd as these were not available in F10.
- **ΔS:** 7,768 RRL (5,196 RRab, 2,572 RRc) for which only ΔS metallicities, in our new calibration, are available.

All these samples are in the same metallicity and chemical abundance scale. As they are made up of HB stars, both RRL and non-variable, they are also coeval with ages greater than 10 Gyr.

Chapter 6

Methodology

Several steps separate the raw products of observations and the chemical abundance values that can be analysed. The ESO spectra were pre-reduced by the ESO Phase 3 program, the HARPS-N spectra by M. Monelli and V. D'Orazi, and the du Pont spectra by G. Preston. In the following section, we describe the line list of atomic transitions used in this work, the tools employed to normalize and put the spectrum in the rest frame wavelengths via Doppler shift correction and, finally, how atmospheric parameters and chemical abundances are derived via the curve-of-growth method.

6.1 Atomic line list

A list of atomic transitions is the backbone of any spectroscopic investigation. Most problems we found during the early development of the present work happened due to issues with the line list. In particular, we found multiple transitions in the Vienna Atomic Line Database (VALD) with incorrect element identification and incorrect transition parameters that led to spurious results. This is a significant problem for Fe lines, as our methodology relies on them for the determination of atmospheric parameters. We also detected a significant problem with Ca measurements in the literature that, as far as we can tell, was only mentioned in passing in one work. Namely, that the set of transition parameters adopted for calcium are so diverse that different works using the same lines can reach results with differences as large as 0.2 dex (Pancino et al., 2010). After multiple delays with misidentification of lines, uncertain transition parameters, uncertain sources of transition parameter values, and blended lines not being marked as such, we opted to start from scratch and build a clean line list over which we had complete control. Moreover, different lines can be more adequate to different types of stars. As our study is centered on the RRLs, the line list was optimized for their range of atmospheric parameters to include as many transitions as possible within the quality control discussed below. This means that it is possible that lines with good transition

parameters were discarded from our list simply because they are too weak or too strong in RRLs. It is also possible that lines that showed robust results in the present analysis would be blended in colder stars. Thus, further tests are necessary when applying this line list to samples of stars that are not RRLs.

As a first step, we gathered a large number of atomic transitions used in the literature, including in particular those of F10. As a second step, we updated their transition parameters using the compilation of laboratory measurements included in the FORTRAN code LINEMAKE, developed and maintained by Christopher Sneden, whenever available, and the National Institute of Standards and Technology (NIST) Atomic Spectra Database 3[1] otherwise. If a line was not present in either of these sources, it was discarded, with the exception of Cu for which only two lines with parameters from the Kurucz Line Lists[2] were available. All lines with hyperfine structure had the hyperfine splitting values taken from LINEMAKE. As a third step, we carefully cleaned the line list of any blended lines using the Moore et al. (1966) Solar spectrum atlas and synthetic spectra produced using LINEMAKE and the 2014 version of MOOG (Sneden, 1973b). Lines that showed as possibly blended in either the Solar spectrum atlas or synthetic spectra but that showed robust results in our analysis were kept. This decision was made because both atlases and synthetic spectra rely on good knowledge of the atomic transitions present in a given wavelength range, and so they are not immune inadequate transition parameters that may overestimate the strength of nearby lines and cause the line of interest to be labeled as blended. Furthermore, molecular lines were not considered in this analysis, because they are not significant at the high effective temperatures of the stars considered in this work. Therefore, atomic lines that are known to be blended with molecular lines in colder stars can still be used in RRLs without problems. As a fourth step, we verified that all lines for the same species were in agreement with one another in all cases where such an analysis was possible. When a given element had too few measurable transitions to perform such a comparison, we discussed it in the text when presenting the results.

The final line list for all chemical species is included in the appendix. The line list for Fe and α elements is included in machine-readable form in (Crestani et al., 2021a) and Crestani et al. (2021b), respectively. The machine-readable line list for the remaining species will be made available in upcoming papers[3].

6.2 Normalization and radial velocities

The output of a reduction pipeline is a wavelength-calibrated spectrum that still carries both the underlying blackbody emission curve and the sensitivity curve of the spectro-

[1] https://www.nist.gov/pml/atomic-spectra-database

[2] Available at http://kurucz.harvard.edu/linelists.html

[3] See the appendix for their working titles.

graph (Fig. 6.1). Spectral normalization was done using the IRAF[4] task *continuum*, which is provided in the *noao.onedspec* library.

Continuum fitting oftentimes is more art than science. Different spectrographs have varying sensitivities on each echèlle order, with some having a smoother continuum while others have cuspy regions. Thus, a single continuum fitting function is not adequate across different instruments. We adopted either cubic spline functions, which are more capable of tracing cuspy regions but can easily overfit other areas, or Legendre polynomials, which are more robust but only suited to smoother continua. Preference was given to the lowest order capable of providing a good fit. Morever, there is no one value of automatic sigma clipping that improves the fit for both metal-rich and metal-poor stars, and fitting functions easily diverge with the presence of enough emission lines or other artifacts such as dead pixels. Thus, each normalization was done individually, with wavelength regions of strong absorption features being carefully removed from the fitting process in order not to bias it.

We developed a novel approach for the du Pont spectra as they were very numerous, mounting up to the thousands. Their normalization was necessary, even when the SNR was too low for a full chemical analysis approach, because they were employed heavily in the new ΔS calibration (Chapter 8). The ΔS method that on the depth of strong absorption feature that can easily be deformed by incorrect continuum fitting. The main issue is that the response of the spectrograph naturally creates continuum shape on each echèlle order, and this shape in the case of the du Pont spectra is particularly cuspy, requiring a higher order spline function that can easily diverge or overfit the echelle order in the presence of strong absorption features, emission lines, or just a high number of lines in general. With this in mind, we wrote a CL script for IRAF that picked the neighboring orders of the CaII K and Balmer lines, which are necessary for the ΔS method, and averaged them in the pixel space instead of the wavelength space so that the effect of emission and absorption lines was mitigated. These orders and the order of interest, being very close by, presented very similar response curves and had a similar overall shape. The continuum function was then determined based on these neighboring orders, and then applied to the order of interest. Note that this process was not necessary for other echelle orders because they are not needed for the ΔS method. For the du Pont spectra used in the HR analysis, far fewer in number, the normalization was simply done by hand as with spectra coming from other spectrographs.

A normalized spectrum is still one step away from being ready for analysis. Spectral lines are identified by their wavelength, yet the Doppler effect due to any movement in the stellar atmosphere introduces a wavelength shift that displaces the whole spectrum approximately ridigly (i.e. the response at all wavelengths is the same) either to longer or

[4]IRAF is distributed by the National Optical Astronomy Observatory, which is operated by the Association of Universities for Research in Astronomy (AURA) under cooperative agreement with the National Science Foundation. The legacy code is now maintained by the astronomical community and available on GitHub at https://iraf-community.github.io

shorter wavelengths. There are two sources of Doppler shift in a variable star. First, its movement along the line-of-sight, with speed V_{rad}. Second, the movement of the surface layers, where detectable lines are formed, as the star contracts and expands during its pulsation cycle.

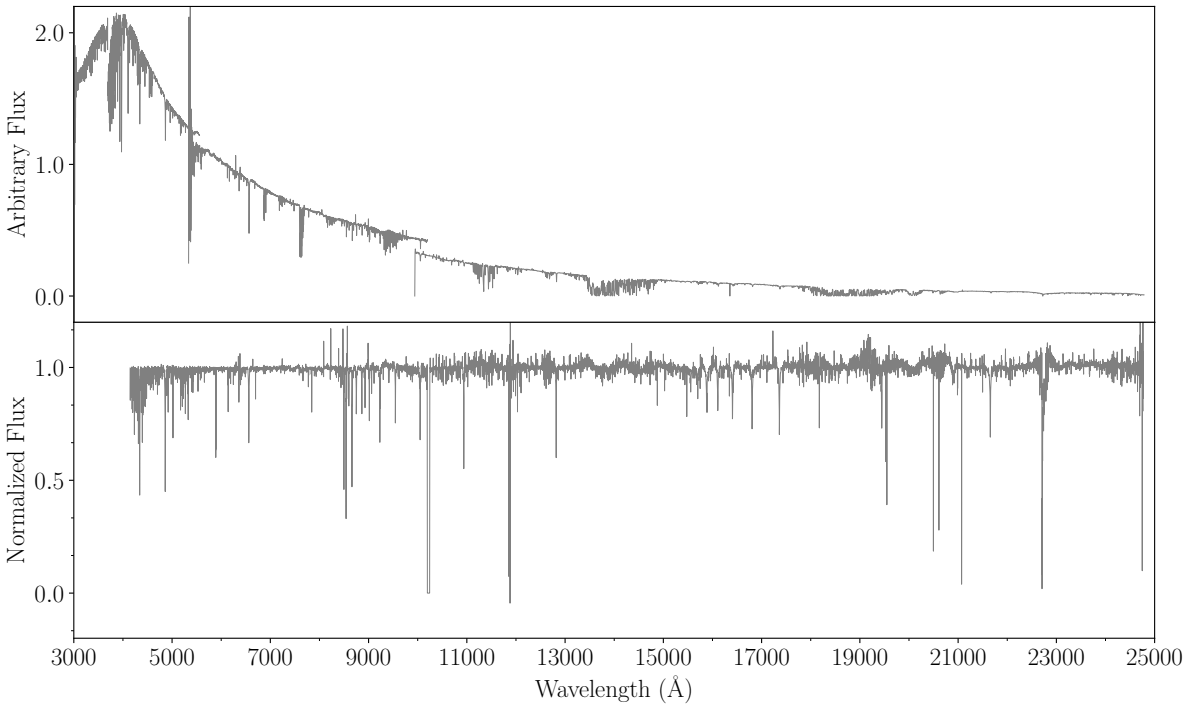

Figure 6.1: *Top:* X-shooter wavelength-calibrated spectrum produced by the reduction pipeline. Only one in every ten poins is shown for clarity. The discontinuities indicate the edges of each of the arms of the spectrograph. The flux values in each arm have been shifted by a constant for better visualization of the underlying blackbody emission curve. *Bottom:* The same spectrum after normalization and removal of telluric lines. Note that the bluemost region was discarded.

The Doppler shift introduced by the line-of-sight velocity V_{rad} of the whole star, i.e. is barycentric velocity, is useful for selection purposes such as to verify its membership of a larger structure such as a GC. The shift caused by pulsation alone is useful for phasing the variable star in the absence of a well known light curve. As we are interested in identifying atomic transition lines in the spectra, all we need is to have it in the rest frame, and the source of the Doppler shift is irrelevant. Thus, for this particular end, the IRAF task *fxcor*, included in the *noao.rv* library, suffices for the computation of the Doppler shift velocity. This allows the user to provide a reference spectrum with lines of interest, which it cross-correlates with the spectrum to be corrected. The user can select specific regions of both science and reference spectra to avoid problematic regions

such as where tellurics dominate. For the reference, we used a synthetic spectrum for a typical RR Lyrae star (T_{eff} = 6500 K, log(g) = 2.5 dex, [Fe/H] = -1.5 dex, and ξ_t = 3.0 km $s^{-}1$), created with the MOOG (Sneden, 1973a, 2014 version) driver *synth*.

Once the best velocity solution was computed, we applied it to the spectra using the IRAF task *dopcor*, included in the *noao.onedspec* library. Afterwards, we superposed the synthetic and science spectra to visually verify if there were any issues with the Doppler shift correction. In case any imprecision was detected, we manually added an additional shift. With the spectrum normalized and put in the rest frame of reference, where absorption lines can be identified by their wavelength, the spectroscopic analysis can begin.

6.3 Atmospheric parameters and chemical abundances

We measured all equivalent widths of interest manually with the IRAF task SPLOT included in the *noao.onedspec* library. For iron, α-elements, and most other chemical species, we only considered lines with equivalent widths between 15 and 150 mÅ in order to avoid spurious measurements and saturated lines. For the heavy elements in the Fe-peak and n-capture families, which have very few unblended lines in the optical, we relaxed the minimum equivalent width criterium in order to maximize the number of results for these poorly studied elements. Note that, even in this case, we carefully avoided small lines in noisy regions. This quality control is one advantage of manually measuring equivalent widths.

It is important to note that the saturation occurs at varying equivalent widths for different lines. In particular, bluer lines saturate earlier, with some strong iron lines theoretically saturating with equivalent widths as small as 90Å, while a line of similar strength near the end of the visual band may saturate at nearly 200Å. The term "theoretically", however, is key. The saturation region of the curve-of-growth of a given line is not firmly constrained, and depends not only on the transition parameters of the line, but also on the thermodynamical parameters of the atmospheric layer where the line is formed. This means that the saturation equivalent width is an estimate, and not a hard limit. With this in mind, we kept the limit of 150Å but also paid close attention to the abundances given by all lines, especially at bluer wavelengths, in order to remove any clearly saturated line. This is a straightforward procedure for elements such as iron and titanium due to their numerous measurable transitions that allow for a quick identification of outliers. For elements with fewer lines, however, this likely introduces larger uncertainties, as is the case with Mg. However, a measurement with larger uncertainties is still better than no measurement at all.

The atmospheric parameters T_{eff}, log(g), [Fe/H], and ξ_t were constrained using the approach described in Chapter 4. In particular, we used the PYTHON wrapper PYMOOGI,

developed by Monika Adamow[5]. It includes the 2014 version of the code MOOG. The MOOG driver *abfind* computes curves-of-growth based on measured transitional parameters for each line, and input atmospheric model and compares them with the input equivalent width in order to provide the corresponding abundance value. It then displays plots and tables with all values of interest for the method, such as line-by-line abundance versus excitation potential that allows for the determination of $T_{\rm eff}$. We employed the atmospheric models computed with the ATLAS9 code (Castelli et al., 1997; Castelli & Kurucz, 2003). They form a grid[6] based on atmospheric parameters for both Solar and α-enchanced mixtures, which is in turn interpolated with the FORTRAN code MAKEKURUCZ, written by Christopher Sneden, in order to create the model that best fulfills the criteria described in Sect. 4.1. In this work, we used the α-enhanced grid with $[\alpha/\mathrm{Fe}] = 0.4$.

With the atmospheric parameters constrained, we computed the abundances for all other species that have no lines with hyperfine structure using the *abfind* driver. For elements presenting lines with hyperfine structure, the MOOG driver *blends* was used instead.

[5]https://github.com/madamow

[6]The grids are available for download in http://kurucz.harvard.edu/grids.html

Chapter 7

Determination of atmospheric parameters and chemical abundances

7.1 The TW-RRL sample

We applied the methodology described in Chapter 6 to the TW-RRL sample spectra in order to obtain their atmospheric parameters and chemical abundances. Whenever possible, at least two measurements were made for the same RRL. The final abundance value for each species was taken to be the median of the [X/H] measurements across different spectra. This approach enabled us to determine uncertainties in a manner more suited to variable stars. As the atmospheric parameters are changing across the pulsation cycle, multiple measurements of the same object allow us to constrain the impact of this variation on individual abundances.

The RRLs can undergo $T_{\rm eff}$ changes as large as 1000 K during its pulsation cycle (e.g. For et al., 2011). Indeed, the main difficulty in the spectroscopic investigation of RRLs is precisely the large and fast changes in their atmospheres. Thus, the robustness of a given method of abundance determination can be assessed by its capacity to recover coherent values across the pulsation cycle and, similarly, the difference between repeated measurements is a reliable determination of the uncertainty of the measurements. With this in mind, we computed the uncertainties for all chemical species including iron by taking the median absolute deviation between multiple measurements for the same star. For the TW-RRL sample, this allowed us to determine the typical uncertainty of each chemical species in each spectrograph, which we adopted for the stars with a single measurement. This means that we do not consider the uncertainties in atmospheric parameters in the computation of the chemical abundance uncertainties.

We averaged the abundances of TiI and TiII in order to derive a total [Ti/Fe] ra-

tio. The [TiI/Fe] and [TiII/Fe] are on average shifted by 0.05 dex in our data. Our approach to the computation of uncertainties means that any disagreements between TiI and TiII abundances are automatically reflected in the [Ti/Fe] uncertainties for each star. For most other elements with both neutral and ionized transitions, such as V, the neutral species usually had very few measurements and were only adopted when in agreement with their ionized counterparts. The exception is Si, which presented very discordant results depending on the ionization level. Consequently, we treated SiI and SiII separately.

To compute the total [α/H] abundance, we took the median of [Mg/H], [Ca/H], [TiI/H], and [TiII/H] according to their availability and weighted by their uncertainties as defined above. The median absolute deviation between the different α-elements was adopted as the uncertainty in the total [α/H] abundance. Finally, we subtracted the iron abundance from [α/H] for each individual star to arrive at the final [α/Fe] value.

7.2 The Lit-RRL and Lit-HB samples

For the Lit-RRL sample, we used the same approach to uncertainties as with the TW-RRL sample. As a first step, we moved all [X/Fe] abundances in the literature to the Asplund et al. (2009) solar scale. The collection of literature values was started by Davide Magurno, and made available in the Asplund et al. (2009) solar scale (Magurno et al., 2018). The solar scale is merely a constant to transform X/Fe into [X/Fe], and does not introduce any trends in the metallicity or chemical abundance scales. For this reason, we kept this first step for the convenience of building upon the data base that was already available.

As a second step, we moved these [X/H] abundances into our chemical abundance scale by using stars in common between the TW-RRL sample and the various literature sources. The third step was then to take the median and absolute median deviation across different measurements for the same [X/H] species and star as the final abundance value for that star and its corresponding uncertainty. In the end, we used the median [X/H] and [Fe/H] to compute [X/Fe] and their uncertainties. For stars with a single measurement in the Lit-RRL sample, we adopted a fixed uncertainty of 0.10 dex for iron and 0.15 dex for the other species.

For the Lit-HB sample, the measurements and uncertainties from F10 were adopted without any further processing. Two stars in F10 were identified as HB stars but later recognized as RRL. One of them was added to the Lit-RRL sample. The measurements for the other RRL were discarded as we had measurements of our own and could add it to the TW-RRL sample.

7.3 The ΔS sample

The spectra in this sample are either natively low resolution, or had their resolution degraded from HR to LR due to low SNR. In both cases, they are not adequate for the chemical abundance analysis applied to the TW-RRL sample. However, the ΔS method is specifically designed to derive metallicities from such spectra. In this work, we developed a new calibration of the ΔS method in the same metallicity scale as the HR results. It will be described in detail in Chapter 8.

Chapter 8

A new calibration of the ΔS method

A subset of 111 RRLs (91 RRab, 20 RRc) from the TW-RRL sample had spectra that reached the CaIIK line and at least one of the Balmer lines H_δ, H_γ, and H_β. We derived metallicities for these RRLs from 171 individual high resolution spectra. This sample was increased by the addition of 20 RRab and 12 RRc stars with more than one measurement from For et al. (2011), Chadid et al. (2017), and Sneden et al. (2017), forming the CHR sample with 143 RRLs (111 RRab, 32 RRc). As explained in Chapter 5.3, these three literature sources are natively in our metallicity scale and, indeed, use the same primary instrument of this investigation, namely the echelle spectrograph at the du Pont telescope.

Our dataset included 6,327 high resolution spectra for the stars in the CHR sample. These spectra were downgraded to a resolution of R$\approx$2000 and rebinned with $\Delta\log(\lambda) =$ 0,0001 in order to mimic the typical spectra that the ΔS method is optimized for. Thus, we were equipped to begin investigating the best way to develop a new calibration of the ΔS method, from the definition of the equivalent widths to the equation that relates them to the metallicity of the RRL of interest. We also tweaked the IDL code EWIMH, one of the codes commonly employed for the measurement of equivalent widths of the ΔS method (Layden94, Fabrizio et al. 2019), in order to reflect not only the new wavelength ranges but also an updated treatment of noise, emission lines, and other spectral defects. With these refined measurements, we finally tacked the equation itself in search of the best way to associate equivalent widths to high resolution metallicities.

The discussion and results of this investigation are presented here and also published in Crestani et al. (2021a), where the interested reader can also find all relevant tables in machine-readable format.

8.1 Wavelength ranges

The Layden94 calibration relied on the behavior of RRLs of different metallicites in the HK plane, that is, a plane of the equivalent width of the CaII K line versus the equivalent width of one or an average of Balmer lines. Indeed, in this plane a clear relation emerges with stars of higher metallicity displaying a steeper slope (Figure 8.1). It is important to note, however, that there are multiple ways to define an *equivalent width*. As mentioned in Chapter 4.1, the approach taken to measure lines in the HR spectra of the present work relies on the fitting of a Gaussian function to the observed line, neglecting their wings (as we are not employing strong lines for the HR investigation and thus the wings are either small or absent), and considering the area of the fitted Gaussian between the wavelength points where it crosses the locally-fitted continuum. This is done automatically by the SPLOT task on IRAF.

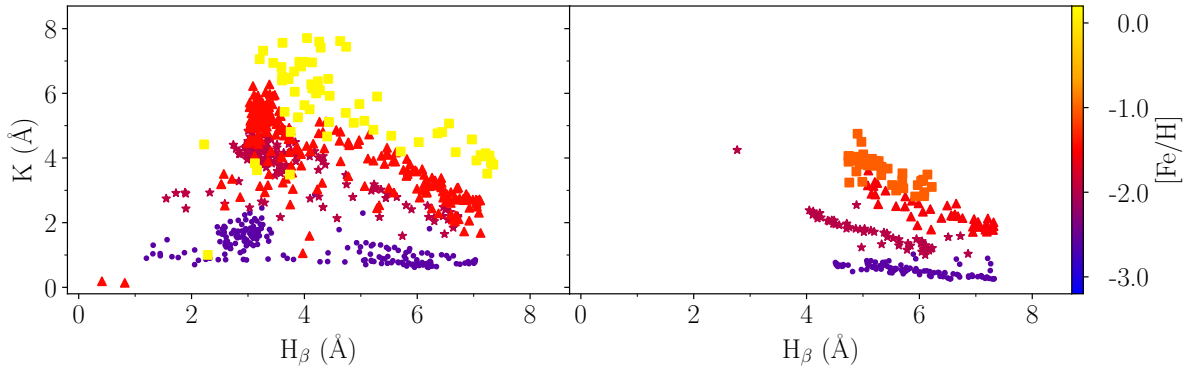

Figure 8.1: The HK plane for H_β for a group of RRab (left) and RRc (right) stars. Each marker corresponds to measurements coming from a single star. Markers are colored by metallicity according to the colorbar at the right edge of the figure.

However, this is not the approach used for the measurement of the lines of the ΔS method. There are two main reasons for this. First, the method is intended for use in LR spectra, and these have a poorer wavelength sampling that may lack enough points for the robust fitting of a function. Second, the CaII K and Balmer lines are very strong features and deviate dramatically from a Gaussian profile. The approach taken by both Layden94 and Fabrizio et al. (2019) is to perform a numerical integration between the observed points of the line, interpolating between them, and the locally-fitted continuum that was computed considering a pre-determined wavelength range. This means that two decisions must be made from the beginning: i) what is the best way to determine the local continuum, and ii) what is the best wavelength range to measure the equivalent width of the line.

The real continuum near strong absorption features is severely deformed by the lines themselves and by the changing sensitivity of the spectrograph. Therefore, a locally-fitted

continuum is adopted instead. The range to be considered for this local fitting is also important because strong lines in the vicinity of the line may limit the usable wavelength band that is not biased by yet another absorption feature. This is particularly critical in the case of the CaII K line, as it is flanked by both the blend of the CaII H at 3,968.5 Å with the H_ϵ line at 3,970.0 Å, and the H_ζ line at 3,889.1 Å. Both of these features have a dramatic effect on the continuum in very hot stars, with wings reaching as far as within ≈15 Å of the central wavelength of the CaII K line, effectively making it impossible to determine a local continuum except at a short wavelength range tightly close to the CaII K line itself.

In order to have the most control over the continuum fitting, continuum normalization was done externally to EWIMH. This allowed us to avoid distorting the features of interest by carefully ensuring that the continuum fitting function "passed over" the features of interest and did not bias their depth (see in particular the paragraph regarding the du Pont spectra in Chapter 6.2). With the normalization finalized, it is possible to move on to determining the ideal wavelength range for the measurements.

For the Balmer lines, Layden94 adopted a measurement band with a width of 20 Å, including only their cores and disregarding their wings. One of the reasons for this decision is that metallic lines may be present in the wings of the Balmer lines, artificially increasing their equivalent width. Another reason is that the Balmer lines have very extended wings that are formed at different optical depths, therefore tracing a different atmospheric layer and different thermodynamical quantities than those traced by the core of the line (see Chapter 4.1). The CaII K undergoes significant change in width and depth during the pulsation cycle, and so two different band widths were adopted, one of 14 Å in the case of the "shallow" CaII K, and one of 20 Å in the case of a "deep" CaII K line (see Figure 3 of Fabrizio et al., 2019). Both wide and narrow definitions included the full line with its wings and avoided nearby lines. Furthermore, in order to tackle the changes of the continuum on both sides of the CaII K line, Layden94 employed a moving band for the continuum. It consisted in a measurement band with a fixed length that is free to move, within a narrow range of wavelength values, in search of the position where the maximum average continuum value is achieved.

The investigation performed by Fabrizio et al. (2019) confirmed that EW(K) and EW(H) are mirrored across the pulsation cycle (see their Figure 10). With this in mind, we performed measurements for a variety of combinations of ranges for line regions and continuum bands and then checked which combination best preserved this mirrored effect. This ensures that the new calibration can be applied to the full pulsation cycle while keeping uncertainties as small as possible. In brief, we tested the following scenarios:

- Using the original wavelength range for the hydrogen lines, which includes only their cores.
- Increasing the aforementioned range in order to include their wings.

- Considering multiple ranges for the CaII K line, from the innermost 2 Å of the core, to the full line with its wings.
- Enabling and disabling the change between "wide" and "narrow" CaII K lines.
- Changing the continuum band ranges in steps from -20% to +20%.
- Enabling and disabling the movement of the continuum band for the CaII K line.

We found that including the wings of the Balmer lines did not improve sensitivity to metallicity, but caused a significant increase in the scatter. The equivalent widths of the Balmer lines are strong temperature tracers, and relating them to the CaII K allows for a temperature-independent estimate of calcium abundance, which in turn is associated to metallicity. Thus, it is expected measuring only the cores of the Balmer lines will provide the tighest value because, as mentioned above, the extended wings of strong lines do not trace the same layer of the atmosphere as their cores. The CaII K line, as a much weaker metallic absorption feature, traces a narrow atmospheric layer, and the best way to constrain the temperature dependence on its equivalent width is to associate it with another indicator of temperature in a narrow atmospheric layer. Furthermore, neglecting the wings of the Balmer lines also decreases the influence of nearby metallic lines, as noted by Layden94.

Increasing the range of the CaII K line to always include both core and wings with a fixed measurement band of 20 Å, disabling the change between "wide" and "narrow" configurations, provided the best sensitivity to metallicity without significant increase in scatter (Figure 8.2). Similarly, disabling the movement of the continuum band had no significant effect, and so we established fixed wavelength limits for the band. This is true even for spectra where the CaII K line was particularly narrow, reflecting either high effective temperature or low calcium abundance. In such cases, a portion of the continuum is considered in the measurement of the line. This was a concern for Layden94 because the equivalent width measurement is a simple numerical integration and will consider every area between the continuum level and what it perceives to be a line, even if the latter is noise. However, it is likely that the higher quality of current spectrographs mitigates this effect. Indeed, a visual inspection of the spectra used by Layden94 (see their Figure 2) supports the careful approach taken by the author of that work. The question that arises is whether the lower continuum noise in our spectra is due to the fact they are degraded high resolution spectra and whether native low resolution spectra also have small enough continuum noise. We address this further below in Chapter 8.5.2.

The final wavelength ranges for the measurement bands of the CaII K and Balmer lines, and of their continuum bands, are shown in Figure 8.3. Their precise values are listed in Table 8.1. Thus, the equivalent widths required by our calibration must be computed by a numerical integration between the observed spectrum and the local continuum level. The local continuum level for each line is defined as the average flux

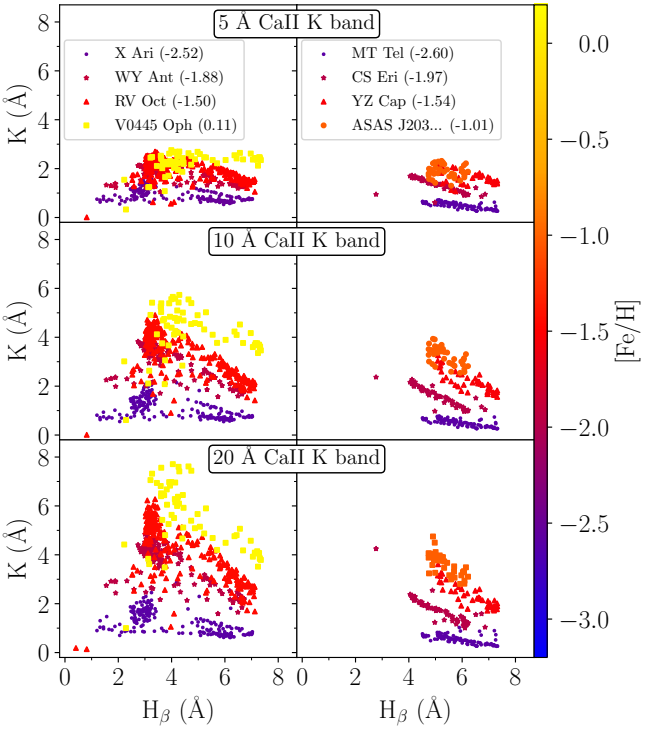

Figure 8.2: The HK plane for H_β considering different measuring band widths (5, 10, and 20 Å) for the equivalent width of the CaII K line. A group of RRab (left) and RRc (right) stars are plotted with markers colored by metallicity according to the colorbar at the right edge of the figure. The considered stars are listed in the legend, with their respective high resolution metallicities between parentheses. The name for the RRc ASAS J203145-2158.7 is shortened for convenience.

computed in the two continuum bands to the red and blue side of the line. The area to be computed is the one within the wavelength range of the measuring band. Multiple codes can be employed for the measurement of equivalent widths, but these characteristics must be present for usage in our ΔS calibration. We verified that valid equivalent widths for individual lines remain in the range of 0.01 to 10.00 Å. Values outside these limits came from distorted lines or badly placed local continuum level, and so they were discarded.

8.2 Equivalent width dependency on metallicity and phase

It bears mentioning once more that different works use different reference epochs for the phasing of the RRL pulsation cycle according to convenience. As long as the period is correct, decisions about the reference epoch simply shift the phase values ridigly.

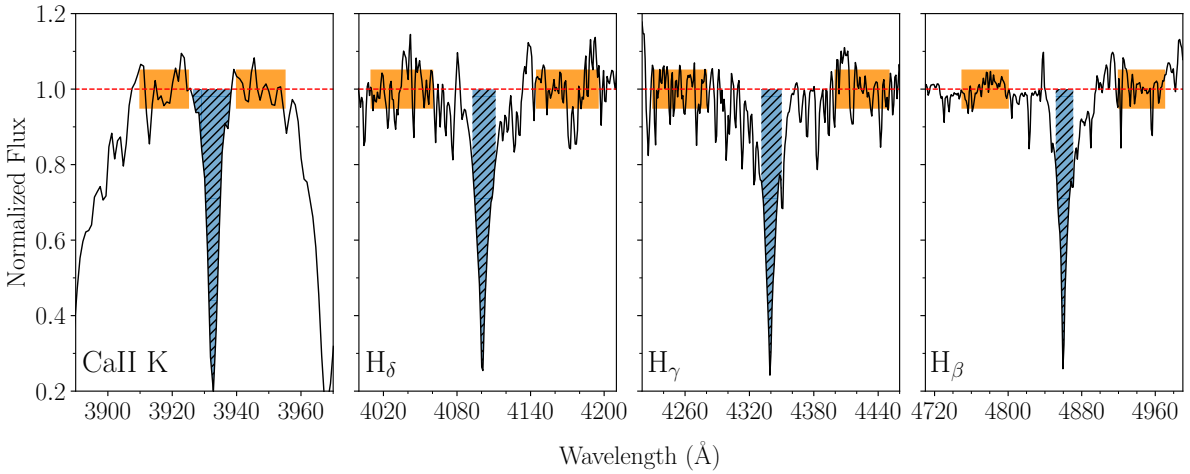

Figure 8.3: Wavelength ranges used in the new ΔS calibration measurements. In black, a du Pont spectrum for AN Ser ([Fe/H] = 0.05) downgraded to a resolution R = 2,000. The red dashed line indicates the continuum level. The hatched blue area denotes the area considered in the equivalent width measurement for each line. The orange shaded area indicates the region considered for the continuum level definition.

Table 8.1: Wavelength intervals for the ΔS measurements in the new calibration.

Line	Measurement band	Blue edge (Å)	Red edge (Å)
CaIIK	Blue continuum	3910.00	3925.00
	Equivalent width	3923.67	3943.67
	Red continuum	3940.00	3955.00
H_δ	Blue continuum	4010.00	4060.00
	Equivalent width	4091.74	4111.74
	Red continuum	4145.00	4195.00
H_γ	Blue continuum	4230.00	4280.00
	Equivalent width	4330.47	4350.47
	Red continuum	4400.00	4450.00
H_β	Blue continuum	4750.00	4800.00
	Equivalent width	4851.33	4871.33
	Red continuum	4920.00	4970.00

Consequently, it is essential to verify which pivot point of the light or velocity curve the reference epoch reflects in a given work in order to know what moment of the pulsation cycle (e.g. minimum light, maximum expansion velocity, etc.) a determined phase value refers to. In all the discussion referring to the calibration of the ΔS method, the reference

epoch was taken to be the point where the decreasing branch of the radial velocity curve reached the average velocity. This is seen in Figure 8.4 where, from top to bottom, the first panel shows the visual band light curve, the second panel shows the radial velocity curve, and the third and fourth panels show the behavior of the CaII K and H_β lines, respectively. Note that H_β is representative of all Balmer lines as they exhibit the same behavior with phase. All curves are phased with the same period and reference epoch. V Ind suffers from Blazhko modulation, and so any multiple sequences for any of these panels were removed for clarity by restricting the range in Julian Date of the observations that are shown. Thus, in this phasing, the critical phases of minimum radius, maximum light, and maximum surface temperature happen between phases $\approx$0.95 and $\approx$0.05.

The main reason Layden94 disregarded phases beyond minimum light is because, in the HK plane, the trend set by equivalent widths acquired during these phases does not follow the same trend set by other phases for the same RRL. Indeed, these phases create a characteristic "loop" in the HK plane (Figure 8.5). Comparing Figures 8.5 and 8.1, it is evident that the lower branch of the "loop" invades, so to say, the region of the HK plane occupied by the upper branch of lower metallicity stars. Therefore, if the ΔS method was applied to a spectrum collected at the critical phases, the metallicity estimate would be underestimated.

Faced with this issue, there are two possible courses of action: the first is to create a calibration that is phase-dependent, and the second is to investigate whether it is possible to pursue a calibration that does not start from the HK plane. The first option would severely limit the application of the ΔS method and compromise two of the main goals of this investigation, which are i) to provide a robust metallicity indicator to be applied to as many RRLs as possible, even those without enough previous photometric studies and consequently without adequate phasing, and ii) to remove the need for carefully timed observations, making proposals easier for telescopes to accomodate and increasing the number of useable spectra from large surveys. With this in mind, we adopted the second course of action.

8.3 Changes in the EWIMH code

We introduced a few other changes in the way the EWIMH code computes equivalent widths beyond the change of wavelength ranges, the deactivation of the moving continuum band and of the changing measurement width for the CaII K line. These changes are not necessary for the application of the ΔS calibration, but they aim at making the best use of the available spectra and can improve the quality of measurements. It is important to note once more that we performed all continuum normalizations outside of EWIMH, and so the changes we introduced rely on a normalized spectrum.

The first modification was to address how the code handles apparent emissions which are caused by cosmic rays, noise or instrumental defect. Equivalent widths rely on

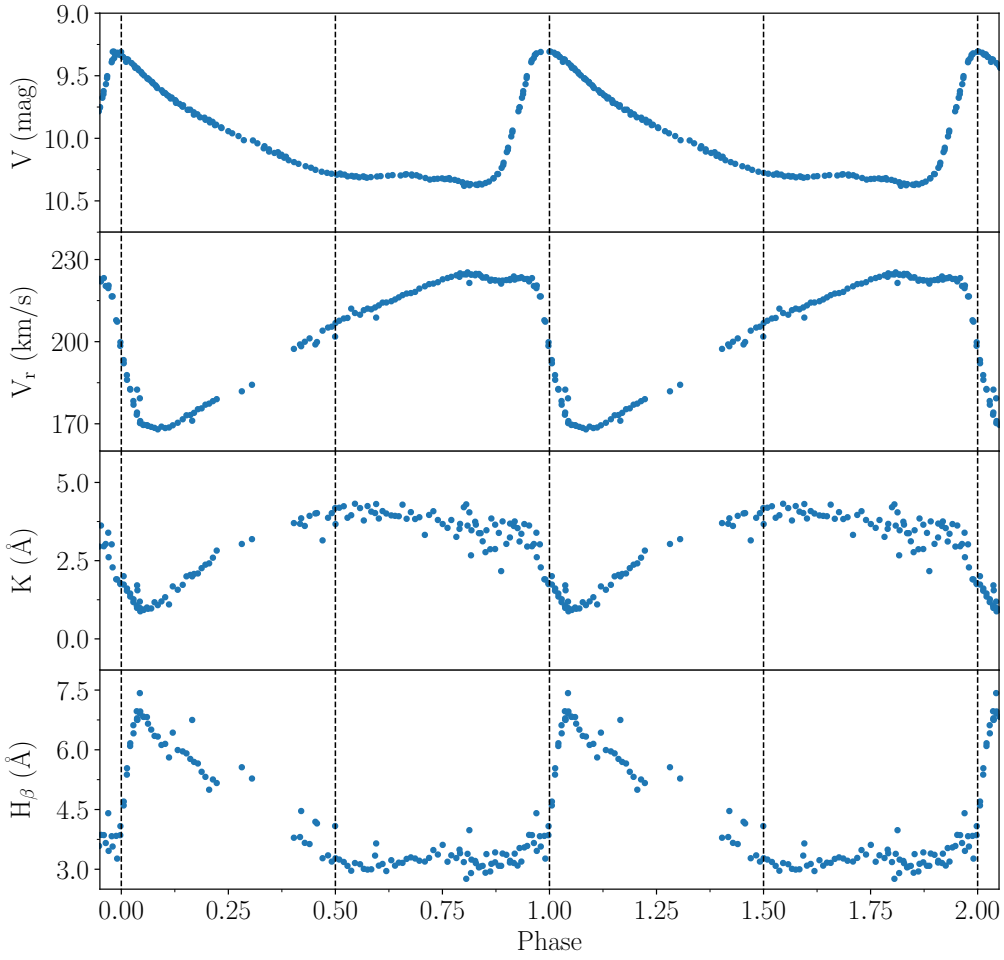

Figure 8.4: From top to bottom: light curve (first panel), radial velocity curve (second panel), equivalent widths for the CaII K (third panel) and H_β lines (fourth panel), plotted against phase for V Ind. The photometric data was taken from Clementini et al. (1990). The curves have been folded, i.e. repeated, and dashed lines added to mark phases 0.0 and 0.5 to aid in the visual comparison of the curves.

a measurement of an area between the line and the continuum. Generally speaking, measurement codes consider the area of an emission feature as negative. This means that the presence of significant emission causes a twofold issue: i) the real area of the line is decreased by the presence of the emission, and ii) if the emission is strong enough to define an area above the continuum, this area is subtracted from the total equivalent width measurment. In order to address both these issues, we introduced a change in the code so that it will discard points with a normalized flux grater than one. This solution addresses the second issue by preventing negative area values. In many cases, it

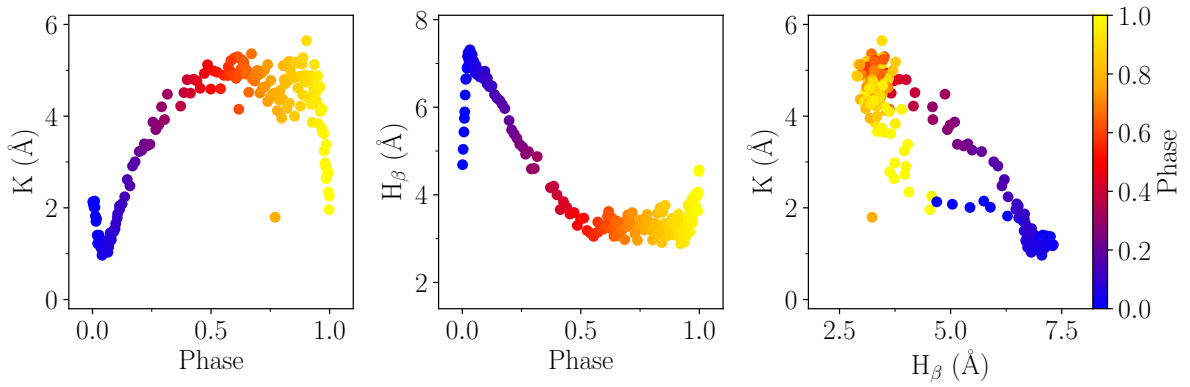

Figure 8.5: Equivalent widths for the CaII K (left) and H_β (middle) lines, and the HK plane (right) for HH Pup. Symbols are colored according to phase in all panels.

adresses the first issue as well because most emissions strong enough to be captured by low resolution spectra do cross the continuum level. The missing value becomes instead a simple interpolation between its closest neighbors.

The second modification was also aimed at correcting emission and emission-like features, but for the continuum computation. We inserted a condition that discards normalized fluxes greater than 1.25 in the continuum bands, thus preventing defective pixels and other similar problems from biasing the continuum level determination.

8.4 The new calibration

Layden94 derived a polynomial fit starting from the HK plane, with the analytical form

$$K = a + bH + c[Fe/H]_{ZW} + dH[Fe/H]_{ZW} \tag{8.1}$$

where K is the equivalent width of the CaII K line, H a linear combination of the Balmer lines, $[Fe/H]_{ZW}$ the metallicity in the Zinn & West (1984) scale, and a, b, and c are constants. The smaller sample size of the Layden94 calibration and the phase cut to consider only spectra acquired at minimum light resulted in a tight dispersion for each star in the HK plane (Figure 8.4). The high resolution measurements they performed are of very good quality and indeed several estimates are compatible with current high resolution results. The transformation of the HR metallicity scale into the Zinn & West (1984) scale, however, introduced important disagreements with modern measurements for the metal-rich and metal-poor tails, as discussed in Chapter 3.7.3.

The first step to derive the new calibration was to take the median equivalent width for each line and RRL, so that each star had one value for each of the four lines of interest. The second step was to perform a nonlinear least squares fit using the IDL

function CURVEFIT for a variety of analytical forms, including the original Layden94 equation. This process consists in establishing a ΔS *index* value that is a function of the K, H_δ, H_γ, and H_β measurements for a given star, and then equaling this index to the star's high resolution [Fe/H] measurement. The code then attempts to minimize the residuals by repeating this process iteratively as it changes the coefficients of the adopted analytical form to account for all RRLs of the CHR sample at once. This means that, instead of starting from the HK plane, our calibration departs directly from the high resolution metallicities.

Other than the original Layden94 analytical form, we also attempted variations of it using the logarithms of the equivalent widths, polynomials, sums of Gaussians, and Moffat functions. The minimum scatter was found with a polynomial with the form

$$[Fe/H]_{\Delta S} = c_0 + c_1 K + c_2 H_\delta + c_3 H_\gamma + c_4 H_\beta \tag{8.2}$$

where K is the equivalent width of the CaII K line, and H_δ, H_γ, and H_β the equivalent widths of the corresponding Balmer lines. The $[Fe/H]_{\Delta S}$ value is already the metallicity estimate of the ΔS method in our high resolution metallicity scale and no further transformations are necessary.

The quality of the new polynomial equation and of a new fit of parameters using the analytical form of Layden94 are comparable. In Figure 8.6, we present $[Fe/H]_{\Delta S}$ versus phase using the original Layden94 calibration (top panel), a new fit of the Layden94 equation (middle panel), and the new equation (bottom panel) for a sample of RRLs of varied metallicities for which the whole pulsation cycle is well-covered. At a first glance, the new fit of the Layden94 equation appears to display a more stable result across the pulsation cycle. However, its sensitivity to metallicity is slightly decreased, with the curves of several metallicities (color-coded) resulting in very similar $[Fe/H]_{\Delta S}$ values.

This effect is even more evident in Figure 8.7. In the top row, the H versus K plane is shown for the same group of RRLs. The straight lines were computed using the analytical forms indicated above each panel. The actual equivalent widths, measured from the spectra, are shown as dots. Both the empirical measurements and the fitted lines are color-coded by metallicity. Thus, it seems that the metal-poor data (purple points) is better fitted by a new fit of the Layden94 equation (purple lines in the middle panel), while the metal rich data (yellow points) are better fitted by the new calibration (yellow lines, right panel). For the data shown in the second row, we inverted the $[Fe/H]_{\Delta S}$ equations for both the new fit and the Layden94 equation fit in order to compute the K line equivalent width $EW(K)_{fit}$ given by the equations, and then we compared this analytical result to the EW(K) measured in each spectrum. It is evident that the Layden94 fit provides a better average value for the K line equivalent width, but the scatter considering all metallicities and phases is significantly smaller in the new fit (σ = 1.32 versus 1.20). The original parameters of the Layden94 calibration (left panels on both rows) result is significantly shifted values of equivalent width.

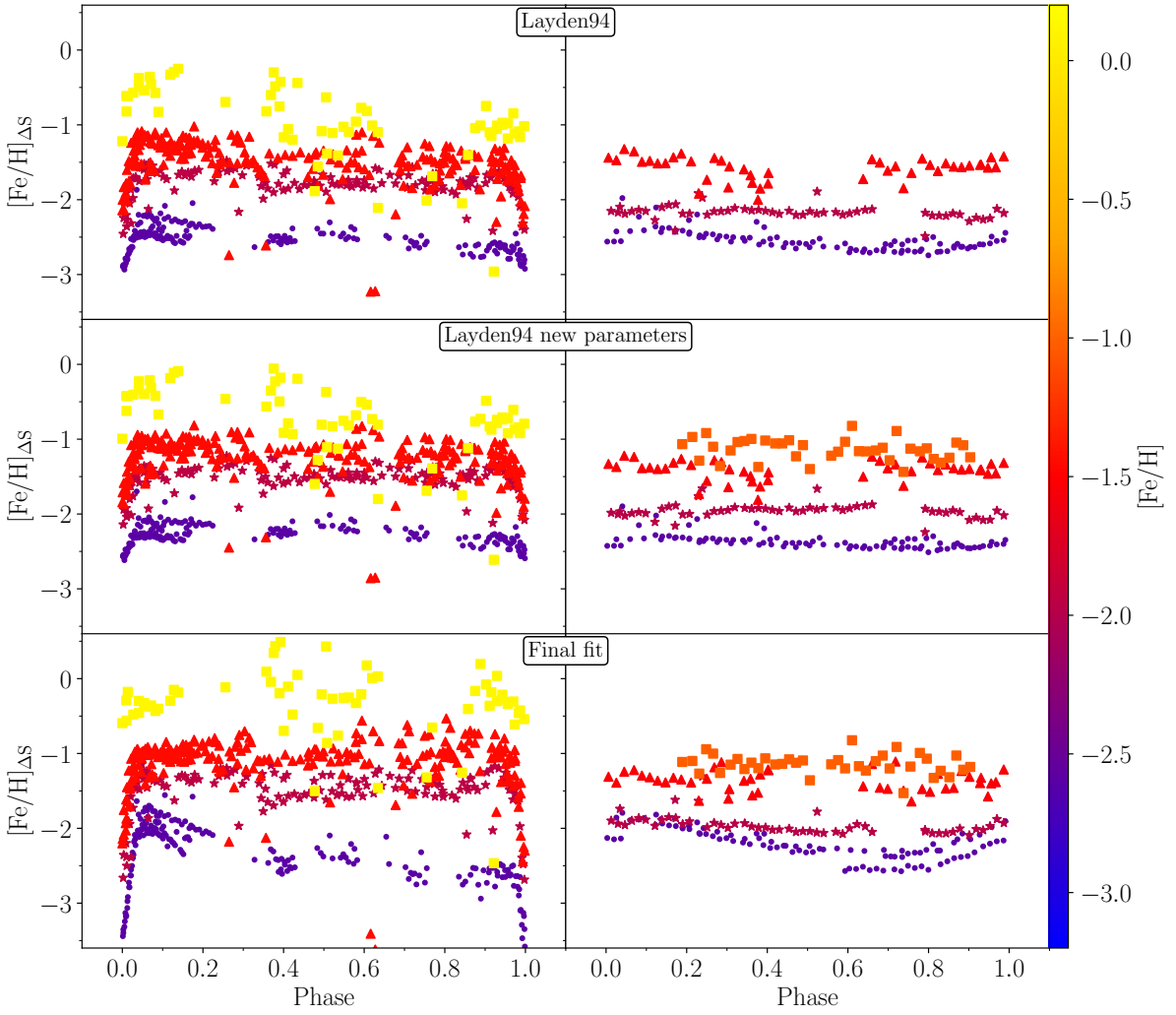

Figure 8.6: Behavior of the equivalent width of the Ca II K line (top), H_β line (middle), and $[Fe/H]_{\Delta S}$ (bottom) across the entire pulsation cycle for a sample of three RRab (left panels) and three RRc (right panels). The points are colored by metallicity according to the colorbar on the right edge of the figure.

Once we established that the new equation was more sensitive to metallicity, we proceeded to investigate the impact of separating the calibrating sample by phase and by pulsation mode. We did not detect improvement in the quality of the fit when the RRab and RRc were separated, nor when spectra acquired during the critical phases were removed. This is shown in Figure 8.8, which includes the full calibrating sample. It is clear that the new equation is capable of recovering the low and high metallicity tails with greater accuracy (see first and third columns). Removing the critical phases (middle column) slightly improved the average values, but also slighly increased the

scatter. We concluded that this modest difference was acceptable given that the new calibration can be applied to RRLs without previous photometric measurements, and without the burdensome planning involved in timed observations.

It is worth noting that there is an apparent increase in scatter in the metal-rich regime (Figure 8.8). This is likely due to the smaller sample size in this metallicity regime, coupled with four stars with particularly deviant results. Two of these stars have significant error bars in their ΔS measurements. An attempt at fitting a higher order polynomial to the [Fe/H] versus $[Fe/H]_{\Delta S}$ plane did not achieve better results. An increase of the sample size for metal-rich RRLs is needed to better constrain this regime.

The quality of the fit considering the whole sample is similar for all combinations of Balmer lines, therefore we provide the c_n coefficients for all seven cases in Table 8.2. The fits for all combinations are shown in Figure 8.9. Thus, if a given spectrum does not have the full set of Balmer lines, $[Fe/H]_{\Delta S}$ can still be estimated using the appropriate coefficients for whatever lines are available. While a large sample is well described by any combination of the Balmer lines, we suggest preference be given to the calibration with all Balmer lines (Hδ, Hγ, Hβ) when possible, followed by combinations that include Hβ.

Table 8.2: Coefficients for the new ΔS calibration (Equation 8.2) for all combinations of hydrogen lines and the corresponding standard deviation of the residuals σ.

Balmer lines	c_0	c_1	c_2	c_3	c_4	σ
H_δ, H_γ, H_β	-3.84323 ± 0.02438	0.36828 ± 0.08481	-0.22182 ± 0.11325	0.00433 ± 0.08793	0.51481 ± 0.18314	0.33
H_δ, H_γ	-3.75381 ± 0.02682	0.39014 ± 0.09433	-0.19997 ± 0.10267	0.38916 ± 0.20318	–	0.37
H_δ, H_β	-3.84160 ± 0.02302	0.36798 ± 0.05519	-0.21936 ± 0.07134	–	0.51676 ± 0.17720	0.33
H_γ, H_β	-3.79074 ± 0.02462	0.35889 ± 0.07550	–	-0.21997 ± 0.08967	0.50469 ± 0.18582	0.34
H_δ	-3.48130 ± 0.02690	0.36105 ± 0.02689	0.14403 ± 0.19890	–	–	0.38
H_γ	-3.70799 ± 0.02682	0.38127 ± 0.02831	–	0.17973 ± 0.20453	–	0.38
H_β	-3.92067 ± 0.02393	0.38194 ± 0.03126	–	–	0.25898 ± 0.18516	0.35

8.5 Validation

8.5.1 Comparison with HR and LR literature measurements

The new ΔS calibration was developed using only the 143 RRLs for which metallicity measurements natively in our scale. No stars from the RRL-Lit, which have HR metallicity measurements, were employed. However, we obtained low SNR spectra for 64 stars in the RRL-Lit sample that allowed us to estimate their $[Fe/H]_{\Delta S}$. We compared the results of the new calibration to the HR measurements brought to our metallicity scale by the addition of a constant Δ (see Section 5.3 for details on the HR scale shifts). We found that the median difference between HR metallicity and $[Fe/H]_{\Delta S}$ for this subsample is $\eta = 0.12 \pm 0.04$, with σ=0.36, in agreement with the same comparison for the CHR

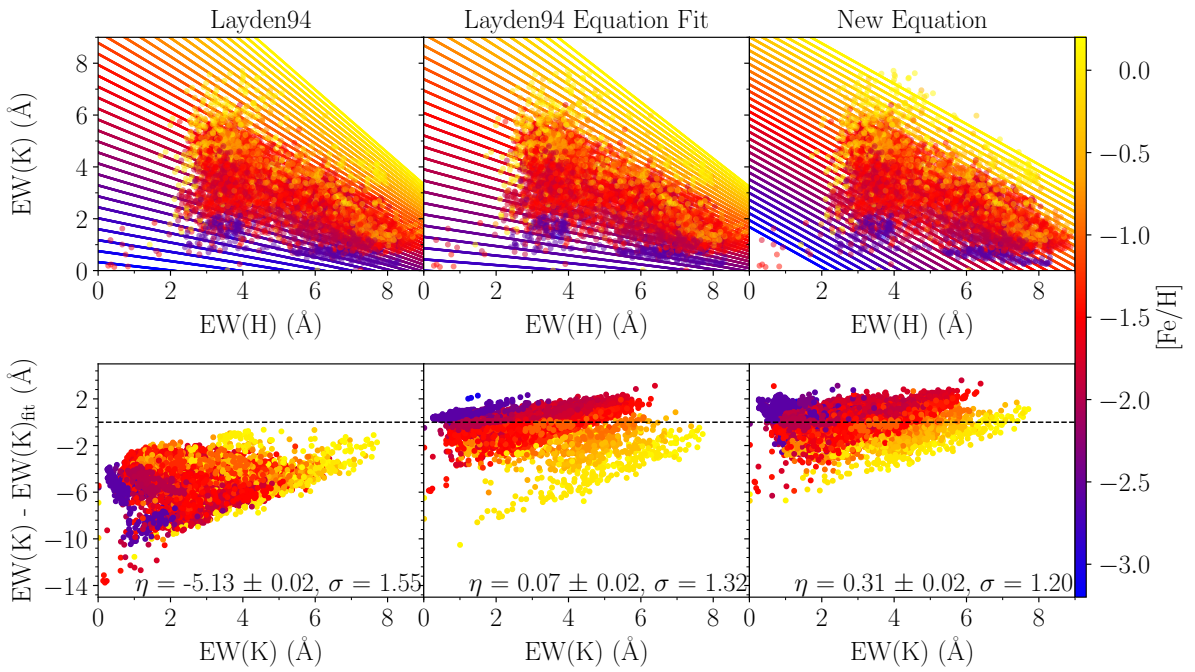

Figure 8.7: The HK plane (top) and residuals of the ΔS (bottom) for the CHR sample considering three cases: the original Layden94 equation (left), a fit of the Layden94 equation with new coefficients (middle), and the new equation (right). The points are the measured equivalent widht values in the new definition of wavelength ranges. The lines in the top panels are the predicted CaII K equivalent width considering each equation for a range of metallicity values. Data points and analytical lines are colored by high resolution metallicity according to the colorbar at the right edge of the figure.

sample (Figure 8.10, top panel).

We also obtained 13 SEGUE-SDSS spectra for stars in four GCs. We compared the $[Fe/H]_{\Delta S}$ estimates for these stars with the HR metallicity for their host GC as measured by Carretta et al. (2009) in an HR analysis. As we do not have HR measurements for GC stars, we did not apply any scale shift to these literature values. We found a median difference of η = -0.08±0.04, with σ=0.16.

A shift of the order of 0.1-0.2 dex is to be expected between modern, i.e. from the last two decades, HR investigations. The spectrographs and atomic transition parameters employed in recent years are roughly on the same scale. The main concern between different scales is not so much the presence of a rigid shift, but of nonlinearity. With this in mind, there is a crucial point to the comparison performed in this chapter. Namely, we see that the scale of the new ΔS calibration is comparable to a HR scale, because it relates to other HR scales linearly without need of further transformations. This is one of the most important aims of a new calibration.

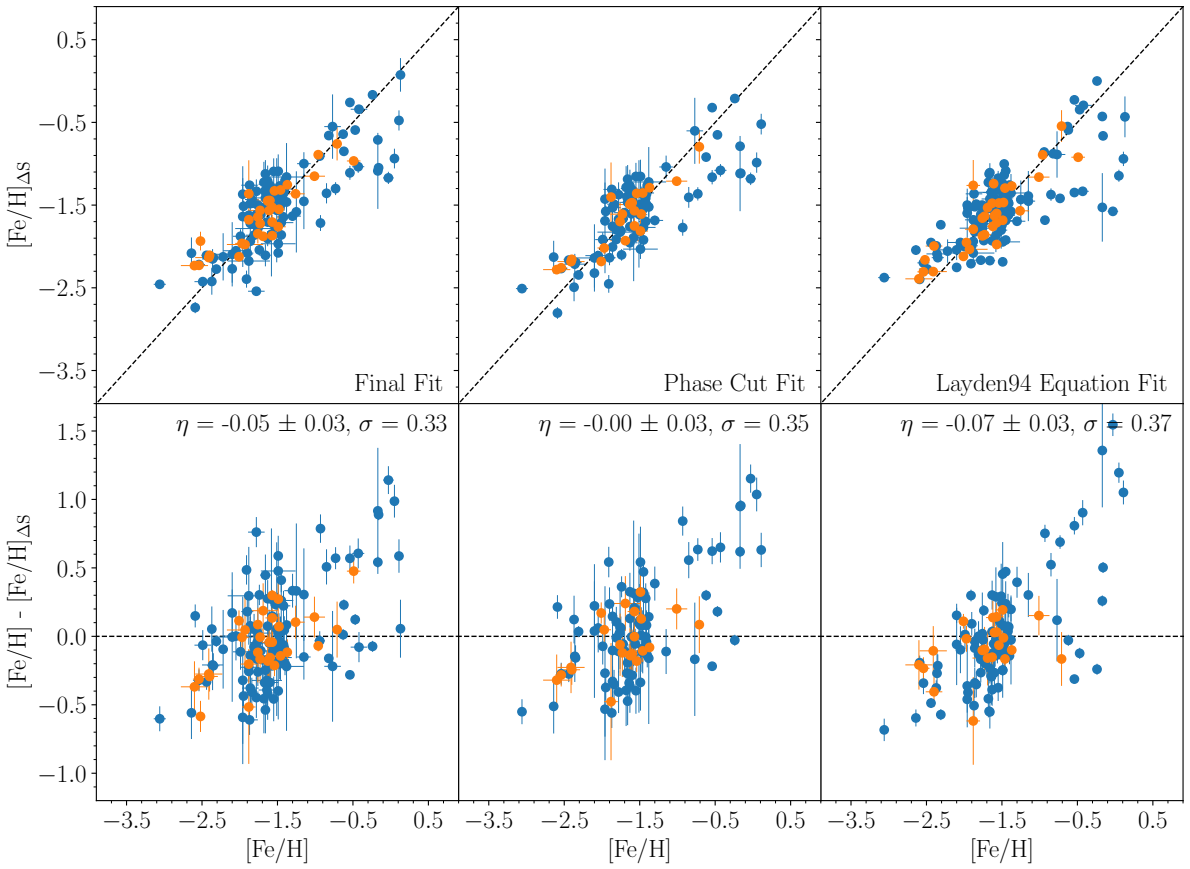

Figure 8.8: The ΔS versus [Fe/H] plane (top) and residuals (bottom) for three cases considering all Balmer lines: the final polynomial fit adopted in this work (left), the polynomial fit derived from the sample with phases between 0.1 and 0.9 (middle), and the fit of the Layden94 equation with new coefficients (right). The RRab are plotted in blue and the RRc in orange.

Considering LR literature estimates, we compared the $[Fe/H]_{\Delta S}$ measurements obtained from the SEGUE-SDSS spectra to those in Fabrizio et al. (2019), which employed 2,385 of the same spectra but a transformation of the Layden94 calibration into an HR metallicity scale, and with those in Liu et al. (2020), which employed 2,634 of the same spectra but derived metallicities through spectrum matching. The results of these comparisons are shown in Figure 8.11. As expected, the HR scale of Fabrizio et al. (2019) is in good agreement with the one in the present work. It is interesting to note that the rigid shift of 0.23 dex between our results and those of Liu et al. (2020) originate not on differences between the ΔS method and their spectral matching method per se, but rather from the HR results they used to calibrate their method. All but one of their calibrating RRLs were taken from the Nemec et al. (2013) and Pancino et al. (2015). Both of these works have a scale shift of ≈0.25 dex when compared to the present work.

8.5.2 Application to native low resolution spectra

We applied the new calibration to the sample of native low resolution spectra described in Section 5.2. We obtained $[Fe/H]_{\Delta S}$ measurements for the same stars using only SEGUE-SDSS spectra, and only LAMOST spectra. This is a critical test because it verifies whether the calibration is indeed universal and does not require the transformation of equivalent width systems, as was the case for the Layden94 calibration. The new calibration itself was built on the assumption that the degraded spectra of a variety of HR spectrographs were were on the same equivalent width system, but the SEGUE-SDSS and LAMOST spectra permitted to test the assumption that modern LR spectrographs also have comparable responses. We note that there was no significant overlap between the SEGUE-SDSS sample and the HR sample, nor between any of the samples included in this work and public data collected with the updated ESO Faint Object Spectrograph and Camera (EFOSC2 Snodgrass et al., 2008). Thus, only LAMOST and SEGUE-SDSS could provide enough native LR data for a comparison.

In Figure 8.12, the horizontal axis shows the $[Fe/H]_{\Delta S}$ estimates obtained exclusively from LAMOST spectra. The vertical axis shows the $[Fe/H]_{\Delta S}$ estimates obtained exclusively from SEGUE-SDSS spectra, and the [Fe/H] measurements from the TW-RRL and Lit-RRL samples (red crosses). The HR results were included as benchmark. The calibration itself was performed using degraded HR spectra, but in this figure it becomes evident that native LR spectra also provide tight results when compared to HR measurements, as evidenced by the small scatter and linear trend across a wide metallicity range in the comparison between LAMOST and the TW-RRL and Lit-RRL samples. Indeed, a scatter of 0.21 dex is comparable to the scatter between the HR results and the $[Fe/H]_{\Delta S}$ measurements from degraded HR spectra (Figure 8.9). Furthermore, the new calibration is capable of recovering metallicity estimates across different LR spectrographs, although with an increase in the scatter to 0.29 dex. This increase in uncertainties reflects the fact that both quantities being compared are LR estimates, thus both axes carry larger intrinsic uncertainties.

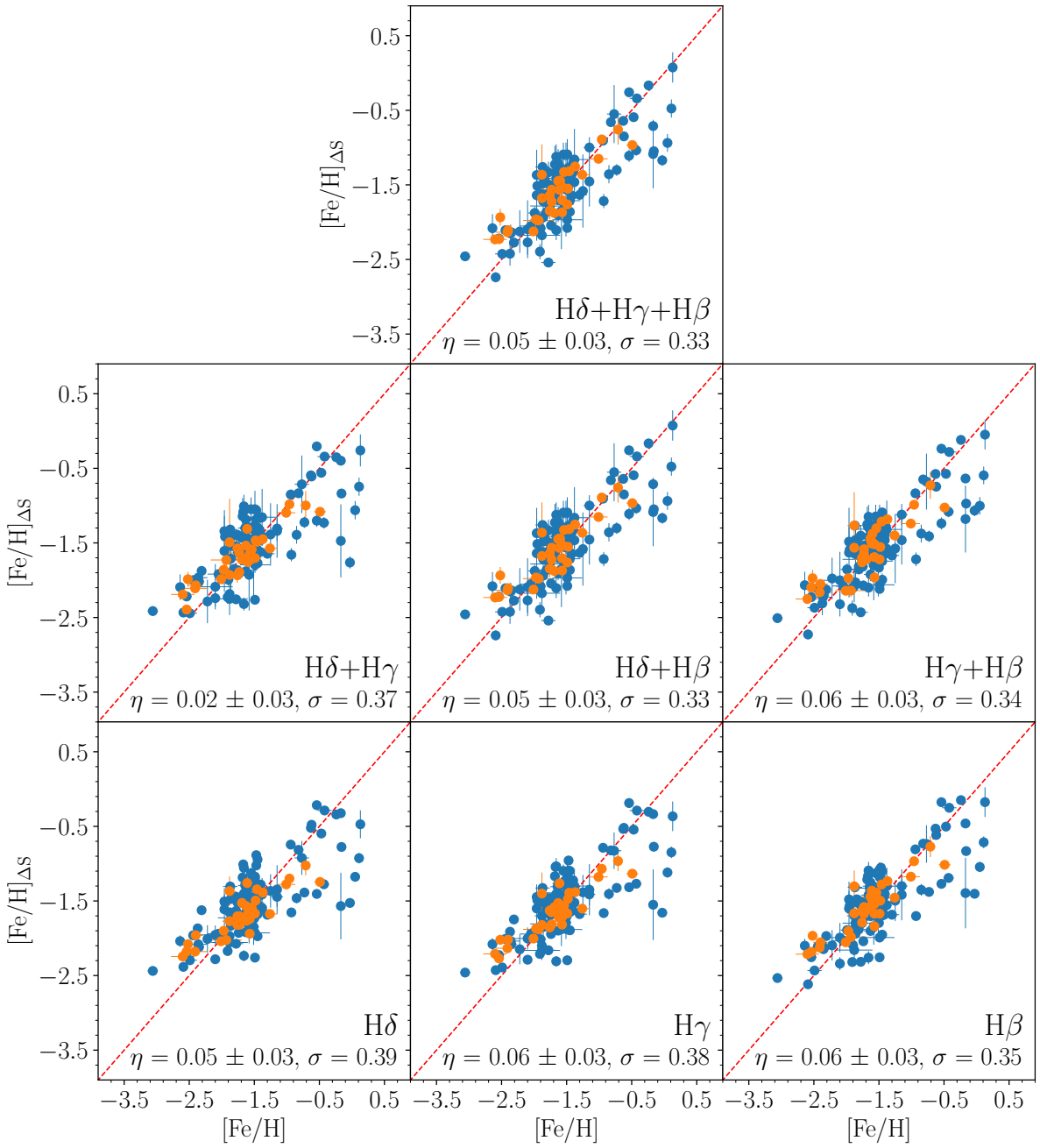

Figure 8.9: The $[Fe/H]_{\Delta S}$ versus high resolution metallicity plane for all combinations of Balmer lines included in the calibration, as indicated in the annotations inside each plot. The median of residuals η and the standard deviaton of residuals σ are also indicated for each case. RRab stars are shown in blue and RRc in orange. The dashed red lines denote the identity line for reference.

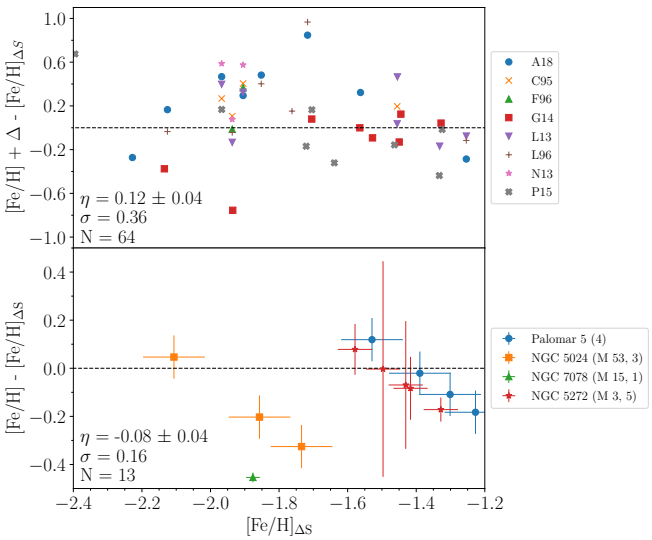

Figure 8.10: Comparison between $[Fe/H]_{\Delta S}$ estimates in the new calibration and literature HR metallicities. *Top:* Field RRL with literature values brought to our scale by the addition of the corresponding shift (Δ). The references as listen in Table 5.2. *Bottom:* Globular cluster RRLs considering the cluster metallicities derived by Carretta et al. (2009), which provides their value on a scale based on HR spectra. No shift has been applied to these values.

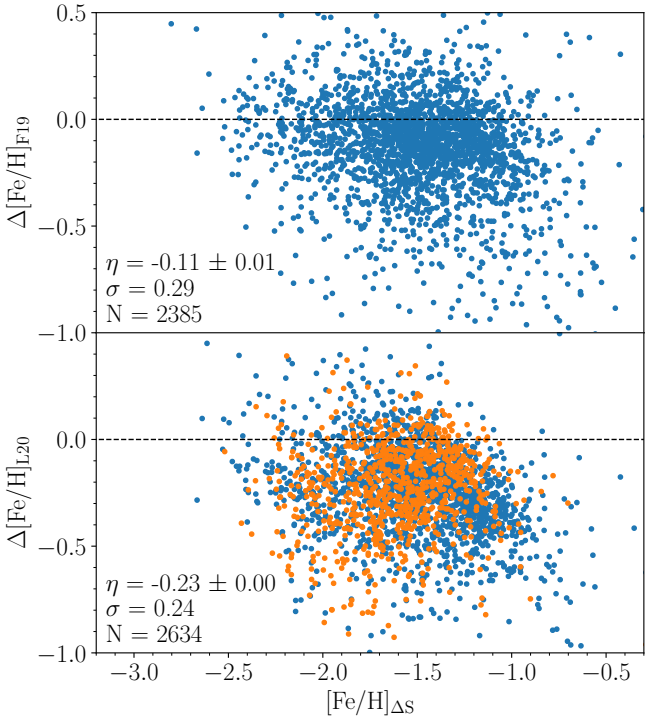

Figure 8.11: Comparison between $[Fe/H]_{\Delta S}$ estimates in the new calibration and literature LR metallicities using the same SEGUE-SDSS data. *Top:* Comparison with the values derived by Fabrizio et al. (2019) with the Layden94 calibration transformed into an HR metallicity scale. *Bottom:* Comparison with the values derived by Liu et al. (2020) using spectral matching.

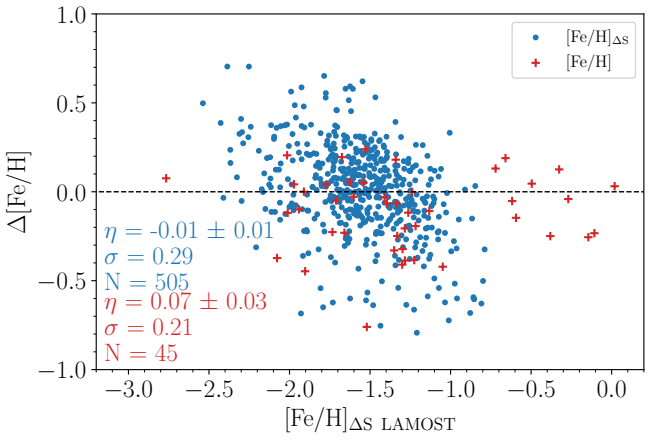

Figure 8.12: Comparison between $[Fe/H]_{\Delta S}$ estimates in the new calibration and literature LR metallicities using the same SEGUE-SDSS data. *Top:* Comparison with the values derived by Fabrizio et al. (2019) with the Layden94 calibration transformed into an HR metallicity scale. *Bottom:* Comparison with the values derived by Liu et al. (2020) using spectral matching.

Chapter 9

The high and low resolution results

The analysis done in this work is the largest and most homogeneous spectroscopic sample of Galactic field RRLs, and in particular including HR measurements. These results offer a wealth of information for investigations of Galactic formation and nucleosynthetic models. The RRL sample includes a wide range of pulsational parameters and metallicities. Perhaps most importantly, these results form a coeval sample that traces the chemistry of the early ages of the Halo. Indeed, they include HR chemical abundances for multiple species covering about 3 dex in [Fe/H], and LR metallicity estimates for an unparalleled number of RRLs with the new calibration of the ΔS method. Furthermore, the calibration itself is made using state of the art spectrographs. It offers a high quality update to the Layden94 calibration that for the first time includes the full pulsation cycle and both fundamental and first overtone pulsators, and requires no previous photometric knowledge the RRLs to be observed. Furthermore, transformations between equivalent width systems or metallicity scales are not necessary. This enables future investigations to increase the sample of RRLs in a homogeneous metallicity scale with minimal effort.

For the sake of convenience, we point once more that the new ΔS calibration can be found in Crestani et al. (2021a). The atmospheric parameters for individual exposures and the α element abundances for Mg, Ca, and Ti per star are included in machine-readable format in Crestani et al. (2021b). The machine-readable values for the remaining species will be included in a forthcoming paper. Note that the values adopted from F10, F11, C17, and S17 are not included in our tables because they underwent no changes. The interested reader may find them directly in their source papers. The homogeneous sample and results included in this thesis were used by our group in multiple investigations involving RRLs. We will comment briefly on those in Chapter 10.

9.1 Metallicity gradient and distribution of Halo RRLs

Due to our focus on the Halo, our selection of RRLs avoids Galactic latitudes close to the Bulge. The lines of sight that include the highly reddened Disk region are also avoided, as stars in these regions carry larger positional uncertainties, and also require longer exposure times in spectroscopic studies. We did not include the HB stars in the current analysis because their sample is inherited biased in metallicity because the investigation in F10 was focused specifically on metal-poor stars, while the additional HB stars in the TW-HB sample were chosen specifically to cover the high-metallicity regime. Considering distances computed in the same way as described in Fabrizio et al. (2019), the bulk of HR measurements comes from RRLs closer to the solar neighborhood, and thus lay within a Galactocentric distance (d_G) smaller than 10 kpc, with 29 objects stretching out from 10 to 20 kpc, and only 4 objects between 20 and 30 kpc. For the LR sample, the bulk of measurements has $d_G = 4 - 15$ kpc, but the sample decreases smoothly to distances as large as 130 kpc, with three objects reaching 155 kpc. This distance bias in the HR sample is a natural consequence of the difficulty in acquiring HR spectra for objects at larger distances.

In Figure 9.1, we show the variation of metallicity with Galactocentric distance. We used two approaches to compute the gradient itself. The first was to merely take the median metallicity within bins of fixed Δd_G width, with results shown as a red dashed lin. The second was to perform a running average, which samples the data at steps of fixed sample size instead of fixed coordinates, and its results are shown as a blue dashed line. The black dashed line is the median of the HR and LR samples considered together. It is clear that the slope computed by both approaches is flat within measurement uncertainties, showing only fluctuations especially at larger d_G where the sampling is poorer. Changing the Δd_G width or the sample size of the running average did not change this result, and thus we detect a sometimes noisy but flat slope, with no evidence of either an increase or decrease beyond measurement uncertainties.

Interestingly, Figure 9.1 also shows that both the HR and LR samples show a very significant spread in metallicity at $d_G \approx 5 - 12$ kpc . Indeed, the full range of metallicities found in this study is found at this Galactocentric distance, while larger distances display a relatively narrow metallicity distribution centered at η = -1.52 dex (black dashed line). This is caused by the fact that the metal-rich RRLs are all located near the Solar neighborhood, at very small heights ($\lesssim$ 3 kpc) from the plane of the Disk, but at varied coordinates in the plane of the Disk, i.e. they do not form a spheroid as would be the case of a inner Halo, but rather remain scattered near the plane of the Disk. This could be interpreted as preliminary evidence for a population of metal-rich RRLs near the Disk. However, we caution that the current sample does not permit strong claims in this regard, because the only region near the Disk covered by our sample is near the Solar neighborhood. The avoidance of the Bulge region and of highly reddened lines-of-sight mean that our sample does not include RRLs near the Disk at any other direction. Thus,

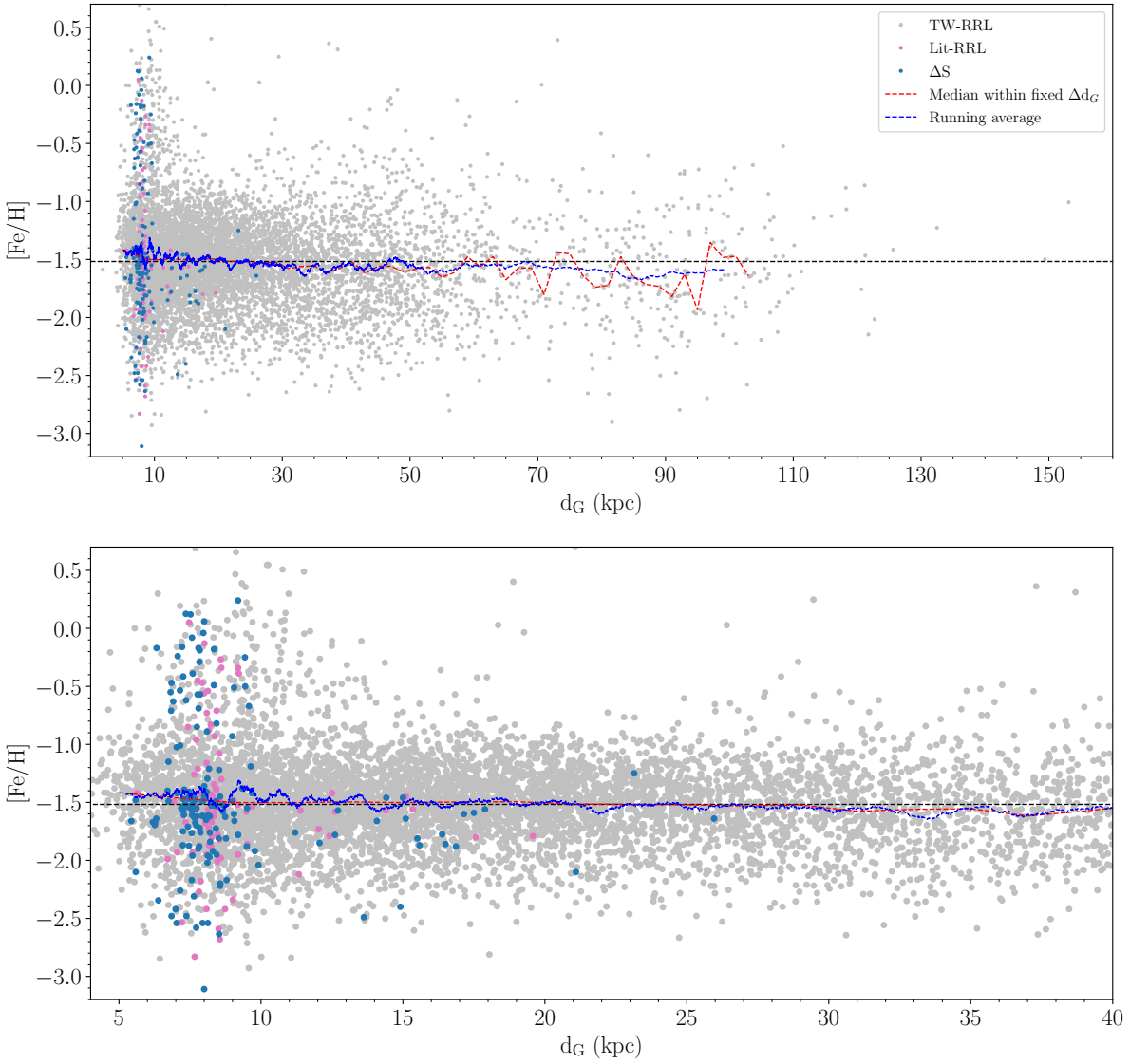

Figure 9.1: *Top:* Metallicity versus Galactocentric distance (d_G) for the TW-RRL (blue), Lit-RRL (pink), and ΔS (grey) samples. The black dashed line indicates the median metallicity considering the three samples together. The red dashed line indicates the median metallicity within bins of 2 kpc. *Bottom:* The same as above, but for distances within 40 kpc.

it is unclear if these metal-rich RRLs are associated with the Disk, or just with the Solar neighborhood. As of the time of writing of this thesis, our group is working on obtaining good quality kinematic constrains for the metal-rich RRLs in order to better characterize their orbits. These stars are likely to display other peculiarities, as will become clearer in the next sessions regarding the chemical abundance of elements other than iron.

In sum, from what is possible with the current homogeneous sample of these very old stellar tracers, we do not detect any signs of a Halo duality. The metallicity gradient remains flat from $d_G \approx 4 - 130$ kpc, with a median $\eta = -1.52$ dex. A metal-rich population is present at distances smaller than $d_G \approx 12$ kpc, but it is made up of RRLs within ≈ 3 kpc from the plane of the Disk that do not form a spheroid, but that may be associated with the Disk itself.

Moving on to the distributions themselves, the full sample of RRLs with HR metallicity measurements contains 247 stars, while the the sample with ΔS metallicities includes 8,627 stars. They are show respectively in the left and right panels of Figure 9.2. Both HR and LR distributions are in excellent agreement, with median values within 0.06 dex of one another.

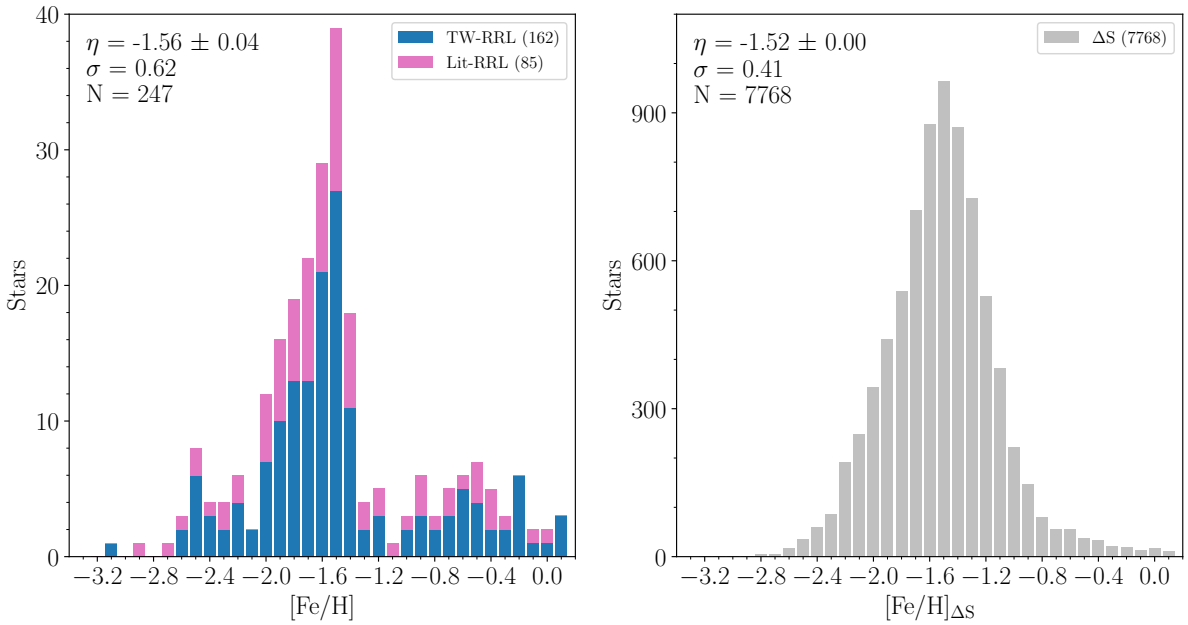

Figure 9.2: *Left:* Metallicity distribution for the TW-RRL (blue) and Lit-RRL (pink) samples. *Right:* The same for the ΔS sample. Note that the left panel shows a stacked histogram, i.e. the bars representing the Lit-RRL values are on top of the ones representing TW-RRL values, not behind them.

The HR and LR distributions display slightly different shapes. This is to be expected due to the larger uncertainties associated with the ΔS method when compared to HR chemical analysis. As mentioned above, the HR sample is biased in distance, and populates the distance range where the largest variation in metallicity is observed. Consequently, the center of its distribution is not as dramatically larger than the wings, as is the case for the LR sample. Both HR and LR distributions are clearly asymmetric, with the metal-rich tail displaying a steeper slope than the metal-poor tail. This level

of skewedness cannot be reproduced by a single Gaussian, a result that is also present in the kinematic distribution of field Halo stars (e.g. Lancaster et al., 2019).

Separating the sample by pulsation mode reveals that the distribution of the RRc peaks at a slightly lower metallicity. All panels in Figure 9.3 show area-normalized histograms for ease of comparison. The top left panel shows a histogram of the HR RRab (blue), superposed with the density distributions of both the HR RRab (full line, blue) and the RRc (full line, orange). The annotations contain the statistics for the RRab and RRc in the HR sample. The right panel shows the same density distributions, but the histogram shows the RRc (orange). The same is shown in the two bottom panels, but considering only the LR data. Thus, it becomes clear that both LR and HR results point to the RRc as slightly more metal-poor than the RRab. This is empirical evidence of the well known metallicity dependence of the morphology of the HB. As shown in Figure 3.5, at higher metallicities only the red portion of the HB is populated. Meanwhile, theoretical pulsation models indicate that this region is populated by the RRab (Figure 3.11). Thus, as metallicity increases, the rate of production of first overtone pulsators decreases, while that of the fundamental mode pulsators increases.

The slopes of the metal-rich tail for both RRab and RRc are in good agreement, while this is not the case for the metal-poor tail. The small sample size of HR RRc limits any strong conclusions, but the LR data show preliminary evidence that the RRc have a more symmetric distribution, while the RRab may have a secondary metal-poor peak. Unfortunately, we did not succeed in disentangling the two Gaussian components in a satisfactory manner.

9.2 A double mode pulsator in HR and LR

The behavior of atmospheric parameters across the pulsation phase of both RRab and RRc has been previously investigated in the literature (e.g. F11, S17, C17, Magurno et al. 2019). These studies confirmed that the metallicities derived at different phases are consistent, supporting the strategy of random phase observations. However, it is important to note that during the critical phases, where effective temperatures are the highest and nonlinear effects are detectable, atmospheric parameters are significantly harder and sometimes even impossible to constrain. Luckily, the critical phase is very short lived in fundamental mode and first overtone pulsators. This is reflected in the fact that metallicities can be recovered across the pulsation phase, even very near critical phases, within reasonable measurement uncertainties. Indeed, with short enough exposures that avoid line smearing due to the quickly changing atmospheric radial velocities, atmospheric parameters can be recovered even when nonlinear effects are taking hold and deforming H lines. The difficulty of the measurement of metallic lines is only due to them becoming shallower, which is a natural consequence of higher effective temperatures and unrelated to nonlinear effects.

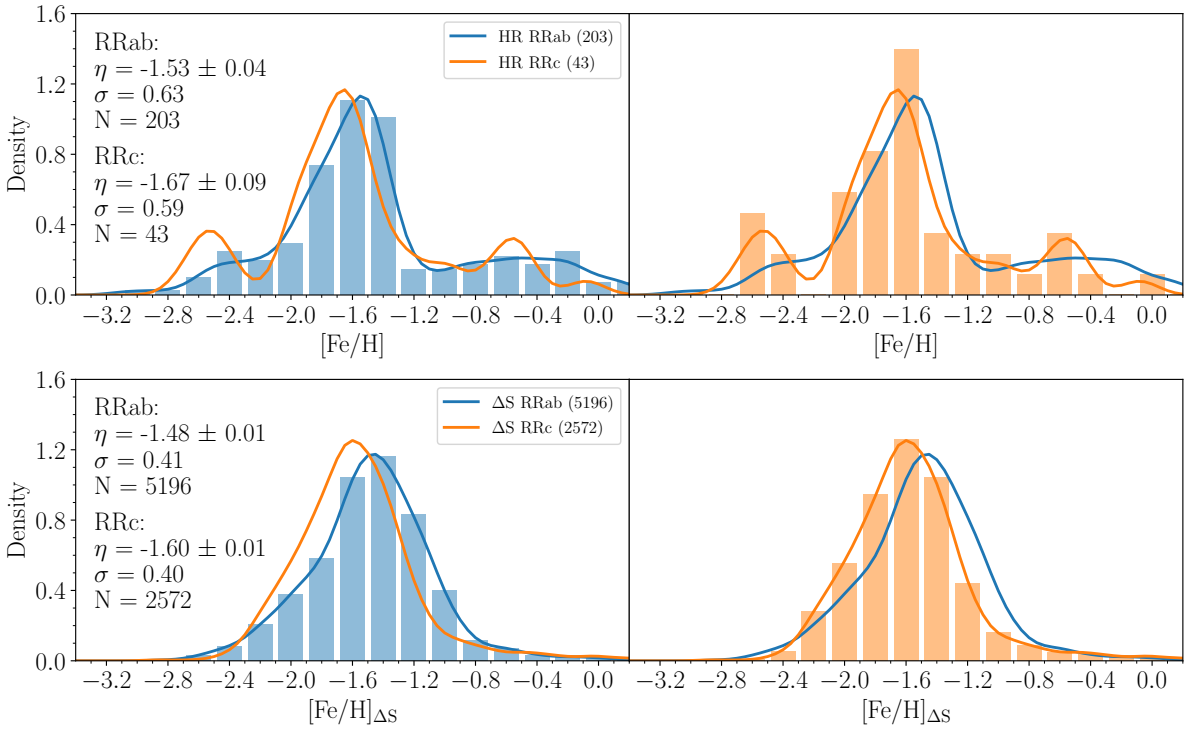

Figure 9.3: *Top left:* Area-normalized histogram for the HR RRab (blue). The solid blue and orange lines are the density distributions for the HR RRab and RRc, respectively. The annotations display the statitics of the HR sample dividing it into RRab and RRc. *Top right:* Area-normalized histogram for the HR RRc (orange). The full lines denote the same as in the top left panel. *Bottom left and bottom right:* The same as the top left and right panels, respectively, but considering the LR data set.

Our data set included 2 FEROS and 10 X-shooter spectra for a mixed mode pulsator, ASAS J183952-3200.9. This allowed us to verify whether the RRd behave in a similar way, with the possibility of obtaining robust metallicity estimates at nearly any phase of its complex pulsation cycle, or whether their envelope kinematics posed a serious impediment to random phase observations. The light curve and phase variation of atmospheric parameters is shown in Figure 9.4, alongside the HR metallicity measurements, the ΔS metallicity estimates, and their difference.

Using the first overtone period for phasing, the effective temperature does not keep to a well defined curve as is the case for the RRb. The values for surface gravity and microturbulent velocity also display scattered values. It is interesting to note that the measurements coming from FEROS are in general in very good agreement with one another, and so the scatter in the parameters coming from X-shooter spectra likely reflects the lower resolution of this spectrograph. This lower resolution is directly responsible for larger uncertainties because some Fe lines that are close to other lines must be dis-

carded in lower resolutions, where different components of a blended feature cannot be disentangled in a satisfactory manner. The HR metallicity measurements, considering all available spectra, remain at [Fe/H] = -1.65, with σ=0.06 dex. For the LR estimates, we found $[Fe/H]_{\Delta S}$ = -1.44, with σ=0.03. The difference between the two metallicity values has a median $\eta = 0.16 \pm 0.03$ and σ=0.09.

The uncertainties in HR and ΔS metallicities, and the difference between them, in this mixed mode pulsator are comparable to the same quantities in the RRab and RRc. This supports that the RRd may be treated in the same way as their fundamental mode and first overtone counterparts, with both the strategy of random phase observations and the application of the ΔS method offering consistent results.

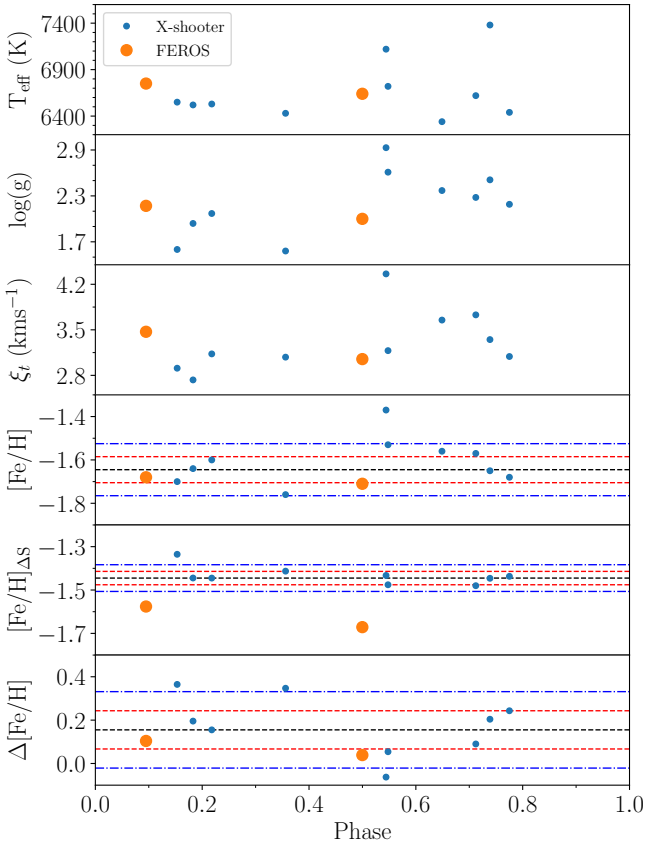

Figure 9.4: Variation of the atmopheric parameters of the double mode pulsator ASAS J183952-3200.9 with phase. From top to bottom: effective temperature, surface gravity, microturbulent velocity, HR metallicity [Fe/H], ΔS metallicity $[Fe/H]_{\Delta S}$, and the difference Δ[Fe/H] = [Fe/H] - $[Fe/H]_{\Delta S}$. Measurements coming from the FEROS spectra are marked by large orange dots, and the ones from X-shooter by small blue dots. In the bottom three panels, the black dashed lines show the median value, the red dashed lines the σ interval, and the blue dot dashed lines the 2σ interval.

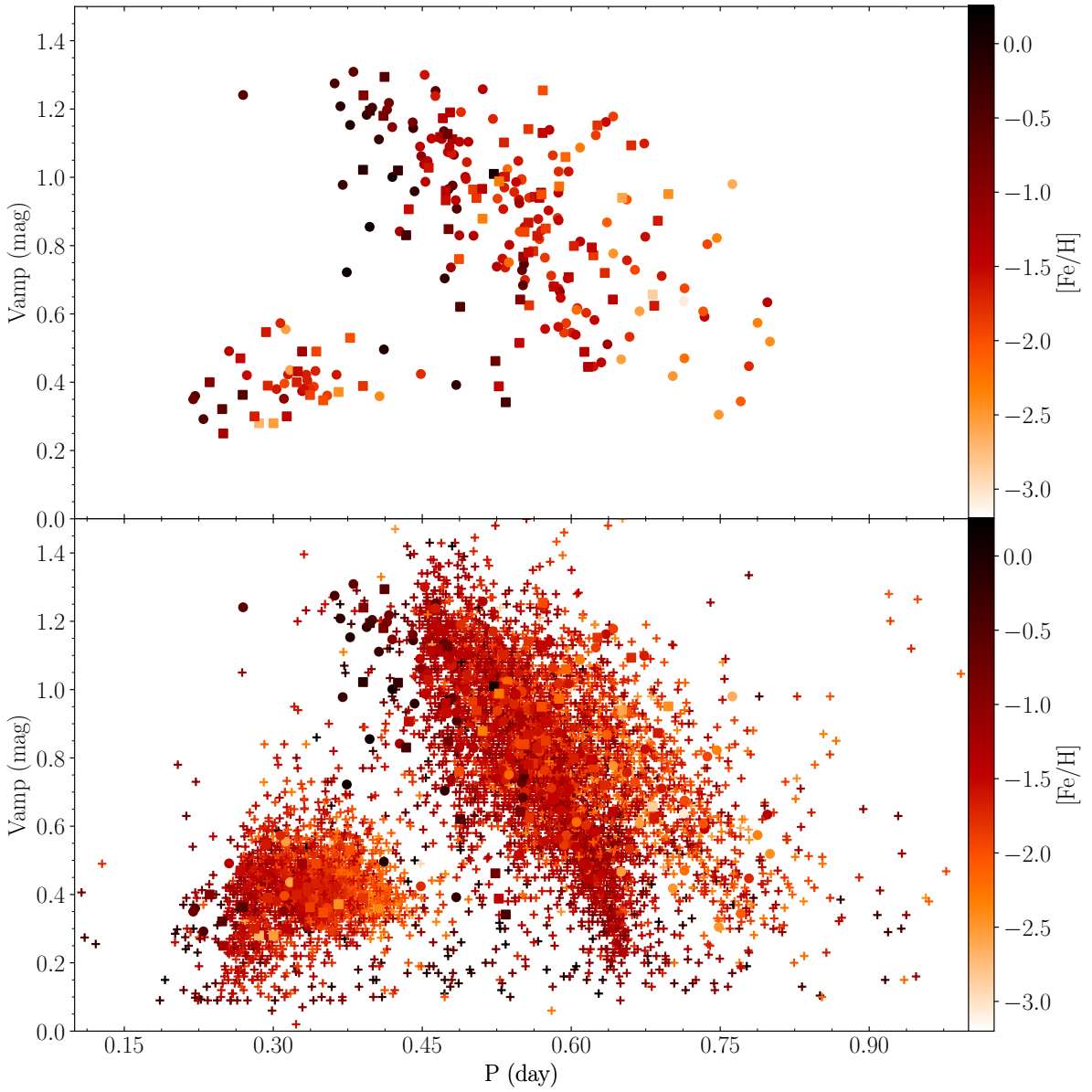

Figure 9.5: *Top:* Bailey diagram for the TW-RRL sample (circles), and the Lit-RRL sample (squares). All markers are colored by metallicity according to the color bar on the right. *Bottom:* The same, but with the inclusion of the ΔS sample (crosses).

9.3 α element abundances

Our sample includes measurements of five α elements, namely Mg, Ca, Ti, Si, and S. As discussed in Chapter 4.3.2, stellar systems with low star formation rate, such as

dwarf galaxies, are expected to show the "knee" in the [X/Fe] versus [Fe/H] plane at lower metallicities, while bulges and elliptical systems, due to a high star formation rate, would manage to produce higher metallicity stars before the SNe Ia became significant, causing the "knee" to occur at higher metallicities. Meanwhile, the value of the plateau of α element abundances in the metal-poor to -intermediate regime is connected to the initial mass function of the stellar system in question, although, as mentioned in Chapter 4.4, absolute values must be taken with caution due to possible zero-point shifts among different elements and different lines of the same element.

The investigated α elements with more robust results, namely Mg, Ca, and Ti, are shown in Figures 9.6 and 9.7 while the remaining two will be discussed in the next Chapter. The first column shows our data sets, while the second column superposes the same data and data for typical field populations of the different Galactic components. All measured elements display high abundances up to [Fe/H] $\approx$ -1.5 dex, after which point there is a steady decrease with increasing metallicity. The plateau for S is unclear due to the absence of measurable lines in the metal-poor regime. For the other elements, it remains at about [X/Fe] $\approx$ 0.4 dex, with Mg possibly displaying a slightly higher value. A few other characteristics of the [X/Fe] versus [Fe/H] plane for the α elements are noticeable:

i) *Similar slopes for Mg, Ca, and Ti* – These three species display a well defined slope when moving from the metal-poor to the metal-rich regime. The steady decrease in α abundance is more clear in Ti and Ca, which display a variation is of the order of $\approx$0.6 dex, but it is also present in Mg.

ii) *An α-poor, metal-rich population in Mg, Ca, and Ti* – Very metal-poor ([Fe/H]$\leq$-2.2) RRLs are strongly enhanced in α elements ([α/Fe]$\approx$0.4 to 0.5), while those approaching solar iron abundance are depleted in α elements ([α/Fe]$\approx$-0.2 to -0.3). Liu et al. (2013), in a sample of five metal-rich RRLs, identified a depletion in Ti but not Mg or Ca. All of the stars considered in Liu et al. (2013) are included in the TW-RRL sample, and this allowed us to verify that their results for Ti are largely identical to the ones derived in the present work, while both Mg and Ca are slightly higher by 0.08 dex in [X/Fe], a difference well within uncertainties. Thus, the absence of detectable depletion in Mg and Ca in their study is likely an effect to their small sample size.

This α-poor RRL population consists of the same metal-rich stars identified in Chapter 9.1. They are all located in the solar neighbhoor and within small distances ($\lesssim$ 3 kpc) from the plane of the Galactic disk. Unfortunately, we do not have data for RRLs near the Disk but outside the Solar neighborhood in order to clarify whether this chemical peculiarity is connected to the whole Disk. Recently, Prudil et al. (2020) investigated the kinematics of a sample of 314 RRLs in the solar neighborhood with LR metallicity estimates based on the Layden94 calibration of the ΔS method. They identified a sample of 22 metal-intermediate to -rich RRLs with disk-like kinematics and, indeed, with orbits that suggest a common origin that is distinct from the Gaia Enceladus.

iii) *Similar dispersion for Ca and Ti* – These two elements display trends in tight

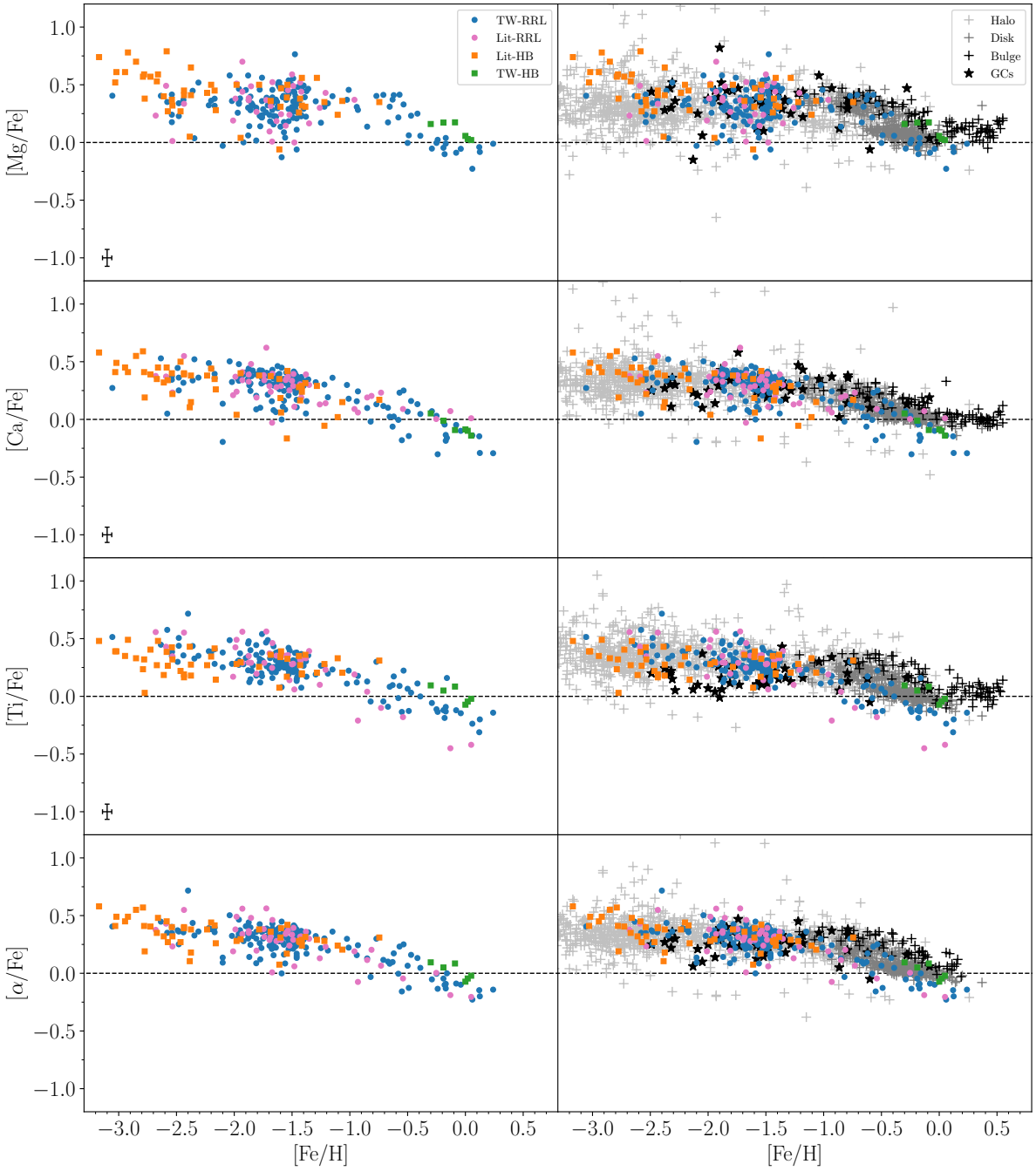

Figure 9.6: *Left:* The α-element abundances (Mg, Ca, Ti, and their median α) versus metallicity for the TW-RRL, Lit-RRL, TW-HB, and Lit-HB samples. Typical errors for each element, considering only our own measurements, are shown in the lower left corner of the corresponding panel. *Right:* The same, but superposed with results for GCs and field stars for the different Galactic components according to the key in the upper right panel. The literature sources on the right column are the same as in Figure 4.4.

agreement and can be considered the same within uncertainties. Their trends exhibit a scatter of the order of 0.4 dex over the entire metallicity range that appears to be intrinsic, because it is over 3 times larger than the typical errors. The Ti measurements were based on transition parameters from very recent laboratory studies, and thus Ti can be taken as the pivot element against which others with similar trends may be compared. As mentioned earlier, Ca suffers from very inhomogeneous transition parameters in the literature, but its small spread that is comparable to the much better constrained Ti is reassuring. Most lines in our Ca line list, taken from NIST, have parameters computed by the same sources in the 1950s, 1960s, and 1990s. This ensures a certain level of homogeinity, although it is possible that new laboratory studies could detect a zero-point difference.

iv) *Larger dispersion for Mg* – It is possible that Mg presents an intrinsic spread because its production depends strongly on progenitor mass and metallicity, which is not the case for Ca and Ti. Theoretical nucleosynthetic models show that the yields of Ca and Ti remain similar across a wide range of progenitor masses, while the yields of Mg significantly increases in massive progenitors (35 $M_{\odot}$, see Figure 6 of McWilliam, 1997). Furthermore, the production of Mg shows a marked decrease when the metallicity of the progenitor goes from metal-poor and -intermediate to metal-rich regimes (see Figures 2 and 4 in Kobayashi et al., 2006). The spread observed in Figure 9.6 for both our data set and the literature stars of different Galactic components is also likely due to measurement difficulties. Like for Ca, there are no recent, homogeneous laboratory studies of Mg transitions. Moreover, the number of measurable Mg lines in stellar spectra is very limited and consists mostly of strong lines that easily saturate in metal-rich and cold stars. This results in a situation where most Mg abundances are computed using only one or two transitions. Meanwhile, our spectra typically contained 5 to 15 lines of varied strengths for both Ca and Ti.

v) *Overall agreement with the metal-intermediate and metal-poor Halo* – As can be seen in the right columns of Figure 9.6, the α element abundances for RRLs and HB stars agree well with the Halo field populations. The number of metal-rich stars included in Halo studies is limited, thus the RRLs offer a invaluable tracer in this metallicity regime. For Ti in particular the different Galactic components are more clearly separated (right column, bottom row), and the RRLs provide a lower envelope in [Ti/Fe] for the Bulge and reach a region where very few field Halo measurements are present. Meanwhile, the Halo field stars in the literature have a large spread, with several stars showing very high [α/Fe] abundances. The same is not true for RRLs. Indeed, the upper envelope of the trend for all three species is very sharp.

vi) *Overall agreement with the Sagittarius dwarf spheroidal* – The nearby dwarf galaxies display the "knee" of the [α/Fe] versus [Fe/H] plane at lower metallicities than the Milky Way. In the metal-rich regime, their stellar populations are already very depleted in α elements. Meanwhile, the Halo simply lacks a significant number of metal-rich stars. Interestingly, the Sgr dSph has a significant metal-intermediate and metal-rich

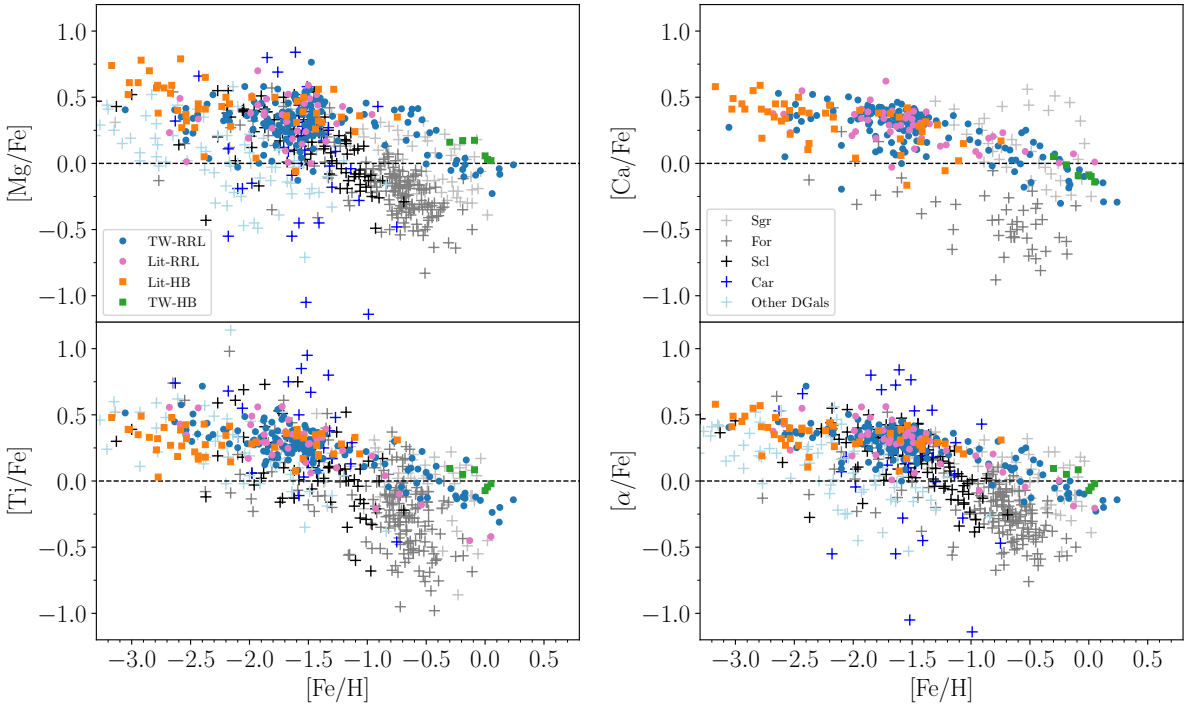

Figure 9.7: The α element abundances (Mg, Ca, Ti, and their median α) versus metallicity for the TW-RRL, Lit-RRL, TW-HB, and Lit-HB samples. The same for nearby dwarf galaxies is also shown, with the same literature sources as Figure 4.7. The markers and colors for each sample are indicated in the legends in the lower left corner of the top two panels. The uncertainties for the TW-RRL sample are reported in Figure 9.6.

population that is α-enhanced when compared to other nearby dwarf galaxies, and follows the trend set by the Halo and the RRLs in this metallicity regime, as can be seen in Figure 9.7.

Both the Halo and the Sgr dSph have scarce measurements super-solar metallicities, but the available data provides evidence that the spread in α element abundances in the metal-rich regime may be higher for Sgr dSph than for the Halo, as can be seen in Figure 9.8. The trend set by the RRLs is considerably tight across the whole metallicity range.

9.4 S and the Si situation

In our investigation, different SiI and SiII lines are in reasonable agreement with each other in the same star, although, as noted repeatedly in the literature, SiII does generally present slightly higher values. We eliminated lines that showed a temperature dependence, and the remaining 6 SiI lines and 2 SiII lines are often present in the same

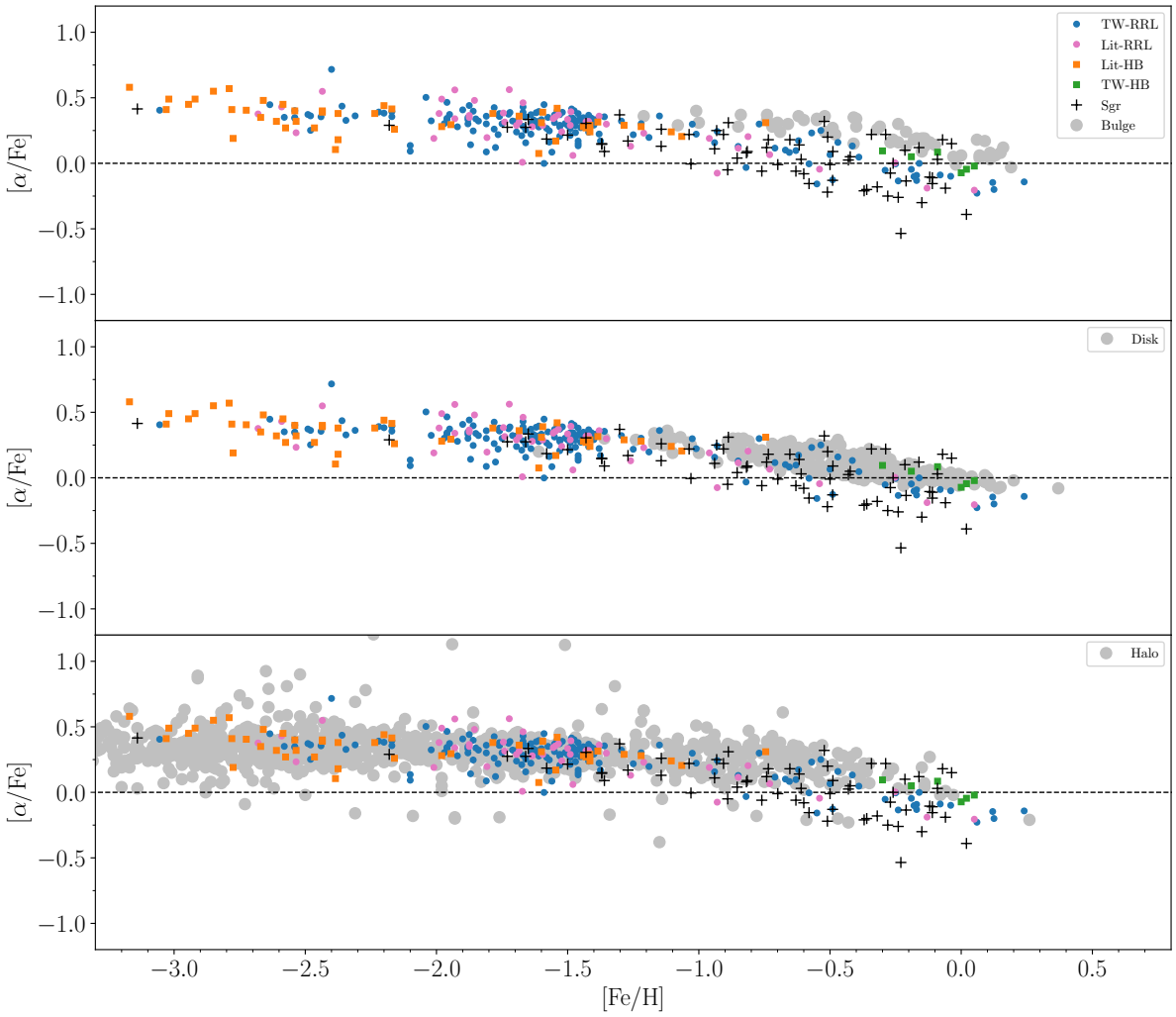

Figure 9.8: The α element abundances considering the median of Mg, Ca, and Ti, for the TW-RRL, Lit-RRL, Lit-HB, and TW-HB samples. From top to bottom, the large grey dots mark stars from the Bulge, Disk, and Halo, respectively, with the same literature sources as Figure 4.4. In all panels, stars from the Sgr dSph are marked by the black crosses.

Table 9.1: Difference Δ[Si/Fe] between Si abundances in literature sources and in this work, considering stars in common.).

Source	C95	F11	K10	L13	G14	P15	S17
Δ[Si/Fe]	-0.10	0.05	-0.16	-0.21	-0.55	0.11	-0.22

See Table 5.2 for references and number of stars in common with each work. Note that the values from F10, F11, and S17 were adopted without change in this work, and no values from K19 were adopted. Their Δ[Si/Fe] shifts are shown for comparison purposes only.

star for metallicities higher than [Fe/H] ≈ -1.2 dex. Below this metallicity, a curious situation arises, as can be seen in Figure 9.9. Individual stars still display a general agreement between SiI and SiII lines when they are present, but several stars in the metal-poor to metal-intermediate regime do not show SiI lines. This latter group also displays somewhat lower Si abundances and is responsible for virtually all Si measurements with metallicities lower than -1.3 dex and [Si/Fe] $\leq$ 0.62. Interestingly, the trend in both SiI and SiII is the same from metallicities higher than approximately -1.4 dex, and the Si abundance is systematically higher for the TW-RRL and Lit-RRL samples, with the exception of values coming from S17, when compared to field stars in the literature (second column of Figure 9.9).

As the sources in the Lit-RRL sample made varied choices regarding how to treat Si, we opted to average their values disregarding whether they came from SiI or SiII. This was done because we realized that the difference between SiI and SiII would not change the overall Si trend with metallicity, and because in several cases it was unclear which lines were used. Considering the literature sources included in the Lit-RRL and Lit-HB samples, the difference Δ[Si/Fe] considering the original value minus the value in our scale, considering the median of SiI and SiII measurements, is shown in Table 9.1. Six literature sources did not include Si measurements, namely L96, F96, H11, N13, C17, and A18. Our own scale is in agreement with F10, F11, C95, K10, and P15 before any shift is applied to values coming from these sources.

We mentioned in Chapter 5.3 that we adopted all abundance values from F10, F11, C17, and S17 without modification as they are natively in our scale. For most species, they exhibit variations, when compared to the present work, that are typical even inside the same study. One exception are the [Si/Fe] measurements coming from S17 (included in the Lit-RRL sample), which are on average 0.22 dex lower than ours. F10, F11, and S17 employed a few Si lines with log(gf) values coming from astrophysical estimates, which we did not employ, but they were coupled with most lines used in this work. C17 did not perform Si measurements. There are three RRLs in the Lit-RRL sample with metallicity higher than [Fe/H] ≈ -1.4, and that display low Si abundances when compared to RRLs in the TW-RRL sample in the same metallicity range (Figure 9.9). All these

stars come from S17. The same is the case for the three RRLs in the Lit-RRL sample with the lowest Si abundances. For the TW-HB sample, we averaged SiII and SiII lines as they displayed similar values. Two stars in this sample have higher values of SiII, namely HIP 99789 and HIP 106775. These two of the coldest HB stars in our sample, with $T_{eff} \approx 5300$ K. However, a third HB star, HIP 75823, is in the same temperature range has SiI and SiII in good agreement.

The trend set by the measurements from S17 appears in agreement with that set by the HB stars from F10. In order to understand this situation better, it is necessary to bear in mind that both S17 in all their RRLs and F10 in their *blue* HB stars (larger squares in Figure 9.9) effectively measured only the SiI line at 3,905.5 Å in most spectra. This is a line we removed from our line list precisely because it was saturated in most RRLs, being thus unusable, or resulted in a systematically lower abundance when not saturated. The authors in S17 underline that their SiI abundances should be taken with caution as this line is known to be unreliable. Regarding the *red* HB stars in F10 (smaller squares in Figure 9.9), several lines were used, and therefore the reason for the systematically lower Si abundances is not as obvious.

Several lines of this species are known to be affected by NLTE effects driven by effective temperature. F11 identified significant changes across the pulsation cycle in the abundances given by both SiI and SiII lines. However, the application of NLTE corrections did not solve the incongruent results. This phase-dependent behavior was not observed by Liu et al. (2013). We verified whether NLTE corrections were available for the Si lines using the MPIA NLTE Spectrum Tools[1]. The two SiII lines and one SiI line were not available in the tool. Of the remaining ones, none required corrections larger than uncertainties except for the SiI line at 5,948 Å for intermediate effective temperatures and intermediate metallicities (T_{eff}=6,500 K, [Fe/H] from -2 to -1 dex). However, this SiI line is in agreement with other lines in our spectra, including lines that are present in the MPIA NLTE Spectrum Tools and are marked there as requiring NLTE corrections. Thus, the suggested NLTE corrections for this line are unecessary in this study, and would not change the trend in Si.

The investigation performed in F10 is the non-variable counterpart to F11, and both studies used the same spectrograph and line list. As mentioned above, we did not detect a shift in metallicity or any Si abundances considering the stars in common in the TW-RRL sample and F11. In order to make sure the situation was the same for the non-variable HB stars in F10, which compose the Lit-HB sample, we applied our Si line list to a sample of five UVES spectra available for stars in F10[2], while keeping the atmospheric parameters they derived (i.e. relying on the shared iron abundance scale). We did not detect a systematic shift between our results and those of F10. This means that our Si scale is indeed the same as that of F10. Therefore, the difference between Si

[1]Available at http://nlte.mpia.de/

[2]Stars: HIP 4960, HIP 71087, HIP 80822, HIP 85487, HIP 96248.

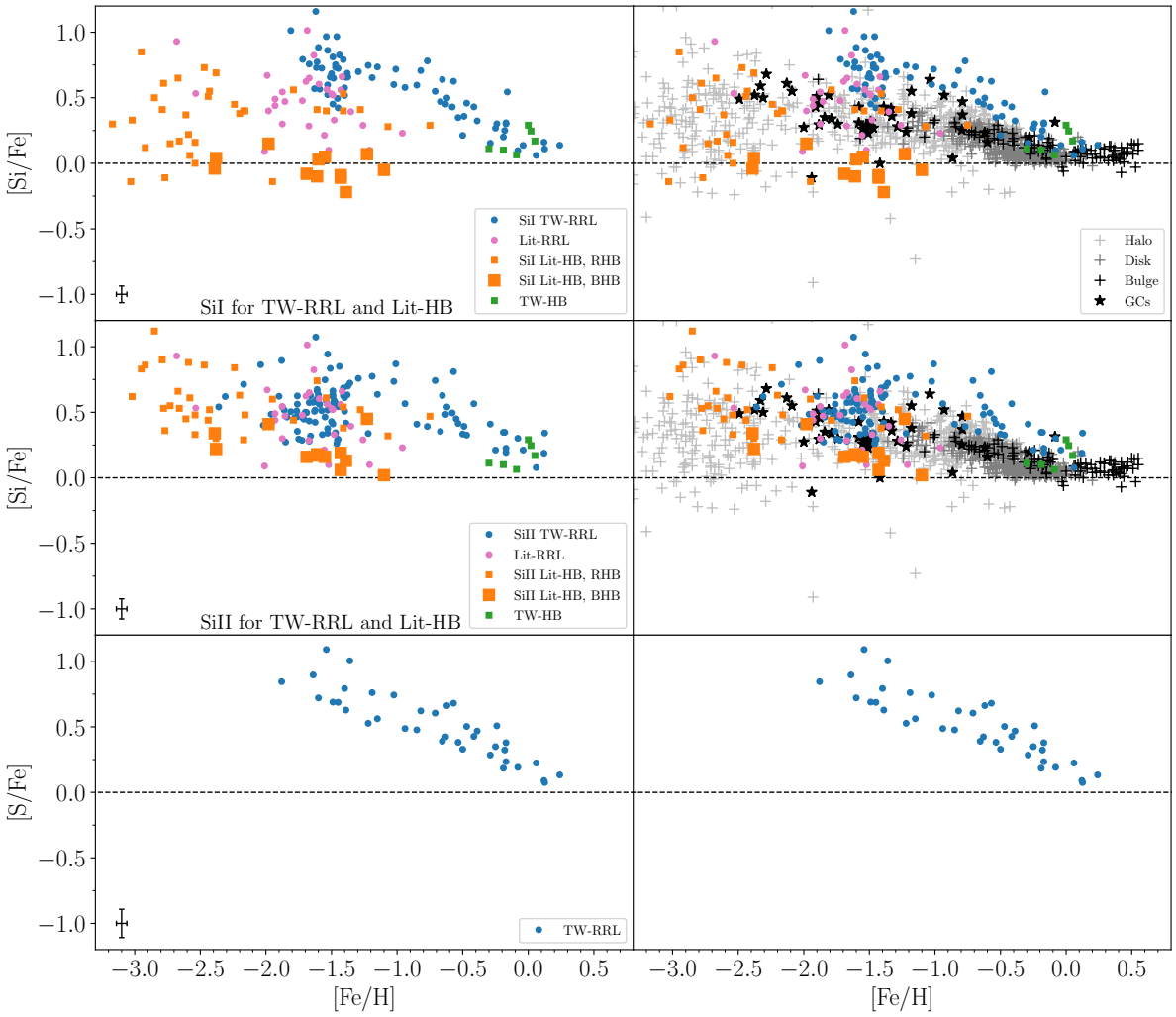

Figure 9.9: The same as Figure 9.6, but for the α elements Si and S. In the first row and second rows the values for the uncertainty and abundances for the TW-RRL and Lit-HB refer to measurements coming from SiI and SiII lines, respectively, according to the legend. For the remaining samples, Si was computed from eithe

abundances in the TW-RRL and Lit-HB samples is not due to line list differences.

The situation is the same for the scale of Nissen & Schuster (2010), included in the Halo field sample in the left panels of Figure 9.9. We obtained a high SNR spectrum from the ESO Archive for the Halo field dwarf HD 103723 included in their sample. This star was found by them to have a metallicity of -0.80 dex, putting it right in the region where the TW-RRL sample displays Si abundances about 0.6 dex higher than the literature, including Nissen & Schuster (2010). We analysed HD 103723 with the exact same methodology we used for the TW-RRL sample, and recovered virtually the same metallicity and Si abundance computed by Nissen & Schuster (2010), with [Fe/H] = -0.83, [SiI/Fe] = 0.14, and [SiII/Fe] = 0.25. As with the RRLs we analysed, the different SiI and SiI lines give very similar abundances in HD 103723, reinforcing that this is not an NLTE effect, as it affects Si abundances computed from a variety of transitions.

Thus, a line list difference can explain the shift between the Si abundances in S17 and the blue HB stars of F10, and the the Si abundances in the TW-RRL sample, but the same cannot be said for the values coming from the red HB stars in F10, or the field dwarfs of Nissen & Schuster (2010). All these tests point to a strong dependence of the derived Si abundance on an intrinsic atmospheric parameter, a dependence that affects several if not all SiI transitions and maybe SiII transitions as well. As mentioned above, we removed all Si lines that showed a T_{eff} dependence. In Figure 9.10, we show [Si/Fe] abundances from all individual line measurements versus log(g) for all individual spectra in the TW-RRL sample. The grey squares are the Si measurements from all lines for the Lit-HB sample, with the red HB stars shown as smaller squares, and the blue HB stars as larger squares. It is clear in the left panel that the SiI lines do show a strong trend with log(g), with the exception of the SiI line at 5,665.5 Å which may also have a dependence that we were unable to detect because it was only measurable at higher values of log(g). It is noteworthy that the spread in SiI is significantly smaller. The trend may also be present in SiII lines, but the large spread hinders any conclusion. Here, we underline once more that the log(g) measurements in RRLs, derived via the HR spectroscopic analysis employed throughout this work, do not reflect only the surface gravity of the star, but rather an effective gravity that contains both the gravitational term and a kinematic term due to the radial displacement of the stellar envelope.

F11 provided SiI and SiII measurements across the pulsation phase, but unfortunately they are not separated by individual lines. As of the writing of this thesis, our group is collecting a series of spectra for bright RRLs with the aim of covering a singificant part of the pulsation cycle for each star. These data can be used to investigate the behavior of individual SiI and SiII lines with phase and all atmospheric parameters, with the added constraint of having several observations of the same star and the guarantee of the same Si abundance. Analysing these spectra is the next step in trying to solve the Si puzzle for RRLs.

It is worth noting that the lack of homogeneous, recent laboratory measurements of Si transitions also hinders comparisons with the literature. The situation is made worse

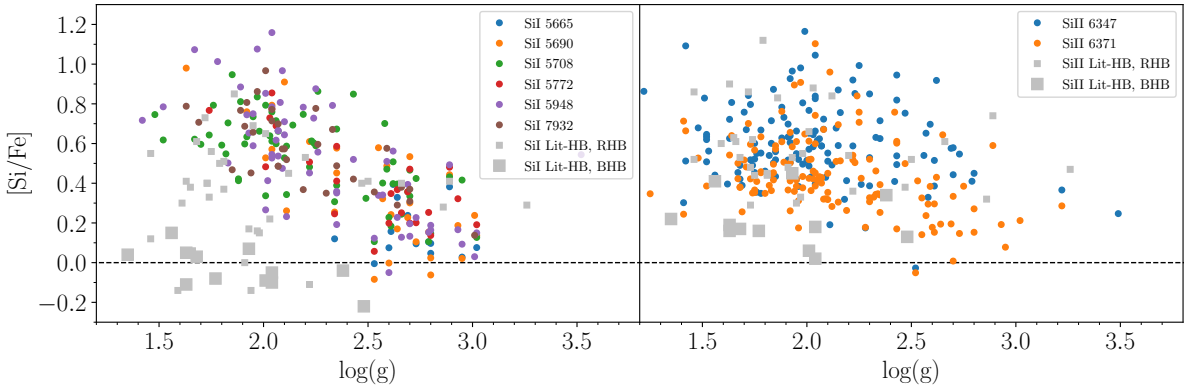

Figure 9.10: The trend of abundance versus log(g) for SiI (left panel) and SiII (right panel). For the TW-RRL, we show measurements coming from individual lines, with markers colored according to the legend) in individual spectra. For the Lit-HB sample, we show the average [SiI/Fe] and [SiII/Fe] per star, with the red HB stars shown as smaller grey squares, and the blue HB stars as larger grey squares.

because literature works often do not include a line list at all, and thus any information regarding their scale is lost unless stars in common are analyzed in order to measure scale shifts. We verified that the study of Bulge field stars performed by Bensby et al. (2017) employed 32 SiI transitions. Only 5 of them are in common with our line list, and all of them have log(gf) values exactly 0.1 dex lower than the ones we adopted. Reddy et al. (2003) and Reddy et al. (2006) employed Disk stars and used a variety of SiI lines of which only one is in common with our list, but with log(gf) 0.12 dex lower. They also used one SiII line, with the same transition parameters we used. Stephens & Boesgaard (2002) investigated Halo stars using only one SiII line which we used too but their log(gf) is 0.17 dex higher, while two of their three SiI lines are identical to ours. Frebel (2010) is a compilation of literature results for Halo field stars, and thus does not include a line list at all. Since the surface gravity is an important concern in Si abundances, we also checked the literature GC values we adopted, as they are likely to come from RGBs. The main source of GC abundances we used was the homogenized compilation by Pritzl et al. (2005), which takes several values from literature and corrects for their log(gf) differences using as default 11 SiI lines, of which 3 are identical to ours. We also adopted GC measurements for NGC 6273 which were performed by Johnson et al. (2017) by measuring three RGB stars in NGC 6273, all of which are in the lower Si trend. They employed no lines in common with us.

Interestingly, the trend in SiI and SiII for metallicities higher than approximately -1.4 dex is shared by S. Unfortunately, measurements of the latter are scarse in the literature. The metal-rich, α-poor population of RRLs detected in Mg, Ca, and Ti is not present for either Si or S. However, it may be the case that the abundances for both these elements

require a zero-point shift to higher values.

9.5 Light odd-Z element abundances

Most discussions of light odd-Z elements in the literature are done in the context of GCs. As discussed in Chapter 4.3.1, it is difficult to compare different literature investigations of Na and in particular Al because the usage of NLTE corrections and the metallicity coverage vary widely from study to study. As with most chemical species that require NLTE corrections, grids are only available for a limited range of atmospheric parameters and a small number of atomic transitions.

The Na lines we adopted do not show a dependence with T_{eff} or log(g), and are in agreement with one another both in a single star and in the general trend in the [X/Fe] versus [Fe/H] plane. None of the lines covers the entire metallicity range of our sample, but their metallicity regimes do overlap. The the metal-poor to -intermediate regime is traced by the lines at 5890.0, 5895.9, and 8283.3 Å, while the metal-intermediate to -rich regime is covered by the lines at 5862.6 and 6160.8 Å. The line at 6154.2 Å is measurable only in metal-rich stars. The Lind et al. (2011) corrections include only the lines 5895.9 and 8183.3 Å for [Fe/H] = -3 and -2, and line 6154.2 Å for [Fe/H] = -1 and 0 dex. For our T_{eff} and log(g) range, the corrections are well within uncertainties as corrections for hot giants are in general vanishing. The only line with significant corrections is 5895.9 Å for [Fe/H] = -2, with corrections of the order of -0.2 to -0.3 dex, but only in the cases where log(g) is larger than 2. Such a large value of surface gravity can appear in atmospheric models of RRLs, although the value reflects an effective gravity that includes a kinematic term and does not reflect gravitational acceleration alone. We opted not to apply the corrections because they would cause negligible changes. It is worth noticing that several temperature ranges require corrections of -0.2 or more for dwarfs, so the spread detected in literature could possibly decrease if NLTE corrections were applied.

For Al, the adopted lines at 3944.0 and 3961.5 Å appear in the whole T_{eff} and log(g) range and do now show any trend. The other lines (6696.0, 7836.1, and 8772.9 Å) have few measurements, all within a limited range of T_{eff} and log(g), and so it is impossible to determine whether there is a trend with T_{eff}. The lines at 3944.0 and 3961.5 cover the metal-poor regime up to -0.5 dex. Above this metallicity, only the lines at 6696.0, 7836.1, and 8772.9 Å can be detected. It is not clear whether these two groups of lines are in agreement with each other due to their limited overlap.

The situation for NLTE corrections for Al is much more complicated due to an even smaller coverage of lines and atmopsheric parameters. We mention that the NLTE corrections computed by Gehren et al. (2004) for a sample of dwarfs with 5700 K $< T_{eff} <$ 6300 K and -2.5 $<$ [Fe/H] $<$ -1.5 increase Al abundances by approximately 0.4 dex, while for higher metallicities the increase is of the order of 0.1 dex. Meanwhile, Andrievsky et al. (2008) analysed only metal-poor stars, and identified corrections as high as 0.9 dex

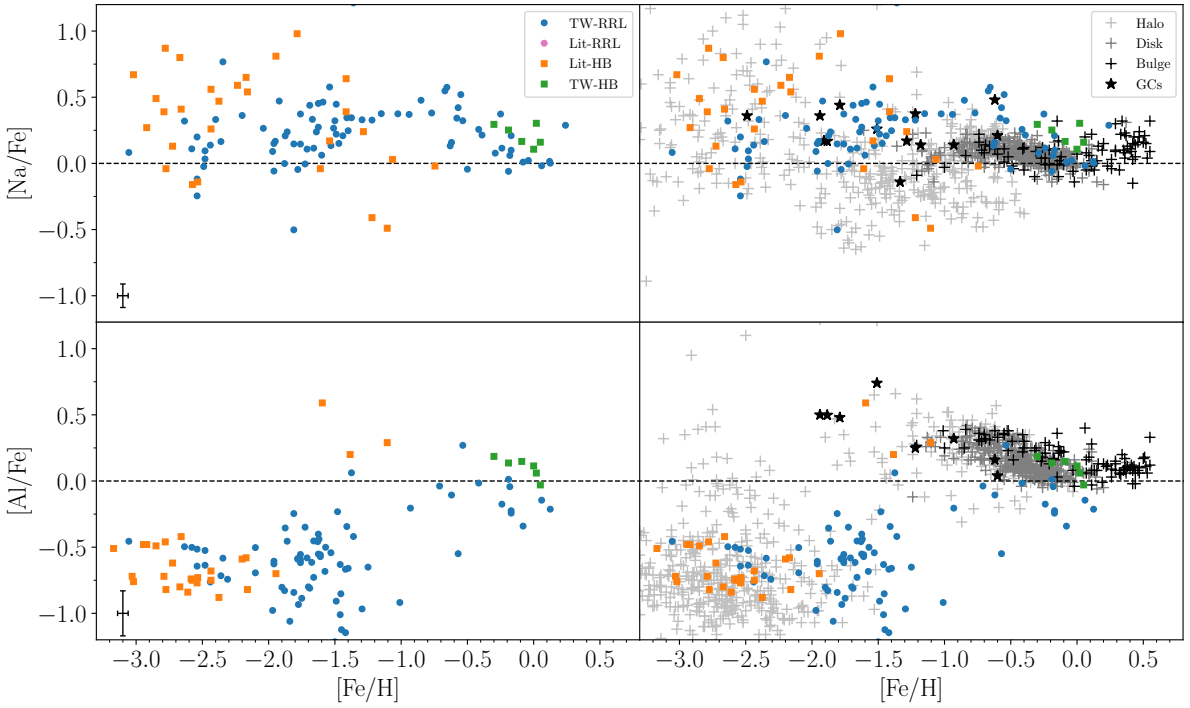

Figure 9.11: Same as Figure 9.6 but for the light odd-Z elements.

upwards, depending on atmospheric parameters including metallicity. Their corrections were computed for temperatures as high as 5200 K for giants, thus being inadequate for RRLs and HB stars. Furthermore, the authors advise against simply adopting the corrections without specific line profile computations. Thus, we opted to present the LTE values and wait until a more homogeneous NLTE grid becomes available.

The results of the present work regarding the odd-Z elements is shown in Figure 9.11, including the troublesome Al for completeness. We also include a comparison with exclusively LTE literature values in Figure 9.12. The blue HB stars in the Lit-HB sample had their abundances corrected for NLTE effects by F10. They adopted a rigid shift for all three stars. The black arrow in Figure 9.12 indicates their LTE abundances.

9.6 Fe-peak element abundances

Literature comparisons of Fe-peak elements are, like the odd-Z elements, hindered by largely inhomogeneous treatment of NLTE effects. Moreover, many widely used transitions present HFS and different investigations may use different computations of line splitting, or ignore it altogether. In the present work, we employed a line list with HFS for all lines where it exists. Like for the species studied in the previous chapters, how-

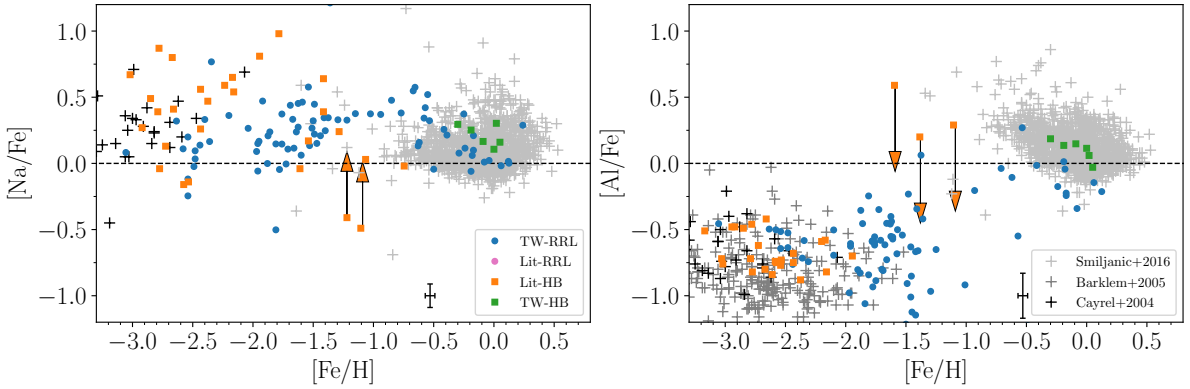

Figure 9.12: Same as the left panels of Figure 9.11 but only considering the LTE results from Cayrel et al. (2004); Barklem et al. (2005); Smiljanic et al. (2016) for the literature comparison. See the legend and TW-RRL error bars on the lower right corner of each panel.

ever, we opted to keep an exclusively LTE abundance analysis due to the current poor coverage of NTLE correction grids for hot giants across a wide metallicity range. The effect of both HFS and NLTE corrections to individual transitions is varied and can be altogether vanishing. As with most atomic transitions considered in this work, we eliminated any lines that provided systematically spurious results, showed a trend with T_{eff} or log(g), or were only detectable in a small number of stars. We show the results for all Fe-peak elements measured in the TW-RRL sample in Figures 9.13 and 9.14.

Sc – The Sc depletion in metal-rich RRLs is at odds with field measurements (Figure 9.13). It was already detected by Clementini et al. (1995); Liu et al. (2013); Chadid et al. (2017), but no explanation was offered except the possibility of measurement errors according to C17. The first question that comes to mind is whether the Halo also contains a metal-rich, Sc-poor population, but the scarcity of metal-rich stars in this Galactic component does not allow for a conclusion. The Bulge and Disk field stars show an enhancement of the order of 0.5 dex when compared to the RRLs at the same metallicity. We note that [Sc/Fe] displays a flat trend with [Ti/Fe], but with values approximately -0.2 dex lower. This supports that Sc has an α-like behavior and, as shown in Chapter 9.3, the metal-rich RRLs are depleted in α elements. Nearby dwarf galaxies also show a depletion in Sc with increasing metallicity that creates a "knee", like for the α elements, at different metallicities. Indeed, the depletion in Sc of the RRLs, like that of α-elements, is similar to that of the Sgr dSph (Figure 9.15).

Cr – According to the MPIA NLTE Spectrum Tools, all adopted CrI lines require NLTE corrections from 0.3 to 1.0 dex for the range of atmospheric parameters covered by the TW-RRL sample while CrII lines are not available. There is a significant line-by-line scatter for the LTE results for the same ionization stage. Considering together lines of both CrI and CrII does not increase the spread. The purely LTE results in Figure 9.13

appear in general good agreement with field stars except for the metal-poor tail, but it bears noting once more that the literature values are a mixture of LTE and NLTE results. A shift as large as 0.3 – 1.0 dex would introduce a dramatic disagreement with the presented field results, but, due to the completeness of the corrections grid of the MPIA NLTE Spectrum Tools, it may be worth it to investigate CrI further alongside a sample of NLTE results for field stars. In particular, the disagreement in the metal-poor tail may be solved with an NLTE approach.

Mn – The application of NLTE corrections to Mn abundances is also necessary, as they introduce significant changes to the trend in the [Mn/Fe] versus [Fe/H] plane but the currently available grids are still in disagreement with nucleosynthetic models (Chapter 4.3.3). The grid developed by Bergemann & Gehren (2008) and further refined in Bergemann et al. (2019) is very promising due to the wide range of atmospheric parameters considered. The former is already available at at the MPIA NLTE Spectrum Tools. As the latter is implemented as well, a NLTE investigation of Mn of RRLs will be invaluable as they can offer excellent constrains for nucleosynthetic models. Moreover, the corrections may solve the disagreement in the metal-intermediate regime between the RRLs and other field stars (bottom panels of Figure 9.13).

Cu – The measurements of Cu are very scarce in the literature other than in the metal-rich regime, where the few, weak Cu transitions can be detected. Interestingly, the metal-rich RRLs also display two of these transitions, despite their high effective temperatures. The Zn measurements in RRLs offer preliminary evidence of a depletion in this element that is not detected in the Bulge and Halo. Whether this decrease is followed by the Halo is again unclear due to the scarcity of metal-rich Halo field stars. The RRLs may be the only metal-rich tracer of this Galactic component and, interestingly, they show disagreement with the Sgr dSph for all Fe-peak elements except for Sc, V, Cr, and Co. The latter element should be taken with caution due to the large effect of NLTE effects as mentioned above. Moreover, it is important to keep in mind that chemical abundances for extragalactic stars, including in nearby dwarf galaxies, are most often derived from medium resolution and low SNR spectra. A dedicated HR, high SNR study of at least a few metal-rich stars in the Sgr dSph would be invaluable for comparisons with Galactic RRLs.

V, Co, Ni, and Zn – The remaining elements do not show marked differences with other field populations. Unfortunatley, we found that only one Co line, out of the 19 we considered, was visible for a significant number of stars. The metal-poor, Ni-rich stars coming from the Lit-RRL and Lit-HB samples in Figure 9.14 have values from F10 and F11. The authors of those works warn that these Ni abundances are to be taken with caution due to the poor quality of the measurable lines.

Comparisons with other samples – The difficulty in obtaining homogeneous literature results for the Fe-peak elements means that comparisons are limited. For this reason, we opted to analyse seven field Halo dwarfs studied by Nissen & Schuster (2010, 2011) and include them in the TW-Dwarfs sample, shown as red triangles in Figures 9.13 to 9.15.

The results from these dwarfs help clarify whether systematics connected to surface gravity are significant. Those two studies included the Fe-peak elements Cr, Mn, Ni, Cu, and Zn. We found no significant zero-point shift between our abundances and theirs, except for [Fe/H] with our results being 0.15 dex lower than theirs.

Moreover, the fact that both the TW-HB and TW-Dwarfs samples display a flat trend in the [Sc/Fe] versus [Fe/H] plot reinforces that there is a real difference in Sc abundances between the RRLs and other field stars that is not caused, at least not completely, by line list differences or surface gravity effects. Indeed, the TW-Dwarfs were specifically chosen among the hottest stars in the Nissen & Schuster (2010) sample, with T_{eff} between 5840 and 6220 K in our analysis. Thus, the temperature regime of these dwarfs is similar to that of the RRLs and HB stars.

9.7 n-capture element abundances

Literature comparisons involving n-capture abundances suffer from the same issues as those involving Fe-peak elements, with the added complication of an even greater scarcity of measurements and of grids of NLTE corrections. In our sample, we were able to secure measurements for a variety of n-capture elements, including the elements of the first (Sr, Y, Zr) and second peak (Ba, La, Ce, Pr, Nd, Eu). Of particular interest are the the s-process tracer Ba, the r-process tracer Eu, and the very scarcely measured rare earth element Pr. For this latter, it is important to mention that we employed the line list of Sneden et al. (2009) as they performed a very careful investigation of Pr. Unfortunately, we found out that one of the strongest lines they used, at 5179.4 Å, is a severely blended line that should not be used at all (Christopher Sneden, private communication).

The [X/Fe] versus [Fe/H] plane for the first n-capture peak elements is shown in Figure 9.16. It is clear that the large spread in Sr abundances seen in the literature is present in the RRL and HB samples as well, at least for the metal-poor and metal-intermediate regimes (Figure 9.16). All the measurements in the TW-RRL, TW-HB, and TW-Dwarfs samples come from SrII lines, except for one RRL where only SrI lines were avaible, and two others that displayed both SrI and SrII transitions in good agreement with one another. As discussed in Chapter 4.3.4, SrII lines are very robust against NLTE effects. Considering also that the RRLs have cover a narrow age range, the spread in this element appears to be intrinsic.

First peak – Both Zr and Y show a depletion in metal-rich RRLs when compared to other field stars in the same metallicity regime. The depletion in Y is very marked and not followed either by the TW-HB nor the TW-Dwarfs samples (green squares and red triangles, respectively, in Figure 9.16). As mentioned in the previous chapter, the metallicities we derived for the TW-Dwarfs sample are on average 0.15 dex lower than in Nissen & Schuster (2011), considering 7 stars in common. The Y abundances, however, are identical within errors. Thus, the trend in Y set by the RRLs is indeed diverse

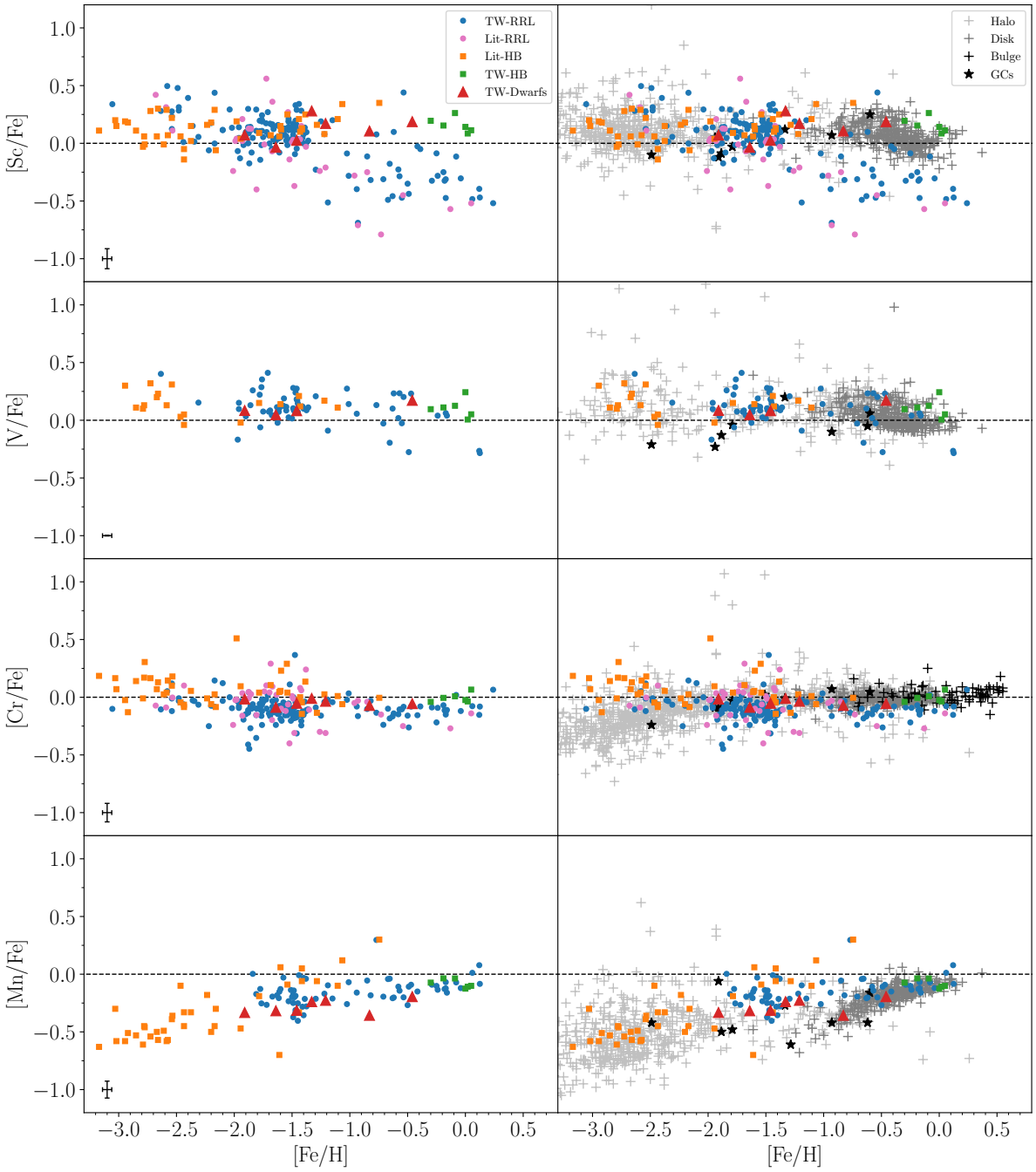

Figure 9.13: Same as Figure 9.6 but for the Fe-peak elements Sc to Mn.

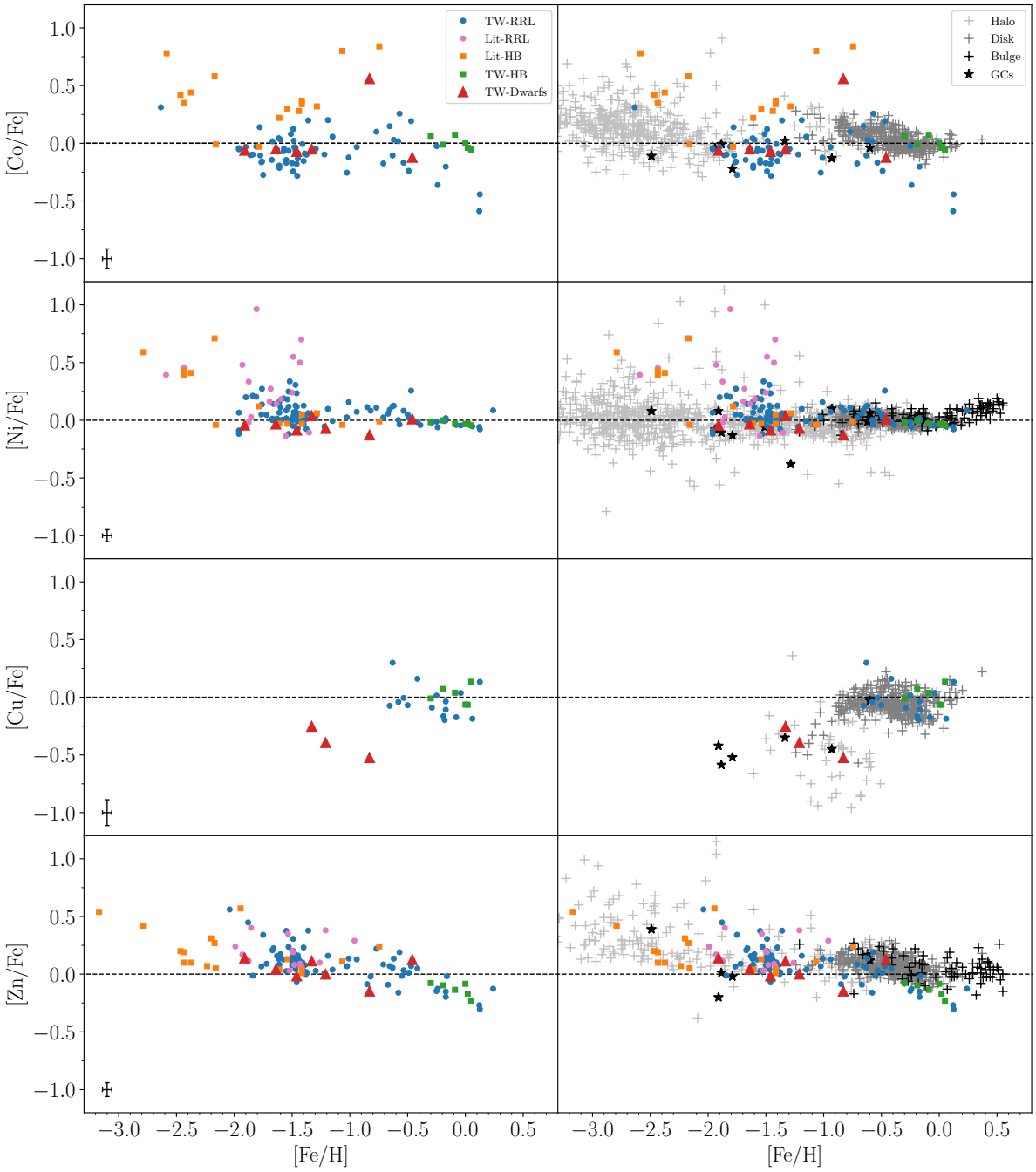

Figure 9.14: Same as Figure 9.6 but for the Fe-peak elements Co to Zn.

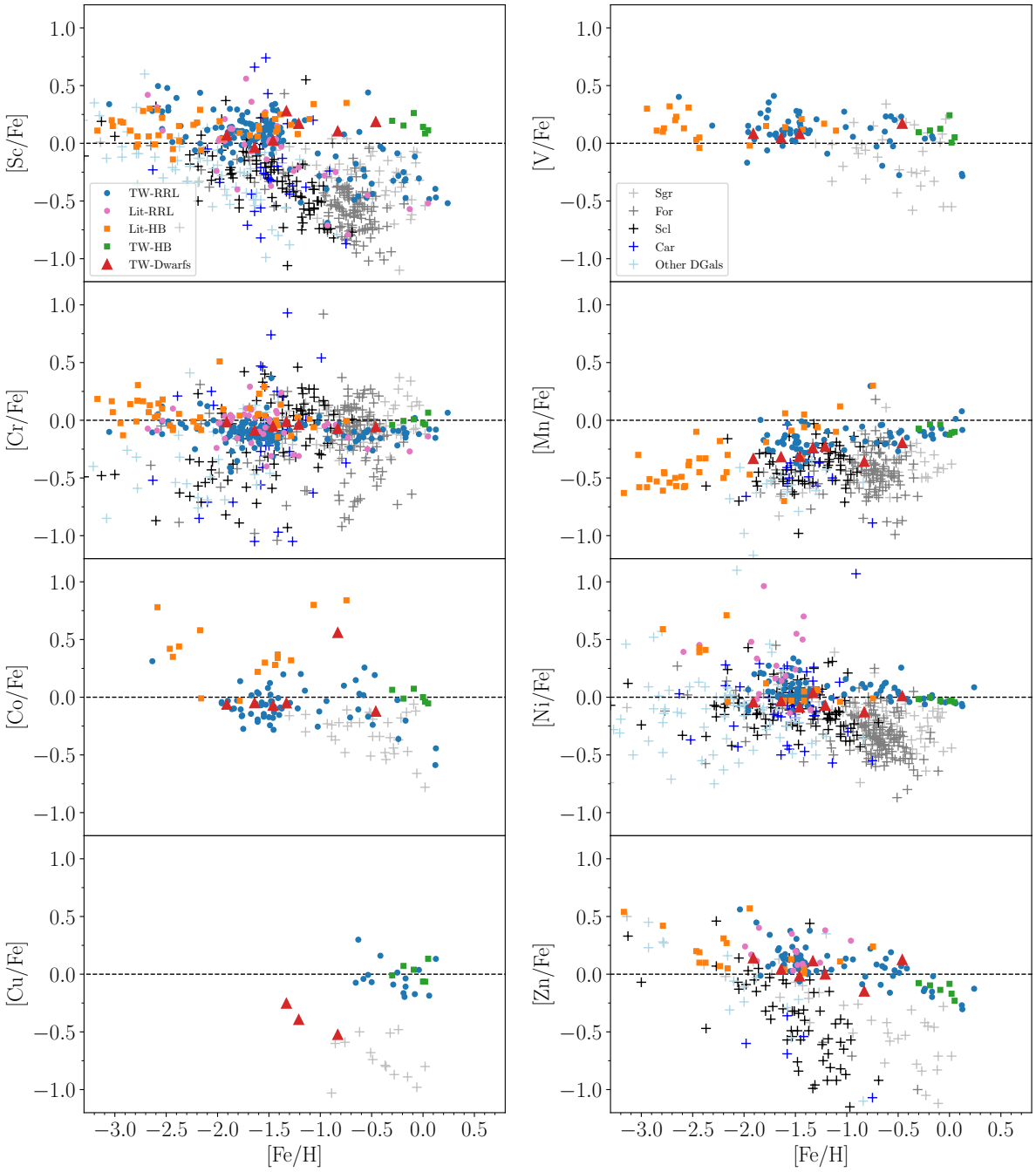

Figure 9.15: Same as Figure 9.7 but for the Fe-peak elements.

from that of other field stars, including the TW-HB and TW-Dwarfs samples, and not a surface gravity nor effective temperature effect. Indeed, the T_{eff} range of the three samples is similar, therefore discarding the possibility of a temperature bias, while the log(g) values from the RRLs and HBs are similar and much lower than that of the dwarfs. For Zr, the depletion in the metal-rich RRLs is not as clear, but it is noteworthy that the literature field stars occupy a very wide range of Zr abundances, while the RRLs remain at the lower envelope of their trend. Furthermore, the TW-HB and TW-Dwarfs, with higher Zr abundances in the metal-rich regime, once more reinforce this peculiarity of the metal-rich RRLs.

Second peak – The peculiar behavior of the metal-rich RRLs extends into the second n-capture peak elements in Figure 9.17. The scatter in Ba abundances is notoriously large, but a lack of Ba-rich metal-rich RRLs is noticeable. The Ba abundances of the TW-Dwarfs sample are on average 0.33 dex higher than in Nissen & Schuster (2011), but even when considering just the values determined in this work, the lower abundances of the RRLs remain. The situation for La and Ce is less clear, but it looks like that, for both of them, the abundances of metal-rich RRLs remain at the lower envelope of the other field stars.

Third peak – The remaining elements of the second n-capture peak are shown in Figure 9.18. The lack of literature measurements of Pr make comparisons difficult, but our measurements are presented as one step towards more data for this element. The 18 stars in which we detected Pr lines make up a flat trend with metallicity. This is not altogether surprising as Pr is believed to be produced by both s-process and r-process in equal parts. Nd is believed to be 58% produced via the s-process (Chapter 4.3.4), but the strong downwards trend with metallicity in field stars, and the modest one set by our samples, point out that a higher rate of production through the r-process is likely. Indeed, the [X/Fe] versus [Fe/H] trend for Nd is nearly identical to that of Eu, the r-process tracer per excellence, shown in the same figure. For these three last n-capture elements, the RRLs do not display a marked difference when compared to the other stars.

Comparison with dwarf galaxies – In Figure 9.19, we show a comparison with nearby dwarf galaxies. For the elements for which data is available, the RRLs show a good agreement with the populations of these satellites. Interestingly, the latter also display the marked depletion in Y found in the RRLs. However, it bears mentioning once more that the quality of chemical abundance measurements for extragalactic populations is limited by both lower resolution and lower SNR.

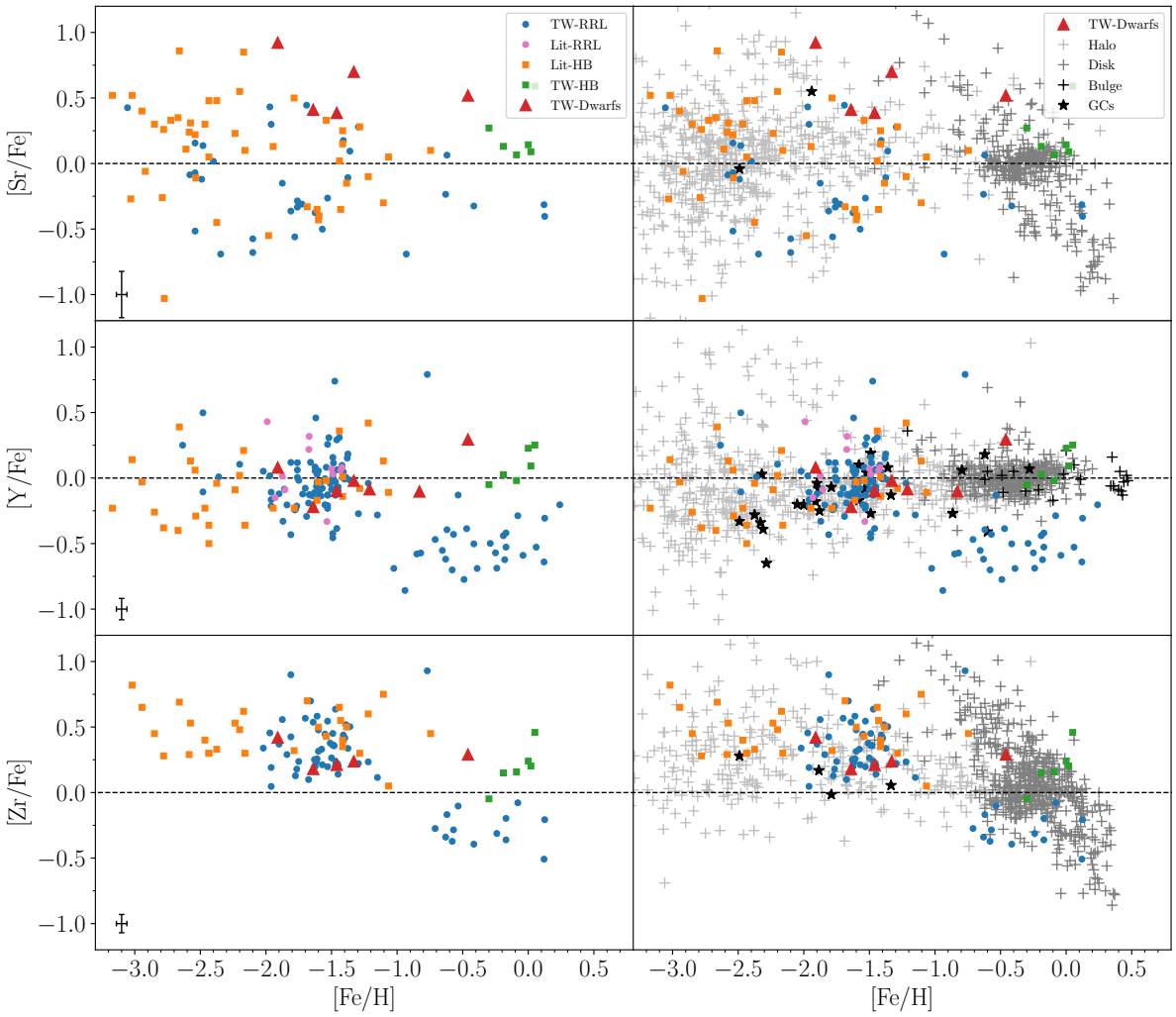

Figure 9.16: Same as Figure 9.6 but for the n-capture elements Sr, Y, and Zr.

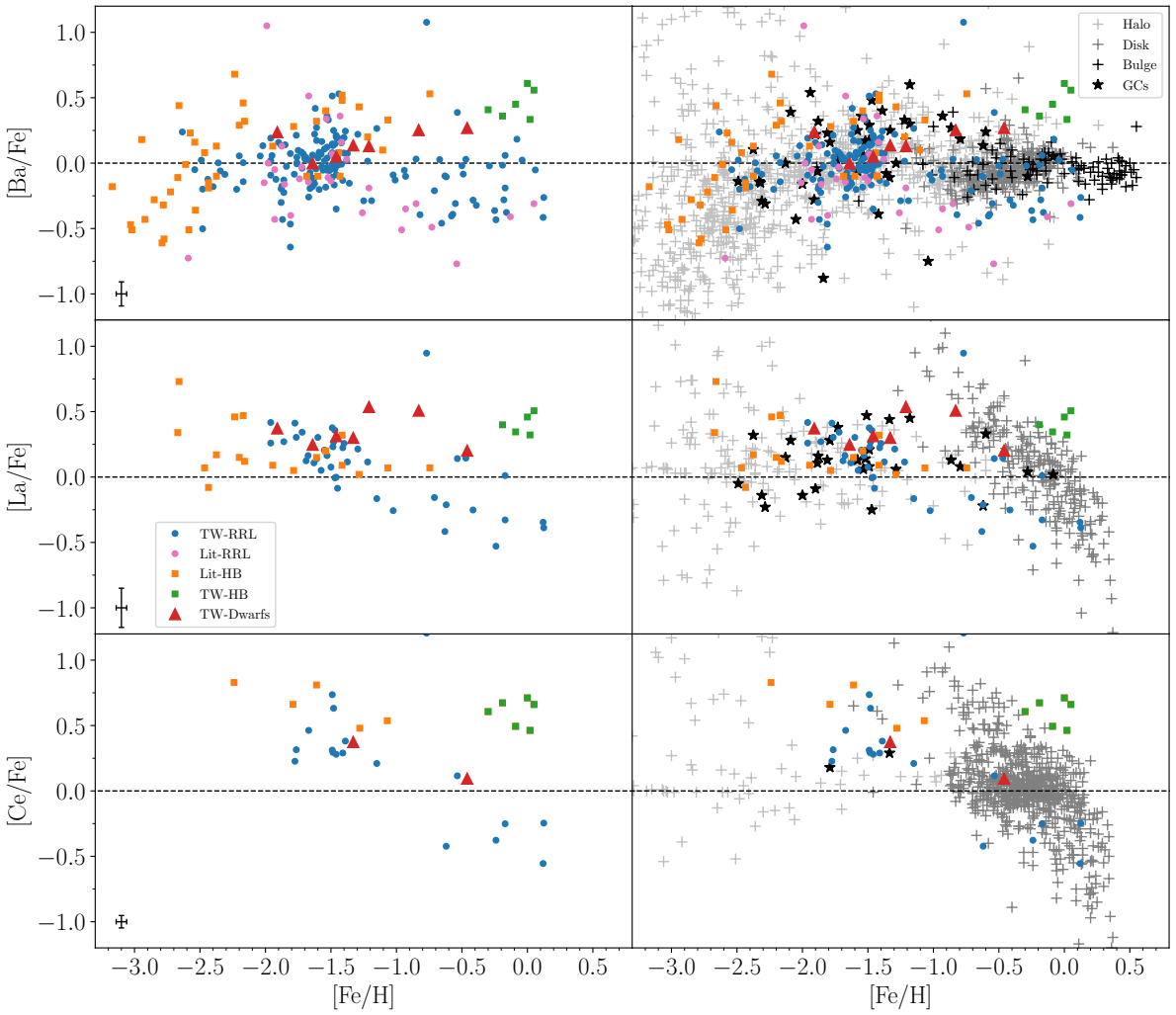

Figure 9.17: Same as Figure 9.6 but for the n-capture elements Ba, La, and Ce. Note that the Ce measurements for the Lit-HB sample were made in this work (see Chapter 5.3 for details).

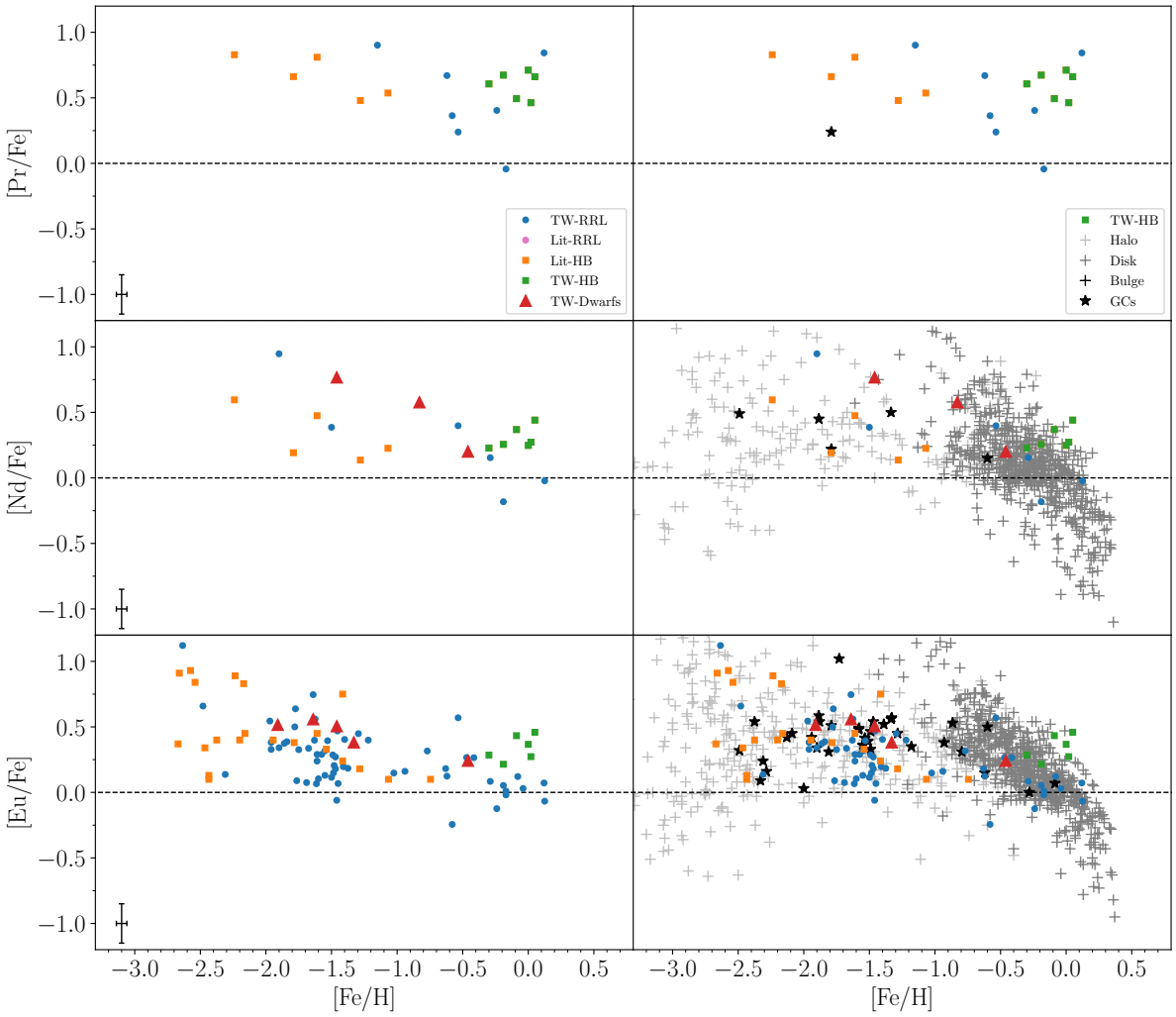

Figure 9.18: Same as Figure 9.6 but for the n-capture elements Pr, Nd, and Eu. Note that the Nd and Pr measurements for the Lit-HB sample were made in this work (see Chapter 5.3 for details).

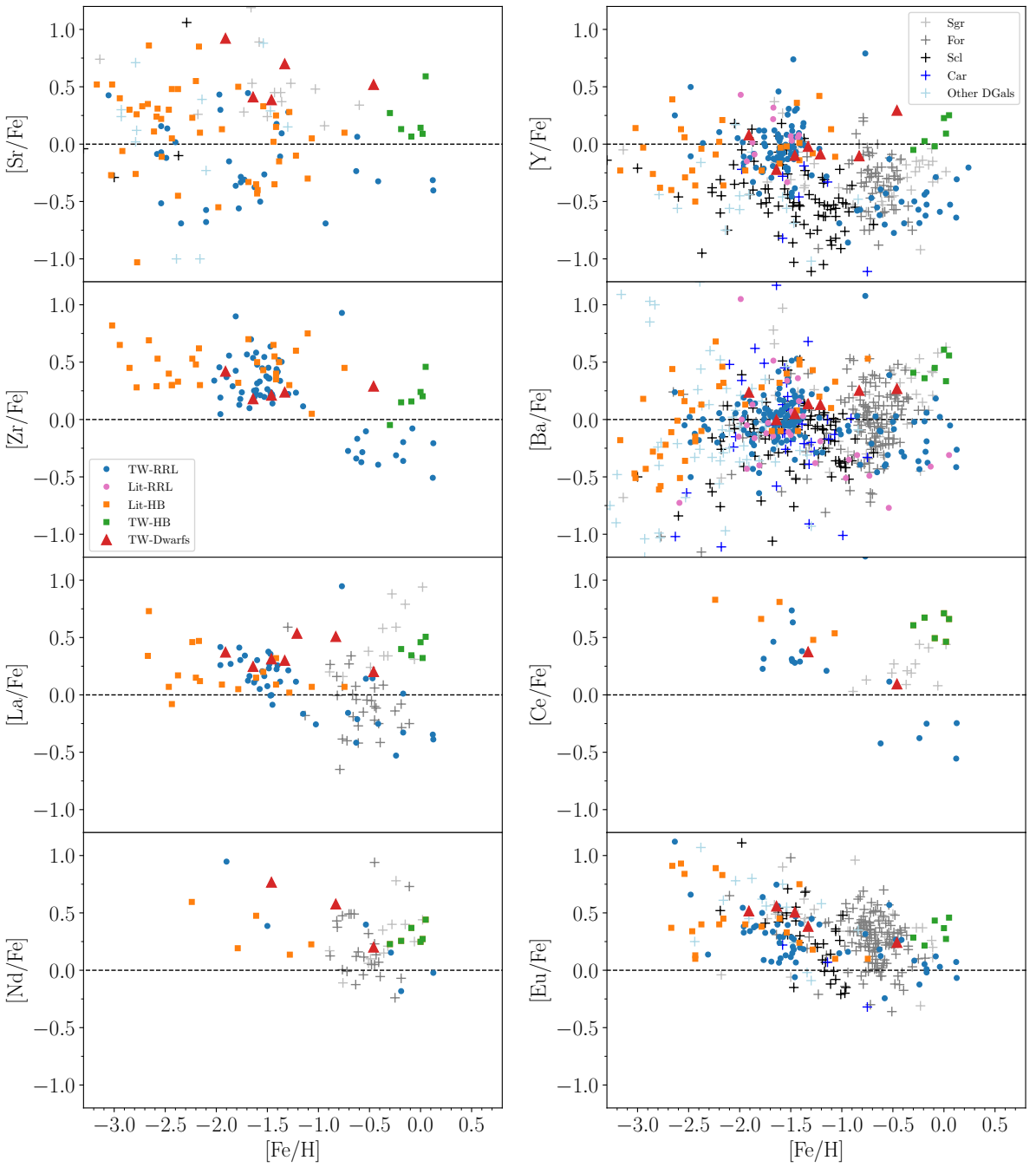

Figure 9.19: Same as Figure 9.7 but for the n-capture elements. Note that the Ce, Nd, and Pr measurements for the Lit-HB sample were made in this work (see Chapter 5.3 for details).

Chapter 10

Consequences of this work

The results of the present work were employed in a few other published investigations of interest to Galactic structure and formation. We will briefly discuss four of them below.

10.1 Unraveling the mystery of the Oosterhoff dichotomy

The Oosterhoff dichotomy has been of great interest to Galactic astrophysicists since it was first described by Oosterhoff (1939). The dichotomy comes from the observation that, in the Milky Way, metal-intermediate/rich GCs host an RRab population with a mean period $<P_{ab}> \approx 0.55$ d and a smaller number ratio of RRc variables ($N_c/N_{\rm total} \approx 0.29$), while in metal-poor GCs the mean period for the RRb population is $<P_{ab}> \approx 0.65$ d and the number ratio of RRc variables is larger ($N_c/N_{\rm total} \approx 0.44$, Braga et al., 2016). This divides the Galactic GCs into the Oosterhoff type I (OoI) and type II (OoII) for the metal-intermediate/rich and metal-poor GCs, respectively. In a period versus metallicity plane, the OoI and OoII groups are separated by a gap, called the Oosterhoff gap, that is not observed in nearby dwarf galaxies.

As explained in Chapter 3.5, a coupling between period and metallicity in the RRLs is expected in theoretical modeling. An increase in metal content causes a steady decrease in luminosity, an increase in average surface gravity and, consequently, an increase in average density as well. The pulsation period, in turn, scales with $\sqrt{1/\rho}$, where ρ is the density, which means that the pulsation period decreases. Therefore, the smaller average period of the metal-rich GCs is entirely expected and, indeed, so is the existence of metal-rich HASPs. The variation in the fraction of RRc variables with metallicity is also unsurprising. Indeed, as mentioned in Chapter 3.3, metallicity is one of the parameters that affects HB morphology, i.e. its color or temperature extension. At the same time, the position of an RRL in the instability strip is tightly related to its pulsation mode and period. Thus, a more metal-poor stellar population is expected to display a

more extended HB, reaching bluer colors and higher effective temperatures. This will naturally cause the bluer side of the instability strip to be more populated, increasing the number of RRc variables. This is observed in the Galactic GCs, i.e. GCs with redder HBs do display a smaller ratio of RRc variables. The oddity is, then, not in the RRLs themselves, but in the fact that Galactic GCs of similar metallicities can have different HB morphologies. This is the case of the metal-intermediate ([Fe/H] $\approx$ -0.9) clusters NGC 6723, NGC 6652, and Palomar 13. The first displays an extended HB, while both NGC 6652 and Palomar 12 have predominantly red HBs. This is the so-called second parameter problem (e.g. Crestani et al., 2019, and references therein).

There is no clear evolutionary reason for the pulsation periods of RRLs and the number ratio of RRc variables to have dichotomic distributions with metallicity. However, it is well known that GCs have a bimodal distribution with metallicity in the Galaxy, with a marked lack of RRLs in metal-intermediate GCs. This suggests that the Oosterhoff dichotomy arises purely from the uniqueness of the GC population in the Milky Way. In order to truly know whether that is the case, the field RRLs ought to be studied in detail as well. Furthermore, if a significant fraction of the Halo field population is built up from disrupted GCs, the field RRL would be similar to cluster RRLs. We already saw in Chapter 9.1 that the field RRLs display a metal-poor tail extending to $\approx$ -3 dex and no bimodality in metallicity, at odds with the GCs, but it is worth investigating their pulsational properties as well.

The investigation developed by Fabrizio et al. (2019) peered into the inner structure of the Bailey diagram using field RRab variables in order to better understand the Oosterhoff dichotomy, and we refer the reader to that paper for an in depth discussion and useful references. They employed a large sample of RRab with ΔS metallicities estimated using the Layden94 calibration. The results of the present work opened the door for the inclusion of first overtone variables, increasing the sample size while at the same time increasing the homogeneity of the measurements with the new ΔS calibration and the large sample of HR metallicities of the TW-RRL and TW-Lit samples. This allowed for new insights into and around the Oosterhoff dichotomy, which are discussed in detail by our group in Fabrizio et al. (2021b) and briefly commented below.

The Bailey diagrams, now color-coded by metallicity according to the color bar at its right edge, are shown in Figure 10.1. It is immediately noticeable in the HR results of the top panel that pulsational periods are strongly correlated with metallicity, with the RRab and RRc forming distinct groups. Inside each of these groups, higher metallicities are mostly segregated in the short period edge and, as the metallicity smoothly decreases, the period increases. The bottom panel includes the ΔS sample as well. The addition of the LR results increases noise, but the period-metallicity structure remains visible, in particular in the RRc region.

The peak of the RRab distribution happens at the short period region, while for the RRc it happens in the long period region (see Figure 5 in Fabrizio et al., 2021b). On a more quantitive basis, the ratio of short period variables is 80% for the RRab, while for

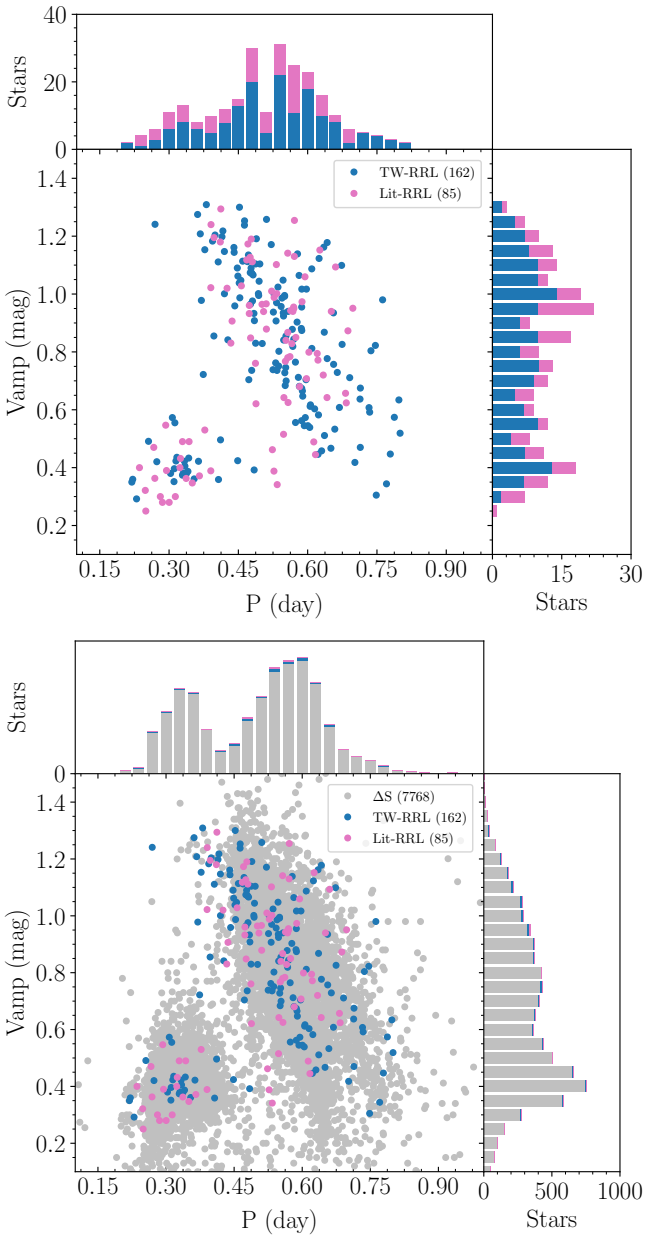

Figure 10.1: *Top:* Bailey diagram for the TW-RRL sample (blue), and the Lit-RRL sample (pink). The top and left histograms show the distribution of period and V-band amplitudes, respectively. *Bottom:* The same, but with the inclusion of the ΔS sample (grey).

the RRc it is 30%. As can be seen in the Bailey diagram (Figure 10.1), the field RRc show no detectable gap between short and long period variables, which is unsurprising due to the narrower range in period that first overtone pulsators can achieve stability. For the RRab the precision is not enough to detect a gap per se, but there is detectable variation of the slope of the density distribution in period and amplitude (see Figure 4 in Fabrizio et al., 2021b) which is expected by evolutionary properties. Indeed, in a Hertzprung-Russel diagram, the evolutionary path off the zero-age HB is very different for different metallicities (see the top panel of Figure 4 in Bono et al., 2020). The most metal-rich stars show a redward evolution, but as the metallicity increases, stars leave the zero-age HB through a series of redward and blueward evolutions. As the position inside the instability strip is tightly related to the pulsational period of the RRL, this means that a given RRL will undergo a series of small period changes and significant amplitude changes as it evolves, and that these changes are metallicity-dependent.

Thus, a decrease in the number of RRab variables at a certain region of the Bailey diagram can be accounted for due to evolutionary properties, and does not mean that the production of RRLs decreases at a given metallicity. This is strongly supported by the fact that both period and pulsational amplitude show a very tight and continuous variation with metallicity (Figure 10.2, see also Figure 8 in Fabrizio et al., 2021b), with the RRc showing a metallicity dependence almost a factor of two larger than the RRab. This smooth variation has very important consequences for Galactic and GC formation. Namely, if the pulsational properties of RRLs are so tightly connected to their metallicity, we can use the distribution of periods and amplitudes (quantities that are reddening-independent) of RRLs in a given stellar population to study its star formation history. Furthermore, if a given stellar population shows a lack of RRLs of a given period range, this means that star formation in that population was not constant across metallicity. Another important point to keep in mind when considering the Oosterhoff dichotomy is that the Oosterhoff gap, present in the Milky Way, is not observed in nearby dwarf galaxies including the Large Magellanic Cloud (Figure 3.12), supporting that the gap is related not to RRL evolution but rather cluster formation itself.

Moreover, the N_c/N_{total} versus [Fe/H] trend in field RRLs and that of Galactic GCs are markedly different (see Figure 12 in Fabrizio et al., 2021b). This evidence contradicts a scenario where the field Halo population has a significant fraction of stars from disrupted GCs. Another important result of this investigation is that the number ratio N_c/N_{total} for field RRLs has a complex behavior with metallicity. It shows a high ratio for metal-poor stars, as expected theoretically. The ratio decreases smoothly as metallicity increases (same figure). However, as the metallicity reaches [Fe/H] $\approx$ -1.0, the ratio begins increasing with metallicity. This behavior is surprising because simple arguments suggest that the number of RRc steady decreases as the metallicity increases due to changes in HB morphology, as mentioned above. Thus, a more elaborate theoretical investigation is necessary. Our group is currently investigating this result using synthetic HB models and predicted instability strips.

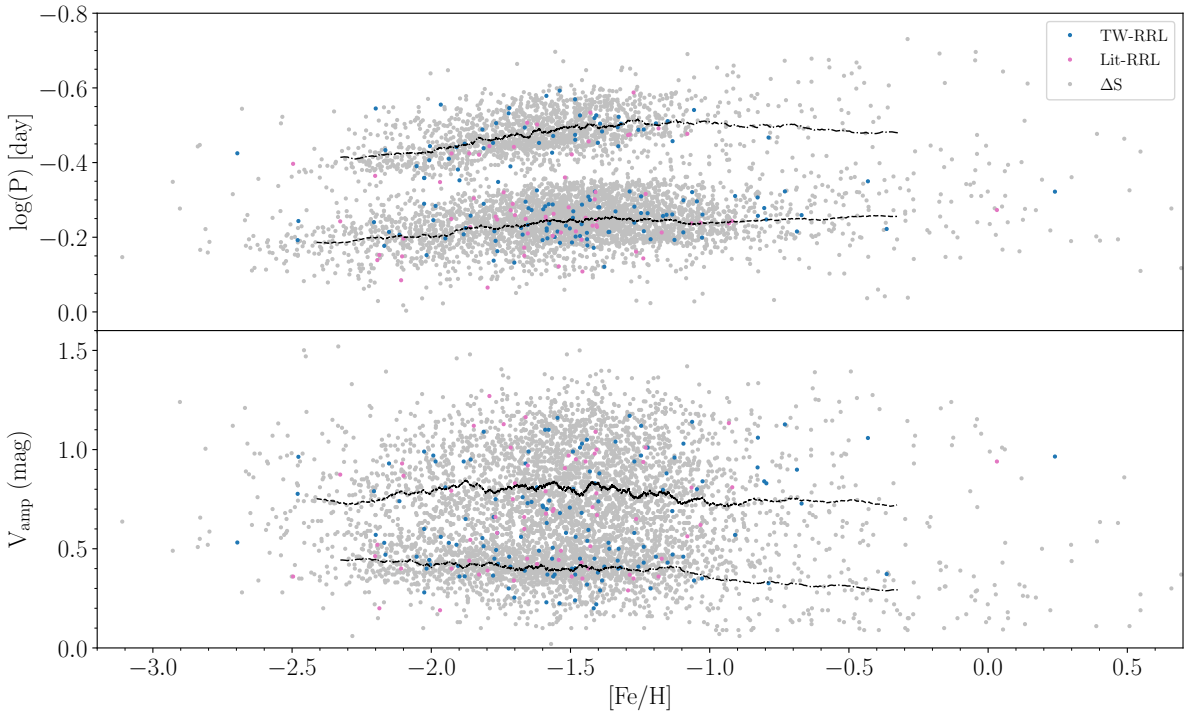

Figure 10.2: *Top:* Period versus metallicity for TW-RRL sample (blue), the Lit-RRL sample (pink), and the ΔS sample (grey). The dashed and dot dashed black lines show the running average for the RRab (long period) and the RRc (short period), respectively. *Bottom:* The same, but for V-band amplitude versus metallicity.

10.2 The shifting morphology of the Bailey diagram

We employed the same sample described in the present work two radial velocity studies. In the first, published in Braga et al. (2021b), we measured a variety of radial velocity tracers separately in each spectrum, such as various groups of metallic lines and Balmer lines. This was done because different lines are formed at different depths of the stellar atmosphere, with weaker lines tracing the inner layers of the envelope, while stronger lines tracing more superficial layers. As the RRLs are pulsating stars, each layer of the stellar atmosphere undergoes different motions. The study and selection of atomic lines to be used as tracers, and the preparation of the spectra to be used in the code for the measurement of Doppler shift velocities, were performed by the author of the present thesis. This investigation was aimed at developing radial velocity templates so that RRLs with few observations could have their barycentric velocity determined, which is essential for kinematic studies. Yet, several interesting results emerged from this analysis, such as the variety of secondary features in the light curve when different lines are used for velocity measurement. These fine details are lost when velocity tracers

are not separated by atmospheric layer. Studying these layers individually, then, offers valuable information regarding the pulsation mechanisms of RRLs.

With this in mind, we used the same results we derived for the velocity templates in order to develop a novel application of the Bailey diagram in Bono et al. (2020). The traditional Bailey diagram is a plane that shows pulsational periods and amplitudes, where the amplitudes refer to the light curve obtained for the photometric band in question. Light curves trace the change in radius and effective temperature across the pulsation cycle, with visual bands being particularly dependent on T_{eff}. Meanwhile, redder bands display a decreasing dependence on temperature and an increasing sensitivity to variations in radius. Velocities are intrinsically independent of T_{eff}, making velocity curves the ideal tracers of radial variations. Thus, we presented the Bailey diagram using amplitudes coming from different photometric bands, and also from different velocity indicators.

A main concern with the Bailey diagram is that the amplitude of light curves is strongly affected by Blazhko modulation and therefore, if a star is affected by this phenomenon, its position in the Bailey diagram changes. We found that this is not the case for velocity curves. Indeed, the variation in amplitude due to Blazhko effect in velocity curves is $\approx$20% for the RRab, while for light curves in visual bands it is twice as large. The sample of RRc variables was too small to draw firm conclusions in this regard, unfortunately. We also found that the amplitudes based on Balmer lines for RRab variables reach a plateau when moving from short to long period, i.e. from the hot to the cold edge of the instability strip. It can be seen clearly in the different panels of Figure 3 in Bono et al. (2020) that visual amplitudes for the RRab decrease as period increases, creating a slope that is present but shallower in the mid-infrared W1 band, barely noticeable in the velocity amplitude from Fe lines, and altogether absent in the velocity amplitude from Balmer lines.

We detected that dispersion in both period and velocity amplitude are larger than measurement errors. Using a set of HB evolutionary models, we found that evolutionary effects as the RRL leaves the zero-age HB are responsible for some of the dispersion in period and most of the dispersion in velocity amplitude in the Bailey diagram. The most significant source of dispersion in period, however, are intrinsic differences between progenitors. This means that the spread in period is mainly driven by differences in envelope mass and metallicity. Furthermore, the HB models also showed that the RRab region of long period and small amplitude is populated by stars at the late and relatively short stages of HB evolution. Thus, the small number of stars in that region of the velocity-based Bailey diagram reflects the lower likelihood of detecting them.

10.3 A new calibration of the Fourier Parameter Decomposition method

The Fourier parameter decomposition method is widely used in the literature to derive metallicity estimates based on light curves (Chapter 3.7.2). While its precision is lower than spectroscopic estimates, it is still an important tool that can be applied to a large number of stars for which no spectra are available. Luckily, photometry is very time-efficient and large data multi-epoch sets are readily available, such as the All-Sky Automated Survey for Supernovae (ASAS-SN, Shappee et al., 2014). With this in mind, our group developed a new calibration of this method using the HR and ΔS results derived in the present work. Thus, these purely photometric estimates can be made in our same metallicity scale and display a much more robust response in the high and low metallicity tails than calibrations using previous ΔS results.

Furthermore, a calibration is available for the first time using the W1 and W2 bands of the Near-Earth Objects reactivation mission (WISE, Mainzer et al., 2011). This opens the door for mid-infrared investigations of the extragalactic RRLs in the Local Group which are well beyond the reach of HR and LR spectroscopy. In particular, mid-infrared photometric observations will soon enter a new age with the advent of dedicated missions such as the James Webb Space Telescope (JWST, Gardner et al., 2006). The calibration for the RRab is published in Mullen et al. (2021), and the calibration for the RRc will be published by Mullen et al. in the coming months.

Chapter 11

Conclusions

In this work, we collected the largest spectroscopic sample of field Halo RRLs ever analysed in the literature, including HR and LR spectra from public surveys, archives, and new proprietary observations. We used data collected with nine HR spectrographs installed at eight different large telescopes (Table 5.1) and by two LR surveys (SEGUE-SDSS, LAMOST) in order to provide results in an homogeneous chemical abundance scale. Our sample covers a wide metallicity range, with [Fe/H] ranging from -3.2 to 0.2 dex. Due to the tight age constraints on the formation of RRL variables (Chapter 3), this means that this sample is over 10 Gyr old and coeval within 2 Gyr. Thus, our results trace the early chemical enrichment history of the Halo, including its metal-rich and yet old component that is poorly constrained by other stellar tracers. Here, we give an overview of the most important aspects and results of the present analysis.

Updated and unblended line list – We compiled a line list of atomic transitions for a large variety of chemical species. Our analysis includes the light odd-Z elements Na and Al; the α elements Mg, Si, S, Ca, and Ti; the Fe-peak elements Sc, V, Cr, Mn, Fe, Co, Ni, Cu, and Zn; and the n-capture elements Sr, Y, Zr, Ba, La, Ce, Pr, Nd, and Eu. The n-capture elements that we investigated include both the first and second n-capture peak, and in particular the bona fide tracer of the s-process Ba, its r-process counterpart Eu, and the scarcely studied rare earth Pr. All lines adopted in this work were updated with recent laboratory measurements whenever available, and otherwise with values compiled by NIST or computed empirically and homogeneously by Meléndez & Barbuy (2009a) in the case of FeII. We carefully verified that no line was blended with other transitions by analysing both the solar spectrum atlas of Moore et al. (1966) and synthetic spectra generated with the continuously updated LINEMAKE code. Moreover, we eliminated all lines that displayed trends with effective temperature. In cases where the lines displayed lower quality or any dependence on log(g), such as Si, we opted to maintain the measurements but discuss their situation clearly in the text where they are presented.

Homogeneous chemical abundances – We used the curve-of-growth approach of HR

spectroscopy to derive atmospheric parameters and abundances for 243 individual spectra of 162 RRLs (TW-RRL sample). We used stars in common with eleven HR studies in the literature (Table 5.2) to bring other 65 stars to our chemical abundance scale (Lit-RRL sample). We also applied the same spectroscopic analysis to six HB stars (TW-HB), and adopted other 46 HB stars from F10 (Lit-HB), which is natively in our same metallicity scale. Furthermore, we also analysed seven field dwarfs for comparison purposes (TW-Dwarfs). The chemical analysis performed in this work was done assuming LTE. Deviations from LTE for elements where these are significant are discussed in the text.

A new, homogeneous calibration of the ΔS method – We paired 163 (111 RRab, 32 RRc) stars in the TW-RRL sample, and therefore with HR metallicity measurements made by us, with 6,327 LR spectra and developed a new calibration of the ΔS method. This new calibration for the first time includes the RRc variables and also measurements coming from the full pulsation cycle of RRLs. This means that it can be applied to spectra collected at random phases, dismissing any need for lengthy photometric studies (in order to derive ephemerides) and strict observation planning (in order to observe the star at a precise point of its pulsation cycle). We verified that the calibration can be applied to mixed mode variables. This new calibration was applied to 7,768 RRLs (5,196 RRab, 2,572 RRc) with SEGUE-SDSS and LAMOST spectra.

Both the HR and ΔS metallicities are in the same scale and provide excellent precision (typically $\approx$ 0.05 and 0.35 dex, respectively). They recover the same peak metallicity for the Halo (η=-1.56$\pm$0.04 and -1.52$\pm$0.00 dex, respectively). Interestingly, both are capable of recovering a difference in metallicity distribution, both in peak and shape, between the RRab and RRc. This difference is predicted HB evolutionary models. Moreover, the present results do not show a metallicity gradient with Galactocentric distance, nor any change in the metallicity distribution that would suggest a Halo duality. A metal-rich RRL population exists at smaller Galactocentric radii, but it is confined to small distances from the Disk. This means that they do not form a spherical component, but are rather likely associated with the ancient Disk which evolved into what is now called the thick Disk. Indeed, some of them are likely to have disk-like orbits (Prudil et al., 2020), supporting a scenario where stars formed in situ in the ancient Disk now inhabit the limit between the current Disk and Halo (Font et al., 2011; McCarthy et al., 2012). Further kinematic investigation of these stars is necessary in order to understand their origins, and whether they can be associated with one or more progenitors either by accretion or by in situ star formation triggered by merging events.

Comparing RRLs, non-variable HB stars, and dwarfs – The HB stars from F10, included in this work without change as the Lit-HB sample, are in excellent agreement with the trends set by the RRLs in all chemical species. This is expected due to the fact that RRLs are simply variable HB stars, and thus share their same age and progenitors. We included in the TW-HB sample six metal-rich stars identified by Afşar et al. (2018) as field HB stars. However, as these show marked differences when compared to the RRLs

in multiple species, it may be the case that they were misidentified and are actually red clump stars. Regardless of their classification, they are very useful in the present analysis as representatives of non-variable giants. Together with the TW-Dwarfs sample, they offer valuable clues regarding temperature gravity-related systematics in derived abundances. Indeed, the TW-HB sample includes cold giants ($T_{eff} \approx 5500$ K) that are in the same log(g) range as the RRLs, while the TW-Dwarfs sample includes only hot field dwarfs that are in the same T_{eff} range as the red HB stars and the RRLs during the cold phase.

The α elements Mg, Ca, Ti – The [α/Fe] versus [Fe/H] plane of a stellar population is tightly related to its chemical enrichment history (Chapter 4.3.2). This plane displays a plateau in the metal-poor regime, which undergoes a sharp decrease (the "knee") in the metal-intermediate or metal-rich regimes. The position of this "knee" is associated with the onset of enrichment driven by SNe Ia and with the initial mass function of the system. The position of the "knee" in the Halo is poorly constrained by most stellar tracers. However, our RRL sample riches super solar metallicities and clearly shows not only the position of the "knee" for the most ancient stellar population of the Galaxy, but also the existence of a metal-rich α-depleted RRL population that is not found in other Galactic components but is in good agreement with the metal-rich stars in the Sagittarius dwarf spheroidal.

The α elements Si and S – We found an overabundance of [Si/Fe] for the RRL sample when compared to other studies. Our analysis of non-variable HB stars and of dwarfs shows that this is not only due to differences in adopted line lists among different studies. Indeed, literature sources use various selections of atomic line and line parameters, and in many cases do not make their line lists available, but even in an homogenous analysis the difference in abundance persists. From our results, most if not all SiI lines and possibly SiII lines have a strong dependence on surface gravity. However, a larger sample of non-variable HB stars and hot dwarfs covering a wide metallicity range and analysed homogeneously with the TW-RRL sample is needed in order to draw a firm conclusion on what is driving the incongruent results. It bears mentioning that the metal-intermediate to metal-rich trend in [Si/Fe], where the difference with literature results is most marked, is in very good agreement with the trend set by S. However this latter element has scarce measurements in the literature and could not be measured in our metal-poor stars, therefore it is unclear whether it is affected by systematics. It is possible that S follows the trend set by Mg, Ca, and Ti, but requires a zero-point shift.

The Fe-peak elements – Comparisons with the literature are difficult for the heavier species due to the variety of line lists, and also due to the need of HFS computations for the odd-Z elements that are treated differently across studies. Furthermore, the number of measurements for these species is markedly lower than for lighter elements. We found that Sc behaves like the α elements, showing a depletion in metal-rich RRLs that is not followed by other field stars. The other chemical species do not show marked differences with other Galactic components. Interestingly, Sc, V, Cr, and Co in the RRLs agree

well with the Sgr dSph, while the other Fe-peak species do not, in particular Mn, Ni, and Cu. However, Mn and Co lines are subjected to strong NLTE effects and should be taken with caution. Furthermore, the spectra available for extragalactic objects are still usually of low quality, with either low resolution or low SNR. A detailed, homogeneous study of at least a few stars in the nearby dwarf galaxies with good quality spectra is needed to disentangle the various difficulties in measuring heavy species.

The n-capture elements – The difficulties in literature comparisons for the n-capture elements are even greater than those for the Fe-peak due to a greater scarcity of measurements. However, the homogeneous sample used in the present work allowed for a few interesting results by itself. The large spread in Sc found in the literature is confirmed here, but now with a coeval and homogeneous sample. As we eliminated lines with temperature or gravity dependence, it is likely that the spread in Sc is indeed intrinsic and not an age effect or a consequence of inhomogeneous analyses. Both Zr and Y show a depletion in the metal-rich RRLs, with Y showing a specially marked difference when compared against not only literature values, but also the TW-HB and TW-Dwarfs samples. This too points to an intrinsic difference in the abundance of the RRLs when compared to likely younger stars. For Ba, the scatter does not allow for strong conclusions to be drawn, but there is a marked lack of metal-rich Ba-rich stars that are seen in literature samples. Similarly, La and Ce also seem slightly depleted in the RRLs.

Chemical enrichment as told by ancient stars – We performed several tests to detect possible systematics in the abundances derived for the TW-RRL sample. RRLs are the perfect laboratory in which to study effective temperature systematics in atomic line formation, as they undergo variations as large as 1000 K during their pulsation cycle, while the abundance of the species in question clearly ought to remain the same. We eliminated all lines that showed a T_{eff} dependence, and indicated the elements where log(g) or NLTE effects are expected or shown to be significant.

The inclusion of the TW-HB and TW-Dwarfs samples allowed for a direct test of surface gravity systematics. As discussed above, even if the TW-HB stars are misclassified red clump stars, they still show that our methodology recovers coherent results for both giants in the log(g) range of RRLs and for dwarfs in the T_{eff} range of RRLs. Furthermore, the TW-Dwarfs sample shows that our chemical abundance scale is not significantly different from that of Nissen & Schuster (2010), and so the differences found between the RRLs and other field populations for species without significant NLTE effects is not simply due to line list differences across studies nor an evolutionary (i.e. surface gravity) effect, but rather intrinsic.

Once differences in line list, treatment of NLTE effects, effective temperature, and surface gravity are accounted for, as done here by using non-RRL comparison stars, differences in chemical abundance can only be driven by differences in progenitors. Unlike most stars, and in particular field stars, the RRLs have strong age constraints. This means that the progenitors are low mass stars formed over 10 Gyr ago. If another Galactic stellar population is found to be in intrinsic disagreement with the RRLs, it can

only mean that they were formed in a different environment or at a different time.

Regarding the structure of the Halo, on the one hand, we found no evidence for a dual Halo in metallicity or chemical abundance. On the other hand, we identified that there are RRLs, i.e. ancient stars, covering a wide range in metallicity, with the metal-rich component being mostly confined to low Galactic heights, but spread across all Galactic quadrants. This means that they do not form a spheroidal structure, but rather a plane structure. There is preliminary evidence that at least some of them follow a disk-like orbit (Prudil et al., 2020). While more investigation of their kinematics is needed, this preliminary evidence supports that the thick and thin Disk being fundamentally different, with the latter being a relic of a primordial Disk that underwent fast chemical enrichment in order to produce metal-rich, α-poor stars. Indeed, this is also supported by the fact that neither RRLs nor GCs have ever been found in a thin Disk orbit, while this Galactic component hosts a large number of Classical Cepheids (ages $\approx$ 200 Myr), open clusters, and star-forming regions. Moreover, the RRLs in the outer Halo and at low Galactic heights (i.e. in inner Halo or thick Disk) form a continuous sequence in the [α/Fe] versus [Fe/H] plane, suggesting a shared origin but with the metal-rich component being concentrated in the higher density regions of the Galaxy.

11.1 Near future perspectives

The next step of the current investigation is to provide other stellar tracers in the same metallicity and chemical abundance scale for the Milky Way and its nearby satellites. A sample of field dwarfs and non-variable giants with effective temperatures in over $\approx$5900 K covering a wide metallicity range would be invaluable. They would aid in constraining systematics and also NLTE effects. A sample of Classical Cepheids would offer the young counterpart for the RRLs. As the Cepheids are bright, very high quality spectra are available for a number of them (e.g. Luck et al., 2006; da Silva et al., 2016). The same cannot be said for stars in the nearby dwarf galaxies, but even a few HR, modest to high SNR observations would shed light on the relationship between the Milky Way and its neighbors. The RRLs offer strong constraints in the building blocks of the Galaxy by their pulsational properties, their number ratio (Fabrizio et al., 2021b), and, with the quality and size of the sample included in the present work, also by their chemistry.

Acknowledgements

The work done in this thesis was partially funded by the Conselho Nacional de Desenvolvimento Científico e Tecnológico (CNPq) of Brazil. This research has made use of the National Aeronautics and Space Administration (NASA) Astrophysics Data System, the National Institute of Standards and Technology (NIST) Atomic Spectra Database, the JVO Portal[1] operated by ADC/NAOJ, and the ESO Science Archive Facility.

This work is based on observations made with: the Italian Telescopio Nazionale Galileo (TNG) operated on the island of La Palma by the Fundación Galileo Galilei of the INAF (Istituto Nazionale di Astrofisica) at the Spanish Observatorio del Roque de los Muchachos of the Instituto de Astrofisica de Canarias; the European Organisation for Astronomical Research in the Southern Hemisphere under ESO programmes 0100.D-0339, 0101.D-0697, 0102.D-0281, 076.B-0055, 077.B-0359, 077.D-0633, 079.A-9015, 079.D-0262, 079.D-0462, 079.D-0567, 082.C-0617, 083.B-0281, 083.C-0244, 094.B-0409, 095.B-0744, 097.A-9032, 098.D-0230, 189.B-0925, 267.C-5719, 297.D-5047, 67.D-0321, 67.D-0554, 69.C-0423, 71.C-0097, 0100.D-0273, 083.C-0244, 098.D-0230; the Southern African Large Telescope (SALT); the du Pont telescope at Las Campanas Observatory, operated by Carnegie Institution for Science; the Subaru Telescope, which is operated by the National Astronomical Observatory of Japan; the STELLA robotic telescopes in Tenerife, an AIP facility jointly operated by AIP and IAC; and the European Organisation for Astronomical Research in the Southern Hemisphere.

We made use of data from the European Space Agency (ESA) mission *Gaia* (https://www.cosmos.esa.int/gaia), processed by the *Gaia* Data Processing and Analysis Consortium (DPAC, https://www.cosmos.esa.int/web/gaia/dpac/consortium). Funding for the DPAC has been provided by national institutions, in particular the institutions participating in the *Gaia* Multilateral Agreement.

We also used data from SDSS and LAMOST. Funding for the SDSS and SDSS-II has been provided by the Alfred P. Sloan Foundation, the Participating Institutions, the National Science Foundation, the U.S. Department of Energy, the National Aeronautics and Space Administration, the Japanese Monbukagakusho, the Max Planck Society, and the Higher Education Funding Council for England. The SDSS Web Site is http://www.sdss.org/. The SDSS is managed by the Astrophysical Research Consor-

[1] http://jvo.nao.ac.jp/portal/

tium for the Participating Institutions. The Participating Institutions are the American Museum of Natural History, Astrophysical Institute Potsdam, University of Basel, University of Cambridge, Case Western Reserve University, University of Chicago, Drexel University, Fermilab, the Institute for Advanced Study, the Japan Participation Group, Johns Hopkins University, the Joint Institute for Nuclear Astrophysics, the Kavli Institute for Particle Astrophysics and Cosmology, the Korean Scientist Group, the Chinese Academy of Sciences (LAMOST), Los Alamos National Laboratory, the Max-Planck-Institute for Astronomy (MPIA), the Max-Planck-Institute for Astrophysics (MPA), New Mexico State University, Ohio State University, University of Pittsburgh, University of Portsmouth, Princeton University, the United States Naval Observatory, and the University of Washington. Guoshoujing Telescope (the Large Sky Area Multi-Object Fiber Spectroscopic Telescope LAMOST) is a National Major Scientific Project built by the Chinese Academy of Sciences. Funding for the project has been provided by the National Development and Reform Commission. LAMOST is operated and managed by the National Astronomical Observatories, Chinese Academy of Sciences.

Appendix A

Complete list of publications by J. Crestani

First author papers:

- Crestani et al. (2019) – *Chemical abundances in the metal-intermediate GC NGC 6723*
- Crestani et al. (2021a) – *On the Use of Field RR Lyrae as Galactic Probes. II. A New ΔS Calibration to Estimate Their Metallicity*
- Crestani et al. (2021b) – *On the Use of Field RR Lyrae as Galactic Probes. III. The α-element Abundances*
- Crestani et al., in preparation – *On the Use of Field RR Lyrae as Galactic Probes. VI. The Fe-peak Abundances (working title)*
- Crestani et al., in preparation – *On the Use of Field RR Lyrae as Galactic Probes. VII. The Neutron-capture Abundances (working title)*

Co-author papers:

- Bono et al. (2020) – *On the Metamorphosis of the Bailey Diagram for RR Lyrae Stars*
- Gilligan et al. (2021) – *Metallicities from high-resolution spectra of 49 RR Lyrae variables*
- Braga et al. (2021b) – *On the Use of Field RR Lyrae as Galactic Probes. V. Optical and Radial Velocity Curve Templates*
- Fabrizio et al. (2021b) – *On the Use of Field RR Lyrae As Galactic Probes: IV. New Insights Into and Around the Oosterhoff Dichotomy*
- da Silva et al., in preparation – *A new and homogeneous metallicity scale for Galactic classical Cepheids. II. The abundances of α elements (working title)*

Other collaborations:

- Prudil et al. (2021) – *Milky Way archaeology using RR Lyrae and type II Cepheids. I. The Orphan stream in 7D using RR Lyrae stars*
- Mullen et al. (2021) – *Metallicity of Galactic RR Lyrae from Optical and Infrared Light Curves. I. Period-Fourier-Metallicity Relations for Fundamental-mode RR Lyrae*
- Matsunaga et al., 2021, ApJ, accepted – *A Very Metal-Poor RR Lyrae Star with a Disk-Like Orbit Found in the Solar Neighborhood*
- Mullen et al., in preparation – *Metallicity of Galactic RR Lyrae from Optical and Infrared Light Curves. II. Period-Fourier-Metallicity Relations for First-overtone RR Lyrae (working title)*

Appendix B

Line list

All lines adopted in this work and their transition parameters are included below in Table B.1, with sources as listed in Table B.2. See Chapter B for a description of the line list and the steps taken when compiling it. The machine-readable line lists for iron and α elements (Mg, Ca, and Ti) can be found in Crestani et al. (2021a) and in Crestani et al. (2021b), respectively. Machine-readable tables for the remaining elements will be published in upcoming papers. Lines with hyperfine splitting are indicated by a minus sign in their wavelengths.

Table B.1: Atomic transition parameters for all lines used in this work. See Table B.2 for the references.

Species	Wavelength Å	Ion	EP eV	log(gf)	Source
NaI	5682.633	11.0	2.102	-0.706	NIST
NaI	5889.950	11.0	0.000	0.108	NIST-JON96
NaI	5895.920	11.0	0.000	-0.194	NIST-JON96
NaI	6154.225	11.0	2.102	-1.547	NIST
NaI	6160.750	11.0	2.104	-1.246	NIST
NaI	8183.256	11.0	2.102	0.237	NIST
MgI	3829.355	12.0	2.709	-0.227	NIST
MgI	4571.096	12.0	0.000	-5.620	NIST
MgI	4702.991	12.0	4.346	-0.440	NIST-CHA90
MgI	5172.684	12.0	2.712	-0.393	NIST
MgI	5183.604	12.0	2.717	-0.167	NIST
MgI	5528.405	12.0	4.346	-0.498	NIST-CHA90
MgI	5711.088	12.0	4.346	-1.724	NIST-CHA90
MgI	8712.689	12.0	5.932	-1.213	NIST-BUT93
MgI	8717.825	12.0	5.932	-0.941	NIST-BUT93

The table continues on the next page

Species	Wavelength Å	Ion	EP eV	log(gf)	Source
AlI	3944.006	13.0	0.000	-0.635	NIST
AlI	3961.520	13.0	0.014	-0.333	NIST
AlI	6696.015	13.0	3.143	-1.569	NIST-MEN95
AlI	7835.309	13.0	4.021	-0.689	NIST-MEN95
AlI	7836.134	13.0	4.022	-0.534	NIST-MEN95
AlI	8772.866	13.0	4.021	-0.349	NIST-MEN95
AlI	8773.896	13.0	4.022	-0.192	NIST-MEN95
SiI	5665.554	14.0	4.920	-2.040	NIST-GAR73
SiI	5690.425	14.0	4.930	-1.870	NIST-GAR73
SiI	5708.397	14.0	4.954	-1.470	NIST-GAR73
SiI	5772.145	14.0	5.082	-1.750	NIST-GAR73
SiI	5948.545	14.0	5.082	-1.231	NIST-GAR73
SiI	7932.349	14.0	5.963	-0.470	NIST-GAR73
SiII	6347.100	14.1	8.121	0.149	NIST-MAT01
SiII	6371.360	14.1	8.121	-0.082	NIST-MAT01
SI	6538.570	16.0	8.046	-1.029	NIST-ZAT06
SI	6757.160	16.0	7.870	-0.351	NIST-ZAT06
SI	9237.538	16.0	6.524	0.025	NIST-ZAT06
CaI	4226.730	20.0	0.000	0.244	NIST-SMI66
CaI	4425.440	20.0	1.879	-0.358	NIST8
CaI	4578.550	20.0	2.521	-0.558	NIST-OLS59
CaI	4685.270	20.0	2.933	-0.880	NIST-KOS64
CaI	5581.970	20.0	2.523	-0.710	NIST-KOS64
CaI	5588.760	20.0	2.526	0.210	NIST-KOS64
CaI	5590.120	20.0	2.521	-0.710	NIST-KOS64
CaI	5601.290	20.0	2.530	-0.690	NIST-KOS64
CaI	5857.450	20.0	2.933	0.230	NIST-KOS64
CaI	6102.720	20.0	1.879	-0.790	NIST
CaI	6122.220	20.0	1.886	-0.315	NIST
CaI	6161.290	20.0	2.523	-1.030	NIST-KOS64
CaI	6162.170	20.0	1.899	-0.089	NIST
CaI	6166.440	20.0	2.521	-0.900	NIST-KOS64
CaI	6169.060	20.0	2.523	-0.540	NIST-KOS64
CaI	6169.560	20.0	2.526	-0.270	NIST-KOS64
CaI	6439.070	20.0	2.526	0.470	NIST-KOS64
CaI	6449.810	20.0	2.521	-0.550	NIST-KOS64
CaI	6455.600	20.0	2.523	-1.360	NIST-OLS59
CaI	6471.660	20.0	2.526	-0.590	NIST-KOS64

The table continues on the next page

Species	Wavelength Å	Ion	EP eV	log(gf)	Source
CaI	6493.780	20.0	2.521	0.140	NIST-KOS64
CaI	6499.650	20.0	2.523	-0.590	NIST-KOS64
CaI	6717.690	20.0	2.709	-0.610	NIST-OLS59
ScII	-4246.822	21.1	0.315	0.24	LAW19
ScII	-4314.083	21.1	0.618	-0.11	LAW19
ScII	-4400.390	21.1	0.605	-0.54	LAW19
ScII	-5239.813	21.1	1.455	-0.76	LAW19
ScII	-5526.790	21.1	1.768	-0.01	LAW19
ScII	-5641.002	21.1	1.500	-0.99	LAW19
ScII	-5657.896	21.1	1.507	-0.54	LAW19
ScII	-5658.361	21.1	1.497	-1.17	LAW19
ScII	-5669.043	21.1	1.500	-1.10	LAW19
ScII	-5684.202	21.1	1.507	-1.03	LAW19
ScII	-6604.601	21.1	1.357	-1.26	LAW19
TiI	3729.807	22.0	0.000	-0.280	LAW13
TiI	3741.059	22.0	0.021	-0.150	LAW13
TiI	4512.734	22.0	0.835	-0.400	LAW13
TiI	4518.022	22.0	0.825	-0.250	LAW13
TiI	4533.239	22.0	0.848	0.540	LAW13
TiI	4534.776	22.0	0.835	0.350	LAW13
TiI	4617.269	22.0	1.748	0.440	LAW13
TiI	4840.874	22.0	0.899	-0.430	LAW13
TiI	4913.613	22.0	1.872	0.220	LAW13
TiI	4981.731	22.0	0.848	0.570	LAW13
TiI	4991.066	22.0	0.835	0.450	LAW13
TiI	4999.503	22.0	0.825	0.320	LAW13
TiI	5016.161	22.0	0.848	-0.480	LAW13
TiI	5022.868	22.0	0.825	-0.330	LAW13
TiI	5024.844	22.0	0.818	-0.530	LAW13
TiI	5036.464	22.0	1.442	0.140	LAW13
TiI	5038.398	22.0	1.429	0.020	LAW13
TiI	5039.957	22.0	0.021	-1.080	LAW13
TiI	5064.653	22.0	0.048	-0.940	LAW13
TiI	5173.743	22.0	0.000	-1.060	LAW13
TiI	5192.969	22.0	0.021	-0.950	LAW13
TiI	5210.384	22.0	0.048	-0.820	LAW13
TiI	5866.451	22.0	1.066	-0.790	LAW13
TiI	6126.214	22.0	1.067	-1.424	NIST-BLA83

The table continues on the next page

Species	Wavelength Å	Ion	EP eV	log(gf)	Source
TiI	6258.102	22.0	1.442	-0.390	LAW13
TiI	6261.099	22.0	1.429	-0.530	LAW13
TiII	4300.042	22.1	1.179	-0.460	WOO13
TiII	4301.923	22.1	1.160	-1.210	WOO13
TiII	4312.860	22.1	1.179	-1.120	WOO13
TiII	4394.059	22.1	1.220	-1.770	WOO13
TiII	4395.031	22.1	1.083	-0.540	WOO13
TiII	4395.839	22.1	1.242	-1.930	WOO13
TiII	4398.292	22.1	1.224	-2.654	NIST-PIC02
TiII	4417.714	22.1	1.165	-1.430	NIST-ROB73
TiII	4443.801	22.1	1.079	-0.710	WOO13
TiII	4444.554	22.1	1.115	-2.200	WOO13
TiII	4464.449	22.1	1.161	-2.080	NIST-ROB73
TiII	4468.493	22.1	1.130	-0.630	WOO13
TiII	4488.324	22.1	3.121	-0.500	WOO13
TiII	4501.270	22.1	1.115	-0.770	WOO13
TiII	4563.758	22.1	1.221	-0.960	NIST-ROB73
TiII	4571.971	22.1	1.571	-0.310	WOO13
TiII	4805.093	22.1	2.061	-1.120	NIST-ROB73
TiII	4865.610	22.1	1.115	-2.700	WOO13
TiII	4911.194	22.1	3.121	-0.640	WOO13
TiII	5005.167	22.1	1.565	-2.730	WOO13
TiII	5129.156	22.1	1.890	-1.340	WOO13
TiII	5154.068	22.1	1.566	-1.920	NIST-WOL73
TiII	5185.902	22.1	1.891	-1.410	WOO13
TiII	5188.687	22.1	1.582	-1.220	NIST-ROB73
TiII	5336.770	22.1	1.581	-1.600	WOO13
TiII	5418.768	22.1	1.581	-2.130	WOO13
TiII	6606.956	22.1	2.061	-2.790	NIST-KOS83
TiII	7214.729	22.1	2.590	-1.750	NIST-KOS83
VI	-4111.779	23.0	0.300	0.40	LAW14
VI	-4379.230	23.0	0.300	0.58	LAW14
VII	-3951.957	23.1	1.475	-0.73	LAW14
VII	-4005.702	23.1	1.816	-0.45	LAW14
CrI	4274.812	24.0	0.000	-0.220	SOB07
CrI	4289.731	24.0	0.000	-0.370	SOB07
CrI	4545.953	24.0	0.941	-1.370	SOB07
CrI	4616.124	24.0	0.982	-1.190	SOB07

The table continues on the next page

Species	Wavelength Å	Ion	EP eV	log(gf)	Source
CrI	4646.162	24.0	1.029	-0.740	SOB07
CrI	4651.291	24.0	0.982	-1.460	SOB07
CrI	4652.157	24.0	1.003	-1.040	SOB07
CrI	5247.565	24.0	0.960	-1.590	SOB07
CrI	5296.691	24.0	0.982	-1.360	SOB07
CrI	5300.745	24.0	0.982	-2.000	SOB07
CrI	5348.314	24.0	1.003	-1.210	SOB07
CrI	5409.783	24.0	1.029	-0.670	SOB07
CrII	4554.989	24.1	4.068	-1.270	LAW17
CrII	4558.644	24.1	4.070	-0.430	LAW17
CrII	4588.198	24.1	4.068	-0.650	LAW17
CrII	4592.053	24.1	4.070	-1.300	LAW17
CrII	4616.624	24.1	4.069	-1.420	LAW17
CrII	4848.250	24.1	3.861	-1.110	LAW17
CrII	5237.322	24.1	4.070	-1.170	LAW17
MnI	-4783.428	25.0	2.296	0.044	DEN11
MnI	-4823.524	25.0	2.317	0.136	DEN11
MnI	5420.360	25.0	2.143	-1.460	NIST-BOO84
MnI	-6013.513	25.0	3.070	-0.354	DEN11
MnI	-6021.819	25.0	3.073	-0.054	DEN11
FeI	3763.78	26.0	0.989	-0.220	OBR91
FeI	3787.88	26.0	1.010	-0.840	OBR91
FeI	3815.84	26.0	1.484	0.240	OBR91
FeI	3820.42	26.0	0.858	0.160	OBR91
FeI	3825.88	26.0	0.914	-0.020	OBR91
FeI	3840.43	26.0	0.989	-0.500	OBR91
FeI	3856.37	26.0	0.052	-1.280	OBR91
FeI	3859.91	26.0	0.000	-0.700	OBR91
FeI	3865.52	26.0	1.010	-0.950	OBR91
FeI	3899.70	26.0	0.087	-1.510	OBR91
FeI	3922.91	26.0	0.052	-1.630	OBR91
FeI	3949.95	26.0	2.174	-1.250	OBR91
FeI	4005.24	26.0	1.556	-0.580	OBR91
FeI	4045.81	26.0	1.484	0.280	OBR91
FeI	4071.73	26.0	1.607	-0.010	OBR91
FeI	4114.44	26.0	2.832	-1.303	NIST-OBR91
FeI	4132.89	26.0	2.845	-1.006	NIST-OBR91
FeI	4134.67	26.0	2.832	-0.649	NIST-OBR91

The table continues on the next page

Species	Wavelength Å	Ion	EP eV	log(gf)	Source
FeI	4147.66	26.0	1.484	-2.070	OBR91
FeI	4157.78	26.0	3.417	-0.403	NIST-OBR91
FeI	4175.63	26.0	2.845	-0.827	NIST-OBR91
FeI	4184.89	26.0	2.832	-0.869	NIST-OBR91
FeI	4187.03	26.0	2.450	-0.560	RUF14
FeI	4199.09	26.0	3.045	0.170	BEL17
FeI	4202.02	26.0	1.484	-0.690	OBR91
FeI	4216.18	26.0	0.000	-3.360	OBR91
FeI	4222.21	26.0	2.450	-0.967	NIST-BLA82
FeI	4227.42	26.0	3.332	0.266	NIST-OBR91
FeI	4233.60	26.0	2.482	-0.600	RUF14
FeI	4248.22	26.0	3.071	-1.286	NIST-OBR91
FeI	4250.11	26.0	2.469	-0.405	NIST-BLA82
FeI	4260.47	26.0	2.399	0.077	NIST-OBR91
FeI	4271.15	26.0	2.450	-0.349	NIST-BLA82
FeI	4271.76	26.0	1.484	-0.170	OBR91
FeI	4282.40	26.0	2.174	-0.780	OBR91
FeI	4352.73	26.0	2.223	-1.287	NIST-OBR91
FeI	4383.54	26.0	1.484	0.210	OBR91
FeI	4388.40	26.0	3.603	-0.682	NIST-OBR91
FeI	4404.75	26.0	1.556	-0.150	OBR91
FeI	4415.12	26.0	1.607	-0.620	OBR91
FeI	4430.61	26.0	2.223	-1.659	NIST-BLA82
FeI	4461.65	26.0	0.087	-3.190	OBR91
FeI	4489.73	26.0	0.121	-3.900	OBR91
FeI	4494.56	26.0	2.196	-1.140	BEL17
FeI	4602.00	26.0	1.607	-3.130	OBR91
FeI	4602.94	26.0	1.484	-2.210	OBR91
FeI	4630.12	26.0	2.277	-2.580	BEL17
FeI	4647.43	26.0	2.949	-1.351	NIST-OBR91
FeI	4707.27	26.0	3.241	-0.960	RUF14
FeI	4736.77	26.0	3.209	-0.670	DEN14
FeI	4779.44	26.0	3.415	-2.020	NIST-OBR91
FeI	4787.82	26.0	2.996	-2.620	DEN14
FeI	4788.75	26.0	3.237	-1.763	NIST-OBR91
FeI	4789.65	26.0	3.547	-0.958	NIST-OBR91
FeI	4793.96	26.0	3.047	-3.470	NIST-MAY74
FeI	4799.40	26.0	3.640	-2.190	NIST-MAY74

The table continues on the next page

Species	Wavelength Å	Ion	EP eV	log(gf)	Source
FeI	4800.64	26.0	4.143	-1.029	NIST-OBR91
FeI	4808.14	26.0	3.251	-2.740	NIST-MAY74
FeI	4809.93	26.0	3.573	-2.680	NIST-MAY74
FeI	4869.46	26.0	3.547	-2.480	NIST-MAY74
FeI	4871.31	26.0	2.865	-0.340	RUF14
FeI	4872.13	26.0	2.882	-0.567	NIST-OBR91
FeI	4873.75	26.0	3.301	-3.010	NIST-MAY74
FeI	4875.87	26.0	3.332	-1.900	RUF14
FeI	4877.60	26.0	2.998	-3.090	NIST-MAY74
FeI	4882.14	26.0	3.414	-1.480	DEN14
FeI	4885.43	26.0	3.882	-0.970	RUF14
FeI	4890.75	26.0	2.876	-0.380	RUF14
FeI	4891.49	26.0	2.851	-0.112	NIST-OBR91
FeI	4896.43	26.0	3.881	-1.890	DEN14
FeI	4905.13	26.0	3.929	-1.730	RUF14
FeI	4907.73	26.0	3.428	-1.700	DEN14
FeI	4917.23	26.0	4.191	-1.160	NIST-MAY74
FeI	4918.01	26.0	4.231	-1.340	NIST-MAY74
FeI	4918.99	26.0	2.865	-0.342	NIST-OBR91
FeI	4920.50	26.0	2.833	0.068	NIST-OBR91
FeI	4924.76	26.0	2.279	-2.114	NIST-OBR91
FeI	4927.41	26.0	3.573	-2.073	NIST-OBR91
FeI	4930.31	26.0	3.960	-1.201	NIST-BAR94
FeI	4938.81	26.0	2.876	-1.077	NIST-OBR91
FeI	4939.68	26.0	0.858	-3.250	OBR91
FeI	4946.38	26.0	3.368	-1.110	RUF14
FeI	4950.10	26.0	3.414	-1.500	DEN14
FeI	4961.91	26.0	3.634	-2.250	NIST-MAY74
FeI	4962.57	26.0	4.178	-1.182	NIST-OBR91
FeI	4966.08	26.0	3.329	-0.790	DEN14
FeI	4973.10	26.0	3.960	-0.690	RUF14
FeI	4985.25	26.0	3.926	-0.440	DEN14
FeI	4985.54	26.0	2.865	-1.331	NIST-OBR91
FeI	4986.22	26.0	4.218	-1.370	NIST-MAY74
FeI	4994.13	26.0	0.914	-2.970	OBR91
FeI	4995.40	26.0	4.260	-1.870	NIST-MAY74
FeI	4999.11	26.0	4.186	-1.710	NIST-MAY74
FeI	5001.86	26.0	3.882	-0.010	RUF14

The table continues on the next page

Species	Wavelength Å	Ion	EP eV	log(gf)	Source
FeI	5002.79	26.0	3.397	-1.460	RUF14
FeI	5006.11	26.0	2.833	-0.615	NIST-OBR91
FeI	5012.69	26.0	4.283	-1.770	NIST-MAY74
FeI	5014.94	26.0	3.940	-0.180	DEN14
FeI	5022.23	26.0	3.984	-0.330	RUF14
FeI	5023.18	26.0	4.283	-1.580	NIST-MAY74
FeI	5023.49	26.0	4.312	-1.670	RUF14
FeI	5028.12	26.0	3.573	-1.020	RUF14
FeI	5029.61	26.0	3.415	-2.000	NIST-MAY74
FeI	5031.91	26.0	4.371	-1.650	NIST-MAY74
FeI	5044.21	26.0	2.851	-2.017	NIST-OBR91
FeI	5048.43	26.0	3.957	-1.000	DEN14
FeI	5049.81	26.0	2.279	-1.355	NIST-OBR91
FeI	5051.63	26.0	0.914	-2.760	OBR91
FeI	5054.64	26.0	3.640	-1.921	NIST-OBR91
FeI	5056.84	26.0	4.260	-1.940	NIST-MAY74
FeI	5068.76	26.0	2.940	-1.042	NIST-OBR91
FeI	5074.74	26.0	4.220	-0.230	NIST-BRI74
FeI	5079.22	26.0	2.196	-2.100	OBR91
FeI	5079.74	26.0	0.989	-3.250	OBR91
FeI	5083.33	26.0	0.957	-2.840	OBR91
FeI	5088.15	26.0	4.150	-1.750	NIST-MAY74
FeI	5090.77	26.0	4.256	-0.440	NIST-BRI74
FeI	5104.43	26.0	4.283	-1.670	NIST-MAY74
FeI	5107.44	26.0	0.989	-3.100	OBR91
FeI	5107.64	26.0	1.556	-2.360	OBR91
FeI	5115.77	26.0	3.573	-2.690	NIST-MAY74
FeI	5121.63	26.0	4.283	-0.810	NIST-BRI74
FeI	5123.72	26.0	1.010	-3.060	OBR91
FeI	5126.19	26.0	4.256	-1.060	NIST-MAY74
FeI	5127.36	26.0	0.914	-3.250	OBR91
FeI	5129.63	26.0	3.943	-1.670	RUF14
FeI	5131.46	26.0	2.223	-2.515	NIST-OBR91
FeI	5133.68	26.0	4.175	0.360	DEN14
FeI	5141.73	26.0	2.424	-2.238	NIST-OBR91
FeI	5143.72	26.0	2.198	-3.690	NIST-MAY74
FeI	5145.09	26.0	2.198	-2.876	NIST-OBR91
FeI	5151.91	26.0	1.010	-3.320	OBR91

The table continues on the next page

Species	Wavelength Å	Ion	EP eV	log(gf)	Source
FeI	5171.59	26.0	1.484	-1.720	OBR91
FeI	5187.91	26.0	4.143	-1.371	NIST-OBR91
FeI	5191.45	26.0	3.038	-0.551	NIST-OBR91
FeI	5192.34	26.0	2.998	-0.421	NIST-OBR91
FeI	5194.94	26.0	1.556	-2.020	OBR91
FeI	5197.93	26.0	4.301	-1.620	NIST-MAY74
FeI	5198.71	26.0	2.223	-2.135	NIST-BLA82
FeI	5202.33	26.0	2.174	-1.870	OBR91
FeI	5215.18	26.0	3.263	-0.860	DEN14
FeI	5216.27	26.0	1.607	-2.080	OBR91
FeI	5217.38	26.0	3.209	-1.070	DEN14
FeI	5223.18	26.0	3.635	-1.783	NIST-OBR91
FeI	5225.52	26.0	0.110	-4.750	OBR91
FeI	5228.37	26.0	4.220	-1.260	NIST-MAY74
FeI	5232.94	26.0	2.940	-0.057	NIST-OBR91
FeI	5236.20	26.0	4.186	-1.497	NIST-OBR91
FeI	5242.49	26.0	3.632	-0.830	BEL17
FeI	5243.77	26.0	4.256	-1.120	NIST-MAY74
FeI	5247.05	26.0	0.087	-4.970	OBR91
FeI	5250.21	26.0	0.121	-4.900	OBR91
FeI	5250.64	26.0	2.196	-2.180	OBR91
FeI	5253.46	26.0	3.281	-1.580	DEN14
FeI	5262.88	26.0	3.251	-2.600	NIST-MAY74
FeI	5263.30	26.0	3.263	-0.870	DEN14
FeI	5267.27	26.0	4.371	-1.596	NIST-BAR94
FeI	5269.53	26.0	0.858	-1.330	OBR91
FeI	5273.16	26.0	3.289	-1.010	DEN14
FeI	5281.79	26.0	3.038	-0.834	NIST-OBR91
FeI	5283.62	26.0	3.239	-0.450	DEN14
FeI	5285.12	26.0	4.435	-1.660	RUF14
FeI	5288.52	26.0	3.695	-1.490	RUF14
FeI	5293.95	26.0	4.143	-1.840	NIST-MAY74
FeI	5294.54	26.0	3.640	-2.810	NIST-MAY74
FeI	5295.31	26.0	4.415	-1.670	NIST-MAY74
FeI	5302.30	26.0	3.281	-0.730	DEN14
FeI	5307.36	26.0	1.607	-2.910	OBR91
FeI	5320.03	26.0	3.642	-2.490	NIST-MAY74
FeI	5321.10	26.0	4.435	-1.090	NIST-OBR91

The table continues on the next page

Species	Wavelength Å	Ion	EP eV	log(gf)	Source
FeI	5322.04	26.0	2.279	-2.803	NIST-OBR91
FeI	5324.17	26.0	3.211	-0.110	RUF14
FeI	5328.03	26.0	0.914	-1.470	OBR91
FeI	5339.92	26.0	3.263	-0.630	DEN14
FeI	5361.62	26.0	4.415	-1.410	NIST-MAY74
FeI	5364.87	26.0	4.446	0.228	NIST-OBR91
FeI	5365.39	26.0	3.573	-1.020	NIST-OBR91
FeI	5367.46	26.0	4.415	0.443	NIST-OBR91
FeI	5369.96	26.0	4.371	0.536	NIST-OBR91
FeI	5373.70	26.0	4.473	-0.710	RUF14
FeI	5376.83	26.0	4.294	-2.280	NIST-MAY74
FeI	5379.57	26.0	3.692	-1.420	BEL17
FeI	5383.36	26.0	4.312	0.645	NIST-OBR91
FeI	5385.57	26.0	3.695	-2.920	NIST-MAY74
FeI	5386.33	26.0	4.154	-1.740	NIST-MAY74
FeI	5393.16	26.0	3.241	-0.720	RUF14
FeI	5395.21	26.0	4.446	-2.150	NIST-MAY74
FeI	5398.27	26.0	4.446	-0.710	NIST-MAY74
FeI	5401.26	26.0	4.320	-1.890	NIST-MAY74
FeI	5405.77	26.0	0.989	-1.850	OBR91
FeI	5409.13	26.0	4.371	-1.270	NIST-MAY74
FeI	5410.91	26.0	4.473	0.398	NIST-OBR91
FeI	5412.78	26.0	4.435	-1.716	NIST-BAR94
FeI	5415.19	26.0	4.386	0.642	NIST-OBR91
FeI	5417.03	26.0	4.415	-1.660	NIST-MAY74
FeI	5434.52	26.0	1.010	-2.130	OBR91
FeI	5436.29	26.0	4.386	-1.510	NIST-MAY74
FeI	5436.59	26.0	2.279	-2.964	NIST-OBR91
FeI	5441.33	26.0	4.312	-1.700	NIST-MAY74
FeI	5461.55	26.0	4.446	-1.880	NIST-MAY74
FeI	5463.27	26.0	4.435	0.070	NIST-BRI74
FeI	5464.27	26.0	4.143	-1.402	NIST-OBR91
FeI	5470.09	26.0	4.446	-1.790	NIST-MAY74
FeI	5473.16	26.0	4.191	-2.110	NIST-MAY74
FeI	5473.90	26.0	4.154	-0.720	RUF14
FeI	5476.56	26.0	4.100	-0.280	DEN14
FeI	5481.24	26.0	4.103	-1.243	NIST-OBR91
FeI	5483.09	26.0	4.151	-1.390	DEN14

The table continues on the next page

Species	Wavelength Å	Ion	EP eV	log(gf)	Source
FeI	5487.14	26.0	4.415	-1.510	NIST-MAY74
FeI	5491.83	26.0	4.186	-2.188	NIST-BAR94
FeI	5494.46	26.0	4.076	-2.050	NIST-MAY74
FeI	5501.46	26.0	0.957	-3.050	OBR91
FeI	5506.77	26.0	0.989	-2.790	OBR91
FeI	5522.44	26.0	4.209	-1.520	NIST-MAY74
FeI	5525.54	26.0	4.231	-1.084	NIST-BAR94
FeI	5531.98	26.0	4.913	-1.600	NIST-MAY74
FeI	5536.58	26.0	2.831	-3.730	NIST-MAY74
FeI	5538.51	26.0	3.634	-1.540	RUF14
FeI	5539.28	26.0	3.642	-2.610	NIST-MAY74
FeI	5543.93	26.0	4.218	-1.110	NIST-MAY74
FeI	5546.50	26.0	4.371	-1.280	NIST-MAY74
FeI	5546.99	26.0	4.218	-1.880	NIST-MAY74
FeI	5549.95	26.0	3.695	-2.860	NIST-MAY74
FeI	5552.69	26.0	4.956	-1.980	NIST-MAY74
FeI	5553.57	26.0	4.435	-1.380	NIST-MAY74
FeI	5554.89	26.0	4.549	-0.270	RUF14
FeI	5560.21	26.0	4.435	-1.160	NIST-MAY74
FeI	5567.39	26.0	2.609	-2.671	NIST-OBR91
FeI	5569.61	26.0	3.414	-0.520	DEN14
FeI	5572.84	26.0	3.394	-0.280	DEN14
FeI	5573.10	26.0	4.188	-1.290	DEN14
FeI	5576.08	26.0	3.430	-0.940	NIST-MAY74
FeI	5584.76	26.0	3.573	-2.270	NIST-MAY74
FeI	5586.75	26.0	3.366	-0.110	DEN14
FeI	5594.65	26.0	4.549	-0.658	NIST-OBR91
FeI	5615.64	26.0	3.332	0.040	RUF14
FeI	5618.63	26.0	4.206	-1.250	DEN14
FeI	5619.59	26.0	4.386	-1.670	NIST-MAY74
FeI	5624.02	26.0	4.386	-1.450	NIST-MAY74
FeI	5633.94	26.0	4.991	-0.320	NIST-MAY74
FeI	5635.82	26.0	4.256	-1.860	NIST-MAY74
FeI	5636.69	26.0	3.640	-2.560	NIST-MAY74
FeI	5638.26	26.0	4.220	-0.720	RUF14
FeI	5641.43	26.0	4.256	-1.150	NIST-MAY74
FeI	5649.98	26.0	5.100	-0.920	NIST-MAY74
FeI	5650.70	26.0	5.086	-0.960	NIST-MAY74

The table continues on the next page

Species	Wavelength Å	Ion	EP eV	log(gf)	Source
FeI	5652.31	26.0	4.260	-1.920	NIST-MAY74
FeI	5653.86	26.0	4.386	-1.610	NIST-MAY74
FeI	5655.17	26.0	5.064	-0.690	NIST-MAY74
FeI	5661.34	26.0	4.284	-1.756	NIST-BAR94
FeI	5662.51	26.0	4.175	-0.410	DEN14
FeI	5667.51	26.0	4.178	-1.576	NIST-OBR91
FeI	5679.02	26.0	4.652	-0.900	NIST-MAY74
FeI	5680.24	26.0	4.186	-2.540	NIST-MAY74
FeI	5686.53	26.0	4.549	-0.446	NIST-OBR91
FeI	5691.49	26.0	4.301	-1.490	NIST-MAY74
FeI	5696.08	26.0	4.549	-1.720	NIST-BAR94
FeI	5698.02	26.0	3.640	-2.630	NIST-MAY74
FeI	5701.54	26.0	2.559	-2.216	NIST-BLA82
FeI	5705.46	26.0	4.301	-1.355	NIST-BAR94
FeI	5717.83	26.0	4.284	-0.960	RUF14
FeI	5731.76	26.0	4.256	-1.270	NIST-MAY74
FeI	5741.84	26.0	4.256	-1.673	NIST-OBR91
FeI	5742.96	26.0	4.178	-2.470	NIST-MAY74
FeI	5754.40	26.0	3.642	-2.650	NIST-MAY74
FeI	5760.34	26.0	3.642	-2.440	NIST-MAY74
FeI	5762.99	26.0	4.209	-0.470	NIST-BRI74
FeI	5775.08	26.0	4.217	-1.080	DEN14
FeI	5778.45	26.0	2.588	-3.430	NIST-BAR94
FeI	5784.65	26.0	3.397	-2.670	RUF14
FeI	5793.91	26.0	4.220	-1.660	NIST-MAY74
FeI	5806.72	26.0	4.608	-1.030	NIST-MAY74
FeI	5809.21	26.0	3.884	-1.790	NIST-MAY74
FeI	5814.80	26.0	4.283	-1.940	NIST-MAY74
FeI	5815.21	26.0	4.154	-2.580	NIST-MAY74
FeI	5838.37	26.0	3.943	-2.290	NIST-MAY74
FeI	5852.21	26.0	4.549	-1.300	NIST-MAY74
FeI	5855.07	26.0	4.608	-1.478	NIST-BAR94
FeI	5856.08	26.0	4.294	-1.328	NIST-OBR91
FeI	5879.48	26.0	4.607	-2.120	NIST-MAY74
FeI	5883.81	26.0	3.960	-1.310	NIST-MAY74
FeI	5905.67	26.0	4.652	-0.770	NIST-MAY74
FeI	5909.97	26.0	3.211	-2.587	NIST-BAR94
FeI	5916.24	26.0	2.453	-2.994	NIST-BLA82

The table continues on the next page

Species	Wavelength Å	Ion	EP eV	log(gf)	Source
FeI	5927.78	26.0	4.652	-1.070	NIST-MAY74
FeI	5929.67	26.0	4.549	-1.380	NIST-MAY74
FeI	5934.65	26.0	3.929	-1.120	NIST-MAY74
FeI	5952.71	26.0	3.984	-1.390	NIST-MAY74
FeI	5956.69	26.0	0.858	-4.500	OBR91
FeI	6003.01	26.0	3.882	-1.100	RUF14
FeI	6008.55	26.0	3.884	-0.980	RUF14
FeI	6012.21	26.0	2.223	-4.038	NIST-BAR94
FeI	6027.05	26.0	4.076	-1.089	NIST-OBR91
FeI	6056.00	26.0	4.733	-0.320	RUF14
FeI	6065.48	26.0	2.609	-1.530	NIST-BLA82
FeI	6079.00	26.0	4.652	-1.100	NIST-MAY74
FeI	6082.71	26.0	2.223	-3.573	NIST-BLA82
FeI	6093.64	26.0	4.608	-1.470	NIST-MAY74
FeI	6094.37	26.0	4.652	-1.920	NIST-MAY74
FeI	6096.66	26.0	3.984	-1.880	NIST-MAY74
FeI	6120.24	26.0	0.915	-5.970	NIST-BLA82
FeI	6127.90	26.0	4.143	-1.399	NIST-OBR91
FeI	6136.61	26.0	2.453	-1.400	NIST-BLA82
FeI	6136.99	26.0	2.196	-2.930	OBR91
FeI	6137.69	26.0	2.588	-1.403	NIST-BLA82
FeI	6151.61	26.0	2.174	-3.370	OBR91
FeI	6157.72	26.0	4.076	-1.220	NIST-MAY74
FeI	6165.36	26.0	4.143	-1.474	NIST-OBR91
FeI	6173.33	26.0	2.223	-2.880	NIST-BLA82
FeI	6180.20	26.0	2.728	-2.649	NIST-OBR91
FeI	6187.99	26.0	3.943	-1.670	NIST-MAY74
FeI	6191.55	26.0	2.433	-1.416	NIST-OBR91
FeI	6200.31	26.0	2.609	-2.437	NIST-BLA82
FeI	6213.43	26.0	2.223	-2.482	NIST-OBR91
FeI	6215.14	26.0	4.186	-1.320	NIST-OBR91
FeI	6219.28	26.0	2.196	-2.450	OBR91
FeI	6229.22	26.0	2.845	-2.805	NIST-BAR94
FeI	6230.72	26.0	2.559	-1.281	NIST-BLA82
FeI	6232.64	26.0	3.651	-1.240	DEN14
FeI	6240.64	26.0	2.223	-3.173	NIST-OBR91
FeI	6246.31	26.0	3.600	-0.770	DEN14
FeI	6252.55	26.0	2.404	-1.687	NIST-BLA82

The table continues on the next page

Species	Wavelength Å	Ion	EP eV	log(gf)	Source
FeI	6265.13	26.0	2.174	-2.540	OBR91
FeI	6270.22	26.0	2.858	-2.609	NIST-OBR91
FeI	6271.27	26.0	3.332	-2.703	NIST-BAR94
FeI	6280.61	26.0	0.858	-4.390	OBR91
FeI	6301.50	26.0	3.651	-0.710	DEN14
FeI	6311.50	26.0	2.832	-3.141	NIST-BAR94
FeI	6315.81	26.0	4.076	-1.630	RUF14
FeI	6322.68	26.0	2.588	-2.426	NIST-BLA82
FeI	6330.84	26.0	4.733	-1.720	NIST-MAY74
FeI	6335.33	26.0	2.196	-2.180	OBR91
FeI	6336.82	26.0	3.684	-0.850	DEN14
FeI	6338.87	26.0	4.795	-1.040	NIST-MAY74
FeI	6344.14	26.0	2.433	-2.923	NIST-BLA82
FeI	6353.83	26.0	0.915	-6.477	NIST-BLA86
FeI	6355.02	26.0	2.845	-2.291	NIST-OBR91
FeI	6358.69	26.0	0.859	-4.468	NIST-BLA79
FeI	6364.36	26.0	4.795	-1.410	NIST-MAY74
FeI	6380.74	26.0	4.186	-1.376	NIST-OBR91
FeI	6393.60	26.0	2.433	-1.576	NIST-OBR91
FeI	6400.00	26.0	3.603	-0.270	RUF14
FeI	6400.31	26.0	0.914	-4.320	OBR91
FeI	6408.01	26.0	3.684	-0.990	DEN14
FeI	6411.64	26.0	3.651	-0.590	DEN14
FeI	6419.94	26.0	4.733	-0.270	NIST-MAY74
FeI	6421.35	26.0	2.279	-2.027	NIST-BLA82
FeI	6430.84	26.0	2.174	-1.950	OBR91
FeI	6469.19	26.0	4.835	-0.810	NIST-MAY74
FeI	6475.62	26.0	2.559	-2.942	NIST-OBR91
FeI	6481.87	26.0	2.279	-2.984	NIST-BLA82
FeI	6494.98	26.0	2.404	-1.273	NIST-BLA82
FeI	6495.74	26.0	4.835	-0.920	NIST-MAY74
FeI	6496.46	26.0	4.795	-0.610	NIST-MAY74
FeI	6498.94	26.0	0.957	-4.690	OBR91
FeI	6518.36	26.0	2.832	-2.298	NIST-OBR91
FeI	6533.92	26.0	4.559	-1.430	NIST-MAY74
FeI	6546.23	26.0	2.759	-1.536	NIST-OBR91
FeI	6569.21	26.0	4.733	-0.450	NIST-MAY74
FeI	6574.22	26.0	0.989	-5.020	OBR91

The table continues on the next page

Species	Wavelength Å	Ion	EP eV	log(gf)	Source
FeI	6575.01	26.0	2.588	-2.710	NIST-OBR91
FeI	6581.21	26.0	1.485	-4.679	NIST-BAR91
FeI	6592.91	26.0	2.728	-1.473	NIST-OBR91
FeI	6593.87	26.0	2.433	-2.422	NIST-BLA82
FeI	6597.56	26.0	4.795	-1.050	NIST-MAY74
FeI	6609.11	26.0	2.559	-2.692	NIST-BLA82
FeI	6625.02	26.0	1.011	-5.336	NIST-BLA86
FeI	6627.54	26.0	4.549	-1.590	RUF14
FeI	6633.74	26.0	4.559	-0.799	NIST-OBR91
FeI	6648.08	26.0	1.011	-5.918	NIST-BLA86
FeI	6667.71	26.0	4.584	-2.112	NIST-BAR94
FeI	6677.98	26.0	2.692	-1.418	NIST-OBR91
FeI	6699.14	26.0	4.593	-2.101	NIST-BAR94
FeI	6703.56	26.0	2.759	-3.060	NIST-MAY74
FeI	6705.10	26.0	4.607	-0.870	RUF14
FeI	6725.35	26.0	4.103	-2.100	RUF14
FeI	6739.52	26.0	1.557	-4.794	NIST-BAR91
FeI	6750.15	26.0	2.424	-2.621	NIST-BLA82
FeI	6752.70	26.0	4.638	-1.204	NIST-BAR94
FeI	6786.86	26.0	4.191	-2.020	NIST-MAY74
FeI	6793.25	26.0	4.076	-2.326	NIST-BAR94
FeI	6804.27	26.0	4.584	-1.813	NIST-BAR94
FeI	6806.84	26.0	2.728	-2.130	NIST-MAY74
FeI	6810.26	26.0	4.607	-0.986	NIST-OBR91
FeI	6820.37	26.0	4.638	-1.290	NIST-MAY74
FeI	6828.59	26.0	4.638	-0.890	NIST-MAY74
FeI	6837.00	26.0	4.593	-1.687	NIST-BAR94
FeI	6839.83	26.0	2.559	-3.350	NIST-MAY74
FeI	6841.33	26.0	4.607	-0.490	RUF14
FeI	6842.68	26.0	4.638	-1.290	NIST-MAY74
FeI	6843.65	26.0	4.549	-0.730	RUF14
FeI	7022.95	26.0	4.188	-1.050	DEN14
FeI	7071.85	26.0	4.610	-1.170	RUF14
FeI	7130.92	26.0	4.214	-0.690	DEN14
FeI	7181.19	26.0	4.220	-1.110	RUF14
FeI	7445.75	26.0	4.253	-0.230	DEN14
FeI	7491.64	26.0	4.298	-1.060	DEN14
FeI	7495.06	26.0	4.220	-0.100	RUF14

The table continues on the next page

Species	Wavelength Å	Ion	EP eV	log(gf)	Source
FeI	7511.02	26.0	4.175	0.120	DEN14
FeI	7586.01	26.0	4.312	-0.270	RUF14
FeI	7710.36	26.0	4.217	-1.070	DEN14
FeI	8514.06	26.0	2.196	-2.200	OBR91
FeI	8515.10	26.0	3.018	-2.073	NIST-OBR91
FeI	8571.80	26.0	5.009	-1.110	RUF14
FeI	8582.25	26.0	2.990	-2.133	NIST-OBR91
FeI	8598.83	26.0	4.383	-1.200	DEN14
FeI	8611.80	26.0	2.845	-1.850	NIST-OBR91
FeI	8621.60	26.0	2.949	-2.321	NIST-OBR91
FeI	8674.74	26.0	2.832	-1.680	NIST-OBR91
FeI	8688.62	26.0	2.174	-1.200	OBR91
FeI	8699.45	26.0	4.956	-0.370	RUF14
FeI	8757.18	26.0	2.845	-1.915	NIST-OBR91
FeI	8784.44	26.0	4.952	-1.140	DEN14
FeI	8824.22	26.0	2.196	-1.540	OBR91
FeI	8846.74	26.0	5.006	-0.560	DEN14
FeII	4122.66	26.1	2.583	-3.260	MEL09
FeII	4128.74	26.1	2.583	-3.630	MEL09
FeII	4178.86	26.1	2.583	-2.510	MEL09
FeII	4296.57	26.1	2.705	-2.920	MEL09
FeII	4303.17	26.1	2.704	-2.520	DEN19
FeII	4369.41	26.1	2.779	-3.650	MEL09
FeII	4384.31	26.1	2.657	-3.440	MEL09
FeII	4385.37	26.1	2.778	-2.640	DEN19
FeII	4416.81	26.1	2.778	-2.570	DEN19
FeII	4489.18	26.1	2.828	-2.960	MEL09
FeII	4491.40	26.1	2.856	-2.710	MEL09
FeII	4508.28	26.1	2.855	-2.420	DEN19
FeII	4515.33	26.1	2.844	-2.600	MEL09
FeII	4541.52	26.1	2.856	-2.980	MEL09
FeII	4555.89	26.1	2.828	-2.400	MEL09
FeII	4576.34	26.1	2.844	-2.950	MEL09
FeII	4582.83	26.1	2.844	-3.180	MEL09
FeII	4620.52	26.1	2.828	-3.210	MEL09
FeII	4666.75	26.1	2.828	-3.280	MEL09
FeII	4893.82	26.1	2.828	-4.210	MEL09
FeII	4923.92	26.1	2.891	-1.260	MEL09

The table continues on the next page

Species	Wavelength Å	Ion	EP eV	log(gf)	Source
FeII	4993.35	26.1	2.807	-3.620	MEL09
FeII	5000.74	26.1	2.779	-4.610	MEL09
FeII	5018.44	26.1	2.891	-1.100	MEL09
FeII	5100.66	26.1	2.807	-4.170	MEL09
FeII	5132.66	26.1	2.807	-4.080	MEL09
FeII	5136.80	26.1	2.844	-4.430	MEL09
FeII	5169.03	26.1	2.891	-1.000	MEL09
FeII	5197.57	26.1	3.231	-2.220	MEL09
FeII	5234.62	26.1	3.222	-2.180	MEL09
FeII	5256.93	26.1	2.891	-4.060	MEL09
FeII	5264.81	26.1	3.230	-3.130	MEL09
FeII	5284.10	26.1	2.891	-3.110	MEL09
FeII	5316.61	26.1	3.153	-1.870	MEL09
FeII	5325.55	26.1	3.222	-3.160	MEL09
FeII	5362.86	26.1	3.200	-2.570	MEL09
FeII	5414.07	26.1	3.222	-3.580	MEL09
FeII	5425.25	26.1	3.200	-3.220	MEL09
FeII	5525.12	26.1	3.268	-3.970	MEL09
FeII	5534.84	26.1	3.245	-2.750	MEL09
FeII	5627.49	26.1	3.387	-4.100	MEL09
FeII	5991.37	26.1	3.153	-3.540	MEL09
FeII	6084.11	26.1	3.200	-3.790	MEL09
FeII	6113.32	26.1	3.222	-4.140	MEL09
FeII	6129.70	26.1	3.200	-4.640	MEL09
FeII	6149.25	26.1	3.889	-2.690	MEL09
FeII	6239.95	26.1	3.889	-3.410	MEL09
FeII	6247.55	26.1	3.892	-2.300	MEL09
FeII	6369.46	26.1	2.891	-4.110	MEL09
FeII	6383.72	26.1	5.553	-2.240	MEL09
FeII	6416.91	26.1	3.892	-2.640	MEL09
FeII	6432.68	26.1	2.891	-3.570	MEL09
FeII	6442.95	26.1	5.549	-2.440	MEL09
FeII	6446.41	26.1	6.223	-1.970	MEL09
FeII	6456.38	26.1	3.904	-2.050	MEL09
FeII	6516.08	26.1	2.891	-3.310	MEL09
CoI	-4121.318	27.0	0.922	-0.33	LAW15
NiI	4904.410	28.0	3.542	-0.170	NIST-KOS82
NiI	5017.576	28.0	3.536	-0.030	WOO14

The table continues on the next page

Species	Wavelength Å	Ion	EP eV	log(gf)	Source
NiI	5035.362	28.0	3.633	0.290	WOO14
NiI	5080.533	28.0	3.652	0.320	WOO14
NiI	5084.080	28.0	3.678	0.030	NIST-KOS82
NiI	6108.116	28.0	1.675	-2.600	WOO14
NiI	6176.812	28.0	4.085	-0.260	WOO14
NiI	6223.984	28.0	4.102	-0.910	WOO14
NiI	6643.630	28.0	1.675	-2.220	WOO14
NiI	6767.772	28.0	1.825	-2.140	WOO14
CuI	-5105.531	29.0	1.388	-1.516	KURUCZ
CuI	-5782.113	29.0	1.641	-1.720	KURUCZ
ZnI	4722.150	30.0	4.030	-0.370	ROE12
ZnI	4810.530	30.0	4.078	-0.150	ROE12
SrI	4607.330	38.0	0.000	0.283	NIST-PAR76
SrII	4077.714	38.1	0.000	0.148	NIST
SrII	4161.796	38.1	2.940	-0.470	NIST
SrII	4215.524	38.1	0.000	-0.173	NIST
YII	3788.697	39.1	0.104	-0.070	BIE11
YII	3950.356	39.1	0.104	-0.490	BIE11
YII	4398.010	39.1	0.129	-1.000	BIE11
YII	4883.682	39.1	1.084	0.070	NIST-HAN82
YII	5087.420	39.1	1.083	-0.170	BIE11
YII	5200.413	39.1	0.992	-0.570	BIE11
ZrII	4208.980	40.1	0.713	-0.510	LJU06
ZrII	5112.270	40.1	1.665	-0.850	LJU06
BaII	-4554.029	56.1	0.000	0.170	GAL67
BaII	-5853.668	56.1	0.604	-1.010	GAL67
BaII	-6141.713	56.1	0.703	-0.077	GAL67
BaII	-6496.897	56.1	0.604	-0.380	GAL67
LaII	-3949.100	57.1	0.403	0.49	LAW01
LaII	-3988.510	57.1	0.403	0.21	LAW01
LaII	-3995.740	57.1	0.173	-0.06	LAW01
LaII	-4086.710	57.1	0.000	-0.07	LAW01
LaII	-4123.220	57.1	0.321	0.13	LAW01
LaII	-4333.750	57.1	0.173	-0.06	LAW01
LaII	4921.780	57.1	0.244	-0.45	LAW01
LaII	-6262.290	57.1	0.403	-1.22	LAW01
LaII	-6390.480	57.1	0.321	-1.41	LAW01
ZrII	4137.645	58.1	0.516	0.40	LAW09

The table continues on the next page

Species	Wavelength Å	Ion	EP eV	log(gf)	Source
ZrII	4165.599	58.1	0.909	0.52	LAW09
ZrII	4382.165	58.1	0.683	0.13	LAW09
ZrII	4486.909	58.1	0.295	-0.18	LAW09
ZrII	4562.359	58.1	0.477	0.21	LAW09
ZrII	4628.161	58.1	0.516	0.14	LAW09
PrII	-4062.805	59.1	0.422	0.33	SNE09
PrII	-4143.131	59.1	0.371	0.60	SNE09
PrII	-4222.946	59.1	0.055	0.23	SNE09
PrII	-4408.810	59.1	0.000	0.05	SNE09
NdII	4023.000	60.1	0.559	0.04	DEN03,ROE08
NdII	4462.980	60.1	0.559	0.04	DEN03,ROE08
NdII	4706.540	60.1	0.000	-0.71	DEN03,ROE08
NdII	4825.480	60.1	0.182	-0.42	DEN03,ROE08
NdII	4959.120	60.1	0.064	-0.80	DEN03,ROE08
NdII	5092.790	60.1	0.380	-0.61	DEN03,ROE08
NdII	5130.590	60.1	1.303	0.45	DEN03,ROE08
NdII	5319.810	60.1	0.550	-0.14	DEN03,ROE08
EuII	-3819.670	63.1	0.000	0.51	LAW01b
EuII	-4129.720	63.1	0.000	0.22	LAW01b
EuII	-6645.071	63.1	1.379	-0.51	LAW01b

Table B.2: References for the atomic transition parameters adopted in our line list. A preffix NIST in the sources denotes the line had its transition parameters updated by NIST. In case only NIST is listed as a source, the source of the original measurement or computation of the transition parameter can be found on the NIST website.

Source	Reference
BAR91	Bard et al. (1991)
BAR94	Bard & Kock (1994)
BEL17	Belmonte et al. (2017)
BIE11	Biémont et al. (2011)
BLA79	Blackwell et al. (1979)
BLA82	Blackwell et al. (1982)
BLA83	Blackwell et al. (1983)
BLA86	Blackwell et al. (1986)
BOO84	Booth et al. (1984)

The table continues on the next page

Source	Reference
BRI74	Bridges & Kornblith (1974)
BUT93	Butler et al. (1993)
CHA90	Chang & Tang (1990)
DEN03	Den Hartog et al. (2003)
DEN11	Den Hartog et al. (2011)
DEN14	Den Hartog et al. (2014)
DEN19	Den Hartog et al. (2019)
GAL67	Gallagher (1967)
GAR73	Garz (1973)
HAN82	Hannaford et al. (1982)
JON96	Jones et al. (1996)
KOC84	Kock et al. (1984)
KOS64	Köstlin (1964)
KOS82	Kostyk (1982)
KOS83	Kostyk & Orlova (1983)
KURUCZ	http://kurucz.harvard.edu/linelists.html
LAW01	Lawler et al. (2001a)
LAW01b	Lawler et al. (2001b)
LAW09	Lawler et al. (2009)
LAW13	Lawler et al. (2013)
LAW14	Lawler et al. (2014)
LAW15	Lawler et al. (2015)
LAW17	Lawler et al. (2017)
LAW19	Lawler et al. (2019)
LJU06	Ljung et al. (2006)
MAT01	Matheron et al. (2001)
MAY74	May et al. (1974)
MEL09	Meléndez & Barbuy (2009b)
MEN95	Mendoza et al. (1995)
NIST	https://www.nist.gov/pml/atomic-spectra-database
OBR91	O'Brian et al. (1991)
OLS59	Olsen et al. (1959)
PAR76	Parkinson et al. (1976)
PIC02	Pickering et al. (2001, 2002)
ROB73	Roberts et al. (1973)
ROE08	Roederer et al. (2008)
ROE12	Roederer & Lawler (2012)
RUF14	Ruffoni et al. (2014)

The table continues on the next page

Source	Reference
SMI66	Smith & Gallagher (1966)
SNE09	Sneden et al. (2009)
SOB07	Sobeck et al. (2007)
WOL73	Wolnik & Berthel (1973)
WOO13	Wood et al. (2013)
WOO14	Wood et al. (2014)
ZAT06	Zatsarinny & Bartschat (2006)

Bibliography

Afşar, M., Bozkurt, Z., Böcek Topcu, G., et al. 2018, AJ, 155, 240, doi: 10.3847/1538-3881/aabe86 ↑70, ↑75, ↑146

Alcock, C., Allsman, R., Alves, D. R., et al. 2000, ApJ, 542, 257, doi: 10.1086/309530 ↑17

Alcock, C., Allsman, R. A., Alves, D. R., et al. 2001, ApJS, 136, 439, doi: 10.1086/322529 ↑42

Andrievsky, S., Wallerstein, G., Korotin, S., et al. 2018, PASP, 130, 024201, doi: 10.1088/1538-3873/aa9783 ↑74

Andrievsky, S. M., Spite, M., Korotin, S. A., et al. 2007, A&A, 464, 1081, doi: 10.1051/0004-6361:20066232 ↑55

—. 2008, A&A, 481, 481, doi: 10.1051/0004-6361:20078837 ↑55, ↑123

Ashman, K. M., & Zepf, S. E. 1992, ApJ, 384, 50, doi: 10.1086/170850 ↑6

Asplund, M., Grevesse, N., Sauval, A. J., & Scott, P. 2009, ARA&A, 47, 481, doi: 10.1146/annurev.astro.46.060407.145222 ↑84

Baade, W. 1956, PASP, 68, 5, doi: 10.1086/126870 ↑21

Bailey, S. I. 1902, Annals of Harvard College Observatory, 38 ↑21

—. 1919, ApJ, 50, 233, doi: 10.1086/142502 ↑19

Bailey, S. I., & Pickering, E. C. 1913, Annals of Harvard College Observatory, 78, 1 ↑20

Barbuy, B., Chiappini, C., & Gerhard, O. 2018, ARA&A, 56, 223, doi: 10.1146/annurev-astro-081817-051826 ↑8

Barbuy, B., Friaça, A. C. S., da Silveira, C. R., et al. 2015, A&A, 580, A40, doi: 10.1051/0004-6361/201525694 ↑61

Bard, A., Kock, A., & Kock, M. 1991, A&A, 248, 315 ↑173

Bard, A., & Kock, M. 1994, A&A, 282, 1014 ↑173

Barklem, P. S., Christlieb, N., Beers, T. C., et al. 2005, A&A, 439, 129, doi: 10.1051/0004-6361:20052967 ↑xii, ↑125

Bastian, N., Covey, K. R., & Meyer, M. R. 2010, ARA&A, 48, 339, doi: 10.1146/annurev-astro-082708-101642 ↑27

Bastian, N., & Lardo, C. 2018, ARA&A, 56, 83, doi: 10.1146/annurev-astro-081817-051839 ↑24, ↑54

Battistini, C., & Bensby, T. 2015, A&A, 577, A9, doi: 10.1051/0004-6361/201425327 ↑58, ↑64

—. 2016, A&A, 586, A49, doi: 10.1051/0004-6361/201527385 ↑viii, ↑56, ↑64

Beaton, R. L., Freedman, W. L., Madore, B. F., et al. 2016, ApJ, 832, 210, doi: 10.3847/0004-637X/832/2/210 ↑26

Beaton, R. L., Bono, G., Braga, V. F., et al. 2018, Space Sci. Rev., 214, 113, doi: 10.1007/s11214-018-0542-1 ↑2, ↑26

Bedin, L. R., Piotto, G., Anderson, J., et al. 2004, Memorie della Societa Astronomica Italiana Supplementi, 5, 105 ↑24

Bekki, K., & Freeman, K. C. 2003, MNRAS, 346, L11, doi: 10.1046/j.1365-2966.2003.07275.x ↑55

Belmonte, M. T., Pickering, J. C., Ruffoni, M. P., et al. 2017, ApJ, 848, 125, doi: 10.3847/1538-4357/aa8cd3 ↑173

Belokurov, V., Erkal, D., Evans, N. W., Koposov, S. E., & Deason, A. J. 2018, MNRAS, 478, 611, doi: 10.1093/mnras/sty982 ↑7, ↑13

Bensby, T., Feltzing, S., & Oey, M. S. 2014, A&A, 562, A71, doi: 10.1051/0004-6361/201322631 ↑12

Bensby, T., Feltzing, S., Gould, A., et al. 2017, A&A, 605, A89, doi: 10.1051/0004-6361/201730560 ↑viii, ↑8, ↑56, ↑122

Bergemann, M., & Cescutti, G. 2010, A&A, 522, A9, doi: 10.1051/0004-6361/201014250 ↑60

Bergemann, M., & Gehren, T. 2008, A&A, 492, 823, doi: 10.1051/0004-6361:200810098 ↑60, ↑126

Bergemann, M., Pickering, J. C., & Gehren, T. 2010, MNRAS, 401, 1334, doi: 10.1111/j.1365-2966.2009.15736.x ↑59

Bergemann, M., Gallagher, A. J., Eitner, P., et al. 2019, A&A, 631, A80, doi: 10.1051/0004-6361/201935811 ↑126

Biémont, É., Blagoev, K., Engström, L., et al. 2011, MNRAS, 414, 3350, doi: 10.1111/j.1365-2966.2011.18637.x ↑173

Bisterzo, S., Gallino, R., Straniero, O., Cristallo, S., & Käppeler, F. 2011, MNRAS, 418, 284, doi: 10.1111/j.1365-2966.2011.19484.x ↑61, ↑64

Bisterzo, S., Travaglio, C., Gallino, R., Wiescher, M., & Käppeler, F. 2014, ApJ, 787, 10, doi: 10.1088/0004-637X/787/1/10 ↑61

Blackwell, D. E., Booth, A. J., Haddock, D. J., Petford, A. D., & Leggett, S. K. 1986, MNRAS, 220, 549, doi: 10.1093/mnras/220.3.549 ↑173

Blackwell, D. E., Menon, S. L. R., & Petford, A. D. 1983, MNRAS, 204, 883, doi: 10.1093/mnras/204.3.883 ↑173

Blackwell, D. E., Petford, A. D., & Shallis, M. J. 1979, MNRAS, 186, 657, doi: 10.1093/mnras/186.4.657 ↑173

Blackwell, D. E., Petford, A. D., Shallis, M. J., & Simmons, G. J. 1982, MNRAS, 199, 43, doi: 10.1093/mnras/199.1.43 ↑173

Blanco-Cuaresma, S., Soubiran, C., Heiter, U., et al. 2015, A&A, 577, A47, doi: 10.1051/0004-6361/201425232 ↑1

Bland-Hawthorn, J., & Gerhard, O. 2016, ARA&A, 54, 529, doi: 10.1146/annurev-astro-081915-023441 ↑8, ↑11

Blažko, S. 1907, Astronomische Nachrichten, 175, 325, doi: 10.1002/asna.19071752002 ↑17, ↑21

Bono, G., Caputo, F., Castellani, V., et al. 1995a, ApJ, 442, 159, doi: 10.1086/175430 ↑31

Bono, G., Caputo, F., Castellani, V., Marconi, M., & Storm, J. 2001, MNRAS, 326, 1183, doi: 10.1046/j.1365-8711.2001.04655.x ↑vii, ↑22, ↑35, ↑37

Bono, G., Caputo, F., Castellani, V., et al. 2003, MNRAS, 344, 1097, doi: 10.1046/j.1365-8711.2003.06878.x ↑35, ↑37, ↑38

Bono, G., Caputo, F., & Marconi, M. 1995b, AJ, 110, 2365, doi: 10.1086/117694 ↑34

Bono, G., Castellani, V., & Marconi, M. 2000, ApJ, 532, L129, doi: 10.1086/312582 ↑22

Bono, G., Marconi, M., & Stellingwerf, R. F. 1999, ApJS, 122, 167, doi: 10.1086/313207 ↑vi, ↑vii, ↑32, ↑33, ↑34

Bono, G., & Stellingwerf, R. F. 1994, ApJS, 93, 233, doi: 10.1086/192054 ↑vii, ↑22, ↑31, ↑33

Bono, G., Genovali, K., Lemasle, B., et al. 2015, in Astronomical Society of the Pacific Conference Series, Vol. 491, Fifty Years of Wide Field Studies in the Southern Hemisphere: Resolved Stellar Populations of the Galactic Bulge and Magellanic Clouds, ed. S. Points & A. Kunder, 148 ↑8

Bono, G., Iannicola, G., Braga, V. F., et al. 2019, ApJ, 870, 115, doi: 10.3847/1538-4357/aaf23f ↑40

Bono, G., Braga, V. F., Crestani, J., et al. 2020, ApJ, 896, L15, doi: 10.3847/2041-8213/ab9538 ↑4, ↑140, ↑142, ↑153

Booth, A. J., Blackwell, D. E., Petford, A. D., & Shallis, M. J. 1984, MNRAS, 208, 147, doi: 10.1093/mnras/208.1.147 ↑173

Braga, V. F., Stetson, P. B., Bono, G., et al. 2016, AJ, 152, 170, doi: 10.3847/0004-6256/152/6/170 ↑v, ↑vii, ↑19, ↑36, ↑137

—. 2018, AJ, 155, 137, doi: 10.3847/1538-3881/aaadab ↑v, ↑vii, ↑19, ↑36

—. 2019, A&A, 625, A1, doi: 10.1051/0004-6361/201834893 ↑26, ↑39

Braga, V. F., Crestani, J., Fabrizio, M., et al. 2021a, arXiv e-prints, arXiv:2107.00923. https://arxiv.org/abs/2107.00923 ↑4

—. 2021b, ApJ, 919, 85, doi: 10.3847/1538-4357/ac1074 ↑141, ↑153

Bragaglia, A., Carretta, E., Gratton, R., et al. 2010, A&A, 519, A60, doi: 10.1051/0004-6361/201014702 ↑24

Bridges, J. M., & Kornblith, R. L. 1974, ApJ, 192, 793, doi: 10.1086/153118 ↑174

Bullock, J. S., & Boylan-Kolchin, M. 2017, ARA&A, 55, 343, doi: 10.1146/annurev-astro-091916-055313 ↑6

Bullock, J. S., Kravtsov, A. V., & Weinberg, D. H. 2001, ApJ, 548, 33, doi: 10.1086/318681 ↑45

Burris, D. L., Pilachowski, C. A., Armandroff, T. E., et al. 2000, ApJ, 544, 302, doi: 10.1086/317172 ↑viii, ↑56, ↑64

Butler, D. 1975, ApJ, 200, 68, doi: 10.1086/153761 ↑42

Butler, K., Mendoza, C., & Zeippen, C. J. 1993, Journal of Physics B Atomic Molecular Physics, 26, 4409, doi: 10.1088/0953-4075/26/23/013 ↑174

Cacciari, C., & Clementini, G. 2003, Globular Cluster Distances from RR Lyrae Stars, ed. D. Alloin & W. Gieren, Vol. 635, 105–122 ↑35

Cacciari, C., Corwin, T. M., & Carney, B. W. 2005, AJ, 129, 267, doi: 10.1086/426325 ↑41

Caputo, F., Castellani, V., Marconi, M., & Ripepi, V. 2000, MNRAS, 316, 819, doi: 10.1046/j.1365-8711.2000.03591.x ↑35

Carollo, D., Beers, T. C., Lee, Y. S., et al. 2007, Nature, 450, 1020, doi: 10.1038/nature06460 ↑10

Carretta, E., Bragaglia, A., Gratton, R., D'Orazi, V., & Lucatello, S. 2009, A&A, 508, 695, doi: 10.1051/0004-6361/200913003 ↑xi, ↑44, ↑99, ↑103

Carretta, E., Bragaglia, A., Lucatello, S., et al. 2017, A&A, 600, A118, doi: 10.1051/0004-6361/201630004 ↑viii, ↑56

Carretta, E., Gratton, R. G., Bragaglia, A., Bonifacio, P., & Pasquini, L. 2004, A&A, 416, 925, doi: 10.1051/0004-6361:20034370 ↑54

Carretta, E., Bragaglia, A., Gratton, R. G., et al. 2010, A&A, 520, A95, doi: 10.1051/0004-6361/201014924 ↑viii, ↑59

Castelli, F., Gratton, R. G., & Kurucz, R. L. 1997, A&A, 318, 841 ↑82

Castelli, F., & Kurucz, R. L. 2003, in IAU Symposium, Vol. 210, Modelling of Stellar Atmospheres, ed. N. Piskunov, W. W. Weiss, & D. F. Gray, A20 ↑82

Catelan, M. 2009a, in IAU Symposium, Vol. 258, The Ages of Stars, ed. E. E. Mamajek, D. R. Soderblom, & R. F. G. Wyse, 209–220 ↑vii, ↑35

Catelan, M. 2009b, Ap&SS, 320, 261, doi: 10.1007/s10509-009-9987-8 ↑21, ↑25

Catelan, M., Pritzl, B. J., & Smith, H. A. 2004, ApJS, 154, 633, doi: 10.1086/422916 ↑35

Catelan, M., & Smith, H. A. 2015, Pulsating Stars ↑21

Cayrel, R., Depagne, E., Spite, M., et al. 2004, A&A, 416, 1117, doi: 10.1051/0004-6361:20034074 ↑xii, ↑55, ↑125

Çalışkan, Ş., Christlieb, N., & Grebel, E. K. 2012, A&A, 537, A83, doi: 10.1051/0004-6361/201016355 ↑viii, ↑56

Chabrier, G. 2003, PASP, 115, 763, doi: 10.1086/376392 ↑27

Chadid, M., Sneden, C., & Preston, G. W. 2017, ApJ, 835, 187, doi: 10.3847/1538-4357/835/2/187 ↑39, ↑43, ↑74, ↑87, ↑125

Chang, T. N., & Tang, X. 1990, J. Quant. Spec. Radiat. Transf., 43, 207, doi: 10.1016/0022-4073(90)90053-9 ↑174

Christy, R. F. 1966, ARA&A, 4, 353, doi: 10.1146/annurev.aa.04.090166.002033 ↑31

Clementini, G., Cacciari, C., & Lindgren, H. 1990, A&AS, 85, 865 ↑x, ↑94

Clementini, G., Carretta, E., Gratton, R., et al. 1995, AJ, 110, 2319, doi: 10.1086/117692 ↑74, ↑125

Conroy, C., Naidu, R. P., Zaritsky, D., et al. 2019, ApJ, 887, 237, doi: 10.3847/1538-4357/ab5710 ↑10

Cosentino, R., Lovis, C., Pepe, F., et al. 2012, in Society of Photo-Optical Instrumentation Engineers (SPIE) Conference Series, Vol. 8446, Proc. SPIE, 84461V ↑70

Cox, J. P. 1967, in IAU Symposium, Vol. 28, Aerodynamic Phenomena in Stellar Atmospheres, ed. R. N. Thomas, 3 ↑31

Crause, L. A., Sharples, R. M., Bramall, D. G., et al. 2014, in Society of Photo-Optical Instrumentation Engineers (SPIE) Conference Series, Vol. 9147, Ground-based and Airborne Instrumentation for Astronomy V, 91476T ↑70

Crestani, J., Alves-Brito, A., Bono, G., Puls, A. A., & Alonso-García, J. 2019, MNRAS, 487, 5463, doi: 10.1093/mnras/stz1674 ↑viii, ↑48, ↑56, ↑138, ↑153

Crestani, J., Fabrizio, M., Braga, V. F., et al. 2021a, ApJ, 908, 20, doi: 10.3847/1538-4357/abd183 ↑78, ↑87, ↑105, ↑153, ↑155

Crestani, J., Braga, V. F., Fabrizio, M., et al. 2021b, ApJ, 914, 10, doi: 10.3847/1538-4357/abfa23 ↑78, ↑105, ↑153, ↑155

Da Costa, G. S., Rejkuba, M., Jerjen, H., & Grebel, E. K. 2010, ApJ, 708, L121, doi: 10.1088/2041-8205/708/2/L121 ↑26

da Silva, R., Lemasle, B., Bono, G., et al. 2016, A&A, 586, A125, doi: 10.1051/0004-6361/201527300 ↑63, ↑64, ↑149

Dambis, A. K., Berdnikov, L. N., Kniazev, A. Y., et al. 2013, MNRAS, 435, 3206, doi: 10.1093/mnras/stt1514 ↑42

D'Antona, F., Caloi, V., Montalbán, J., Ventura, P., & Gratton, R. 2002, A&A, 395, 69, doi: 10.1051/0004-6361:20021220 ↑24

Deason, A. J., Belokurov, V., & Evans, N. W. 2011, MNRAS, 416, 2903, doi: 10.1111/j.1365-2966.2011.19237.x ↑12

Dekker, H., D'Odorico, S., Kaufer, A., Delabre, B., & Kotzlowski, H. 2000, in Society of Photo-Optical Instrumentation Engineers (SPIE) Conference Series, Vol. 4008, Proc. SPIE, ed. M. Iye & A. F. Moorwood, 534–545 ↑70

Den Hartog, E. A., Lawler, J. E., Sneden, C., & Cowan, J. J. 2003, ApJS, 148, 543, doi: 10.1086/376940 ↑65, ↑174

Den Hartog, E. A., Lawler, J. E., Sneden, C., Cowan, J. J., & Brukhovesky, A. 2019, ApJS, 243, 33, doi: 10.3847/1538-4365/ab322e ↑174

Den Hartog, E. A., Lawler, J. E., Sobeck, J. S., Sneden, C., & Cowan, J. J. 2011, ApJS, 194, 35, doi: 10.1088/0067-0049/194/2/35 ↑174

Den Hartog, E. A., Ruffoni, M. P., Lawler, J. E., et al. 2014, ApJS, 215, 23, doi: 10.1088/0067-0049/215/2/23 ↑174

Den Hartog, E. A., Wickliffe, M. E., & Lawler, J. E. 2002, ApJS, 141, 255, doi: 10.1086/340039 ↑65

Deras, D., Arellano Ferro, A., Muneer, S., Giridhar, S., & Michel, R. 2018, Astronomische Nachrichten, 339, 603, doi: 10.1002/asna.201813489 ↑42

Di Criscienzo, M., Marconi, M., & Caputo, F. 2004, ApJ, 612, 1092, doi: 10.1086/422742 ↑35, ↑36

Di Matteo, P., Haywood, M., Lehnert, M. D., et al. 2019, A&A, 632, A4, doi: 10.1051/0004-6361/201834929 ↑13

Dorman, B. 1995, in Liege International Astrophysical Colloquia, Vol. 32, Liege International Astrophysical Colloquia, 291 ↑24

Drake, A. J., Catelan, M., Djorgovski, S. G., et al. 2013, ApJ, 763, 32, doi: 10.1088/0004-637X/763/1/32 ↑26, ↑39

Drake, A. J., Djorgovski, S. G., Catelan, M., et al. 2017, MNRAS, 469, 3688, doi: 10.1093/mnras/stx1085 ↑v, ↑18

Drout, M. R., Piro, A. L., Shappee, B. J., et al. 2017, Science, 358, 1570, doi: 10.1126/science.aaq0049 ↑61

Duong, L., Asplund, M., Nataf, D. M., Freeman, K. C., & Ness, M. 2019, MNRAS, 486, 5349, doi: 10.1093/mnras/stz1183 ↑55

Eddington, A. S. 1918, MNRAS, 79, 2 ↑20

—. 1926, The Internal Constitution of the Stars ↑29

Eggen, O. J., Lynden-Bell, D., & Sandage, A. R. 1962, ApJ, 136, 748, doi: 10.1086/147433 ↑1, ↑5

Ernandes, H., Barbuy, B., Alves-Brito, A., et al. 2018, A&A, 616, A18, doi: 10.1051/0004-6361/201731708 ↑59, ↑60

Fabrizio, M., Bono, G., Braga, V. F., et al. 2019, ApJ, 882, 169, doi: 10.3847/1538-4357/ab3977 ↑vii, ↑xi, ↑34, ↑42, ↑43, ↑44, ↑87, ↑88, ↑89, ↑100, ↑104, ↑106, ↑138

Fabrizio, M., Braga, V. F., Crestani, J., et al. 2021a, arXiv e-prints, arXiv:2107.00919. https://arxiv.org/abs/2107.00919 ↑4, ↑13

—. 2021b, ApJ, 919, 118, doi: 10.3847/1538-4357/ac1115 ↑138, ↑140, ↑149, ↑153

Fernández-Alvar, E., Carigi, L., Allende Prieto, C., et al. 2017, MNRAS, 465, 1586, doi: 10.1093/mnras/stw2861 ↑10

Fernley, J., & Barnes, T. G. 1996, A&A, 312, 957 ↑74

Fiorentino, G., Bono, G., Monelli, M., et al. 2015, ApJ, 798, L12, doi: 10.1088/2041-8205/798/1/L12 ↑13, ↑46

Fiorentino, G., Monelli, M., Stetson, P. B., et al. 2017, A&A, 599, A125, doi: 10.1051/0004-6361/201629501 ↑vii, ↑14, ↑26, ↑45, ↑46

Fleming, W. P. 1893, Project PHAEDRA: Preserving Harvard's Early Data and Research in Astronomy (https://library.cfa.harvard.edu/project-phaedra). Harvard College Observatory observations, 24, 826 ↑v, ↑20

Font, A. S., Johnston, K. V., Bullock, J. S., & Robertson, B. E. 2006, ApJ, 646, 886, doi: 10.1086/505131 ↑13

Font, A. S., McCarthy, I. G., Crain, R. A., et al. 2011, MNRAS, 416, 2802, doi: 10.1111/j.1365-2966.2011.19227.x ↑9, ↑146

For, B.-Q., & Sneden, C. 2010, AJ, 140, 1694, doi: 10.1088/0004-6256/140/6/1694 ↑63, ↑70, ↑74

For, B.-Q., Sneden, C., & Preston, G. W. 2011, ApJS, 197, 29, doi: 10.1088/0067-0049/197/2/29 ↑2, ↑23, ↑39, ↑74, ↑83, ↑87

Frebel, A. 2010, Astronomische Nachrichten, 331, 474, doi: 10.1002/asna.201011362 ↑viii, ↑55, ↑56, ↑63, ↑64, ↑122

Freeman, K., & Bland-Hawthorn, J. 2002, ARA&A, 40, 487, doi: 10.1146/annurev.astro.40.060401.093840 ↑1

Gaia Collaboration, Prusti, T., de Bruijne, J. H. J., et al. 2016, A&A, 595, A1, doi: 10.1051/0004-6361/201629272 ↑1

Gallagher, A. 1967, Physical Review, 157, 24, doi: 10.1103/PhysRev.157.24 ↑174

García Pérez, A. E., Allende Prieto, C., Holtzman, J. A., et al. 2016, AJ, 151, 144, doi: 10.3847/0004-6256/151/6/144 ↑10

Gardner, J. P., Mather, J. C., Clampin, M., et al. 2006, Space Sci. Rev., 123, 485, doi: 10.1007/s11214-006-8315-7 ↑143

Garz, T. 1973, A&A, 26, 471 ↑174

Gehren, T., Liang, Y. C., Shi, J. R., Zhang, H. W., & Zhao, G. 2004, A&A, 413, 1045, doi: 10.1051/0004-6361:20031582 ↑123

Genovali, K., Lemasle, B., da Silva, R., et al. 2015, A&A, 580, A17, doi: 10.1051/0004-6361/201525894 ↑10

Gilligan, C. K., Chaboyer, B., Marengo, M., et al. 2021, MNRAS, 503, 4719, doi: 10.1093/mnras/stab857 ↑153

Gingerich, O. 1999, PASP, 111, 254, doi: 10.1086/316324 ↑21

Goranskij, V. P. 1981, Information Bulletin on Variable Stars, 2007, 1 ↑17

Govea, J., Gomez, T., Preston, G. W., & Sneden, C. 2014, ApJ, 782, 59, doi: 10.1088/0004-637X/782/2/59 ↑74

Gratton, R., Sneden, C., & Carretta, E. 2004a, ARA&A, 42, 385, doi: 10.1146/annurev.astro.42.053102.133945 ↑55

Gratton, R. G., Bragaglia, A., Clementini, G., et al. 2004b, A&A, 421, 937, doi: 10.1051/0004-6361:20035840 ↑42

Gratton, R. G., Carretta, E., & Bragaglia, A. 2012, A&A Rev., 20, 50, doi: 10.1007/s00159-012-0050-3 ↑24, ↑55

Gratton, R. G., & Sneden, C. 1991, A&A, 241, 501 ↑59

Gratton, R. G., Lucatello, S., Sollima, A., et al. 2013, A&A, 549, A41, doi: 10.1051/0004-6361/201219976 ↑viii, ↑56

Gray, D. F. 2005, The Observation and Analysis of Stellar Photospheres ↑47

Grisoni, V., Spitoni, E., Matteucci, F., et al. 2017, MNRAS, 472, 3637, doi: 10.1093/mnras/stx2201 ↑8

Grosse, E., & Schorr, R. R. E. 1932, Astronomische Abhandlungen der Hamburger Sternwarte, 4, 39 ↑21

Hajdu, G., Dékány, I., Catelan, M., Grebel, E. K., & Jurcsik, J. 2018, ApJ, 857, 55, doi: 10.3847/1538-4357/aab4fd ↑41

Hanke, M., Koch, A., Hansen, C. J., & McWilliam, A. 2017, A&A, 599, A97, doi: 10.1051/0004-6361/201629650 ↑viii, ↑56

Hannaford, P., Lowe, R. M., Grevesse, N., Biemont, E., & Whaling, W. 1982, ApJ, 261, 736, doi: 10.1086/160384 ↑174

Hansen, C. J., Bergemann, M., Cescutti, G., et al. 2013, A&A, 551, A57, doi: 10.1051/0004-6361/201220584 ↑61, ↑63

Hansen, C. J., Nordström, B., Bonifacio, P., et al. 2011, A&A, 527, A65, doi: 10.1051/0004-6361/201015076 ↑74

Helmi, A., Babusiaux, C., Koppelman, H. H., et al. 2018, Nature, 563, 85, doi: 10.1038/s41586-018-0625-x ↑7

Helmi, A., Irwin, M. J., Tolstoy, E., et al. 2006, ApJ, 651, L121, doi: 10.1086/509784 ↑12

Holtzman, J. A., Shetrone, M., Johnson, J. A., et al. 2015, AJ, 150, 148, doi: 10.1088/0004-6256/150/5/148 ↑10

Horta, D., Schiavon, R. P., Mackereth, J. T., et al. 2021, MNRAS, 500, 1385, doi: 10.1093/mnras/staa2987 ↑14

Hoyle, F., & Schwarzschild, M. 1955, ApJS, 2, 1, doi: 10.1086/190015 ↑20

Hubble, E. 1929, Proceedings of the National Academy of Science, 15, 168, doi: 10.1073/pnas.15.3.168 ↑21

Hubble, E. P. 1925, The Observatory, 48, 139 ↑21

Ibata, R. A., Gilmore, G., & Irwin, M. J. 1994, Nature, 370, 194, doi: 10.1038/370194a0 ↑6

Iben, Icko, J. 1971, PASP, 83, 697, doi: 10.1086/129210 ↑vi, ↑28, ↑29

Inno, L., Matsunaga, N., Bono, G., et al. 2013, ApJ, 764, 84, doi: 10.1088/0004-637X/764/1/84 ↑36

Iorio, G., Belokurov, V., Erkal, D., et al. 2018, MNRAS, 474, 2142, doi: 10.1093/mnras/stx2819 ↑11, ↑12

Ishigaki, M. N., Aoki, W., & Chiba, M. 2013, ApJ, 771, 67, doi: 10.1088/0004-637X/771/1/67 ↑viii, ↑56

Ivezić, Ž., Kahn, S. M., Tyson, J. A., et al. 2019, ApJ, 873, 111, doi: 10.3847/1538-4357/ab042c ↑26, ↑40

Jang, S., Lee, Y. W., Joo, S. J., & Na, C. 2014, MNRAS, 443, L15, doi: 10.1093/mnrasl/slu064 ↑24

Jean-Baptiste, I., Di Matteo, P., Haywood, M., et al. 2017, A&A, 604, A106, doi: 10.1051/0004-6361/201629691 ↑13

Johnson, C. I., Caldwell, N., Rich, R. M., et al. 2017, ApJ, 836, 168, doi: 10.3847/1538-4357/836/2/168 ↑viii, ↑56, ↑122

Johnson, J. A. 2019, Science, 363, 474, doi: 10.1126/science.aau9540 ↑47

Jones, K. M., Julienne, P. S., Lett, P. D., et al. 1996, EPL (Europhysics Letters), 35, 85, doi: 10.1209/epl/i1996-00536-9 ↑174

Jørgensen, H. E., & Petersen, J. O. 1967, Zeitschrift fur Astrophysik, 67, 377 ↑22, ↑30

Jurcsik, J., Hajdu, G., Dékány, I., et al. 2018, MNRAS, 475, 4208, doi: 10.1093/mnras/sty112 ↑17

Jurcsik, J., & Kovacs, G. 1996, A&A, 312, 111 ↑39, ↑41

Karakas, A. I., & Lattanzio, J. C. 2014, PASA, 31, e030, doi: 10.1017/pasa.2014.21 ↑57, ↑61

Karakas, A. I., & Lugaro, M. 2016, ApJ, 825, 26, doi: 10.3847/0004-637X/825/1/26 ↑61

Karlsson, T., Bromm, V., & Bland-Hawthorn, J. 2013, Reviews of Modern Physics, 85, 809, doi: 10.1103/RevModPhys.85.809 ↑27

Kaufer, A., Stahl, O., Tubbesing, S., et al. 1999, The Messenger, 95, 8 ↑70

Kemper, E. 1982, AJ, 87, 1395, doi: 10.1086/113229 ↑42

Kervella, P., Gallenne, A., Remage Evans, N., et al. 2019, A&A, 623, A116, doi: 10.1051/0004-6361/201834210 ↑2, ↑15

Kinman, T. D., Cacciari, C., Bragaglia, A., Smart, R., & Spagna, A. 2012, MNRAS, 422, 2116, doi: 10.1111/j.1365-2966.2012.20747.x ↑10

Kobayashi, C., Karakas, A. I., & Umeda, H. 2011, MNRAS, 414, 3231, doi: 10.1111/j.1365-2966.2011.18621.x ↑59

Kobayashi, C., & Nakasato, N. 2011, ApJ, 729, 16, doi: 10.1088/0004-637X/729/1/16 ↑59

Kobayashi, C., Umeda, H., Nomoto, K., Tominaga, N., & Ohkubo, T. 2006, ApJ, 653, 1145, doi: 10.1086/508914 ↑56, ↑115

Koch, A., & Côté, P. 2019, A&A, 632, A55, doi: 10.1051/0004-6361/201936710 ↑viii, ↑56

Koch, A., Grebel, E. K., & Martell, S. L. 2019a, A&A, 625, A75, doi: 10.1051/0004-6361/201834825 ↑13

Koch, A., Xu, S., & Rich, R. M. 2019b, A&A, 627, A70, doi: 10.1051/0004-6361/201935467 ↑viii, ↑56

Kock, M., Kroll, S., & Schnehage, S. 1984, Physica Scripta Volume T, 8, 84, doi: 10.1088/0031-8949/1984/T8/013 ↑174

Kolenberg, K., Fossati, L., Shulyak, D., et al. 2010, A&A, 519, A64, doi: 10.1051/0004-6361/201014471 ↑74

Köstlin, H. 1964, Zeitschrift fur Physik, 178, 200, doi: 10.1007/BF01377942 ↑174

Kostyk, R. I. 1982, Astrometriia i Astrofizika, 46, 58 ↑174

Kostyk, R. I., & Orlova, T. V. 1983, Astrometriia i Astrofizika, 49, 39 ↑174

Kovacs, G., & Zsoldos, E. 1995, A&A, 293, L57 ↑40

Kramers, H. A. 1923, The London, Edinburgh, and Dublin Philosophical Magazine and Journal of Science, 46, 836, doi: 10.1080/14786442308565244 ↑29

Kroupa, P. 2001, MNRAS, 322, 231, doi: 10.1046/j.1365-8711.2001.04022.x ↑27

Kruijssen, J. M. D., Pfeffer, J. L., Reina-Campos, M., Crain, R. A., & Bastian, N. 2019, MNRAS, 486, 3180, doi: 10.1093/mnras/sty1609 ↑24

Kunder, A., & Chaboyer, B. 2008, AJ, 136, 2441, doi: 10.1088/0004-6256/136/6/2441 ↑42

Lambert, D. L., Heath, J. E., Lemke, M., & Drake, J. 1996, ApJS, 103, 183, doi: 10.1086/192274 ↑74

Lancaster, L., Koposov, S. E., Belokurov, V., Evans, N. W., & Deason, A. J. 2019, MNRAS, 486, 378, doi: 10.1093/mnras/stz853 ↑109

Lardo, C., Salaris, M., Bastian, N., et al. 2018, A&A, 616, A168, doi: 10.1051/0004-6361/201832999 ↑54

Lawler, J. E., Bonvallet, G., & Sneden, C. 2001a, ApJ, 556, 452, doi: 10.1086/321549 ↑174

Lawler, J. E., Guzman, A., Wood, M. P., Sneden, C., & Cowan, J. J. 2013, ApJS, 205, 11, doi: 10.1088/0067-0049/205/2/11 ↑174

Lawler, J. E., Hala, Sneden, C., et al. 2019, ApJS, 241, 21, doi: 10.3847/1538-4365/ab08ef ↑174

Lawler, J. E., Sneden, C., & Cowan, J. J. 2015, ApJS, 220, 13, doi: 10.1088/0067-0049/220/1/13 ↑174

Lawler, J. E., Sneden, C., Cowan, J. J., Ivans, I. I., & Den Hartog, E. A. 2009, ApJS, 182, 51, doi: 10.1088/0067-0049/182/1/51 ↑65, ↑174

Lawler, J. E., Sneden, C., Nave, G., et al. 2017, ApJS, 228, 10, doi: 10.3847/1538-4365/228/1/10 ↑174

Lawler, J. E., Wickliffe, M. E., den Hartog, E. A., & Sneden, C. 2001b, ApJ, 563, 1075, doi: 10.1086/323407 ↑174

Lawler, J. E., Wood, M. P., Den Hartog, E. A., et al. 2014, ApJS, 215, 20, doi: 10.1088/0067-0049/215/2/20 ↑174

Layden, A. C. 1994, AJ, 108, 1016, doi: 10.1086/117132 ↑3, ↑39

Leavitt, H. S., & Pickering, E. C. 1912, Harvard College Observatory Circular, 173, 1 ↑21

Lee, J.-W., López-Morales, M., Hong, K., et al. 2014, ApJS, 210, 6, doi: 10.1088/0067-0049/210/1/6 ↑v, ↑16

Lee, Y.-W., Demarque, P., & Zinn, R. 1994, ApJ, 423, 248, doi: 10.1086/173803 ↑24, ↑25

Lemasle, B., de Boer, T. J. L., Hill, V., et al. 2014, A&A, 572, A88, doi: 10.1051/0004-6361/201423919 ↑viii, ↑59

Lind, K., Asplund, M., Barklem, P. S., & Belyaev, A. K. 2011, A&A, 528, A103, doi: 10.1051/0004-6361/201016095 ↑123

Liu, G. C., Huang, Y., Zhang, H. W., et al. 2020, ApJS, 247, 68, doi: 10.3847/1538-4365/ab72f8 ↑xi, ↑100, ↑104

Liu, S., Zhao, G., Chen, Y.-Q., Takeda, Y., & Honda, S. 2013, Research in Astronomy and Astrophysics, 13, 1307, doi: 10.1088/1674-4527/13/11/003 ↑23, ↑63, ↑74, ↑113, ↑119, ↑125

Ljung, G., Nilsson, H., Asplund, M., & Johansson, S. 2006, A&A, 456, 1181, doi: 10.1051/0004-6361:20065212 ↑174

Lomaeva, M., Jönsson, H., Ryde, N., Schultheis, M., & Thorsbro, B. 2019, A&A, 625, A141, doi: 10.1051/0004-6361/201834247 ↑59

Longmore, A. J., Dixon, R. I., & Buckley, D. R. V. 1990, in Astronomical Society of the Pacific Conference Series, Vol. 11, Confrontation Between Stellar Pulsation and Evolution, ed. C. Cacciari & G. Clementini, 36–40 ↑35

Longmore, A. J., Fernley, J. A., & Jameson, R. F. 1986, MNRAS, 220, 279, doi: 10.1093/mnras/220.2.279 ↑22, ↑35

Luck, R. E., Kovtyukh, V. V., & Andrievsky, S. M. 2006, AJ, 132, 902, doi: 10.1086/505687 ↑149

Mackereth, J. T., & Bovy, J. 2020, MNRAS, 492, 3631, doi: 10.1093/mnras/staa047 ↑11

Madore, B. F. 1982, ApJ, 253, 575, doi: 10.1086/159659 ↑36

Madore, B. F., Hoffman, D., Freedman, W. L., et al. 2013, ApJ, 776, 135, doi: 10.1088/0004-637X/776/2/135 ↑17, ↑38

Magurno, D., Sneden, C., Braga, V. F., et al. 2018, ApJ, 864, 57, doi: 10.3847/1538-4357/aad4a3 ↑39, ↑63, ↑84

Magurno, D., Sneden, C., Bono, G., et al. 2019, ApJ, 881, 104, doi: 10.3847/1538-4357/ab2e76 ↑2, ↑39, ↑63, ↑109

Mahadevan, S., Ramsey, L., Bender, C., et al. 2012, in Society of Photo-Optical Instrumentation Engineers (SPIE) Conference Series, Vol. 8446, Ground-based and Airborne Instrumentation for Astronomy IV, ed. I. S. McLean, S. K. Ramsay, & H. Takami, 84461S ↑70

Mainzer, A., Bauer, J., Grav, T., et al. 2011, ApJ, 731, 53, doi: 10.1088/0004-637X/731/1/53 ↑143

Majewski, S. R., Skrutskie, M. F., Weinberg, M. D., & Ostheimer, J. C. 2003, ApJ, 599, 1082, doi: 10.1086/379504 ↑1

Majewski, S. R., Schiavon, R. P., Frinchaboy, P. M., et al. 2017, AJ, 154, 94, doi: 10.3847/1538-3881/aa784d ↑1

Marconi, M. 2009, in American Institute of Physics Conference Series, Vol. 1170, American Institute of Physics Conference Series, ed. J. A. Guzik & P. A. Bradley, 223–234 ↑vii, ↑34

Marconi, M., Bono, G., Pietrinferni, A., et al. 2018, ApJ, 864, L13, doi: 10.3847/2041-8213/aada17 ↑24, ↑25, ↑36, ↑38

Marconi, M., Coppola, G., Bono, G., et al. 2015, ApJ, 808, 50, doi: 10.1088/0004-637X/808/1/50 ↑v, ↑vi, ↑16, ↑24, ↑30, ↑35, ↑38

Marino, A. F., Milone, A. P., Przybilla, N., et al. 2014, MNRAS, 437, 1609, doi: 10.1093/mnras/stt1993 ↑24

Martin, C., & Plummer, H. C. 1915, MNRAS, 75, 566, doi: 10.1093/mnras/75.7.566 ↑20

Matheron, P., Escarguel, A., Redon, R., Lesage, A., & Richou, J. 2001, J. Quant. Spec. Radiat. Transf., 69, 535, doi: 10.1016/S0022-4073(00)00087-X ↑174

Matteucci, F. 2003, Ap&SS, 284, 539, doi: 10.1023/A:1024089402368 ↑47

May, M., Richter, J., & Wichelmann, J. 1974, A&AS, 18, 405 ↑174

Mayor, M., Pepe, F., Queloz, D., et al. 2003, The Messenger, 114, 20 ↑70

McCarthy, I. G., Font, A. S., Crain, R. A., et al. 2012, MNRAS, 420, 2245, doi: 10.1111/j.1365-2966.2011.20189.x ↑9, ↑146

McWilliam, A. 1997, ARA&A, 35, 503, doi: 10.1146/annurev.astro.35.1.503 ↑viii, ↑57, ↑115

—. 2016, PASA, 33, e040, doi: 10.1017/pasa.2016.32 ↑8, ↑55, ↑56, ↑59, ↑60, ↑64

Meléndez, J., & Barbuy, B. 2009a, A&A, 497, 611, doi: 10.1051/0004-6361/200811508 ↑145

—. 2009b, A&A, 497, 611, doi: 10.1051/0004-6361/200811508 ↑174

Mendoza, C., Eissner, W., LeDourneuf, M., & Zeippen, C. J. 1995, Journal of Physics B Atomic Molecular Physics, 28, 3485, doi: 10.1088/0953-4075/28/16/006 ↑174

Milone, A. P., Marino, A. F., Renzini, A., et al. 2018, MNRAS, 481, 5098, doi: 10.1093/mnras/sty2573 ↑24

Minniti, D., Lucas, P. W., Emerson, J. P., et al. 2010, New Astronomy, 15, 433, doi: 10.1016/j.newast.2009.12.002 ↑41

Moehler, S., Dreizler, S., LeBlanc, F., et al. 2014, A&A, 565, A100, doi: 10.1051/0004-6361/201322953 ↑25

Monachesi, A., Gómez, F. A., Grand, R. J. J., et al. 2019, MNRAS, 485, 2589, doi: 10.1093/mnras/stz538 ↑8

Monelli, M., Fiorentino, G., Bernard, E. J., et al. 2017, ApJ, 842, 60, doi: 10.3847/1538-4357/aa738d ↑26

Moore, C. E., Minnaert, M. G. J., & Houtgast, J. 1966, The solar spectrum 2935 A to 8770 A ↑78, ↑145

Mullen, J. P., Marengo, M., Martínez-Vázquez, C. E., et al. 2021, ApJ, 912, 144, doi: 10.3847/1538-4357/abefd4 ↑4, ↑143, ↑154

Muraveva, T., Delgado, H. E., Clementini, G., Sarro, L. M., & Garofalo, A. 2018, MNRAS, 481, 1195, doi: 10.1093/mnras/sty2241 ↑17

Myeong, G. C., Vasiliev, E., Iorio, G., Evans, N. W., & Belokurov, V. 2019, MNRAS, 488, 1235, doi: 10.1093/mnras/stz1770 ↑7

Naidu, R. P., Conroy, C., Bonaca, A., et al. 2020, ApJ, 901, 48, doi: 10.3847/1538-4357/abaef4 ↑14

Nemec, J. M. 1985, AJ, 90, 204, doi: 10.1086/113727 ↑17

Nemec, J. M., Cohen, J. G., Ripepi, V., et al. 2013, ApJ, 773, 181, doi: 10.1088/0004-637X/773/2/181 ↑74, ↑100

Nissen, P. E., & Schuster, W. J. 2010, A&A, 511, L10, doi: 10.1051/0004-6361/200913877 ↑viii, ↑11, ↑12, ↑56, ↑72, ↑75, ↑121, ↑126, ↑127, ↑148

—. 2011, A&A, 530, A15, doi: 10.1051/0004-6361/201116619 ↑viii, ↑11, ↑56, ↑126, ↑127, ↑131

Noguchi, K., Aoki, W., Kawanomoto, S., et al. 2002, PASJ, 54, 855, doi: 10.1093/pasj/54.6.855 ↑70

Nomoto, K., Kobayashi, C., & Tominaga, N. 2013, ARA&A, 51, 457, doi: 10.1146/annurev-astro-082812-140956 ↑59

Nomoto, K., Tominaga, N., Umeda, H., Kobayashi, C., & Maeda, K. 2006, Nucl. Phys. A, 777, 424, doi: 10.1016/j.nuclphysa.2006.05.008 ↑56

O'Brian, T. R., Wickliffe, M. E., Lawler, J. E., Whaling, W., & Brault, J. W. 1991, Journal of the Optical Society of America B Optical Physics, 8, 1185, doi: 10.1364/JOSAB.8.001185 ↑174

Olsen, K. H., Routly, P. M., & King, R. B. 1959, ApJ, 130, 688, doi: 10.1086/146758 ↑174

Oosterhoff, P. T. 1939, The Observatory, 62, 104 ↑21, ↑33, ↑137

Osborn, W. 1971, The Observatory, 91, 223 ↑24

Pancino, E., Britavskiy, N., Romano, D., et al. 2015, MNRAS, 447, 2404, doi: 10.1093/mnras/stu2616 ↑74, ↑100

Pancino, E., Carrera, R., Rossetti, E., & Gallart, C. 2010, A&A, 511, A56, doi: 10.1051/0004-6361/200912965 ↑67, ↑77

Parkinson, W. H., Reeves, E. M., & Tomkins, F. S. 1976, Journal of Physics B Atomic Molecular Physics, 9, 157, doi: 10.1088/0022-3700/9/2/006 ↑174

Payne, C. H. 1925, PhD thesis, RADCLIFFE COLLEGE. ↑20

Pickering, E. C. 1895, Popular Astronomy, 3, 197 ↑20

Pickering, E. C., Colson, H. R., Fleming, W. P., & Wells, L. D. 1901, ApJ, 13, 226, doi: 10.1086/140808 ↑19

Pickering, J. C., Thorne, A. P., & Perez, R. 2001, ApJS, 132, 403, doi: 10.1086/318958 ↑174

—. 2002, ApJS, 138, 247, doi: 10.1086/323910 ↑174

Pietrinferni, A., Cassisi, S., Salaris, M., & Castelli, F. 2006, ApJ, 642, 797, doi: 10.1086/501344 ↑v, ↑16

Pietrukowicz, P., Udalski, A., Soszyński, I., et al. 2012, ApJ, 750, 169, doi: 10.1088/0004-637X/750/2/169 ↑42

Pietrzyński, G., Thompson, I. B., Gieren, W., et al. 2012, Nature, 484, 75, doi: 10.1038/nature10966 ↑2, ↑15

Piotto, G., Bedin, L. R., Anderson, J., et al. 2007, ApJ, 661, L53, doi: 10.1086/518503 ↑24

Prantzos, N., & Charbonnel, C. 2006, A&A, 458, 135, doi: 10.1051/0004-6361:20065374 ↑55

Preston, G. W. 1959, ApJ, 130, 507, doi: 10.1086/146743 ↑3, ↑42

—. 1961, ApJ, 134, 633, doi: 10.1086/147185 ↑22

Pritzl, B. J., Venn, K. A., & Irwin, M. 2005, AJ, 130, 2140, doi: 10.1086/432911 ↑viii, ↑56, ↑63, ↑64, ↑65, ↑122

Prochaska, J. X., & McWilliam, A. 2000, ApJ, 537, L57, doi: 10.1086/312749 ↑53, ↑58, ↑59

Prudil, Z., Dékány, I., Grebel, E. K., & Kunder, A. 2020, MNRAS, 492, 3408, doi: 10.1093/mnras/staa046 ↑113, ↑146, ↑149

Prudil, Z., Skarka, M., Liška, J., Grebel, E. K., & Lee, C. U. 2019, MNRAS, 487, L1, doi: 10.1093/mnrasl/slz069 ↑2, ↑15

Prudil, Z., Hanke, M., Lemasle, B., et al. 2021, A&A, 648, A78, doi: 10.1051/0004-6361/202140422 ↑154

Ramírez, I., Allende Prieto, C., & Lambert, D. L. 2013, ApJ, 764, 78, doi: 10.1088/0004-637X/764/1/78 ↑12

Recio-Blanco, A., Aparicio, A., Piotto, G., de Angeli, F., & Djorgovski, S. G. 2006, A&A, 452, 875, doi: 10.1051/0004-6361:20053006 ↑25

Reddy, B. E., Lambert, D. L., & Allende Prieto, C. 2006, MNRAS, 367, 1329, doi: 10.1111/j.1365-2966.2006.10148.x ↑viii, ↑56, ↑63, ↑64, ↑65, ↑122

Reddy, B. E., Tomkin, J., Lambert, D. L., & Allende Prieto, C. 2003, MNRAS, 340, 304, doi: 10.1046/j.1365-8711.2003.06305.x ↑viii, ↑56, ↑63, ↑64, ↑122

Reichert, M., Hansen, C. J., Hanke, M., et al. 2020, A&A, 641, A127, doi: 10.1051/0004-6361/201936930 ↑viii, ↑59

Rey, S.-C., Lee, Y.-W., Joo, J.-M., Walker, A., & Baird, S. 2000, AJ, 119, 1824, doi: 10.1086/301304 ↑39, ↑40

Rich, R. M., Sosin, C., Djorgovski, S. G., et al. 1997, ApJ, 484, L25, doi: 10.1086/310758 ↑25

Roberts, J. R., Andersen, T., & Sorensen, G. 1973, ApJ, 181, 587, doi: 10.1086/152074 ↑174

Robertson, B., Bullock, J. S., Font, A. S., Johnston, K. V., & Hernquist, L. 2005, ApJ, 632, 872, doi: 10.1086/452619 ↑13

Roederer, I. U., & Lawler, J. E. 2012, ApJ, 750, 76, doi: 10.1088/0004-637X/750/1/76 ↑174

Roederer, I. U., Lawler, J. E., Sneden, C., et al. 2008, ApJ, 675, 723, doi: 10.1086/526452 ↑174

Ruffoni, M. P., Den Hartog, E. A., Lawler, J. E., et al. 2014, MNRAS, 441, 3127, doi: 10.1093/mnras/stu780 ↑174

Sakari, C. M., Venn, K. A., Irwin, M., et al. 2011, ApJ, 740, 106, doi: 10.1088/0004-637X/740/2/106 ↑viii, ↑56

Salaris, M., & Cassisi, S. 2005, Evolution of Stars and Stellar Populations ↑47

Salaris, M., Chieffi, A., & Straniero, O. 1993, ApJ, 414, 580, doi: 10.1086/173105 ↑52

Sandage, A. 1990, ApJ, 350, 603, doi: 10.1086/168415 ↑35

Sbordone, L., Bonifacio, P., Buonanno, R., et al. 2007, A&A, 465, 815, doi: 10.1051/0004-6361:20066385 ↑viii, ↑59

Schönberg, M., & Chandrasekhar, S. 1942, ApJ, 96, 161, doi: 10.1086/144444 ↑20

Schönrich, R., Asplund, M., & Casagrande, L. 2011, MNRAS, 415, 3807, doi: 10.1111/j.1365-2966.2011.19003.x ↑10

—. 2014, ApJ, 786, 7, doi: 10.1088/0004-637X/786/1/7 ↑10, ↑11

Schwarzschild, M. 1940, Harvard College Observatory Circular, 437, 1 ↑21, ↑22

Searle, L., & Zinn, R. 1978, ApJ, 225, 357, doi: 10.1086/156499 ↑1, ↑6, ↑45

Sellwood, J. A. 2014, Reviews of Modern Physics, 86, 1, doi: 10.1103/RevModPhys.86.1 ↑8

Sesar, B., Jurić, M., & Ivezić, Ž. 2011, ApJ, 731, 4, doi: 10.1088/0004-637X/731/1/4 ↑11

Sesar, B., Ivezić, Ž., Stuart, J. S., et al. 2013, AJ, 146, 21, doi: 10.1088/0004-6256/146/2/21 ↑11

Shapley, H. 1914, ApJ, 40, 448, doi: 10.1086/142137 ↑20

—. 1916, ApJ, 43, 217, doi: 10.1086/142246 ↑20, ↑21

—. 1918, ApJ, 48, 154, doi: 10.1086/142423 ↑21

Shappee, B. J., Prieto, J. L., Grupe, D., et al. 2014, ApJ, 788, 48, doi: 10.1088/0004-637X/788/1/48 ↑143

Shetrone, M. D., Côté, P., & Sargent, W. L. W. 2001, ApJ, 548, 592, doi: 10.1086/319022 ↑13

Simmerer, J., Sneden, C., Cowan, J. J., et al. 2004, ApJ, 617, 1091, doi: 10.1086/424504 ↑64

Smiljanic, R., Romano, D., Bragaglia, A., et al. 2016, A&A, 589, A115, doi: 10.1051/0004-6361/201528014 ↑xii, ↑125

Smith, W. W., & Gallagher, A. 1966, Physical Review, 145, 26, doi: 10.1103/PhysRev.145.26 ↑175

Smolec, R. 2005, Acta Astron., 55, 59. https://arxiv.org/abs/astro-ph/0503614 ↑41

Smolinski, J. P., Lee, Y. S., Beers, T. C., et al. 2011, AJ, 141, 89, doi: 10.1088/0004-6256/141/3/89 ↑3

Sneden, C. 1973a, ApJ, 184, 839, doi: 10.1086/152374 ↑49, ↑81

Sneden, C., Cowan, J. J., & Gallino, R. 2008, ARA&A, 46, 241, doi: 10.1146/annurev.astro.46.060407.145207 ↑61, ↑65

Sneden, C., Lawler, J. E., Cowan, J. J., Ivans, I. I., & Den Hartog, E. A. 2009, ApJS, 182, 80, doi: 10.1088/0067-0049/182/1/80 ↑127, ↑175

Sneden, C., Preston, G. W., Chadid, M., & Adamów, M. 2017, ApJ, 848, 68, doi: 10.3847/1538-4357/aa8b10 ↑2, ↑39, ↑74, ↑87

Sneden, C., Afşar, M., Bozkurt, Z., et al. 2021, AJ, 161, 128, doi: 10.3847/1538-3881/abd7ee ↑70

Sneden, C. A. 1973b, PhD thesis, THE UNIVERSITY OF TEXAS AT AUSTIN. ↑78

Snodgrass, C., Saviane, I., Monaco, L., & Sinclaire, P. 2008, The Messenger, 132, 18 ↑101

Sobeck, J. S., Lawler, J. E., & Sneden, C. 2007, ApJ, 667, 1267, doi: 10.1086/519987 ↑175

Sollima, A., Cassisi, S., Fiorentino, G., & Gratton, R. G. 2014, MNRAS, 444, 1862, doi: 10.1093/mnras/stu1564 ↑34

Soszyński, I., Dziembowski, W. A., Udalski, A., et al. 2011, Acta Astron., 61, 1. https://arxiv.org/abs/1105.6126 ↑41

Stellingwerf, R. F. 1974, ApJ, 192, 139, doi: 10.1086/153043 ↑31

—. 1975, ApJ, 195, 441, doi: 10.1086/153343 ↑31

Stephens, A., & Boesgaard, A. M. 2002, AJ, 123, 1647, doi: 10.1086/338898 ↑viii, ↑56, ↑122

Stothers, R. B. 1987, ApJ, 319, 260, doi: 10.1086/165451 ↑17

Suntzeff, N. B., Kinman, T. D., & Kraft, R. P. 1991, ApJ, 367, 528, doi: 10.1086/169650 ↑42

Thielemann, F. K., Arcones, A., Käppeli, R., et al. 2011, Progress in Particle and Nuclear Physics, 66, 346, doi: 10.1016/j.ppnp.2011.01.032 ↑61

Thorsbro, B., Ryde, N., Schultheis, M., et al. 2018, ApJ, 866, 52, doi: 10.3847/1538-4357/aadb97 ↑58

Tolstoy, E., Venn, K. A., Shetrone, M., et al. 2003, AJ, 125, 707, doi: 10.1086/345967 ↑13

Torelli, M., Iannicola, G., Stetson, P. B., et al. 2019, arXiv e-prints, arXiv:1907.09568. https://arxiv.org/abs/1907.09568 ↑24

Travaglio, C., Gallino, R., Arnone, E., et al. 2004, ApJ, 601, 864, doi: 10.1086/380507 ↑61

Vernet, J., Dekker, H., D'Odorico, S., et al. 2011, A&A, 536, A105, doi: 10.1051/0004-6361/201117752 ↑70

Walker, A. R., & Terndrup, D. M. 1991, ApJ, 378, 119, doi: 10.1086/170411 ↑42

Weber, M., Granzer, T., & Strassmeier, K. G. 2012, in Society of Photo-Optical Instrumentation Engineers (SPIE) Conference Series, Vol. 8451, Software and Cyberinfrastructure for Astronomy II, 84510K ↑70

Wolnik, S. J., & Berthel, R. O. 1973, ApJ, 179, 665, doi: 10.1086/151906 ↑175

Wood, M. P., Lawler, J. E., Sneden, C., & Cowan, J. J. 2013, ApJS, 208, 27, doi: 10.1088/0067-0049/208/2/27 ↑175

—. 2014, ApJS, 211, 20, doi: 10.1088/0067-0049/211/2/20 ↑175

Woosley, S. E., Heger, A., & Weaver, T. A. 2002, Reviews of Modern Physics, 74, 1015, doi: 10.1103/RevModPhys.74.1015 ↑58, ↑61

Woosley, S. E., & Weaver, T. A. 1994, ApJ, 423, 371, doi: 10.1086/173813 ↑56

—. 1995, ApJS, 101, 181, doi: 10.1086/192237 ↑59

Xue, X.-X., Rix, H.-W., Ma, Z., et al. 2015, ApJ, 809, 144, doi: 10.1088/0004-637X/809/2/144 ↑10, ↑11

Yanny, B., Rockosi, C., Newberg, H. J., et al. 2009, AJ, 137, 4377, doi: 10.1088/0004-6256/137/5/4377 ↑10, ↑72

Zatsarinny, O., & Bartschat, K. 2006, Journal of Physics B Atomic Molecular Physics, 39, 2861, doi: 10.1088/0953-4075/39/12/019 ↑175

Zhang, H. W., Gehren, T., & Zhao, G. 2008, A&A, 481, 489, doi: 10.1051/0004-6361:20078910 ↑59

Zhao, G., Zhao, Y.-H., Chu, Y.-Q., Jing, Y.-P., & Deng, L.-C. 2012, Research in Astronomy and Astrophysics, 12, 723, doi: 10.1088/1674-4527/12/7/002 ↑72

Zhevakin, S. A. 1963, ARA&A, 1, 367, doi: 10.1146/annurev.aa.01.090163.002055 ↑22, ↑30

Zinn, R. 1985, ApJ, 293, 424, doi: 10.1086/163249 ↑6

Zinn, R., & West, M. J. 1984, ApJS, 55, 45, doi: 10.1086/190947 ↑2, ↑4, ↑42, ↑43, ↑44, ↑95